Preparation and characterization of polyethylene based nanocomposites for potential applications in packaging

by

Yasir Qayyum Gill

A doctoral thesis submitted in partial fulfilment of the requirements

for the award of Doctor of Philosophy of

Loughborough University

Supervisor: Professor Mo Song
Department of Materials
School of Aeronautical, Automotive,
Chemical and Materials Engineering
Loughborough University

ACKNOWLEDGEMENTS

I would like to express my profound thankfulness to Professor Mo Song for his instrumental support, suggestion, inspiration, administration and useful recommendations throughout this research work. I have learned a great deal of nanocomposites research and development activity during my stay in the department of materials at Loughborough University, for which I owe large debt of gratitude to him. His moral and financial support along with continuous guidance enabled me to complete my work successfully. I am also thankful to Dr. Jie Jin for helping me with many different aspects of research, testing and analysing the results and her valuable suggestions throughout this study. I thank Dr. Ali ansarifar for his support and guidance throughout my PhD. His positive and critical comments at crucial stage of my work have been of great help for improving my thesis.

I would also like to express my sincere thanks to the technicians of the Department of Materials, Loughborough University, for their training of research and manufacturing machinery and also for their advises during my work.

And finally my deepest gratitude goes to my parents and my brothers for their moral support and their prayers, which were in unremitting and enabled me to reach this stage. I would also like to thank my friends who have been supporting me so patiently throughout my research.

Y.Q.Gill

TABLE OF CONTENTS

LIST OF FIGURES

LIST OF TABLES

Key Words

High density polyethylene (HDPE), Linear low density polyethylene (LLDPE), Nylo12, Kaolin, Sodium montmorillonite (Na-MMT), Multi walled carbon nanotubes (MWCNT), Carbon black (CB), Graphene oxide (GO), Xray diffraction (XRD), Transmission electron microscope (TEM), Scanning electron microscope (SEM), Rheology, Melt flow singularity, Water vapour transmission rate (WVTR), Oxygen transmission rate (O2TR), nanocomposites.

ABSTRACT

The objective of my work was to develop HDPE clay nanocomposites for packaging with superior barrier (gas and water) properties by economical processing technique. This work also represents a comparative study of thermoplastic nanocomposites for packaging based on linear low density polyethylene (LLDPE), high density polyethylene (HDPE) and Nylon12. In this study properties and processing of a series of linear low density polyethylene (LLDPE), high density polyethylene (HDPE) and Nylon 12 nanocomposites based on Na-MMT clay and two different aspect ratio grades of kaolinite clay are discussed. The nanocomposites were fabricated by melt compounding method without using any compatiblizers or surface treating agent for organoclay. A number of techniques including wide angle X-ray diffraction (XRD), transmission electron microscopy (TEM), scanning electron microscopy (SEM) and optical microscopy (OM), were employed to study microstructure and morphology of these nanocomposites. The water and oxygen barrier properties were studied in detail because they are the main indicator of a product quality that is to be used as a packaging material. The XRD and TEM results for kaolin clay based specimens indicated that by the addition of clay neither exfoliated nor is intercalated nanocomposite formed. The TEM and OM results on the other hand indicated that the dimensions of the dispersed clay particles were less than 100 nm which indicated the formation of a nanocomposite. The OM results also indicated the excellent dispersion of clay platelets in the polymer matrix. This dispersion resulted in the formation of tortuous path of clay particles in the

polymer matrix which caused a considerable reduction in the water and oxygen barrier properties for nanocomposites. The HDPE/Na-MMT composites showed the most broadened extrusion window up to 6.5^{o}C, the best result reported so far. In comparison to the exfoliated clay composites of HDPE, the intercalated and the micro-composites showed a reduced window with a maximum of 5.2^{o}C window observed for bentone clay composites. In case of HDPE the crystallization temperature and the melting temperature were also improved on the addition of kaolin clay, whereas no such phenomenon was observed in LLDPE and Nylon12 nanocomposites. Maximum enhancement in barrier properties was achieved for HDPE kaolin clay nanocomposites with water barrier properties showing a reduction of more than 60 % in comparison to pure HDPE. The effect of filler characteristics (shape and dimensions) on the final properties of HDPE was also studied for various HDPE/carbon filler nanocomposites In comparison to 1D and 2D nanofillers, the 3D-CB filler showed remarkable contribution to toughness but caused a reduction in extrusion window and barrier properties of HDPE, whereas the 1D and 2D nanofillers improved the barrier and thermal characteristics of HDPE.

List of abbreviation

PCN - Polymer clay nanocomposites

MMT - Montmorillonite

HDPE – High density polyethylene

LLDPE – Linear low density polyethylene

Na-MMT – Sodium montmorillonite

PETG - Polyethylene terephthlate glycol-modified

PBT - Polybutylene terephthalate

PPS - Polyphenylene sulphide

PC – Polycarbonate

UHMWPE – Ultra high molecular weight polyethylene

PVDC – Poly vinylidene chloride

EVOH – Ethylene-vinyl alcohol

PA – Polyamide

PCTFE – Polychloro trifluoro ethylene

LCPs - Liquid crystalline polymers

PHAE - Polyhydroxy amino ethers

PAN – Polyacrylonitrile

PE – Polyethylene

HOCP - hydrogenated-oligo(cyclopentadiene)

PS – Polystyrene

CB – Carbon black

MWCNT – Multi walled carbon nanotubes

GO – Graphene oxide

DMSO - Dimethyl sulfoxide

XRD - X-ray diffraction

TEM - Transmission electron microscopy

DSC – Differential scanning calorimetry

TGA – Thermo gravimetric analysis

SEM – Scanning electron microscopy

IFWIT – Instrumental falling weight impact testing

MFS – Melt flow singularity

0D, 1D, 2D and 3D – Zero dimensional, one dimensional, two dimensional and three dimensional

CHAPTER 1: INTRODUCTION AND AIMS OF THE PROJECT

1.1: Introduction

Nanotechnology is a multidisciplinary field which combines the knowledge of chemistry, physics, material science, electronics and biosciences to offer technological applications with novelty and multi-functionality not observed in any other filed [1]. Nanocomposites are a new class of materials that have bypassed the classic micro-composites and parent materials performance limits in the last 2 decades by acquiring morphological and property enhancement effects at the nano-scale [2]. In recent years polymer composites based on nano-reinforcements have gained great interest from researchers and manufacturers and as a result polymer nanocomposites are now developed into a new class of material which is growing rapidly and is being considered a good alternative to polymer blends and filled polymers [1].

Polymer nanocomposites are based on a polymer matrix and an inorganic filler material which has at least one dimension below about 100nm, so that achieving this nano size can offer performance enhancement which is better than the one achieved by using macro scale modification of polymer (Table 1.1). The up arrow head in table 1.1 indicates increase and down arrowhead indicates decrease in the respective properties of nanocomposites and their numbers indicate intensity of change in property. Due to the nanoscale dispersion of inorganic filler particles in the polymer matrix the interface between polymer and filler phases forms a considerable part of the nanocomposites [3]. The developed interface has very much different morphology and properties from the bulk polymer.

During the actual product testing and product life cycle these interfaces help to ensure enhanced, 1: Mechanical performance by generating better load transfer, 2: Heat resistance by better heat transfer to the inorganic part of the nanocomposite, 3: Barrier resistance by offering resistance to the gas molecules trying to penetrate through the composites [3].

Table 1.1: Comparison of micro and nano composite properties (4)

Property	**Microcomposite**	**Nanocomposite**
Toughness	↓ ↓ ↓	↓
Barrier properties	↓	↑ ↑ ↑
Temperature resistance	↑	↑ ↑
Transparency	↓ ↓ ↓	↓
Cost	↓	↑
Common loading (wt %)	20-50	0.1-5
Young Modulus	↑	↑

Apart from increasing the barrier, thermal, mechanical and optical properties (transparency) of the matrix polymer the addition of nanomaterial's at low weight percentages also insures that the inherent processability of the matrix is not sacrificed.

Polymer nanocomposites have been widely prepared and researched by using a number of nano materials such as layered silicates (clays), carbon nanotubes, silica, talc and graphene. Although these nano materials are being utilized in different applications but the major interest has been on the usage of clays and carbon nanotubes [1].

Polymer clay nanocomposites (PCNs) have existed in literature for more than 40 years, however it was in the early 1990s that this technology was investigated and exploited on a larger scale by industrialists and researchers [5].The revival of PCNs technology was based on two pioneering works:

1: The development of Nylon 6/exfoliated MMT clay nanocomposites by the research group of Toyota Motor Corporation [6]. This nanocomposite was manufactured by using in-situ polymerization of the monomers in the presence of clay particles. The final products developed exhibited improved thermal and mechanical properties. 2: Vaia et al. [7] discovering that polymer clay nanocomposites can be synthesized by blending layered silicates with polymers in the molten state. This method offers a versatile and environmentally benign approach for manufacturing polymer clay nanocomposites.

Polymer clay nanocomposites offer significant improvement of properties at very low volume fractions of filler. Due to the use of such low volume fractions the optical clarity and density of the matrix is more or less retained in the nanocomposite [3].

Over the last three decades, food packaging products are being manufactured primarily from polymers and this usage has increased enormously because polymers offer reduced cost, toughness, clarity, ease of processing, chemical resistance, impact resistance and acceptable barrier properties [4]. In 2004 [8], the global packaging industry turnover was around $485 million out of which $460 million was made from packaging container sales and the rest was made from packaging machinery sales. The scale of growth of global packaging market is huge and in 2004 [8] it was projected to increase from 372 million to 563 million US$ during 1999-2009 (fig. 1.1).

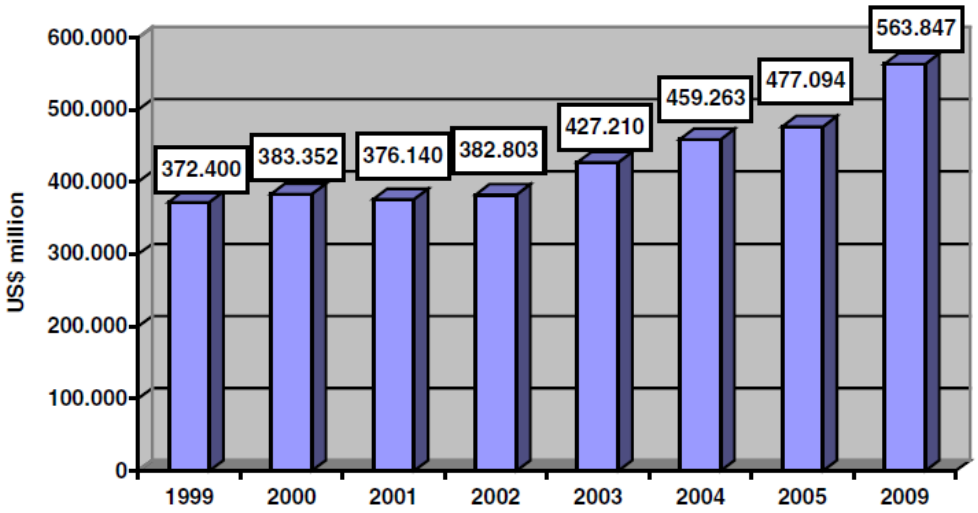

Fig.1.1: The global packaging market, 1999-2009 [8]

The main packaging materials used in the world include paper and board, metal, glass, rigid and flexible plastics and others (biodegradable and natural materials). After paper and board (39 %), rigid and flexible plastics had the highest share (30 %) in world packaging consumption in 2003 (fig 1.2) [8].

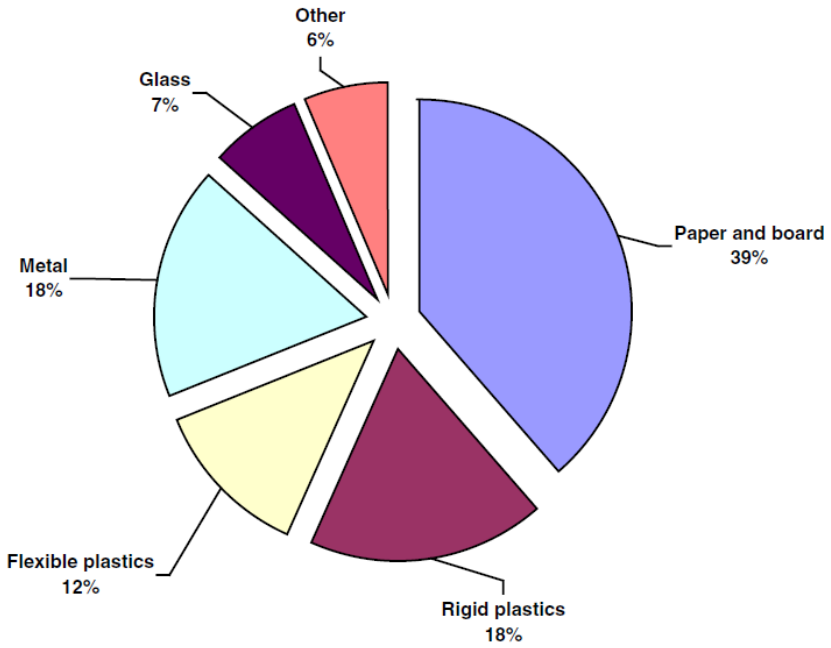

Fig.1.2: World packaging consumption by sector in 2003 [8]

In the polymer global market (fig.1.3) 42 % of the products made are used in packaging applications and for developed countries the packaging industry is itself worth 2 % of Gross National Product [4].

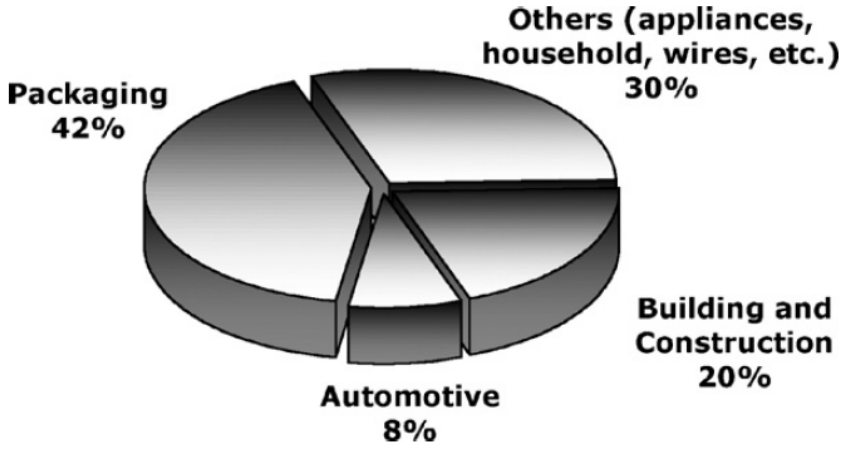

Fig.1.3: Polymer global market [4]

Due to the development of supermarkets and trading of food materials between countries, nowadays even food packaging products are required to have high performance structures which can maintain good barrier properties and decent mechanical and flow properties for longer period of time, so that the shelf life of the packaged food can be improved [9]. Nanotechnology can help produce such polymeric materials for food packaging with novelty and efficiency.

If polymer nanocomposites are to be used for food packaging they should (4); 1: Increase the barrier protection to gases, water and light, 2: Reduce the production, transport and storage energy inputs, 3: Increase the biodegradability by changing the morphology, 4: Reduce the volume of waste materials to be disposed of in landfills by having long lasting products so that the CO_2 emissions can be reduced. Disposal of waste materials is a major problem in developing countries which use the majority [10] of the packaging.

1.2: Aims of Research

The principal aim of this research is the preparation of HDPE clay nanocomposites for packaging with superior barrier (gas and water) and flow properties. This work also represents a comparative study of thermoplastic nanocomposites for packaging based on linear low density polyethylene (LLDPE), high density polyethylene (HDPE) and Nylon12. The basic idea behind this research is to produce nano scale well dispersed clay based nanocomposites by employing physical mixing techniques rather than using compatiblizer or surface treating agents. In order to develop these packaging products the following aspects are focused in the research.

1: To fabricate a set of compounds of HDPE, LLDPE and Nylon12 based on different nanofillers addition levels by using physical mixing and melt compounding technique

2: Characterization of the morphology of nanocomposites to understand the mechanism of interaction at the semicrystalline interface between filler and matrix

3: To study the influence of various nanofillers with distinct morphologies on broadening the processing window of HDPE with the help of capillary rheometer.

4: Investigation of the barrier (water and oxygen), thermal and mechanical properties of nanocomposites

5: Investigation of influence of 1D-2D-3D (D= Dimensional) carbon based nanofillers addition for improving the properties of HDPE

The experimental data obtained is intended for increasing the final product quality of polyethylene nanocomposites and for advancing the knowledge and understanding of polymer nanocomposites. The scientific goal of this research is fundamental understanding of the clay polymer interaction mechanism in changing the barrier properties of nanocomposites and broadening the extrusion window of HDPE. The

technical goal is to produce packaging products that have improved shelf life and economical processability.

All the novelty in this work is based on the physical mixing of the fillers and matrix materials by using patented method and using no chemical modifiers for preparing the nanocomposites. Since the developed products are intended to be used in food related packaging, the usage of minimum chemicals is always an advantage. One of the disadvantage in adopting this technique is that the mechanical and optical properties will not improve but if they stay at the same level as that of the matrix and the barrier properties improve then these factors can significantly increase the shelf life of food products and this is the main goal behind this research.

1.3: Thesis Outline

The basic layout of this research thesis is that of an academic report presenting experimental results and the technical discussion of these results. This thesis is divided into eight chapters.

Chapter 1 presents a general introduction to the field of nanocomposites and packaging industry. Apart from the introduction, all the research goals and the outline of the thesis are also presented in this chapter.

Chapter 2 describes a detailed literature review to support the research carried out during this project. This chapter provides a general understanding of polymers nanocomposites along with their properties and methods of manufacturing. In this chapter a detailed review of the barrier properties of polymers is presented along with the background literature related to the low temperature processing of HDPE.

Chapter 3 covers the materials used during this research and the basic method used for the preparation of nanocomposites. This chapter also presents a brief description of the instruments utilized during the property characterization of the specimens.

Chapter 4 presents a comprehensive analysis of the morphology of the individual fillers along with their nanocomposites to better understand the internal structure and properties of the prepared specimens.

Chapter 5 explores the effect of filler quantity, shape, morphology, dimension and size on the low temperature extrusion window of HDPE. This chapter presents a detailed analysis of the rheograms obtained during the dynamic cooling experiment of HDPE and its nanocomposites. Apart from the rheological data this chapter also presents a detailed analysis of the final physical characteristics of the extrudates in terms of their die swell. Also the molecular origin of the low temperature processing window and its modification for filled nanocomposites is presented in this chapter.

Chapter 6 encompasses the barrier properties of HDPE filled with two grades of kaolin clay and Na-MMT clay. The chapter then presents a comparison of the barrier properties of HDPE with LLDPE and Nylon12 nanocomposites to establish the basic understanding of various parameters involved during permeability analysis of polymers. This chapter also presents a detailed comparison of the experimental results with the theoretical models used in the literature for predicting the barrier properties of polymers. Finally in this chapter the thermal properties of the specimens are also presented.

Chapter 7 explores the effect of filler shape and size on the mechanical, barrier and thermal properties of HDPE. This chapter also represents a comparative study of the effect of 1D, 2D and 3D fillers on the final characteristics of HDPE matrix.

And finally in chapter 8 the main conclusions of the research project are presented along with the main points to be considered for further research in this field.

References:

1. Thomas, S.; Stephen, R. Rubber nanocomposites: preparation, properties, and applications, chapter 1, page 1, 2010.
2. Kotsilkova, R. Thermoset Nanocomposites for Engineering Applications, chapter 1, page 1, 2007.
3. Mittal, V. Barrier properties of polymer clay nanocomposites, chapter 1, page 2, 2010.
4. Silvestre,C.; Duraccio, D.; Cimmino, S. Food packaging based on polymer nanomaterials. *Prog Polym Sci*,36, 1766, 2011.
5. Kiliaris, P.; Papaspyrides, C.D.Polymer/layered silicate (clay) nanocomposites: An overview of flame retardancy. *Prog Polym Sci*, 35, 902, 2010.
6. Okada, A.; Kawasumi, M.; Usuki, A.; Kojima, Y.; Kurauchi, T.; Kamigaito, O. Synthesis and properties of nylon-6/clay hybrids, *Materials Research Society Symposium Proceedings,* 171, 45, 1990.
7. Vaia, R.A.; Ishii, H.; Giannelis, E.P. Synthesis and properties of two dimensional nanostructures by direct intercalation of polymer melts in layered silicates, *Chem Mater* 5, 169, 1993.
8. http://www.worldpackaging.org/publications/documents/marketstatistics.pdf

9. Vasile, C.; Pascu, M. Practical Guide to Polyethylene, chapter 1, 2005.

10. http://www.lga.gov.uk/lga/aio/1098124

Chapter 2: LITERATURE REVIEW

2. 1: Composites

Composites are a versatile and important class of engineering materials with a wide range of applications. A composite is defined as any material which is made up of two or more material constituents. Most of the composite materials have two main constituents: matrix and filler. The fillers are stiff and strong materials which form the backbone of the composite material while the matrix acts as a binder to keep the fillers in a set place. The composite materials generally have good tensile strength combined with excellent compressibility which makes them versatile in different applications.

Generally the composite materials are classified according to the type of matrix into three categories (Table 2.1): i) polymer matrix composites, ii) ceramic matrix composite and iii) metal matrix composites [1].

Table 2.1: Different composite materials [2]

Matrix Material	Reinforcement material	Examples of properties modified
Polymer	Glass, aramid, carbon, graphite, whisker, metal, etc.	Mechanical strength, wear resistance, elevated temperature resistance, energy absorption, thermal stability
Metal	Metal, ceramic, carbon, glass fiber, etc.	Elevated temperature strength, thermal stability, etc.
Ceramic	Metallic and ceramic particles and fibers	Elevated temperature strength, chemical resistance, thermal resistance, etc.

Among these three types of composite materials polymer matrix composites are very popular due to their lower costs and simple manufacturing techniques. The

properties of polymer matrix composites are dependent on the individual properties of filler and matrix, orientation of the filler in the matrix and the concentration of filler. The properties of individual filler and matrix are quite different and as a result there are a number of combinations of polymer matrix composites that are possible. Because of these different combinations the range of applications of polymer matrix composites are diverse. Two of the important areas of applications for polymer matrix composite are the aerospace and packaging industries in which they are widely used because of their low weights and high strength properties [3].

2. 2: Polymer Nanocomposites

Nanocomposites are widely defined as composites materials reinforced with fillers that have at least one dimension less than 100 nm. Modification of the properties of polymers has opened numerous practical applications for them. These applications range from simple house hold items to complicated biomedical and defense materials. The modification of polymer properties has been achieved by two main routes: blending with other polymers or by incorporation of strong and stiff fillers to produce composites. Few of the examples of the blending of polymers include high impact polystyrene (HIPS) and thermoplastic olefins (TPO). The thermoplastic olefins are generally manufactured by blending polypropylene, various grades of polyethylene, block copolymer polypropylene, rubber, and a filler. The thermoplastic olefins are used extensively in the automotive industry for manufacturing products like bumpers, dashboards, etc, while the development of high impact polystyrene has extensively broadened the application areas of polystyrene [4].

The polymer matrix composites can be fiber reinforced or particle reinforced. The most commonly used fibers are glass, carbon and Kevlar. The demand of structural

materials that are strong but light weight, have relatively simple manufacturing techniques that are cost effective, environmental friendly and can widen the application range of a particular product have resulted in the development of polymer matrix composites based on particulate fillers (tubular, spherical, platelet etc). The nanocomposites fall into the particle filled composites category. The incorporation of strong and stiff fillers in polymers usually results in polymer composites which have superior mechanical, barrier and rheological properties.

The main advantages offered by polymer matrix nanocomposites are the utilization of small amounts of filler (0.1-10 wt %) as compared to the conventional fiber filled composites (30-50 wt %), molecular level distribution of the filler in the matrix to produce better polymer filler interface and lesser costs. Nanoscale reinforcements do not significantly alter the processability and the clarity of the product because of their utilization in small amounts [4]. The enhancements of nanocomposites physical and mechanical properties without sacrificing the inherent processability of the matrix is one of the attractive attributes of the field of polymer nanocomposites and in some cases the processability of the matrix is even improved by blending them with nanofillers [3].

The enhanced properties of polymer nanocomposites are due to their low percolation threshold (~0.1-2 vol.%), particle-particle correlation arising at low volume fractions, high specific area and absorption, large number density of particles per particle volume (10^6-10^8 particles/μm^3), extensive interfacial area per volume of particles (10^3-10^4 m^2/ml), short distances between particles (10-50nm at filler content of 1-8 vol%); and comparable size scales among the rigid nanoparticle inclusion, distance between particles, and the relaxation volume of polymer chains [5]. It is due to these excellent properties that a number of industrial manufacturers have not only

developed polymer nanocomposites products but have also now commercialized them. A list of such suppliers [6,7] is given in table 2.2.

Table 2.2: Suppliers of nanocomposites [6,7]

Supplier &Trade name	Matrix Resin	Nano-Filler	Target Market
Bayer AG (Durethan LPDU)	Nylon 6	Organo-clay	Barrier films
Clariant	PP	Organo-clay	Packaging
Creanova (Vestamid)	Nylon 12	Nano-tubes	Electrically conductive
GE Plastics (Noryl GTX)	PPO/Nylon	Nano-tubes	Automotive painted parts
Honeywell (Aegis)	Nylon 6	Organo-clay	Multi-purpose
	Barrier Nylon	Organo-clay	Bottles and film
Hyperion	PETG, PBT PPS, PC, PP	Nano-tubes	Electrically conductive
Kabelwerk Eupen of Belgium	EVA	Organo-clay	Wire & cable
Nanocor (Imperm)	Nylon 6	Organo-clay	Multi-purpose
	PP	Organo-clay	Molding
	Nylon MDX6	Organo-clay	PET beer bottles
Polymeric Supply	Unsaturated polyester	Organo-clay	Marine, transportation
RTP	Nylon 6, PP	Organo-clay	Multi-purpose, electrically conductive
Showa Denko (Systemer)	Nylon 6	Clay, mica	Flame retardant
	Acetal	Clay, mica	Multi-purpose
Ube (Ecobesta)	Nylon 6, 12	Organo-clay	Multi-purpose
	Nyon 6, 66	Organo-clay	Auto fuel systems
Unitika	Nylon 6	Organo-clay	Multi-purpose
Yantai Haili Ind. & Commerce of China	UHMWPE	Organo-clay	

2. 3: Nanofillers

Nanocomposites are notable for using relatively low amount of reinforcements (1-2 wt. %) as compared to traditional composites (10-20 wt.%). These reinforcements which have size of the order of nanometer are often termed as nanofillers. Example of materials (fig. 2.1) that have been commonly used as nanofillers include: carbon nanotubes, layered silicate clays, cellulose nanocrystals and graphene nanosheets. Layered silicate clays and carbon nanotubes based nanocomposites are the ones that have gained commercial significance in the recent years. Among these two types, layered silicate platelet reinforced polymer nanocomposites are the most dominant commercial nanocomposites accounting for nearly 70% of the volume used with the biggest share formed by automotive and packaging applications [8].

Carbon nanotubes (CNT) have exceptionally high mechanical strength and versatile electronic properties. However, the major issue with carbon nanotubes in the field of polymer nanocomposite is that they do not easily disperse in polymers. Mostly carbon nanotubes create aggregates that are often heavily entangled with one another and result in the formation of bundles of carbon nanotubes in the polymer matrix. These carbon nanotubes can be untangled under shearing conditions but attractive forces between carbon nanotubes are often very strong so the dispersion at the single-tube level is difficult to achieve. Carbon nanotubes reinforced nanocomposites are also difficult to process because they increase the viscosity of the polymer melt especially at higher concentration [9].

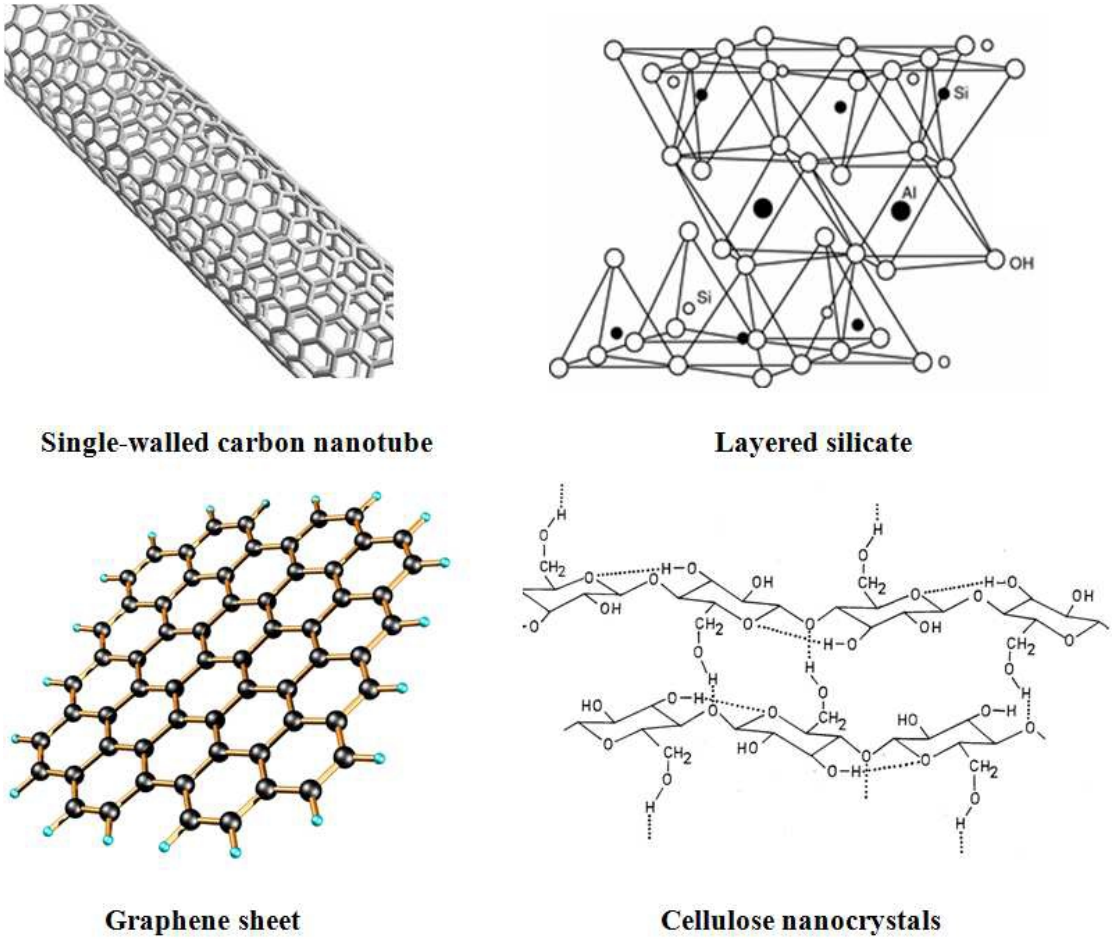

Fig. 2.1: Nanofiller structures

2.3.1: Clay

There are a number of definitions both technical and nontechnical of term ‘clay’ that exists in the literature. These definitions create confusion because each application field of clay has its own definition. Geology, civil engineering, material science/engineering, chemistry and other groups have chosen different basis (mechanical properties, origin of the material, particle size, composition etc) for defining the term clay [10,11]. Georgius Agricola (1494–1555), the founder of geology, was the first to have formalized a definition of clay (25). A precise and most recent technical definition [12] of clay was reported by International association for the study of clays (AIPEA) and clay mineral society, USA (CMS):

*''The term **Clay** refers to a naturally occurring material composed primarily of finegrained minerals, which is generally plastic at appropriate water contents and will harden when dried or fired. Although clay usually contains phillosilicates, it may contain other materials that impart plasticity and harden when dried or fired. Associated phases in clay may include materials that do not impart plasticity and organic matter''.*

The report [12] also explained that clay should not be used as a mineral term, and that a clear distinction must be made between terms clay and clay mineral. The AIPEA and CMS proposed a formal definition of term clay mineral [12]:

"*The term **clay mineral** refers to phillosilicate minerals and to minerals which impart plasticity to clays and which harden upon drying or firing*."

According to the above definition clay mineral (unlike clay) may be synthetic, since the origin of the material is not part of the definition. Clay minerals are the class of minerals belonging to the family of layered silicates (phyllosilicates). The fundamental building units of clay minerals are tetrahedral and octahedral sheets. In the nature, clay minerals are extremely abundant materials with an estimated presence of ~ 16 % in the Earth's crust [13]. The main constituents of clay minerals are metal atoms such as Al, Mg or Fe, along with silicon, oxygen and hydrogen atoms. Apart from these main constituents sodium, potassium, calcium, zinc or others may also be present. Silicon is always present in tetrahedral sheets while aluminum, magnesium and other metals are present in octahedral sheets.

The tetrahedral sheets consist of individual tetrahedrons, in which a silicon atom is equidistant from four oxygen atoms. The tetrahedral sheets are arranged in a hexagonal pattern in which the basal oxygen's are linked and the apical oxygen's take part in the adjacent octahedral sheet. The octahedral sheets consist of individual octahedrons that share edges composed of oxygen and hydroxyl anion groups coordinated by cations like Al, Mg, Fe^{3+} and Fe^{2+}, etc.

The valence of the cations like Al and Mg can be used for distinguishing di-octahedral or tri-octahedral sheets. In case of Al which is a trivalent cation, electric neutrality can be maintained if the cation to oxygen ratio is 1:3. This results in a structure in which only 2 out of 3 sites are occupied. This arrangement is called di-octahedral or Gibbsite-like sheet. Instead, for a divalent cation like Mg the cation to oxygen ratio has to be 1:2 and hence every lattice site is filled. This arrangement is called tri-octahedral or Brucite-like sheet. The general characteristics and TEM micrographs of the most commonly used clays in polymer nanocomposites are given in table 2.3 and fig 2.2.

Table 2.3: The different types of clay used in nanocomposite preparation [14]

Mineral	**Type**	**Interlayer bonding**	**Cation exchange capacity**	**Swelling**	**Specific surface area, $m^2 g^{-1}$**	**Basal spacing nm**
Kaolinite	1:1 nonexpanding	Strong hydrogen bonding	3-15	Almost none	5-20	0.72
Montmorillonite	2:1 expanding	Very weak bonding	80-150	High	700-800	0.98-1.8
Vermiculite	2:1 expanding	Weak bonding	100-150	High	500-700	1-1.5
Hydrous mica	2:1 nonexpanding	Strong bonding	10-40	Low	500-200	1.0
Chlorite	2:1:1nonexpanding	Moderate to strong bonding	10-40	None	—	1.4

The packing order of different tetrahedral, di- and tri-octahedral sheets is the main criterion of classification for phyllosilicates. A general classification of clay minerals is shown in table 2.4. The structure of kaolinite is built by combining tetrahedral and

octahedral sheets in equal proportions to form a layer unit in which apical oxygen is shared between the tetrahedral and octahedral sheets, such minerals are called 1:1 clay minerals. Smectite is composed of units made up of two silica tetrahedral sheets with a central alumina octahedral sheet (2:1). The structure of chlorite, instead, can be imagined as consisting of alternating smectite-like layers and a brucite-like tri-octahedral sheet.

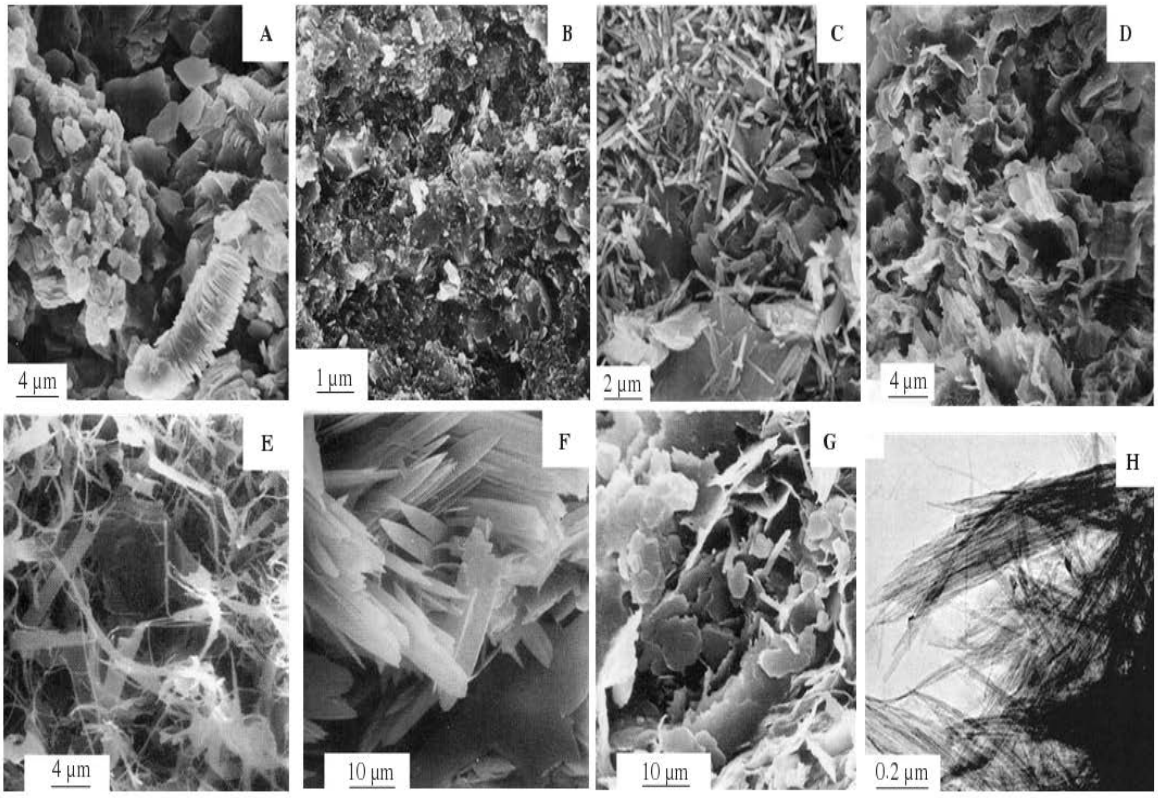

Fig. 2.2: Transmission electron micrographs of some clay minerals: (A) kaolinite; (B) high-quality flint clay; (C) tubular halloysite particles alongside kaolinite plates; (D) smectite or illite/smectite; (E) filamentous illite; (F) lath-shaped; (G) pseudo-hexagonal illite; (H) fibrous palygorskite [15]

Table 2.4: General classification of clay minerals [16]

I. Amorphous
Allophane group

II. Crystalline

A. Two-layer type (sheet structures composed of units of one layer of silica tetrahedrons and one layer of alumina octahedrons.

1. Equidimensional
Kaolinite group
Kaolinite, Nacrite, etc.

2. Elongate
Halloysite group

B. Three-layer types (sheet structures composed of two layers of silica tetrahedrons and one central di-octahedral or tri-octahedral layer)

1. Expanding lattice
a. Equidimensional
Montmorillonite group
Montmorillonite, sauconite, etc.
Vermiculite
b. Elongate
Montmorillonite group
Nontronite, Saponite, hectorite

2. Nonexpanding lattice
Illite group

C. Regular mixed-layer types (ordered stacking of alternate layers of different types)
Chlorite

D. Chain-structure type (hornblende-like chains of silica tetrahedrons linked together by octahedral groups of oxygens and hydroxyls containing Al and Mg atoms)
Attapulgite
Sepiolite
Palygorskite

For clay minerals a ‘particle’ is defined as assembly of layers and an assembly of particles is defined as an ‘aggregate’ (figure 2.3). The arrangement of the particles or aggregates leads to different morphologies, such as platelets, tubules, laths, and fibres. All phyllosilicates are therefore porous, containing pores of varied size and shape.

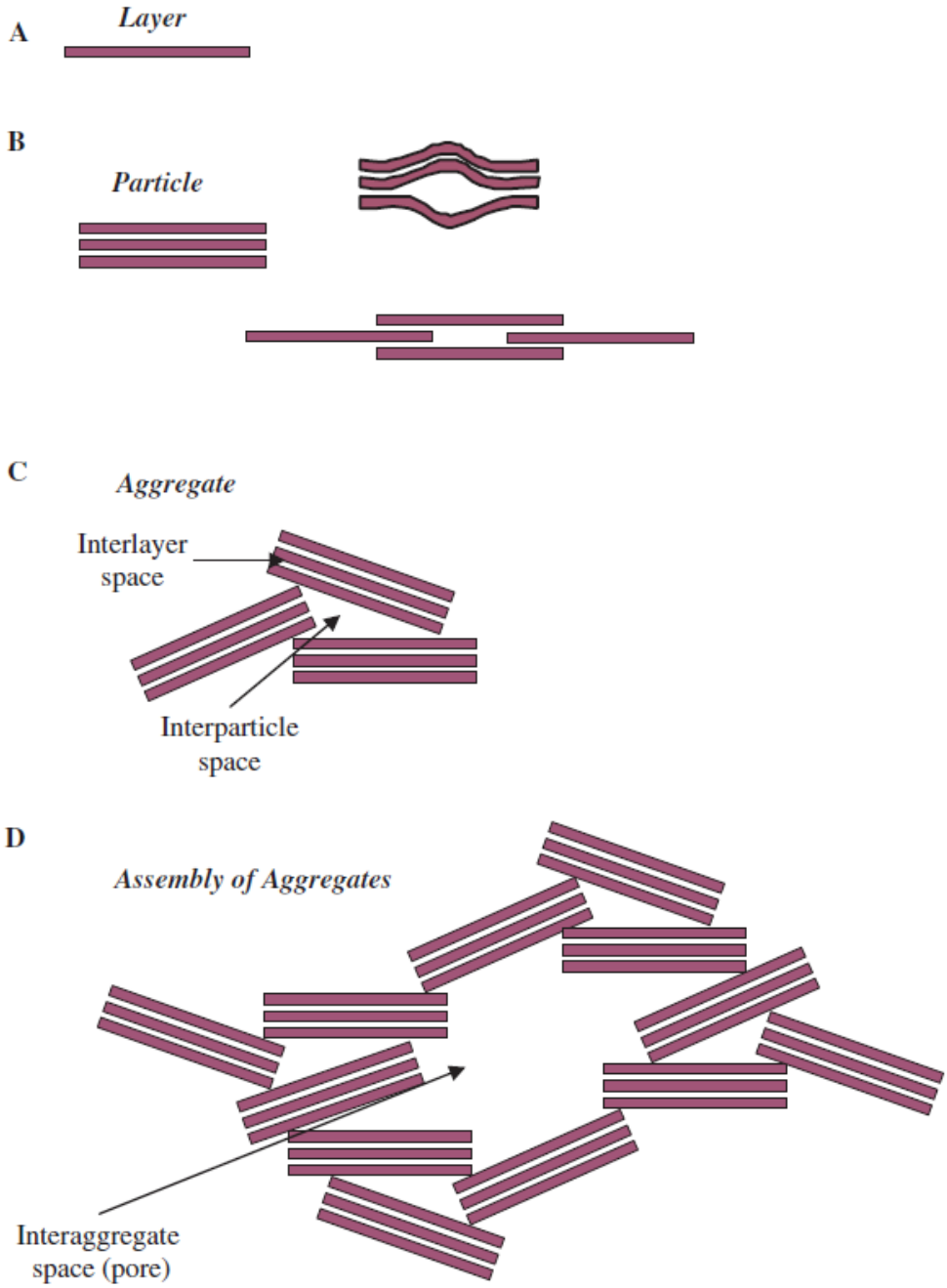

Fig. 2.3: Diagram of clay layer, particle, aggregate, and assembly of aggregates [15]

2.3.1.1: Kaolin

Kaolin is used in the literature as a rock term and a mineral term. The term China Clay is also used synonymously for kaolin, particularly in Great Britain. As a rock, the term kaolin means that the rock is comprised predominantly of kaolinite and other kaolin minerals. As a mineral, the term kaolin means the group of clay minerals that consists of four basic minerals, kaolinite, halloysite, dickite and nacrite. These four species have the same chemical composition of $Al_2Si_2O_5(OH)_4$, which means they are polymorphs [16]. In addition, kaolinite, dickite and nacrite are also polytypes, since they have the common structure of the individual layer and only the layer-stacking scheme is different. Kaolinite is the most abundant mineral of this group after halloysite. Nacrite and dickite are rather rare minerals, occurring in just a few locations [16].

The structure of kaolinite consists of one tetrahedral silica sheet and one octahedral alumina sheet. These sheets are joined by sharing a common layer of oxygen and hydroxyls (fig 2.4). Such a structure is classed as a 1:1 layer clay. Both the silica tetrahedral sheet and the alumina sheet have little substitution so the layers of kaolinite are electrically neutral since no excess charge is left unbalanced in kaolinite. Such layers can stack on each other and are held together by hydrogen bonds between adjacent octahedral hydroxyl groups from one layer and tetrahedral oxygen atoms from the next layer as well as by van-der-Waals forces [16]. The Important properties of kaolin are given in table 2.5

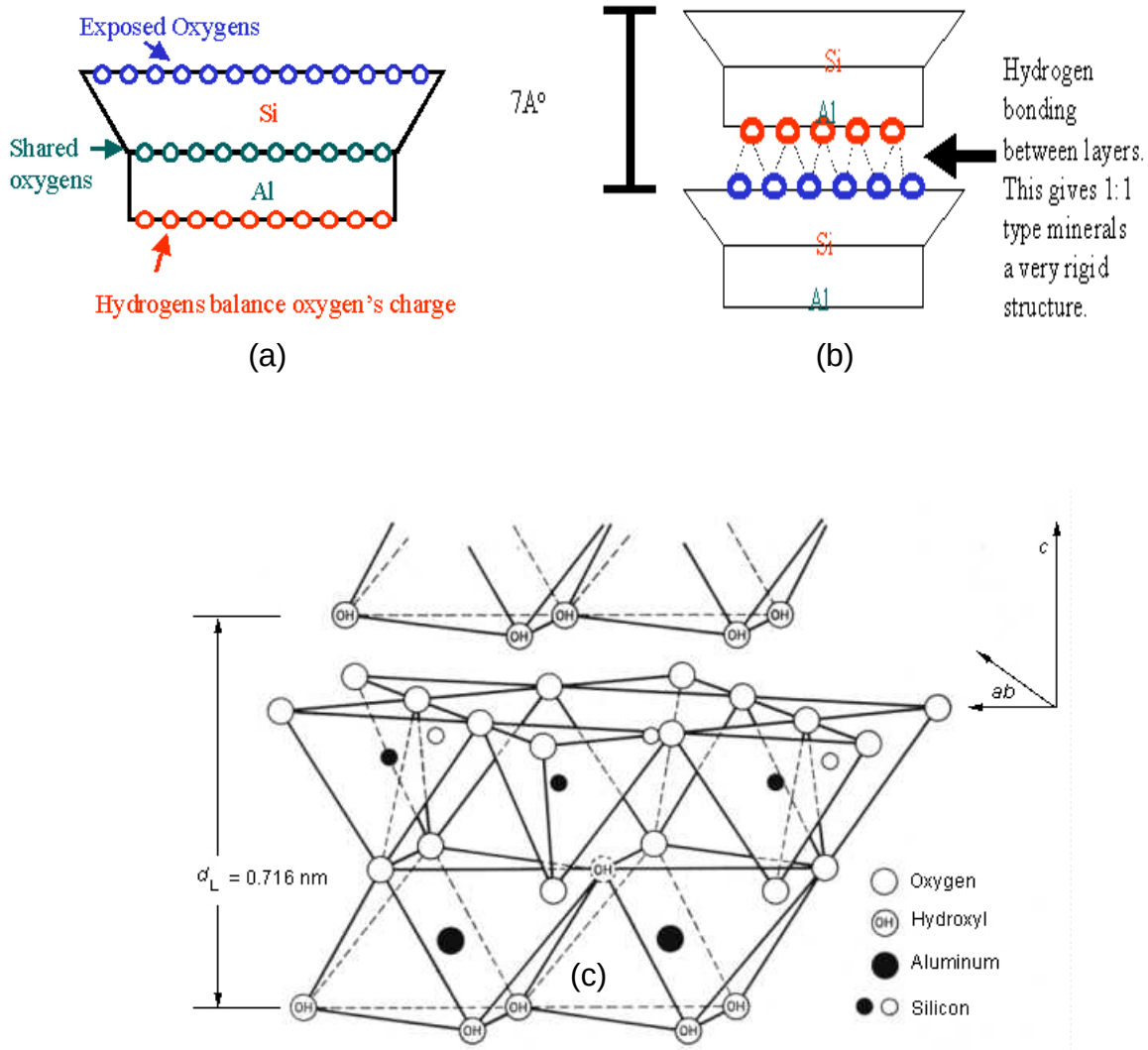

Fig. 2.4: (a) A single layer of kaolinite, (b) Hydrogen bonding between layers (c) : Schematic view of the structure of kaolinite [14]

The interlayer bonding in the kaolin arises from van der Waals attraction forces between its layers, from hydrogen bonding between octahedral OH group on one layer and tetrahedral oxygen atoms of the next layer, and from dipole–dipole interactions. Due to these forces the interclataion of kaolin clay is very difficult in most cases require lengthy and precise conditions. Intercalation is the penetration of organic molecules into the interlayer space of kaolin clay minerals.

Table 2.5: Important properties of kaolin [16]

1: White or near-white in color
2: 1:1 Layer clay and chemically inert over a wide pH range (4–9)
3: Fine in particle size
4: Soft and non-abrasive
5: Platy with the plate surface dimensions relatively large compared to the thickness but has very limited substitutions in the structure
6: Hydrophilic and disperses readily in water
7: Because of its shape, it has good covering and hiding power when used as a pigment or extender in coatings
8: Plastic, refractory and fires to a white or near-white color
9: Low conductivity of both heat and electricity
10: A very low charge on the lattice and cation exchange capacity
11: A low surface area as compared with other clay minerals
12: Some kaolins have a low viscosity and flow readily at 70% solids
13: Relatively low in cost

The molecules that intercalate kaolin clay can be divided into three groups:

1. Compounds capable of forming hydrogen bonds like hydrazine, urea, and formamide. In order to break the hydrogen bonding between the layers, the guest molecules must contain two separated groups to accept and donate hydrogen bonds, like acid, amides, and urea. Molecules in which the donor and acceptor group are on the same atom (alcohol, water) will not intercalate kaolin.

2. Compounds having high-dipole moments like dimethyl sulphoxide (DMSO) and pyridine-N-oxide.

3. Potassium, rubidium, caesium, and ammonium salts of short-chain fatty acids (acetates, propionates, butyrates, and isovalerates).

Intercalation compounds are usually prepared in the form of liquids, melts, or concentrated solutions before reacting them with kaolinite at about 60–80^{o}C. Intercalation is a slow process that often requires several days (Table 2.6). The reaction rate depends not only on the type of guest compound, temperature, and concentration (if solutions are used) but also on the type of kaolinite and the particle size.

Table 2.6: Intercalating chemicals for kaolin [16]

Guest compound	Basal spacing (nm)	Reaction conditions
None	0.71	
Formamide	1.01	4 days, 60^{o}C
Hydrazine hydrate	1.04	1 day, 60^{o}C
Urea	1.07	8 days, 60-110^{o}C
N-methylformamide	1.08	2 days, 60^{o}C
Dimethyl sulphoxide	1.12	30 h, 50^{o}C
	1.12	20 min, 150^{o}C
Potassium acetate	1.40	1 day, 65^{o}C, pH = 8
Ammonium acetate	1.41	20 days, 20^{o}C, pH =8-9

Kaolin is mainly used in the paper industry as filler and also as one of the ingredient of coating compositions. These coatings are applied to make paper smoother, brighter, glossier, more opaque and to improve its printability. Ceramic industry is one of the major users of kaolin clay, many products like dinnerware, sanitary ware, tile, electrical porcelain, pottery, and refractories Ceramic and paper industry use more than 70 % of the kaolin produced throughout the world. Kaolin is also used as filler in the paint, inks, rubber, plastic and enamel industry. In rubber industry kaolin

is used in non-black rubber goods because of its reinforcing and stiffening properties and relatively low cost. In plastic products manufacturing kaolin aids in producing a smooth surface finish, reduces cracking and shrinkage during curing, obscures the fiber pattern in fiberglass composites, and improves thermal stability, impact strength, and resistance to chemical action and flow properties. Kaolin loading in various plastic products varies from about 15% to as high as 60 wt. % [16]. The kaolin minerals worldwide reserves are estimated to be around 17.3 billion tons. Most of the deposits (88 %) are located in United States (47 %) and Brazil (41%). Imerys (France), J. M. Huber (USA) and CADAM (Brazil) are the major supplier of kaolin clay throughout the world as they detain most of the production of kaolin [17].

2.4: Polyethylene in food packaging

Over the last two decades food packaging products are being manufactured primarily from polymers. This usage has increased enormously because polymers offer clarity, toughness, low cost, ease of processing, chemical resistance, low coefficient of friction, impact resistance and decent barrier properties. In recent years food packaging products are required to have high performance structures that can improve the shelf life of the packaged food by maintaining good barrier properties and together with appropriate mechanical characteristics. Nanotechnology can offer products that have superior barrier and mechanical properties than the regular packaging materials and can help reduce the volume of waste material that is disposed of in landfills.

One of the major polymers used in the production of food packaging is polyethylene. Polyethylene represents a versatile class of materials which offer good properties, vast availability, easy manufacturing and low cost. There are various grades of

polyethylene available in the market such as high density polyethylene (HDPE), low density polyethylene (LDPE), linear low density polyethylene (LLDPE), ultra high molecular weight polyethylene (UHMWPE) etc. These grades have applications in areas ranging from everyday use commodities to high value engineering products (fig 2.5) outside packaging.

HDPE is mainly used in producing milk bottles, containers, crates, food cutting boards, pipes, petroleum tanks etc. LDPE has been one of the major grades of polyethylene used for producing food packaging films, but this application has seen a decline (2-3 % annually) in recent years because of the increasing use of LLDPE (table 2.7). LLDPE usually offers superior properties than LDPE at decent cost [18].

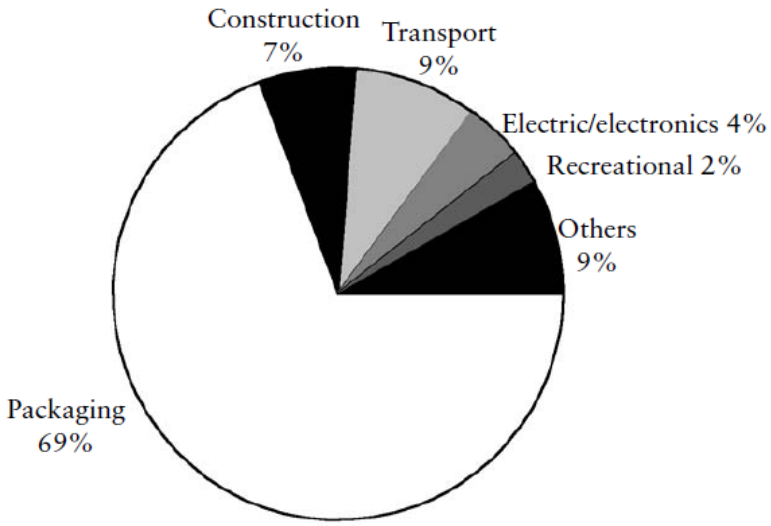

Fig. 2.5: Main applications of PE [18]

The major areas in which LLDPE has replaced LDPE are construction films; take away food bags, rubbish bin liners etc. However LDPE is still the favored material in

the industry for producing films with high clarity. The capacities and worldwide consumption of grades of PE are given in table 2.7.

Table 2.7: Capacities and worldwide consumption of PE (million tonnes) [19]

PE type	1990		2001		2005	
	Capacity	Consumption	Capacity	Consumption	Capacity	Consumption
LDPE	16.2	13.7	20.3	16.5	21.4	17.0
LLDPE	7.1	5.1	26.8	11.9	29.8	14.9
HDPE	11.2	11.8	20.1	21.1	21.5	24.8
Total PE	34.5	30.4	67.2	49.5	72.7	56.7

2.5: Polymer/clay nanocomposites

Polymer/clay nanocomposites consist of clay nanoparticles reinforcing the polymer matrix. These nanocomposites show considerable increase in performance and properties with the addition of relatively small amounts of clay nanoparticles [20-26]. One of the most widely used clay for reinforcing polymers is montmorillonite, although there are many other types of clay available such as cloisite and kaolin. Depending on the interfacial tensile strength between polymer matrix and nano-clays, three different structures [27] of polymer clay nanocomposites can be distinguished (fig 2.6):

i. Micro-composites

If the polymer chains are not able to penetrate into the interlayer spaces of the clay, due to low affinity of the organic and inorganic phases and poor interface properties agglomerated stacked structure will be preserved and a micro-composite structure will be formed. In this case we cannot expect properties superior to those of conventional filled composites.

ii. Intercalated nanocomposites

If the polymer chains penetrate into the clay inter layers and wet the clays with few polymer layers then an intercalated nanocomposites is formed. In this case basal spacing increases but the clays are still found in an ordered stacked manner.

iii. Exfoliated nanocomposites

If the single clay platelets are completely and randomly dispersed into the continuous polymer matrix then an exfoliated nanocomposites is formed. The distance between clay platelets depends mainly on the filler loading.

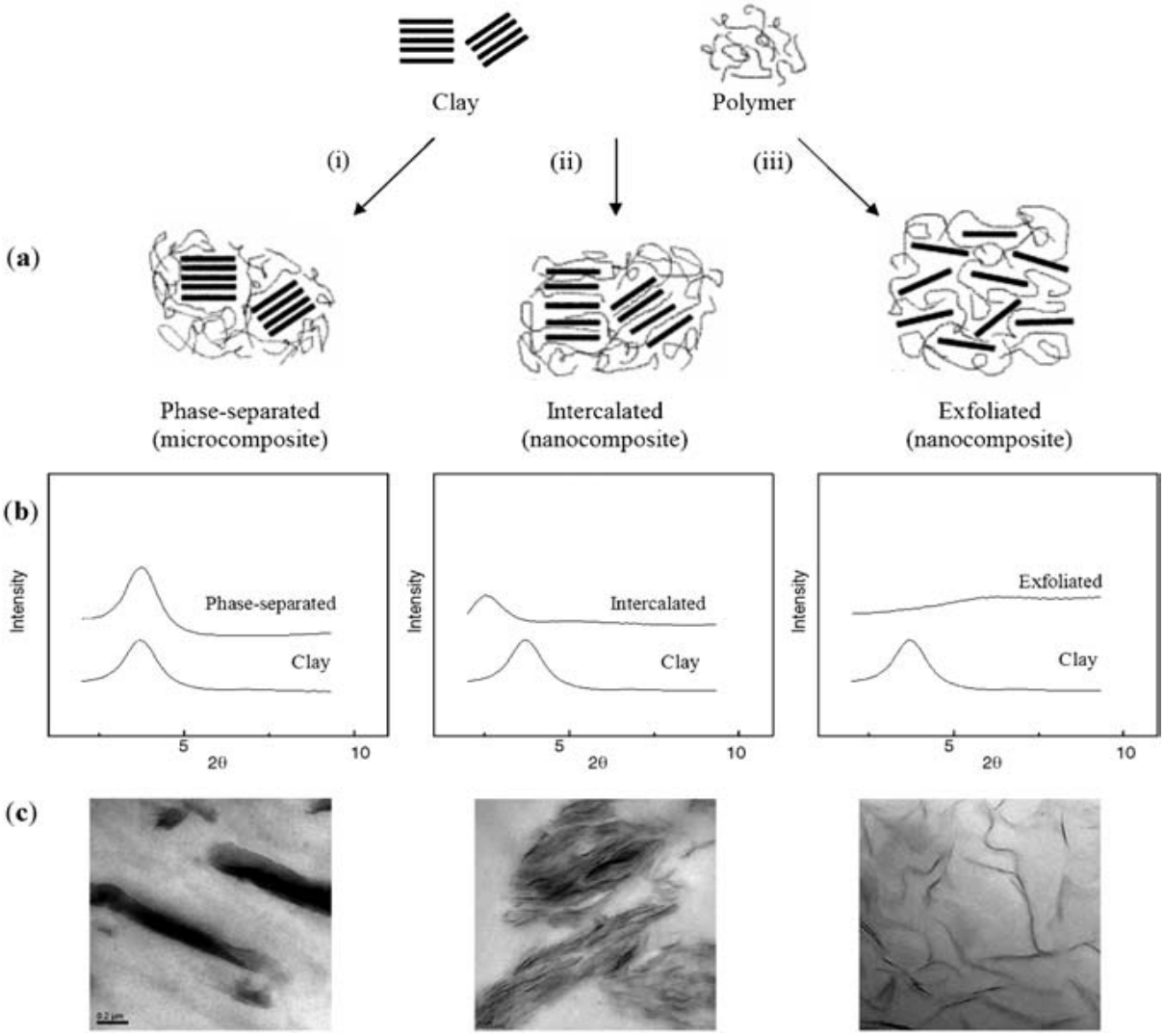

Fig. 2.6: (a) Schematic illustration of the morphologies of polymer/clay hybrids: (i) phase separated microcomposite; (ii) intercalated nanocomposite; and (iii) exfoliated nanocomposite, and typical (b) XRD patterns and (c) TEM images corresponding to each type of morphology [27]

The main methods used for manufacturing polymer/clay nanocomposites are in situ polymerization, intercalation of polymer from solution and melt compounding. In addition, another alternative method which is also used in industry is template synthesis, which is also called sol–gel technology. By using these methods either intercalated nanocomposites or exfoliated nanocomposites are produced.

In-situ polymerization involves swelling the clay layers in a monomer or a monomer solution. In this method, polymerization of the monomer can occur between the intercalated layers. The initiators used for the polymerization can be heat, radiation or an inorganic substance. In order to acquire high degree of mixing the clays must be compatibilized to allow the monomers to intercalate, at which point the polymerization reaction can take place in the inter-layer galleries. If the polymerization reaction is catalyzed by the clay surface layer or some silicate-bound functionality then the rate will be enhanced at the interlayer with respect to material outside of the interlayer galleries. In such a situation dispersion will be strongly enhanced. This method can be encouraged through the use of silicate-bound monomers or initiators. Another route is that emulsion polymerization may be performed by dispersing an unmodified silicate in a water/monomer emulsion. The dispersion obtained via in-situ polymerization may improve the barrier and thermal properties but may or may not improve the mechanical performance, depending on the level of polymer/clay interactions [22, 23, 27].

Solvent casting is based on swelling the clay layers using polymers dissolved in a solvent. It is one of the simplest techniques for producing nanocomposites. During this method, the polymer matrix intercalates into the clay layers and replaces the solvent. The driving force is the increased entropy caused by desorption of the solvent. This method is a two-stage process. During this method, the first step is that

the clay layers are exfoliated to get good dispersion in a soluble solvent. After the clay layers swell due to the weak forces between each layer, the matrix is added and intercalated into the clay layers. The second step is the remove the solvent. The conventional methods of getting rid of the solvent are vaporization under vacuum condition and precipitation. The advantage of using intercalation of polymer from solution is the low level of polarity of the nanocomposites. However, the disadvantage is obvious. One disadvantage is that this method only works for certain systems which need certain solvent, polymer and clay. Another disadvantage is the difficult application in industry by the solvent method because of the large required amount of solvent which can is environmentally unfriendly [22, 25, 4].

In melt blending the polymer is given enhanced degree of freedom that polymer chains need, combined with physical mixing required to disperse compatibilized layered silicates on the nanoscale. The thermal energy produced during melting of polymer gives the enhanced degree of freedom of the polymer chain. In this process by using an extruder or heated rolls, the molten polymer and the compatibilized layered silicate are physically mixed, and a nanocomposite is obtained. Compared to in-situ polymerization and polymer solution intercalation, melt intercalation has advantages of being environmentally and economically friendly since no solvents are involved and allow the use of polymers which are not suitable for the former two methods. The other main advantages of this method are that it is more economical and easier than other methods. Melt compounding can form nanocomposites with conventional machines, such as extruder whose knowledge base is wide, and there is no need for resin production. Therefore companies can reduce their costs and make more benefits [22,27].

Two main processes are involved in the characterization of polymer clay nanocomposites: structural analysis and material property measurements. Structural analysis is carried out using microscopic and spectroscopic techniques, while material property characterization involves measurement of barrier, thermal, mechanical properties.

The structure of polymer clay nanocomposites is generally characterized by X-ray diffraction (XRD) and transmission electron microscopy (TEM). The presence of intercalated or exfoliated nanostructure can be studied by monitoring the position, shape and intensity of the basal reflections of XRD patterns of the materials. Moreover, TEM can provide direct qualitative information of structure, morphology and spatial distribution of the various components.

General polymer characterization techniques are also used to measure materials properties of polymer clay nanocomposites. Among them, DSC is used to measure the thermal transitions such as melting, glass transition and crystallinity; TGA is used to evaluate the thermal stability at elevated temperatures. Melt rheology is another important area where the processability of nanocomposites is studied and the effects of clays on the polymer processing examined.

The final properties of the polymer clay nanocomposites are highly dependent on the volume fraction of clay in the nanocomposites, geometry of the clay particles, aspect ratio of the clay platelets, alignment of the clay particles and the delamination in the polymer matrix. Since their development in the 1980s polymer clay nanocomposites have been mainly developed and researched for improving the mechanical and thermal performance of polymer products. Such polymer products were generally used as engineering plastics in cars, construction and equipment etc. Apart from

these main advantages barrier properties can also be improved by incorporating clay nanoparticles in polymers.

2.6: Barrier properties of nanocomposites

Polymeric materials are now being used throughout the world in packaging industries as alternatives to traditional packaging materials such as glass, metals, paper etc. Polymeric materials are widely used in food, toys, clothes, beverages and a number of other packaging industries. Although polymeric materials have the distinct advantages of balanced properties such as: light weight, low cost, toughness, flexibility, easy processing, recycling and post-formation printing but they do permeate different gases and vapours to some extent. The use of glass and metal in most of the beverages packaging throughout the world is due to their total barrier to the transfer of different gases and vapours.

Various theories have been proposed to explain this mechanism. One popular theory is torturous path model. In this model, as the clay layers are dispersed into the polymer matrix, the permeating molecules, such as O_2 and H_2O, have to permeate in a torturous path. As the path is longer, the time for diffusion is longer and therefore the barrier properties are improved. There are two factors which decide the barrier properties. One is exfoliated clay morphology and the other one is the good dispersion of clay layers.

2.6.1: Barrier properties of polymers: Fundamentals and measurement

A number of phenomenon's are involved in the mass transport in polymer packaging for food and pharmaceutical products such as: permeation, adsorption and migration [28]. Permeation is the transfer of molecules between the product and the external

environment through the polymer packaging. Migration is defined as the take up of molecules originally contained in the packaging by the product, whereas adsorption is the transfer of molecules from the product into the packaging. These phenomenons can cause physiochemical changes and damage to the product and packaging [29].

In a dense polymer film, the permeability or permeability co-efficient (P) is defined as '*the molar flux of penetrant through the polymer relative to a fixed coordinate system (N_A) normalized by the film thickness, L, and the difference between the upstream (p_1) and downstream (p_2) partial pressures*' [30]:

$$P = \frac{N_A\, L}{(p_1 - p_2)} \tag{2.1}$$

The permeability co-efficient is commercially measured directly as a material property. During analysis the transmission rate is determined, which is measure for the volume of gas passing through a film of known area per unit time. Based on eq. 2.1, the permeability can also be represented as [31]:

$$P = \frac{(quntity\ of\ permeant).(film\ thickness)}{(area).(time).(pressure\ difference\ across\ the\ film)} \tag{2.2}$$

A number of units are used in the literature to report the permeability co-efficient. The most commonly used unit to present P is [cm^3.µm/m^2.day.mmHg]. It can be converted to the SI unit [cm^3.cm/cm^2.s.Pa] by multiplying with 8.68 x 10^{-16} [31].

The permeation process through a polymer packaging film occurs in five consecutive steps, as shown in fig 2.7:

1. Mass transfer from the bulk of phase 1 (high pressure side) to the adjacent surface of package film
2. Sorption from the adjacent surface into package film (by chemical affinity or by solubility)
3. Molecular diffusion inside the polymer film
4. Desorption from package film into the adjacent surface in contact with phase 2
5. Mass transfer from the adjacent surface to the bulk of phase 2.

The above five steps form the so called solution-diffusion model [30]. The rate limiting step in the permeation process is the molecular diffusion of permeant through the film. This process can be quantitatively described in terms of Fick's first law of diffusion, which expresses the flux N_A, in the direction of flow is proportional to the concentration gradient (dc/ dx) as [31]:

$$N_A = -D \frac{dC}{(dx)} \quad (2.3)$$

where D is the effective diffusion coefficient for the penetrant in the polymer. The diffusion process can be Fickian and non-Fickian (where D varies with time).

In the steady state, diffusion flow is constant and the diffusion coefficient is independent of concentration. Then Integration of equation 6.3 yields the following expression of $N_{A:}$

$$N_A = \frac{D}{l} \Delta c \quad (2.4)$$

where l or $(x_2 - x_1)$ is the thickness of the film and Δc or $(c_1 - c_2)$ is the difference in permeant concentration between the two surfaces of the film.

Experimental determination of c_1 and c_2 is very difficult and therefore they are converted to the partial pressure (p) in bulk phase, which can be easily measured and is represented by Henry's law of solubility [28]:

$$c = Sp \tag{2.5}$$

where S is the solubility coefficient of permeant in the film.

Combining equations 2.4 and 2.5

$$N_A = \frac{DS}{l} \Delta p \tag{2.6}$$

where Δp or (p_1-p_2) is the drop of partial pressure across the film. Also the product of D and S is the permeability co-efficient:

$$P = DS \tag{2.7}$$

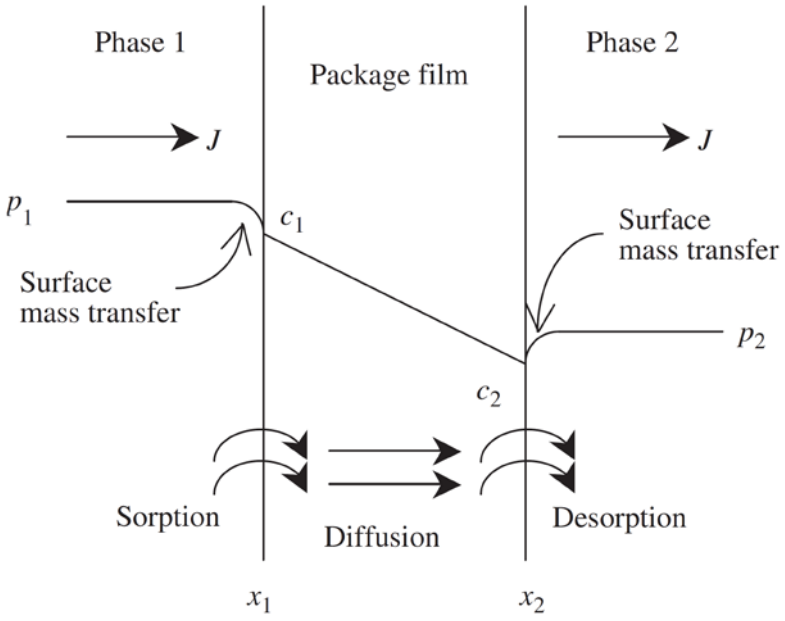

Fig. 2.7: Schematic diagram of gas or vapor permeation through a package film.[28]

During dynamic analysis for the measurement of permeability, in the first step the sample is conditioned so that $c_1 = c_2$. After preconditioning the concentration is step changed so that $c_1 \neq c_2$ and c_1 and c_2 are kept at a constant value. If the amount of gas passing the polymer film is time integrated, then after certain time span the

integrated curve, which describes the amount of gas per unit time (q), becomes linear (fig 2.8). If the linear part of the curve is extended back with the time axis, the time-lag value (t_L) is obtained [31]. Mathematically t_L is represented as:

$$t_L = \frac{l^2}{6D} \tag{2.8}$$

Hence, from a single experiment the permeability (equation 2.1), diffusion (equation 2.8) and solubility (equation 2.7) can be measured if the thickness of the film is known.

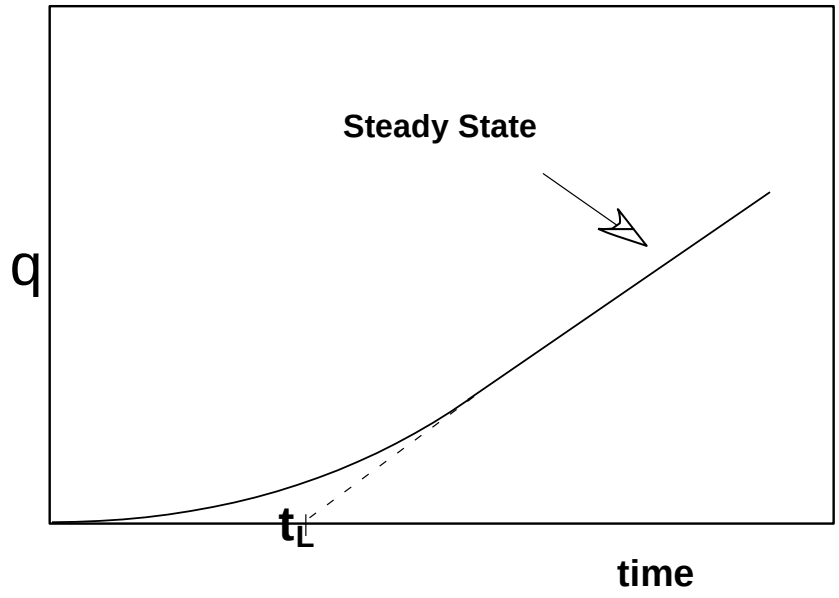

Fig. 2.8: Mass of permeating penetrant per unit film area (q) as a function of time

Another coefficient frequently used in commercial polymers is permeance (R), whose physical meaning is similar to that of mass transfer coefficient and is given as:

$$R = \frac{DS}{l} \tag{2.9}$$

The above equations are only applicable in scenarios where D is independent of permeant concentration and S follows Henry's law. Also D is a kinetic factor which characterizes the velocity of penetrant through the film due to a concentration

gradient and has the units of cm^2/s. On the other hand S is thermodynamic term which describes the amount of permeant that can dissolve in a polymer.

The measurements of gas, aroma and water permeation through a given polymeric matrix requires direct or indirect measurement of the mass transfer of permeant through the polymer under precisely controlled environment. The direct method of permeability analysis involves the measurement of pressure change or any other physical property change as result of penetrant diffusion through the polymer. The indirect permeability measurement involves using indirect indicator of permeation, such as chemical reaction of the penetrant with another substance. The final method of analysis adopted in the testing machines depends on the type of penetrant being analysed.

2.6.2: Variables affecting barrier properties of polymers

2.6.2.1: Structure of polymer

The structure of the polymer selected for a packaging application will decide its barrier properties because both solubility and diffusivity are dependent on structure. With regards to the chemical structure of polymers the most important characteristics often considered or modified are: fractional free volume, chain interaction, side group's polarity, crystallinity, chain orientation, and density. The effect of modification in most of these factors on the permeability of polymer and the possible reason for the change in permeation are given in table 2.8.

Table 2.8: Effect of structural factors on the permeability of polymer and the possible reason for the change in permeation

Factor	Factor effect	Permeability of polymer	Possible reason
Fractional free volume (FFV)	Increase	Increases	The FFV is the space available in a polymer for the penetrant to pass through it. With more FFV available in a polymer the permeability will increase as the penetrant will have more space to diffuse through the polymer. The dependence of solubility on FFV is weaker than the diffusivity of penetrant especially for amorphous polymers (32). The effect of increase of FFV on the permeability of several polymers is shown in fig 2.9. The results show a linear relationship between oxygen permability and FFV (33).
Crystallinity	Increase	Decreases	The crystalline region is denser, well ordered than amorphous region and is impermeable to gases and vapours. The crystallites act as impermeable site that can increase the diffusion time for penetrants. Also an increase in crystallinity causes the free volume of polymers to decrease which ultimately leads to reduced permeability. [32]
Chain interaction	Increase	Decreases	Increasing chain interaction by hydrogen bonding, polarity and by crystallinity can produce tighter packing of polymer chains and also help reduce their dynamic motion. Also the increase in cohesive energy density which quantifies chain interaction causes the activation energy of diffusion to increase

			as a result of which diffusivity decreases.
Chain orientation	Increase	Decreases	The tortuous path created by the orientation, alignment and disentanglement of chains will increase the permeation time of permeant. Also orientation produces higher degree of packing and decreases the free volume fraction of amorphous phase [34].
Density	Increase	Decreases	The increase in density causes a decrease in free volume of polymer, and an increase in crystallinity and higher cross linking which could decrease solubility and diffusion of penetrant. In case of polyethylene all the polymer properties are correlated to the density of polymer. (fig 2.10) [29].
Glass transition temperature	Increase	Decreases	With the increase in glass transition temperature the chain mobility decreases which in turn causes an increase in the activiation energy of diffusion and hence leading to a decrease in the permeability of the polymer.

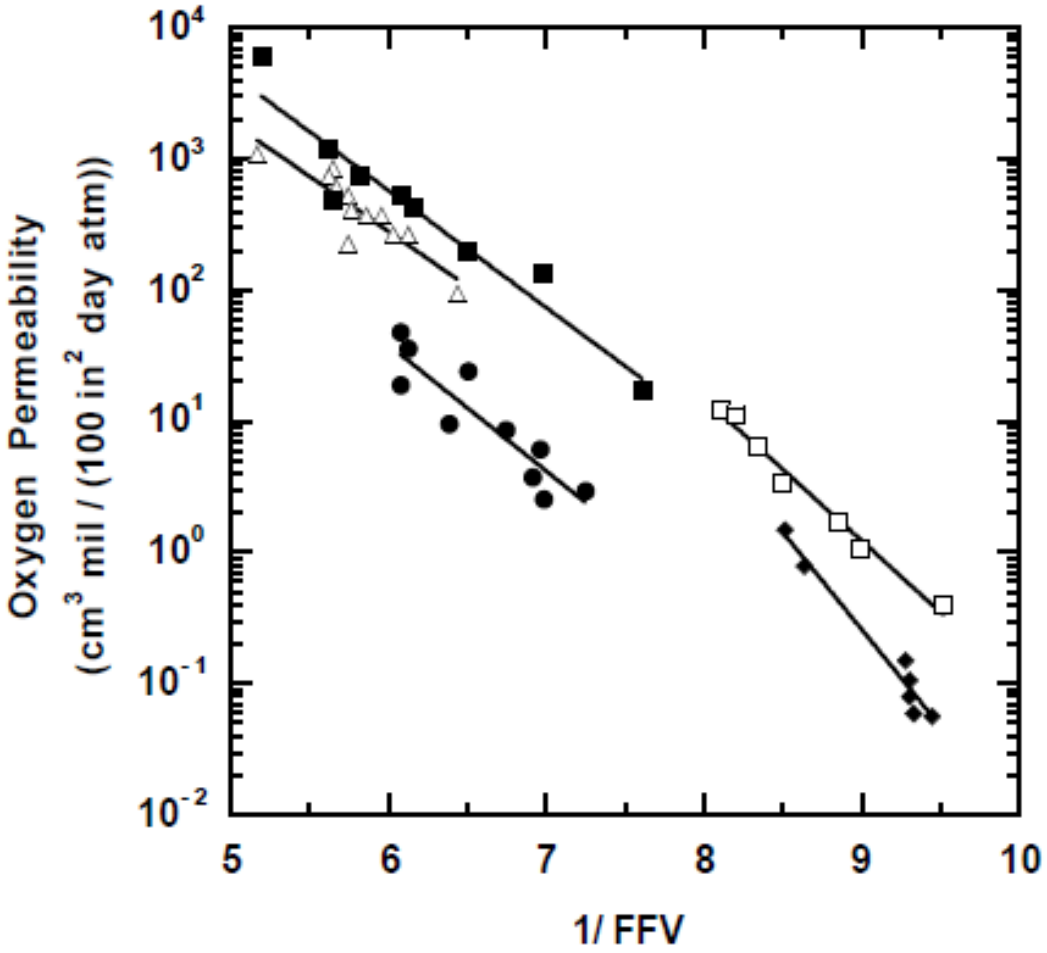

Fig: 2.9 : Oxygen permeability correlation with inverse of polymer fractional free volume for several polymers■-Polystyrene (35°C), Δ-Polycarbonates (35°C), - □ Polyesters (30°C), ●- Polyamides (25°C), ◆- Liquid Crystalline Polymers (35°C) [33].

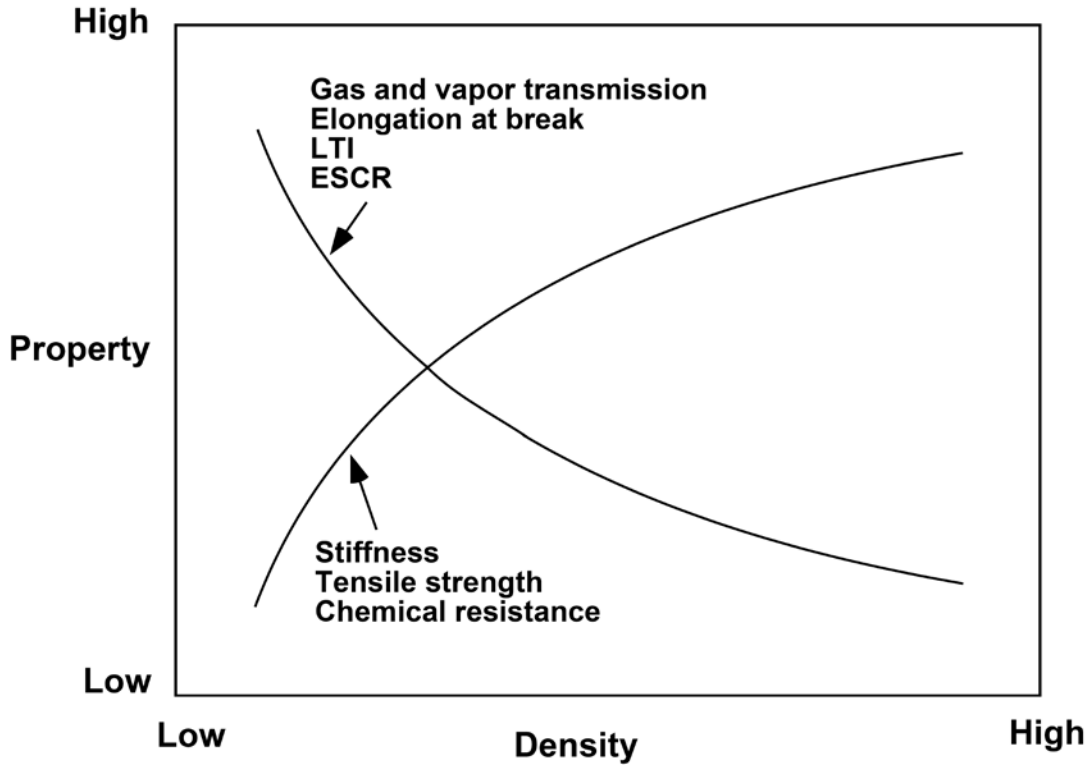

Fig. 2.10: Property density relationship for polyethylene. LTI= low temperature impact strength, ESCR= environmental stress crack resistance [29].

2.6.2.2: Humidity

The interaction of polymer packaging with the surrounding environment plays an important role in determining the shelf life of a product. With regards to the surrounding environment one of the major factors often considered is the water polymer interactions. The presence of water inside the polymer can increase, decrease or have no effect on its gas permeability, because the adsorption and diffusion of the gaseous penetrant through the polymer will be changed [35]. If the presence of water has a plasticizing effect on the polymer, then its free volume can increase and that could increase its permeability.

The change in oxygen permeability with humidity for some of the commercial barrier polymers is shown in fig 2.11. Polyolefins, vinylidene chloride copolymers and certain other copolymers shows no effect of gas permeability change with humidity

[36]. Also certain amorphous nylon grades, PET and other polymers had shown a slight improvement in the barrier properties with the increase in humidity [29]. This improvement has been attributed to the ability of small water molecules to occupy the polymer free volume sites.

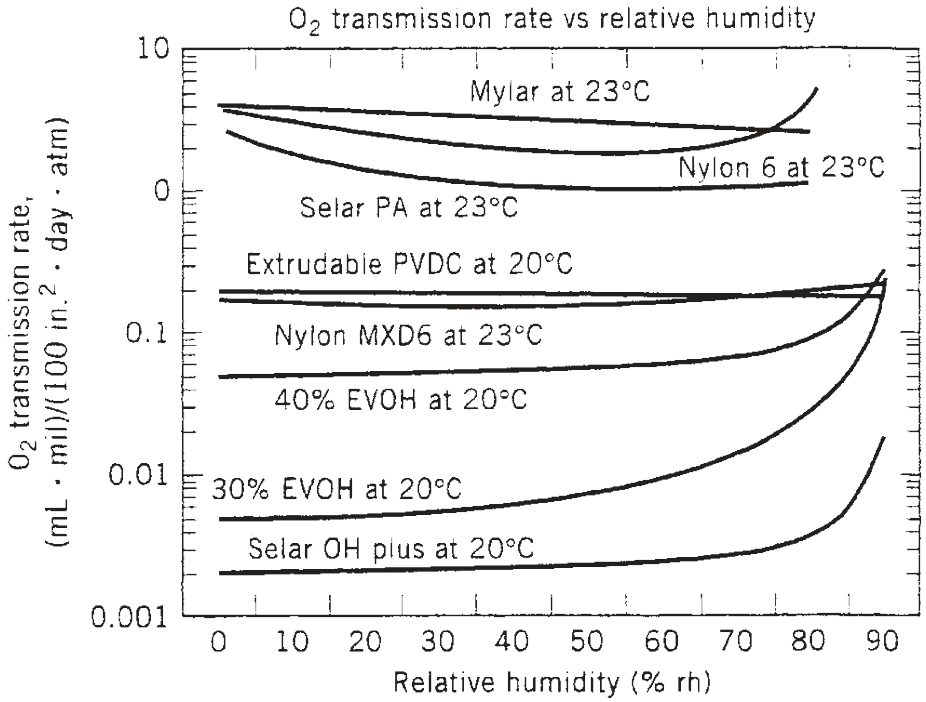

Fig. 2.11: Change in oxygen permeability of certain polymers with the increase in relative humidity [37].

2.6.2.3: Type of Penetrant

The permeability of a polymeric film is also dependent on the nature of the penetrant. With regards to gaseous molecules penetrants, their permeability is dependent on their size. In case of large molecular size gaseous particles large free volume is required for diffusion. In case of aroma and liquid penetrants, carbon chain length, polarity due to functional groups and boiling point are the important characteristics which determine their permeation through polymers [29].

2.6.2.4: Temperature

The temperature of the surrounding also affects the permeability of polymer packaging materials. The permeability in the polymer is directly proportional to the temperature, because the diffusivity increases with temperature.

The activation energy of permeation (E_P) is defined as the sum of activation energy of diffusion (E_D) and the heat of sorption (∇H_s) of penetrant in the polymers [30]:

$$E_P = E_D + \nabla H_s \tag{2.10}$$

Also permeability, diffusion and solubility coefficients and the temperature are correlated by a van't Hoff-Arrhenius relationship:

$$P = P_o \exp\left(\frac{-E_p}{R_c T}\right) \tag{2.11}$$

$$D = D_o \exp\left(\frac{-E_D}{R_c T}\right) \tag{2.12}$$

$$S = S_o \exp\left(\frac{\nabla H_s}{R_c T}\right) \tag{2.13}$$

where P_o, D_o and S_o are pre-exponential constants. The value of E_D is always positive but ∇H_scan be negative or positive. Experimental results [30] had shown that for LDPE and PVC, E_P is always positive so the permeability according to equations (2.9-2.12) will always increase with temperature. The increase in oxygen transmission rate with temperature increase for PET, nylon and PVDC is shown in fig.2.12.

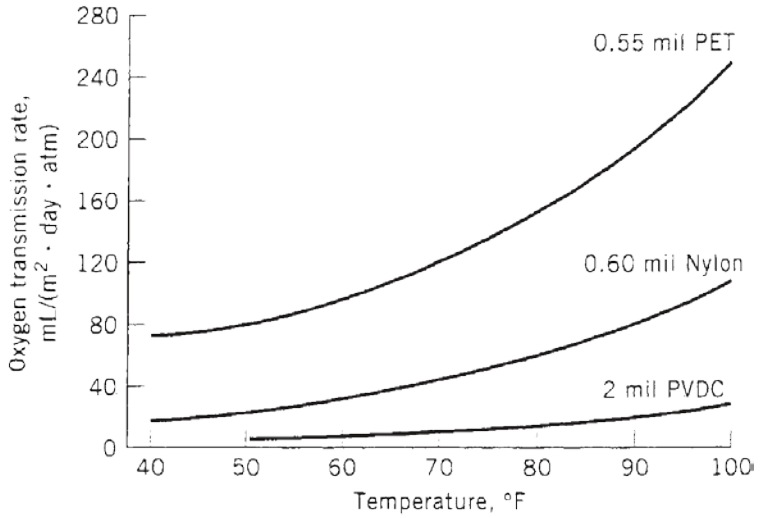

Fig. 2.12: Effect of temperature on oxygen transmission rate [37]

2.6.3: Types of barrier polymers

Based on their ability to restrict the flow of permeant such as gas (O_2, N_2, CO_2 etc.), aroma and water vapours and increase the shelf life of their products, the barrier polymers can be divided into three basic types:

1: High barrier polymers

2: Moderate barrier polymers

3: Low barrier polymers

The high barrier polymers are normally specialized engineering polymers which offer high resistance to the permeation of gases, vapours and aroma. The polymers generally regarded as high barrier polymers are ethylene-vinyl alcohol(EVOH) resins, polyacrylonitrile(PAN), copolymers of vinylidene chloride(VDC), poly(hydroxy amino ethers)(PHAE), Liquid crystalline polymers(LCPs), polychlorotrifluoroethylene (PCTFE) etc [38]. These polymers possess low enough gas permeability that can significantly reduce the shelf life of packaged products. A comparison of barrier properties of different polymers widely used in the packaging industry is shown in fig 2.13.

The moderate barrier polymers are the commodity thermoplastics such as Poly(ethylene terephthalate) (PET), Polyethylene (PE), Polystyrene (PS), Poly(vinyl chloride) (PVC),different grades of nylon such as nylon 6, nylon6,6,nylon 12 and polypropylene (PP)etc. This project focuses on the permeability of the following three basic moderate barrier commodity thermoplastics: High density PE (HDPE), linear low density PE (LLDPE) and nylon 12.

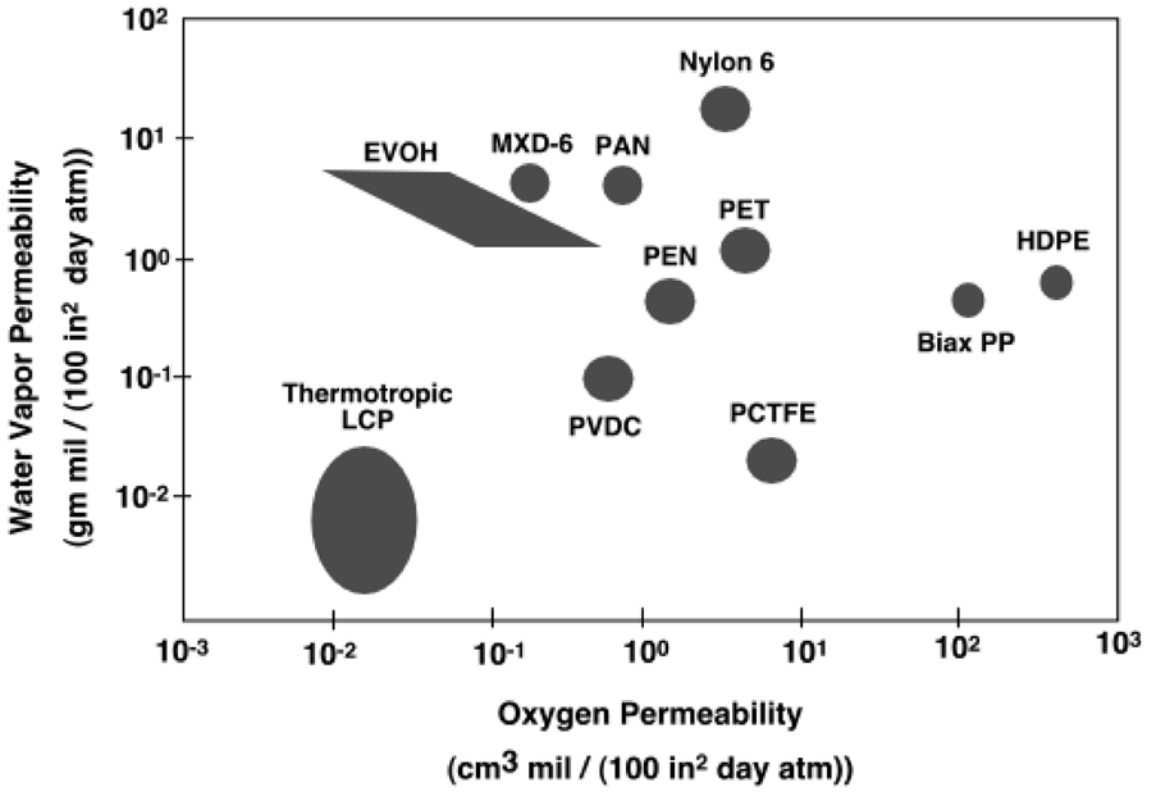

Fig. 2.13: Comparison of barrier properties of different polymers widely used in the packaging industry [39]

2.6.4: Approaches for improving barrier properties of polymers

The barrier polymers are primarily used in the food and beverage packaging industry to enhance the shelf life of the product and because they are cheap and economical source of packaging material. Although the permeability of some of the polymers

such as PET and nylon 6 are very low but still they are not enough for them to be used in certain conditions such as wine packaging or for flexible packaging for food products such as potato chips or caramelised chocolates. For such scenarios, there are a number of techniques which have been adopted in the industry for improving the barrier properties of polymers:

2.6.4.1: Annealing

Annealing during the processing of polymers to produce packaging materials is a widely used technique because of its ability to enhance the crystallinity of the polymer by removing crystal defects, letting the crystal grow in thickness and by sharpening the boundary between crystalline and amorphous phases of polymer [40]. As discussed earlier the increase in crystallinity can lower its permeability because the permeation takes place by the combination of diffusion and solubility in the amorphous region. W.Perkins [41] reported improvement in the oxygen permeability of biaxially oriented films of PET by increasing their annealing temperature (fig 2.14).

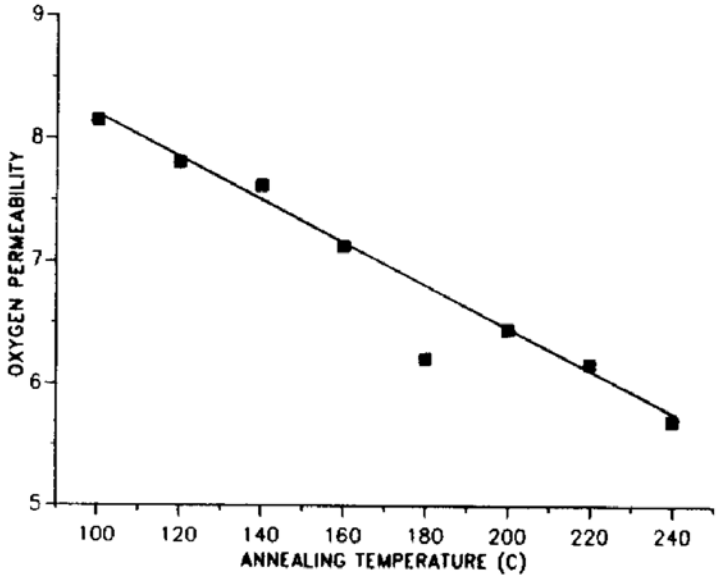

Fig. 2.14: Effect of annealing temperature on the oxygen permeability of oriented PET films [41].

2.6.4.2: Biaxial stretching

Biaxial stretching of polymer packaging films can increase its chain orientation and help decrease its permeability. The orientation of polymer films can decrease the permeability of polymers by reducing the mobility of its amorphous chains and also by stretching and tightening the amorphous tie molecules between the crystalline phases [42]. Y.J. Lin et. al. [43] have recently reported decrease in the barrier properties of polypropylene by biaxial orientation. They reported a linkage between the β relaxation intensity of polypropylene and its oxygen permeability. In PP the intensity of β relaxation is related to the amorphous phase chain motions and its decrease is related to better orientation.

2.6.4.3: Polymer blends

The barrier properties of certain polymers can be improved by blending it with small amounts of a higher barrier polymer. Generally the major phase is a low cost polymer such as PET to which a high barrier and costly polymers such as liquid crystal polymers (LCP) are added to balance the properties and cost [44]. Polymer blends are generally classified as miscible and immiscible blends. For miscible blends and copolymers, the permeability coefficient (P) can be calculated by an empirical semi-logarithmic rule [45]:

$$\ln P = \emptyset_1 \ln P_1 + \emptyset_2 \ln P_2 \qquad (2.14)$$

where $\emptyset_1$, $\emptyset_2$, $P_1$and P_2 represents the volume fractions and permeability coefficient of the two components. This additive rule is only obeyed if there is no interaction between the components. On the other hand the permeability of immiscible blends depends on the permeability and volume fractions of individual component, aspect

ratio of the dispersed phase and the continuity in the phase [45]. In case of immiscible blends the permeability is often decreased by increasing the tortuosity for the penetrant.

Barrier properties of various grades polyethylene (PE) and PET can be improved by blending them with ethylene vinyl alcohol and polyvinylidene chloride [44]. Fig 2.15 shows an improvement in the oxygen barrier characteristics of PE-EVOH blends with the increase in EVOH volume fraction [45]. Kurray Co. have commercialised a PET-EVOH blend for applications in the beverage industry [46].

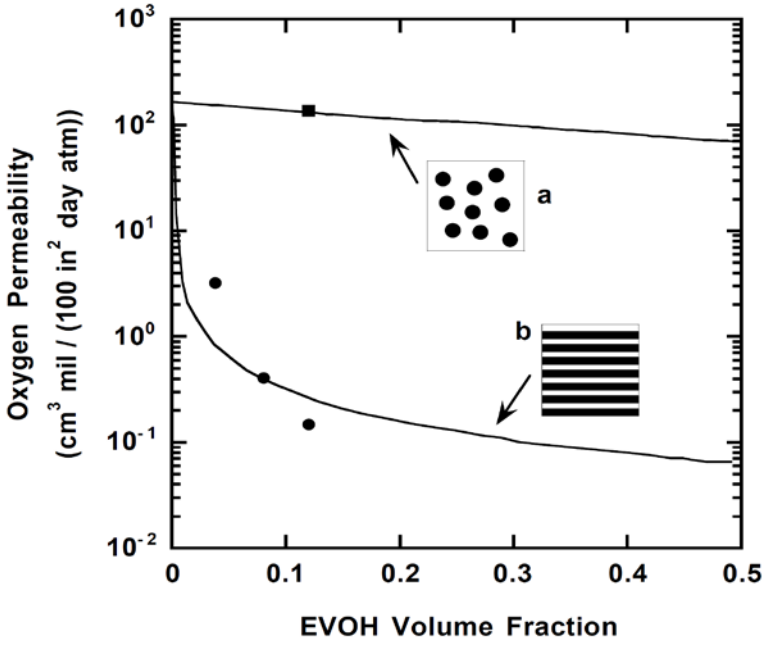

Fig. 2.15: Effect of EVOH content on oxygen permeability of PE-EVOH blends that exhibit (a) discontinuous morphology and (b) co-continuous lamellar morphology [47]

Oxygen permeability of PP/hydrogenated-oligo(cyclopentadiene)-(HOCP) blends films was studied as a function of the weight fraction of HOCP. The results showed that oxygen permeability and diffusivity through the films was lowered with increasing HOCP content. The HOCP content was reported to have an antiplasticizing effect and produced a limitation in oxygen permeability through the blend [48].

2.6.4.4: Multilayer structures

One of the most widely used techniques in the industry to create high barrier structure is by combining different layers of materials to create a hybrid packaging. These multilayer structures can combine all the favourable barrier characteristics of different materials if the layer adherence, thermal stability, processing window and the miscibility problems are sorted out during material selection. Lamination and co-extrusion are the most widely used techniques for making such structures. In case of polymeric multilayer packaging, high barrier polymer such as poly(ethylene terephthalate) (PET), poly(vinylidene chloride) (PVDC), poly (vinyl alcohol) (PVOH), ethylene vinyl alcohol (EVOH), or different types of polyamides (PA) are often used as laminates [29].

2.6.4.5: Polymer nanocomposites

The addition of small quantities of nanofillers as an impermeable particle phase in polymer matrix had proved to be an attractive method of producing polymer packaging with enhanced barrier characteristics. The strong interaction between the high surface area nanoparticles and polymers along with the decreased inter-particle distances can produce significant morphological changes in the polymer matrix even at small quantities of filler addition. In the past these structural changes were thought to bring only change in the thermal and mechanical characteristics of polymers, but now these nanofillers are also being used to improve the barrier characteristics because of their ability to give high performance at low filler content without sacrificing the optical characteristics of the polymer. The barrier properties of polymer nanocomposites are very strongly dependent on the filler aspect ratio, their volume fraction and their dispersion and orientation. There are a number of

nanofillers that are used for the improvement of basic polymer properties such as MWCNT, CB, graphene etc, all of these are expensive nanofillers that can also impart their black colour to the nanocomposites, a trait normally not required by the packaging industry. On the other hand there are different layered silicates such as MMT, bentone, kaolinite etc that can be used in polymer nanocomposites for improving its barrier characteristics without changing its optical characteristics.

A. J. Monsiváis-Barrón et. al. [98] studied the oxygen barrier characteristics of different HDPE/MMT nanocomposites produced by using two different processing routes which basically compared the performance of a single screw extruder and twin screw extruder. The nanocomposites were produced by incorporation of two different commercial compatiblizers for HDPE. Their results indicated that the barrier properties were dependent on the type of pre-blending, extruder screw configuration and the type of compatiblizers utilized. Their best results were obtained by combining a mixing chamber and single screw extruder assembly. They reported an increase in permeability for nanocomposites produced by twin screw extrusion because of the higher shear forces involved in the twin screw extruder which could cause the compatiblizer to be separated from the clay and produce more free volume inside HDPE matrix.

2.7: Rheological properties and processing of nanocomposites

The inclusion of nanoparticles into polymer matrixes produces products with enhanced or novel properties. The biggest advantage that the addition of nanofiller offers is their ability to achieve the desired properties at very low concentrations. This low concentration means that the overall processing requirements for the nanocomposites production should be very much similar to the virgin polymer

matrices. Indeed all the methods used for processing virgin polymers are being utilized for producing nanocomposites. One of the main disadvantages of the conventional processing techniques is their requirement to process the virgin polymers like HDPE at temperatures that are considerably higher than their equilibrium melting temperature to avoid the melt flow irregularities. Numerous studies [49, 50] have been conducted to examine the molecular origin of flow instabilities by either adjusting the processing conditions or the polymer parameters. Since flow instabilities set up the boundary condition of polymer processing, it is an essential requirement to minimise the flow instabilities so that the industrial polymer processing window can be broadened. In order to explain the appearance of flow discontinuities two molecular theories have been suggested. According to the first theory, the mechanism responsible is stick-slip flow, which arises due to polymer desorption from the melt–wall interface. During the flow inside the polymer processing machinery the chains of polymer melt which are closest to the capillary wall fail to adsorb on the capillary wall and, as a result, a slip flow occurs. This theory is usually related to the low surface energy die that is coated to provide a low surface energy. Another suggested theory is that the stick-slip flow occurs due to the disentanglement of the adsorbed polymer chains from the bulk of the melt at the melt-wall interface. This disentanglement is likely to arise within the capillary flow of a high surface energy die. With the energy crisis rising throughout the world, new methods have to be developed that can help process the polymers at temperatures closer to their equilibrium temperatures.

Recent studies [51-58] have shown the presence of an extrusion window for linear polyethylene in between the flow instability and flow induced solidification regions. The extrusion window effect is a specific melt flow singularity in extrusion and is

described by the appearance of a pressure reduction occurring at and around 150 ^{o}C, while maintaining a constant material throughput with no distortion. The existence of an extrusion window for linear PE was first reported by Keller [51]. For polymer process industries the extrusion window has the advantages of an energy efficient processing route (low extrusion pressure and temperature) that can provide the usual continuous flow without any flow instabilities and a smooth extrudate with minimum die swell. On the other hand, the research conducted so far on most of the commercial PE grades [51-60] had shown that the window effect is conspicuously too narrow (1-2 ^{o}C) to be adopted in polymer process industries in an industrial scale extruder where temperature variations in various zones can be ± 3^{o}C, i.e. the width of window has to be about 6^{o}C. In order to make the process industrially viable the extrusion window has to be broadened to several degrees so that the thermal fluctuations in the polymer processing industries can be tolerated.

Conventional rheological theories of extrusion instabilities cannot predict or even explain the observed melt flow singularity phenomenon and its flow criticalities. Lately, the molecular origin of melt flow singularity was studied in detail by Han Xu et.al [58]. Previous research carried out by Keller [54-57] had concluded that the capillary flow gives rise to the window effect and the convergence flow at the die entry which can induce a transient mobile hexagonal mesophase into the aligned chains at the die wall surface. The mesophase structure is basically liquid crystals which are produced during the transformation of polyethylene melt into fibrous crystals during dynamic cooling inside a capillary experiment. Although Keller et.al. [60] carried out insitu-WAXD analysis during flow in a specially designed capillary rheometer to confirm the formation of such a mesophase, but later studies [58] confirmed that window effect appeared due to shear flow rather than convergence

flow. One of the primary factors in enhancing the convergence flow is the die surface entry angle. Han Xu [58] carried out detailed flow analysis to study the effect of entry angle of die surface on the window and concluded that the extrusion window remains unaffected by the die entry angle. Keller in his extensive work [54-57] also suggested that the extrusion window can only appear in samples with a molecular weight in the range of $1.3*10^5$ to $1.0*10^6$ g/mol. Although work carried out on low molecular weight grades of HDPE [58] and LLDPE [53] have reported the appearance of extrusion window for these polymers. The molecular origin of melt flow singularity phenomenon of linear polyethylene has been attributed to slip flow which can usually promote smooth extrudate production with minimum die swell. The slip flow is produced due to the disengagement of adsorbed chains from the anchored chains at the melt/wall interface. This disengagement is also supported by the production of a flow induced mesophase structure.

Recent studies have shown that different nano clays such as sodium montmorillonite (Na-MMT), bentone etc. can be exfoliated in polymers by different routes [61-64]. The nanoscale dispersion of individual clay layers achieved by exfoliation can increase the interaction between the polymer chains and the clay layers and can also influence chain dynamics during melt flow in different geometries. The aspect ratio, surface to volume ratio and the relaxation time of clay layers is generally very high because of their rigid and stiff surface and hence they can promote the stretched chain conformation of linear polyethylenes at high temperature. The dispersion of agglomerates of filler inside these nanocomposites can be very high and these individual agglomerates can be considered as particles with spherical or square shape. The effect of these agglomerates on chain dynamics of polymer melt and their role in disengaging the bulk free chains from the adsorbed chains on the

capillary metal wall is expected to be different from the exfoliated clay layers. A number of studies have reported that the melt flow behaviour of polymers can be modified in the presence of nanofillers. In broadening the extrusion window nanofiller addition can play a vital role because of their ability to influence the disengagement between the adsorbed chain on capillary wall and free bulk chains of the polymeric melt. The addition of 1D, 2D and 3D nanofillers will each have different effect on the chain dynamics because of their varying aspect ratios, surface to volume ratio, relaxation time and epitaxial matching capacity.

A schematic plot of extrusion pressure vs. temperature for linear polyethylene flowing in capillary rheometer under dynamic cooling at a constant shear rate is shown in fig 2.16. The plot shows the four different flow regions encountered at or around the typical melt flow singularity phenomenon: (1) stick flow, (2) stick-slip flow, (3) slip flow and (4) flow induced solidification. In the stick flow region extrusion pressure increases with the decrease in the temperature and we have a typical liquid polymer melt inside the capillary die whose viscosity increase with the decrease in temperature and in this region the viscosity and the temperature obey an Arrhenius type relationship:

$$\eta = Ae^{E_a/RT} \tag{2.15}$$

In the above equation η is the shear viscosity, Ea is the melt-solid state flow activation energy, R is the universal gas constant and T is the flow temperature. During the stick flow region the extrudate surface becomes rough and it shows surface melt fracture with loss of gloss and the die swell also increases with the decrease in temperature. During the stick-slip flow region pressure oscillations with the decrease in temperature are observed and extrudate obtained consists of

alternating regions of melt fracture and smooth extrudate surface. In the slip flow region the phenomenon of melt flow singularity (unique phenomenon) is observed and this region is the extrusion window where a reduction in pressure is observed along with a smooth and glossy extrudate with minimum die swell is obtained.

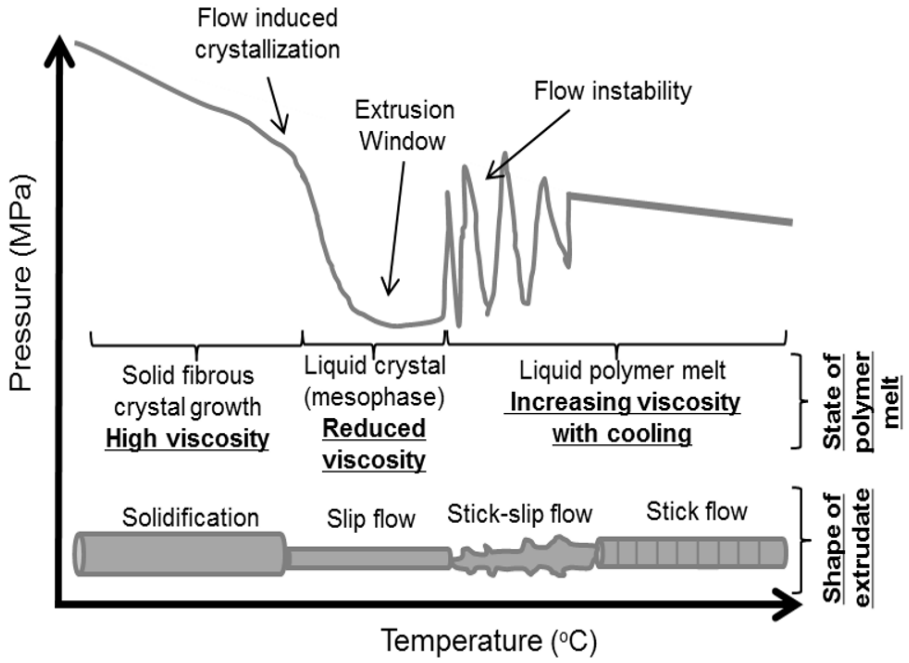

Fig. 2.16: Extrusion Pressure vs. temperature schematic plot, demonstrating melt flow singularity phenomenon of polyethylene in capillary rheometer. The bottom of the graph shows the four different flow regions encountered at or around the MFS phenomenon i.e. (1) stick flow, (2) stick-slip flow, (3) slip flow and (4) flow induced solidification, along with the state of polymer melt and the shapes of the extrudate achieved in the different stages of extrusion

2.7.1: Capillary rheometer: Basics and corrections

The rheometers used for analysing the rheological analysis of polymers can be divided into two broad categories: (a) rotational rheometers and (b) capillary rheometers. The rotational rheometers (plate-plate, cone-plate etc) have the distinct advantages of maintaining a uniform shear rate throughout the specimen and a smaller specimen size. On the other hand the capillary rheometers are more widely used throughout the polymer process industries because of the following advantages: They cover the strain rate range (0.001 – 10,000 s^{-1}) and shear stress

range (10^3 – 10^6 N/m^2) of interest in polymer processing machinery, the specimen size is usually less than 100 grams, the data reproducibility is good and the data obtained is more meaningful for simulating the processing behaviour of polymers, and finally the biggest advantage of the capillary rheometer is that they provide an extrudate which can be analysed to study the effect of changing parameters just like in all the polymer processing .

The derivation of Poiseuille law for capillary flow yields the following equations for wall shear rate γ_{app} and wall shear stress $(\tau_w)_{app}$:

$$(\tau_w)_{app} = \frac{R\nabla P}{2L} \tag{2.16}$$

$$\gamma_{app} = \frac{4Q}{\pi R^3} \tag{2.17}$$

where ∇P is the pressure drop, R is the capillary radius, L is the capillary length and Q is the volumetric flow rate.

There are two basic modes of operation used for operating the capillary rheometer: controlled pressure by dead weight loading or gas pressure and controlled volume displacement. In case of controlled pressure method the volumetric flow rate is measured whereas in case of controlled volume mode of operation the direct measurement of pressure drop directly in the melt just above the die entry is carried out. Capillary rheometer data interpretation using eqs 1 and 2 yield an apparent viscosity rather than true viscosity of the polymer melt because of number of principal errors involved in measuring high viscosity by capillary rheometer. The principle sources of these errors are: Reservoir and friction losses, end pressure drop (Bagley correction), non-parabolic velocity profile (Rabinowitsch correction), slip

at the die wall, influence of pressure on viscosity and volume and influence of heat generation.

2.7.2: Bagley correction:

The pressure drop measured in capillary rheometer by the pressure transducer also has some pressure contributions from the extensional properties of the polymer melt which produce some entry and exit pressure drop at the die. The entry pressure drop occurs due to the convergent flow of the polymer melt at the die entrance whereas the elastic recovery of the deformed polymer at the die exit produces the end pressure drop. A schematic diagram illustrating the pressure drop distribution in a die of capillary rheometer is shown in fig. 2.17.

Since the shear stress is dependent on the pressure drop therefore an end correction is required to derive true wall shear stress. Bagley correction is used to provide a correction for the end pressure drop error. Bagley observed that a plot of pressure drop versus die length to radius ratio at varying fixed shear rate gives a series of straight lines which can be extrapolated back to zero pressure. A schematic diagram of Bagley correction plot is shown in fig 2.18.

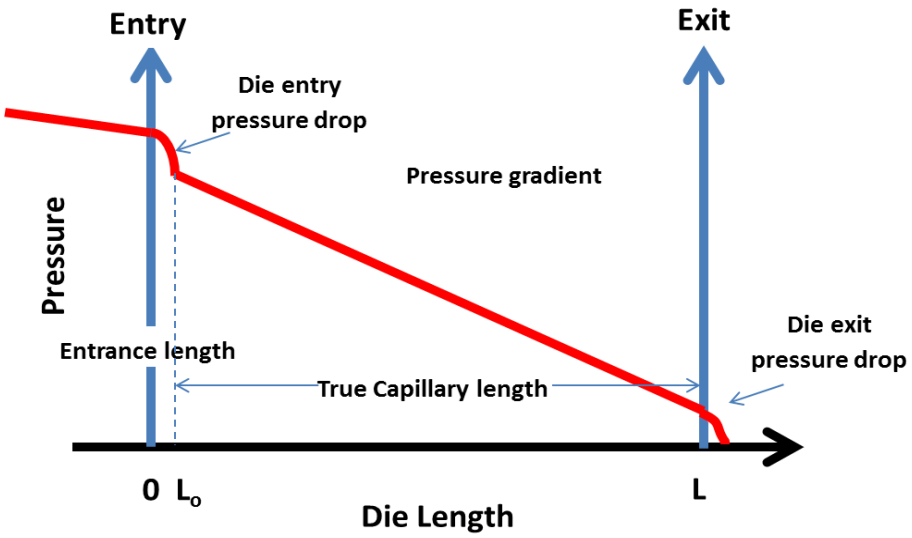

Fig. 2.17: Schematic diagram of die length pressure drop distribution

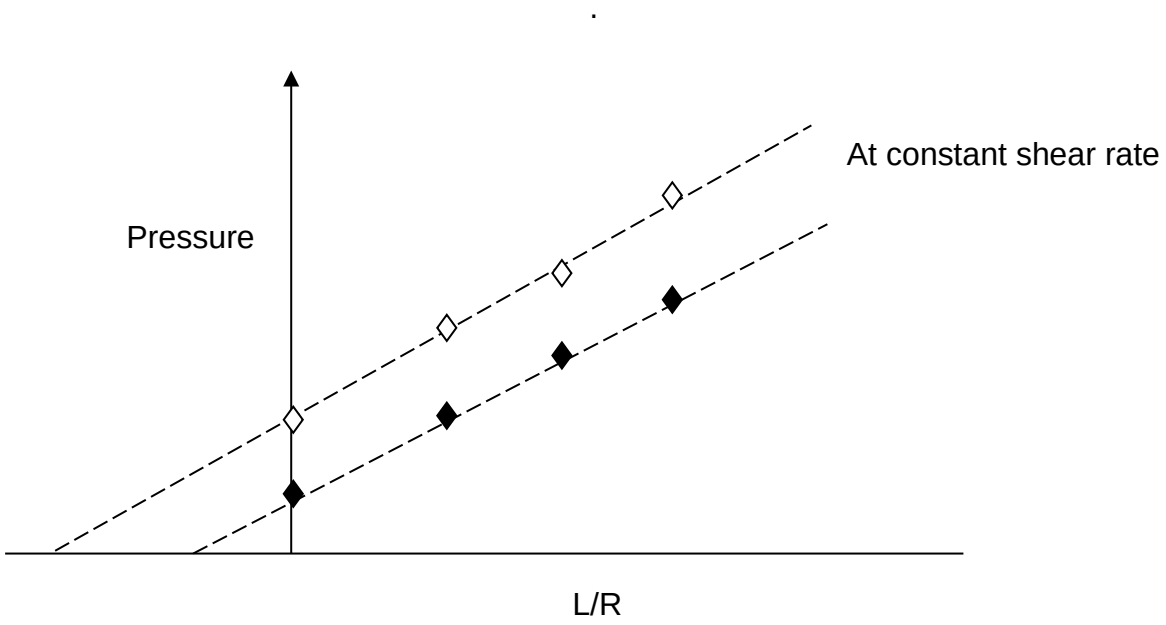

Fig. 2.18: Schematic diagram of Bagley correction, where L/R represents the length to radius ratio of the capillary die

The intercept of these straight lines on zero pressure gives a correction on capillary die length which is referred to as effective die length. If the material inside the capillary rheometer only undergoes shear flow, the intercept would be at the origin but the polymeric melts shows varying degree of extensional flow and the intercept at ΔP = 0 is a negative L/R value,e. This value can then be used for calculating the true wall shear stress by the following formula:

$$\tau_w = \frac{\Delta P}{2\left(\frac{L}{R} + e\right)} \tag{2.17}$$

Where τ_w is the true wall shear rate, ΔP is the pressure drop and e is the Bagley correction factor. The application of Bagley correction to the rheological data obtained from a capillary rheometers requires extensive experiments using at least three or more capillary dies with different L/D ratio in order to achieve accurate results.

2.7.3: Rabinowitsch correction:

The Rabinowitsch correction is frequently made to take into account the variations which arrive due to the presumed parabolic velocity profile of the polymer melt in the capillary die. The polymer melt velocity profile is actually more plug-like in the die because of their pseudo-plastic nature. The Rabinowitsch correction (1) is expressed as:

$$\gamma_T = \left(\frac{3n+1}{4n}\right)\frac{4Q}{\pi R^3} \tag{2.18}$$

where n is the power law index in the above equation. The effect of Rabinowitsch correction on a typical flow curve is shown in figure 2.19. The correction factor (3n+1)/4n varies in magnitude from 1 to infinity as n can vary from 1 to 0, but in practice the error in viscosity at any shear rate without applying this correction has a maximum value of 15% when n=0.23. When the rheological data obtained from a capillary rheometer is to be used for comparative purposes, the comparability of the data will not alter if the correction is not applied.

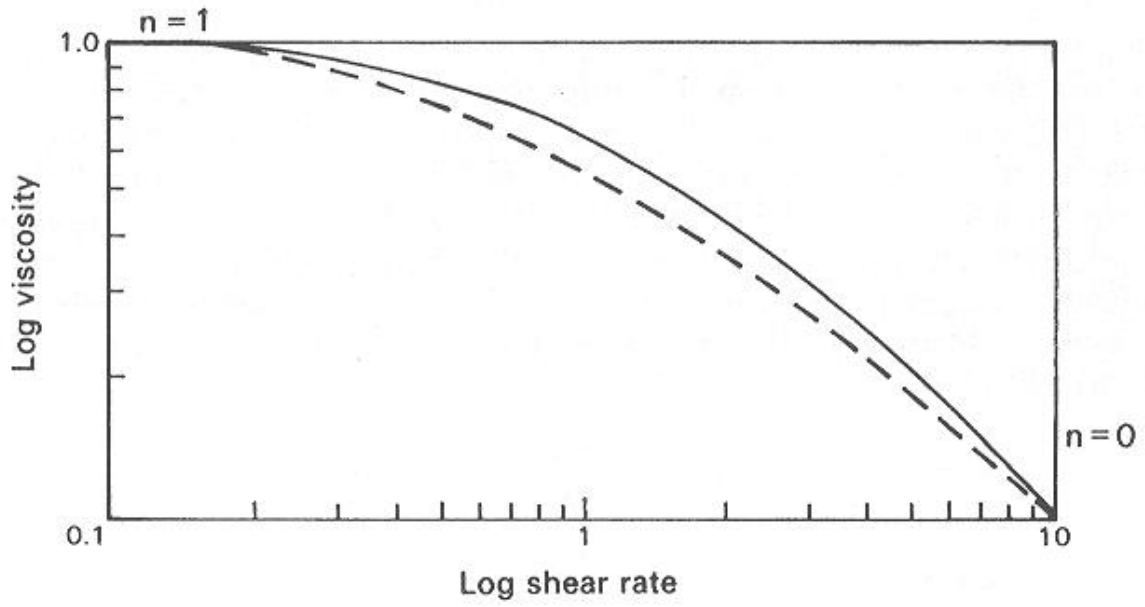

Fig. 2.19: Effect of Rabinowitsch correction on a typical flow curve (----- corrected data)

(____ Uncorrected data) [66]

2.8: Mechanical properties of polymer nanocomposites

In the recent years, a number of studies have shown that the properties of polymers such as toughness, yield stress, impact energy absorption, ultimate tensile strength etc. can be improved by blending small quantities of nano-size fillers [67]. Rehman et. al reported that the toughness for graphene based nylon12 nanocomposites can be improved up to 75% by incorporating only 0.6 wt% graphene [68]. Significant enhancement in the tensile modulus and the tensile strength of nylon6 by 115% and 120% respectively was achieved by incorporation of only 1 wt% of multi-walled carbon nanotubes (MWCNT) in nylon6 [69]. Also in case of polyurethane-nanoclay composites, an increase of 120% in tensile strength has been reported [70]. Al Lafi et. al. [71] has reported an increase in impact strength of HDPE at high strain rates by incorporating only 0.6 wt % of MWCNT. Apart from MWCNT other fillers such as CB, graphene and silica nanofiller [72, 73] are also being utilized for producing advanced nanocomposites. In all of these studies the size of the nanofiller played an important role in producing a high interfacial area between the filler and the polymer,

which results in great enhancement in the mechanical properties of polymers for very small weight fraction of nanofiller added. This result in little increase in the final product price and weight but these products can be a better alternative to the micro composites. Enhanced interfacial load transfer is one of the significant effects that nanofillers impart to polymer matrix.

To achieve better load transfer, nanofillers must be able to generate larger contact area that can provide better mechanical interlocking with polymer chains. The contact area that nanofillers can generate is dependent upon its inherent shape, size and its ability to disperse inside polymer matrix. The shape and dimensions of all nanofillers being used nowadays varies from 0D-SiO_2 to 3D-CB particles. In a nanocomposite, 0D nanoparticles can interact with polymer chains at a single 0D point in comparison to 1D CNT or carbon nanofibres which can form a much better contact due to their large surface area. On the basis of dimensionality, the fillers can be divided into four basic categories: 0D, 1D, 2D and 3D materials. 0D nanoparticles have all their dimensions at the nanometer scale, where as 1D and 2D nanofillers have two dimensions and one dimension at the nanometer scale respectively. In case of 3D none of their dimensions are to the nanometer scale. The 0D, 1D and 2D fillers are generally referred to as particulate, fibrous and layered materials respectively. 3D fillers are generally powder of multilayer materials in which the 0D, 1D and 2D nanofiller elements are in close proximity with each other. Generally the addition of 0D nanofillers (POSS, SiO_2, Al_2O_3 etc.) increases the thermal, optical and biodegradable properties of the polymer matrix; however 1D nanofillers (MWCNT, carbon fibres etc.) can enhance electrical and mechanical properties and 2D nanofillers (graphene, clay etc.) can improve barrier, thermal and mechanical properties. 2D nanofillers exhibiting large aspect ratio and surface area due to its

nanoscale flat surface and high lateral dimensions can produce better nanocomposites than MWCNT. The production of 0D and 1D nanofillers is an expensive process and the cost they add to final polymer product can limit their use as nanofillers. Graphene on the other hand can be produced by a much cheaper production route and along with CB offers a better alternative to the expensive CNT and carbon fibres [74, 75, 76].

During tensile testing of polymers various phenomenon's such as crazing, adiabatic heating, necking, cold drawing etc. can take place. A number of studies [77, 78, 79, 80] have reported the occurrence of adiabatic heating during the tensile testing of polymers. The local adiabatic heating can lead to thermal softening of the specimen during tensile testing. Generally in the literature a temperature increase of 30-80^{o}C has been reported. During tensile testing of Nylon12-clay nanocomposites [80], a considerable amount of heat generation inside the dumbbell samples has been reported. The heat measurement carried out by an infrared camera revealed that temperature of nanocomposites increased from 23 to 70 ^{o}C, regardless of the strain rate used. The heat generation was attributed to the nanoclay ability to uniformly dissipate internal friction as heat. Microscopic analysis of Nylon 12-clay nanocomposites carried out in another work [80] also proposed the similar deformation process. Gorwade et. al. [81] carried out high strain rate testing of ultra-high molecular weight polyethylene also found considerable heat generation during the tensile testing.

Shen et. al. [82] carried out detailed analysis of PET/clay based nanocomposites and found that the strain hardening behaviour of their samples was dependant on the strain rate. Although PET has a glass transition temperature around 70 ^{o}C but the temperature increase with the increase in strain rate was attributed to the strain

hardening. A.S. Alghamdi et. al. [83] carried out detailed analysis to review the effect of quantity and dispersion of carbon black particles and strain rate on the heat generation during the plastic deformation of 75/25 wt. % HDPE and UHMWPE blends (U75H25) nanocomposites. They found that the increase in strain rate from 0.02-0.3 s^{-1} caused the temperature generation to increase rapidly (fig.2.20) and also the incorporation of CB nanoparticles into the blend produced more heat due to the increase in internal friction (fig.2.21).

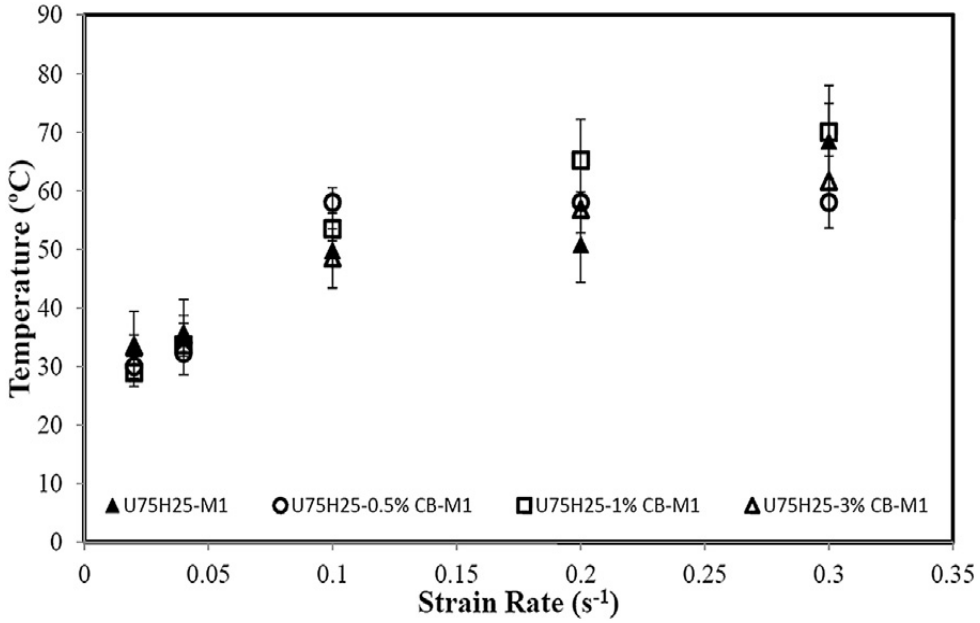

Fig. 2.20: Strain rate effect on the temperature increase during tensile test of U75H25/CB nanocomposites

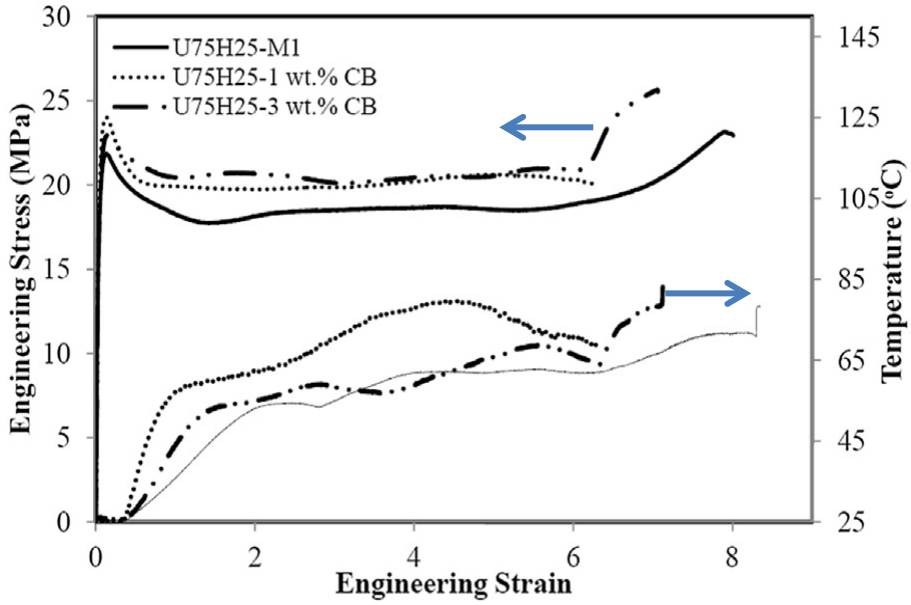

Fig. 2.21: Temperature change for U75H25 / (0,1 and 3) wt.% CB during tensile testing at 0.2 s^{-1} strain rate

2.9: Kaolin clay – polymer composites previous case studies

The effect of kaolin clay on the final properties of polyolefins composites that are produced by melt blending, has not been studied in detail in the literature. There are only few papers which describe the effect of kaolin clay on the final properties of polymer matrixes when melt blending is utilized. M.P.Villaneva. et.al [84] utilized a twin screw extruder for incorporating a master batch of kaolin in low density polyethylene without any binding agent or compatibilizer. The master batch used was kaolin blended with small amount of low density polyethylene. They studied the effect of adding 7 wt % of kaolinite clay and organo-modified MMT on the rheological, morphological and mechanical properties of low density polyethylene. There results indicated no exfoliation or intercalation but the thickness of the clay agglomerates in the matrix was less than 100nm and the clay was more uniformly dispersed than organo-modified MMT in low density polyethylene. The dispersion was reported to be caused by the higher affinity between polyethylene and kaolin.

The uniform dispersion of kaolin improved the melt strength of the samples and the sample surface was also more uniform and free from air bubbles in comparison to the organo-modified MMT samples. The sample surface uniformity is a very important requirement in the production of plastic products from blow molding, film extrusion and thermoforming. M. P.Villaanueva et.al. [85] in another paper utilized an organo-modified kaolin (OK) clay which had a d-spacing of 1.11 nm. The nanocomposites were prepared by using 5 wt% of OK with EVA, PEAA, PEMA, and an ionomer containing a small amount of polyamide 6 in a Haake polylab mixer. The nanocomposites prepared were not exfoliated or intercalated but the intensity of the kaolinite peak was reduced which indicate that the clay was uniformly dispersed. The samples prepared had improved young modulus and stress at break. The kaolin tactoids formed were once again 10-20 nm in thickness (measured by TEM) but the aspect ratio was lower than that estimated for MMA systems with same polymers. The thermal properties were only slightly improved and the oxygen barrier properties were reduced by 20 %. L. Cabedo et.al. [86] optimized the properties of a PLA/PCL (polylactic acid/polycaprolactone) blend nano-composites based on chemically modified kaolinite. The blending was carried out in an internal mixer at 150 ^{o}C and 60 rpm rotor speed. The results indicated complete intercalation for pure PLA/kaolin nano-composites and for blends of PLA/PCL modified with kaolin. No intercalation was observed for PCL/kaolin samples due to the thermal degradation. The samples also indicated enhanced mechanical and barrier properties for blends containing kaolin clay.

One of the widely used approaches in the preparation of polyolefin nanocomposites is the utilization of coupling agents. These coupling agents improve the properties of the final nano-composites by forming strong bonds between the inorganic and

organic phases. Domka et.al. [87] utilized different silane coupling agents to modify the surface of kaolin clay. This modified kaolin clay (4 wt %) was incorporated into HDPE using twin screw extruder. The silane coupling agent not only improved the physic-chemical properties of raw kaolin but also improved the mechanical properties due to the strong bond between filler and HDPE. The SEM pictures also revolved homogeneous distribution of the filler in the matrix. Domka et.al [88] in another paper reported the effect of surface modification of kaolin on the morphological and mechanical properties of polymer clay nanocomposites. Although, no exfoliation or intercalation was achieved in the polymer clay nanocomposites, the final mechanical properties were significantly improved and clay dispersion in the nano-composite was better for silane modified kaolin clay than the pure kaolin based nano-composite. L. Xuening et.al. [89] utilized two different coupling agents (NDZ 501 and PP-g-MAH) for surface treatment of kaolin and mixing it with the PP for preparing polymer clay nano-composites. A combination of two-roll mill and twin screw extruder was used for incorporating 3 wt % of surface treated clay in PP. The XRD and TEM results confirmed complete exfoliation of the kaolin layers in the PP matrix. The results are in contrast to the one achieved by using silane coupling agents or by using organomodified kaolin. The crystallization properties indicated that because of large chain, PP-g-MAH based nano-composites grow more heterogeneous nucleus than PP/NDZ nano-composites. The crystallization rates of PP/kaolin nano-composites were also faster than that of pure PP which indicates that the non-isothermal crystallization process of PP can be accelerated. Z.M. Chang et.al. [90] demonstrated the effect of nano kaolin on the flame retardant properties of LDPE/EPDM composites. They used LDPE-g-MAH as coupling agent for producing various (6-60 wt%) composites in twin screw extruder. Nano-hydroxyl aluminum

oxalate (nano-HAO) was used as filler in LDPE/EPDM blends for comparison. The addition of nano-kaolin enhanced the thermal stability of the composites but also had a synergistic effect with nano-HAO on the flame retardency in LDPE/EPDM systems. The results showed that when combination of nano-HAO and nano-kaolin were added to LDPE/EPDM system they provided maximum flame retardency.

Kaolin clay can be intercalated and then exfoliated by using combination of chemical and physical modification. One of the most widely used materials that can intercalate kaolinite in direct reaction is DMSO, because of its large dipole moment and high polarity. L. Cabedo et.al. [91] utilized a combination of DMSO, methanol, and octaadecylamine to increase the basal spacing greater than 3 nm, which indicates a fully exfoliated kaolin sample. The addition of DMSO and methanol to kaolin-DMSO samples only caused the basal spacing to increase up to 1.13 nm. The addition of octadecylamine caused full exfoliation. This surfactant binds to DMSO molecules which are in turn attached to the silicon oxide part of kaolinite layer. The organic tail of the attached surfactant was reported to offer strong steric and polar hindrance for the clay layers to bind to one another. The role of methanol was described to intercept the self-association of DMSO molecules. The modified kaolin sample (0-8 wt %) were incorporated into EVOH using a twin screw extruder. The nano-composites produced were not exfoliated or intercalated fully because the kaolinite basal peak was retained in the nano-composites. The intensity of the clay peak was reduced considerably which indicated most of the clay is intercalated in the matrix. The addition of fully exfoliated kaolin in EVOH caused the degradation temperature to be increased by more than 21 ^{o}C and the glass transition temperature by 6 ^{o}C.

J. G. Gardolinski et.al. [92] utilized DMSO to intercalate kaolin and then incorporated it in polyethylene oxide and polyhydroxy butyrate. The DMSO modified kaolin and matrix were mixed in two step, first the modified clay and polymer were physically mixed and then they were fused together in a reaction beaker using heating for period of 4-5 days. The nano-composites retained the intercalated clay structure and the samples had increased thermal-oxidate stability along with high intercalation index (79%). V. P. Privalko et.al. [93-96] in a series of papers described the effect of calcinated kaolin on the properties of kaolin/HDPE composite systems. They used two grades of HDPE, injection molding and blow molding grade. The calcination of kaolin was reported to destroy its crystal structure and improve its surface catalytic activity. They utilized a coupling agent for decreasing the void formation in the composite and for facilitating better melting of the filler by polymer matrix. A very high weight fraction of kaolin (23-54 wt% or 10-30 vol %) was used in the preparation of composites. This high amount of kaolin makes it conventional filler rather than a nanofiller and hence their results cannot be used for comparison with recent nano-composites based on low volume fraction of kaolin. They reported uniform distribution of filler in the matrix and no considerable change in the crystallinity of composites for both injection molding and blow molding grades HDPE. One of the important observations was the absence of the X-ray reflections due to the kaolin in the composites, which indicated that the crystalline structure of kaolin was completely destroyed.

Kaolin has also been used in the preparation of polymer nano-composites using polymerization filling technique. This technique is used especially in the preparation of PE and nylon grades. X. Wang et.al. [97, 98] reported the common viscoelastic flow for UHMWPE filled with kaolin. The composites were prepared via

polymerization filling of UHMWPE. The polymerization was carried out on the surface of kaolin clay with filler content varied from 0-24 wt%. Their results indicated a significant increase in the melting temperature of the composites for filler content up to 5 wt%. The rheological data indicated that for the composites with kaolin content greater than 16 wt%, the sample behaved like normal polymer melts and they had viscosities less than that of the pure UHMWPE. Their results also indicated that the UHMWPE filled with kaolin can be produced by regular polymer processing technique. The decrease in viscosity and easy processability was attributed to the excellent interface adhesion between the polymer and clay which can cause a decrease in the number of entanglement points of UHMWPE and promote better flow for UHMWPE.

Summary

In this chapter a detailed literature review of the field of nanocomposites is presented. Based on all the research carried out so far in the field of low temperature processing of HDPE, we can conclude that there is a shortage of research which can provide methods to enhance the processing window of HDPE, so that HDPE can be processed at low temperature on the available polymer processing machinery. Also the literature review indicated a deficiency of data for using HDPE kaolin composites in the field of packaging. Based on all the research carried out so far on the internal heat generation due to the plastic deformation during the tensile testing of nanocomposites we can conclude that there is a deficiency of data available which can link the filler size, dimensionality and morphology inside the polymer matrix with such heat generation phenomenon. The aim of this research is to link the dimensionality, size and morphology of the filler with low temperature processing, barrier properties, thermal characteristics and plastic deformation of HDPE and also

to compare the barrier and thermal characteristics of HDPE nanocomposites with LLDPE and Nylon12 nanocomposites.

References:

1. Utracki, L.A. Clay-Containing Polymeric Nanocomposites, Volume 1, chapter 1, 2004.
2. Rosato, D.; Rosato, D. Reinforced Plastics Handbook, chapter 1, 2004.
3. Mallick, P.K. Fiber Reinforced Composites Materials, Manufacturing and Design, chapter 1, 2008.
4. Koo, J. Polymer nanocomposites: processing, characterization, and applications, chapter 1, 2006.
5. Vaia, R. A.; Wagner, H. D. Framework for nanocomposites. Mater. Today 2004, 7, 32–37.
6. http://www.plasticstechnology.com/articles/199906fa4.html
7. http://zeus.plmsc.psu.edu/~manias/news/plastics_tech_oct_2001.pdf
8. Markarian, J. Automotive and packaging offer growth opportunities for nanocomposites. Plast. Addit. Compd. 2010, 7, 18–21.
9. Harper, C. Handbook of plastics technologies: the complete guide to properties and performance, McGraw-Hill Professional, 2006.
10. Moore, D.M.; Reynolds. Jr. R.C. X-ray Diffraction and the identification and analysis of clay minerals, 2nd edition, 1997.
11. Weaver, C.E.; Pollard, L.D. The chemistry of clay minerals. Developments in sedimentology, Elsevier, Amsterdam, 1973.
12. Guggenheim, S.; Martin, R.T. Definition of clay and clay mineral: joint report of the AIPEA nomenclature and CMS nomenclature committees, Clays and Clay Minerals. 1995, 43, 255-256.

13. http://www.gly.uga.edu/schroeder/geol6550/CM01.html
14. http://soils.cals.uidaho.edu/soil205-90/Lecture%208/index.html
15. Bergaya, F.; Theng, B.K.G.; Lagaly, G. Handbook of Clay Science, Developments in Clay Science, Vol. 1; 2006 .
16. Murray H.H. Applied Clay Mineralogy, Vol. 2; 2007.
17. http://www.dnpm.gov.br/dnpm_legis/sm2004.html
18. Raff, R.A.V. Encyclopedia of Polymer Science and Technology, Volume 6, Interscience, New York, NY, USA, 1967.
19. Vasile, C.; Pascu, M. Practical Guide to Polyethylene, Rapra Technology Limited, 2005.
20. Balazs, A. C.; Emrick, T.; Russell, T. P. Nanoparticle Polymer Composites : Where Two Small Worlds Meet. Science (80-.). 2006, 314, 1107–1111.
21. Chen, B.; Evans, J. R. G.; Greenwell, H. C.; Boulet, P.; Coveney, P. V; Bowden, A. a; Whiting, A. A critical appraisal of polymer-clay nanocomposites. Chem. Soc. Rev. 2008, 37, 568–94.
22. Kiliaris, P.; Papaspyrides, C. D. Polymer/layered silicate (clay) nanocomposites: An overview of flame retardancy. Prog. Polym. Sci. 2010, 35, 902–958.
23. Pinnavaia, T.J.; Beall, G. W. Polymer Clay Nano-composites, Chichester, U.K.: John Wiley & Sons Ltd, 2000.
24. Sinha Ray, S.; Okamoto, M. Polymer/layered silicate nanocomposites: a review from preparation to processing. Prog. Polym. Sci. 2003, 28, 1539–1641.
25. Phang, I. Y.; Liu, T.; Mohamed, A.; Pramoda, K. P.; Chen, L.; Shen, L.; Chow, S. Y.; He, C.; Lu, X.; Hu, X. Morphology, thermal and mechanical properties of

nylon 12/organoclay nanocomposites prepared by melt compounding. Polym. Int. 2005, 54, 456–464.

26. Zheng, Q.H.; Yu, A.B.; Lu, G.Q.; Paul, D.R. Clay-based polymer nanocomposites research and commercial development, J. Nanosci. Nanotechnol., 5, 1574–1592, 2005.
27. Nwabunma, D.; Kyu,T. Polyolefin Composites, John Wiley & Sons Ltd, chapter 10, 2008.
28. Yam, K. L. The Wiley Encyclopedia of packaging technology; Third Edit.; John Wiley & Sons, Inc., Publication, 2009.
29. Baker, M. The Wiley Encyclopedia of packaging technology; John Wiley & Sons, Inc., Publication, 1986.
30. Ghosal, K.; Freeman, B. D. Gas Separation Using Polymer Membranes : An Overview. Polym. Adv. Technol. 1994, 5, 673–697.
31. Mittal, V. Barrier properties of polymer clay nanocomposites; Nova Science Publishers, Inc. New York, 2010.
32. Weinkauf, D.H.; Paul, D.R. Barrier Polymers and Structures, edited by W. J. Koros, American Chemical Society, Washington, DC, 423,60-61, 1990.
33. Weinkauf, D. H.; Paul, D. R. Gas Transport Properties of Thermotropic Liquid-Crystalline Copolyesters . II. The Effects of Copolymer Composition. J. Polym. Sci. Part B Polym. Phys. 1992, 30, 837–849.
34. McGonigle, E. –.; Liggat, J. .; Pethrick, R. .; Jenkins, S. .; Daly, J. .; Hayward, D. Permeability of N2, Ar, He, O_2 and CO_2 through biaxially oriented polyester films dependence on free volume. Polymer (Guildf). 2001, 42, 2413–2426.
35. Lim, L.; Britt, I. A. N. J.; Tung, M. A. Sorption and Transport of Water Vapor in Nylon 6 , 6 Film. J. Appl. Polym. Sci. 1998, 71, 197–206.

36. Strupinsky, G.; Brody, A. L. A Twenty-Year Retrospective on Plastics: Oxygen Barrier Packaging Materials. Polymers, Laminations & Coatings Conference, San Francisco, CA, 1998, 119-125.
37. Massey, L.K. Permeability Properties of Plastics and Elastomers, A Guide to Packaging and Barrier Material, 2nd Edition, Plastics Design Library, 2003
38. Hughes, H. A. Barrier Design in Plastics in Food Packaging, Marcel Dekker, Inc., New York, 1992
39. Lusignea, R. High-Barrier Packaging with Liquid Crystal Polymers. Tappi J.1997, 80 (6), 205-210.
40. Peterlin, A. Dependence of diffusive transport on the morphology of crystalline polymers. J Macromol Sci Phys, 1975, B11 (1), 57–87.
41. Perkins, W. Effect of molecular weight and annealing temperature on the oxygen barrier properties of oriented PET film, Polym Bull. 1988,19, 397-401.
42. Nie, H.; Walzak, M. J.; Mcintyre, N. S. Draw-ratio-dependent morphology of biaxially oriented polypropylene films as determined by atomic force microscopy. Polymer. 2000, 41, 2213–2218.
43. Lin, Y. J.; Dias, P.; Chen, H. Y.; Chum, S.; Hiltner, A.; Baer, E. Oxygen Permeability of Biaxially Oriented Polypropylene Films. Polym. Eng. Sci. 2008, 48, 642–648.
44. Nwabunma, D.; Kyu,T. Polyolefin Blends, Wiley-Interscience; a John Wiley & Sons, Inc., publication, 2008.
45. Paul, D. R.; Bucknall, C. B. Barrier Materials by Blending in Polymer Blends, John Wiley & Sons, 2000.

46. Strupinsky,G.; Brody, A. L. A Twenty-Year Retrospective on Plastics: Oxygen Barrier Packaging Materials. Polymers, Laminations & Coatings Conference, San Francisco, CA, 1998, 119-125.
47. Marcandalli, B.; Testa, G.; Seves, A.; Martuscelli, E. Oxygen permeation through films of polypropylene/hyd rogenated oligocyclopentadiene blends. Polymer. 1990, 32, 3376–3380.
48. Monsiváis-Barrón, a. J.; Bonilla-Rios, J.; Ramos de Valle, L. F.; Palacios, E. Oxygen permeation properties of HDPE-layered silicate nanocomposites. Polym. Bull. 2013, 70, 939–951.
49. Palza, H.; Reznik, B.; Kappes, M.; Hennrich, F.; Naue, I. F. C.; Wilhelm, M. Characterization of melt flow instabilities in polyethylene/carbon nanotube composites. Polymer. 2010, 51, 3753–3761.
50. Wang, S.Q.; Drda, P. a. Superfluid-Like Stick−Slip Transition in Capillary Flow of Linear Polyethylene Melts. 1. General Features. Macromolecules 1996, 29, 2627–2632.
51. Waddon, A.J; Keller, A. The Temperature Window of Minimum Flow Resistance in Melt Flow of Polyethylene. Further Studies on the Effect of Strain Rate and Branching. J. Polym. Sci. Part B Polym. Phys. 1992, 30, 923–929.
52. Waddon, A. J., Keller, A. A Temperature Window of Extrudability and Reduced flow Resistance in high-molecular weight polyethylene; Interpretation in terms of flow-induced mobile hexagonal phase," J. Polym. Sci. 1990, 28, 1063-1073.
53. Pudjijanto, S., Denn, M. J. A stable ''island'' in the slip-stick region of linear low density polyethylene," Rheology, 1994, 38, 1735-1745.

54. Kolnaar, J. W. H.; A. Keller A temperature window of reduced flow resistance in polyethylene with implications for melt flow rheology: 1. The basic effect and principal parameters. Polymer. 1994, 35, 3863–3874.
55. Kolnaar, J. W. H.; Keller, a. A temperature window of reduced flow resistance in polyethylene with implications for melt flow rheology: 2. Rheological investigations in the extrusion window. Polymer (Guildf). 1995, 36, 821–836.
56. Kolnaar, J. W. H.; Keller, a. A temperature window of reduced flow resistance in polyethylene with implications for melt flow rheology: 3. Implications for flow instabilities and extrudate distortion. Polymer (Guildf). 1997, 38, 1817–1833.
57. Kolnaar, J. W. H.; Keller, A. A singularity in the melt flow of polyethylene with wider implications for polymer melt flow rheology. J. Non-Newtonian Fluid Mech. 1996, 67, 213–240.
58. Xu, H.; Lele, A.; Rastogi, S. The influence of carbon-based nanofillers on the melt flow singularity of linear polyethylene. Polymer (Guildf). 2011, 52, 3163–3174.
59. Narh, K. a.; Keller, a. Phase transition in high molecular weight polyethylene during capillary extrusion: the reversibility of the temperature window. Polymer. 1991, 32, 2512–2518.
60. van Bilsen, H. M. M.; Fischer, H.; Kolnaar, J. W. H.; Keller, A. A Temperature Window of Reduced Flow Resistance in Polyethylene: In Situ WAXS. Macromolecules 1995, 28, 8523–8527.
61. Dazhu, C.; Haiyang, Y.; Pingsheng, H.; Weian, Z. Rheological and extrusion behavior of intercalated high-impact polystyrene/organomontmorillonite nanocomposites. Compos. Sci. Technol. 2005, 65, 1593–1600.

62. Aalaie, J.; Malmir, S.; M. Hemmati, “Steady shear behavior and morphology of nanocomposites based on polyethylene/high impact polystyrene blends,” J. Macromol. Sci., Phys. 2012, 52, 1-12.
63. Galgali, G.; Ramesh, C.;A. Lele, “A rheological study on the kinetics of hybrid formation in polypropylene nanocomposites,” Macromolecules. 2001,34, 852-858.
64. Muksing, N.; Nithitanakul, M.; Grady, B. P.; Magaraphan, R. Melt rheology and extrudate swell of organobentonite-filled polypropylene nanocomposites. Polym. Test. 2008, 27, 470–479.
65. Cogswell, F.N. Polymer melt rheology, A guide for industrial practice. Woodhead Publishing ltd. 1994.
66. White, J.L. Principles of polymer engineering rheology, John Wiley & Sons Ltd, 1990.
67. Sun, L.; Gibson, R. F.; Gordaninejad, F.; Suhr, J. Energy absorption capability of nanocomposites: A review. Compos. Sci. Technol. 2009, 69, 2392–2409.
68. Rafiq, R.; Cai, D.; Jin, J.; Song, M. Increasing the toughness of nylon 12 by the incorporation of functionalized graphene. Carbon N. Y. 2010, 48, 4309–4314.
69. Phang, I. Y.; Shen, L.; Chow, S. Y.; Zhang, W.-D. Morphology and Mechanical Properties of Multiwalled Carbon Nanotubes Reinforced Nylon-6 Composites. Macromolecules 2004, 37, 7214–7222.
70. Song, M.; Hourston, D. J.; Yao, K. J.; Tay, J. K. H.; Ansarifar, M. A. High Performance Nanocomposites of Polyurethane Elastomer and Organically Modified Layered Silicate. J. Appl. Polym. Sci. 2003, 90, 3239–3243.

71. Al-Lafi, W.; Jin, J.; Xu, S.; Song, M. Performance of MWCNT/HDPE Nanocomposites at High Strain Rates. Macromol. Mater. Eng. 2010, 295, 519–522.
72. Saeed, F.; Ansarifar, A.; Ellis, R. J.; Farid, A. S. Effect of the Blooming of Chemical Curatives on the Cyclic Fatigue Life of Natural Rubber Filled with a Silanized Silica Nanofiller. J. Appl. Polym. Sci. 2010, 120, 2497–2507.
73. Saeed, F.; Ansarifar, A.; Ellis, R. J.; Haile-meskel, Y.; Irfan, M. S. Two Advanced Styrene-Butadiene / Polybutadiene Rubber Blends Filled with a Silanized Silica Nanofiller for Potential Use in Passenger Car Tire Tread Compound. J. Appl. Polym. Sci. 2011, 123, 1518–1529.
74. Mai, Y.W.; Yu, Z.Z.; Polymer nanocomposites. New York, USA, UK: WoodHead publishing; 2006.
75. Pavildou, S.; Papaspyrides, C.D. A review on polymer-layered silicate nanocomposites. Prog. Polym. Sci. 2008, 33, 1119-1198.
76. Papaspyrides, C.D.; Kiliaris P. Polymer Green Flame Retardants: A comprehensive Guide to Additives and Their Applications. Elsevier; 2013.
77. Fager, L.-O.; Bassani, J. L. Neck propagation in polymers with adiabatic heat generation. Mech. Mater. 1990, 9, 183–194.
78. Hillmansen, S.; Haward, R. N. Adiabatic failure in polyethylene. Polymer. 2001, 42, 9301–9312.
79. McNally, T.; Raymond Murphy, W.; Lew, C. Y.; Turner, R. J.; Brennan, G. P. Polyamide-12 layered silicate nanocomposites by melt blending. Polymer. 2003, 44, 2761–2772.

80. G.M., K.; Lee, D. H.; Hoffmann, B.; Kressler, J.; Sto, G. Influence of nano fillers on the deformation process in layered silicate / polyamide-12 nanocomposites. Polymer. 2001, 42, 1095–1100.
81. Gorwade, C. V; Alghamdi, A.S.; Ashcroft, I. A; Silberschmidt, V. V; Song, M. Finite element analysis of the high strain rate testing of polymeric materials. J. Phys. Conf. Ser. 2012, 382, 1-6.
82. Shen, Y.; Harkin-Jones, E.; Hornsby, P.; McNally, T.; Abu-Zurayk, R. The effect of temperature and strain rate on the deformation behaviour, structure development and properties of biaxially stretched PET–clay nanocomposites. Compos. Sci. Technol. 2011, 71, 758–764.
83. Alghamdi, a. S.; Ashcroft, I. a.; Song, M.; Cai, D. Morphology and strain rate effects on heat generation during the plastic deformation of polyethylene/carbon black nanocomposites. Polym. Test. 2013, 32, 1105–1113.
84. Villanueva, M. P.; Cabedo, L.; Giménez, E.; Lagarón, J. M.; Coates, P. D.; Kelly, a. L. Study of the dispersion of nanoclays in a LDPE matrix using microscopy and in-process ultrasonic monitoring. Polym. Test. 2009, 28, 277–287.
85. Villanueva, M. P.; Cabedo, L.; Lagaro´n, J. M.; Gime´nez, E. Comparative Study of Nanocomposites of Polyolefin Compatibilizers Containing Kaolinite and Montmorillonite Organoclays. J. Appl. Polym. Sci. 2010, 115, 1325–1335.
86. Domka, L.; Malicka, A.; Stachowiak, N. The effect of kaolin modification of silane coupling agents on the properties of the polyethylene composites. Polish J. Chem. Technol. 2008, 10, 5–10.

87. Domka, L.; Malicka, A.; Stachowiak, N. Production and Structural Investigation of Polyethylene Composites with Modified Kaolin. Polish J. Chem. Technol. 2008, 114, 413–421.
88. Xuening, L..; Nan, H.; Hongtao, Z.; Chengyong, H.; Zhizhong, Y. Effects of modified kaolin on the crystallization property of PP/Kaolin nanocomposites. Sci. China Ser. B 2005, 48, 326–333.
89. Chang, Z.-H.; Guo, F.; Chen, J.-F.; Yu, J.-H.; Wang, G.-Q. Synergistic flame retardant effects of nano-kaolin and nano-HAO on LDPE/EPDM composites. Polym. Degrad. Stab. 2007, 92, 1204–1212.
90. Cabedo, L.; Giménez, E.; Lagaron, J. M.; Gavara, R.; Saura, J. J. Development of EVOH-kaolinite nanocomposites. Polymer (Guildf). 2004, 45, 5233–5238.
91. Gardolinski, J. E.; Carrera, L. C. M.; Cantao, M. P.; Wypych, F. Layered polymer-kaolinite nanocomposites. J. Mater. Sci. 2000, 5, 3113–3119.
92. Privalko, E. G.; Pedosenko, a. V.; Privalko, V. P.; Walter, R.; Friedrich, K. Composition-dependent properties of polyethylene/kaolin composites. i. degree of crystallinity and melting behavior of polyethylene. J. Appl. Polym. Sci. 1999, 73, 1267–1271.
93. Privalko, V. P.; Calleja, F. J. B. Composition-dependent properties of polyethylene / Kaolin composites Part II Thermoelastic behaviour of blow-moulded samples. 1999, 4, 497–508.
94. Privalko, V. P.; Sukhorukov, D. I.; Privalko, E. G.; Walter, R.; Friedrich, K.; Balta, F. J. Composition-Dependent Properties of Polyethylene / Kaolin Composites . III . Thermoelastic Behavior of Injection-. 1999, 1041–1048.

95. Walter, R.; Friedrich, K.; Privalko, V.; Savadori, a. On Modulus and Fracture Toughness of Rigid Particulate Filled High Density Polyethylene. J. Adhes. 1997, 64, 87–109.
96. Privalko, V. P.; Baltá-calleja, F. J.; Sukhorukov, D. I.; Privalko, E. G.; Walter, R.; Friedrich, K. Thermophysical characterization of the deformation behavior of polyethylene/kaolin composites. J. Macromol. Sci. Part B 1999, 38, 931–943.
97. Wang, X.; Wu, Q.; Qi, Z. Unusual rheology behaviour of ultra high molecular weight polyethylene/kaolin composites preparedvia polymerization-filling. Polym. Int. 2003, 52, 1078–1082.
98. Wu, Q.; Wang, X.; Gao, W.; Hu, Y.; Qi, Z. Unusual rheological behaviors of linear PE and PE/kaolin composite. J. Appl. Polym. Sci. 2001, 80, 2154–2161.

CHAPTER 3: MATERIALS AND EXPERIMENTATION

3.1: Materials

3.1.1: High density polyethylene (HDPE),linear low density polyethylene (LLDPE) and Nylon12

HDPE and LLDPE are both semi-crystalline commodity thermoplastics. In order to achieve better distribution and exfoliation of clay, both HDPE and LLDPE were required in powdered form. HDPE powder was supplied by Exxon Mobil Corporation, while LLDPE powder was supplied by ICO Polymers Technical Centre. The specification of both the thermoplastics used as base matrix for the preparation of thermoplastic clay nanocomposites is summarized in table 3.1.

Table 3.1: Manufacturer specification of HDPE and LLDPE

Materials	Melt Flow Index (g/10 min)	Melting Temperature Tm (^oC)	Density (g/cm^3)
HDPE	4.0	133	0.96
LLDPE	4.2	122	0.94

Nylon 12 (PA 2200, weight average molecular weight= 76950, number average molecular weight=38800) was provided by 3TRPD Ltd. UK. In order to achieve better distribution of clay, Nylon 12, HDPE and LLDPE were used in fine powdered form (particle size = 85μm).

3.1.2: Barrisurf™ LX (BLX) and Barrisurf™ HX (BHX) – Kaolin

Kaolin (also known as China Clay) is a natural mineral based material containing variable proportions of kaolinite, mica and quartz. Both BLX and BHX were supplied by IMERYS Minerals Ltd. BLX and BHX are IMERYS natural, dry, platy china clay products consisting primarily of kaolinite with small amounts (<1%) of other minerals.

The specifications of both the clays used as functional filler for the preparation of thermoplastic clay nanocomposites are summarized in table 3.2. The shape factor shown in table 3.2 describes an average value of the ratio between the mean particle diameter to particle thickness of kaolin clay.

Table3.2: Manufacturer specification of BLX and BHX

Materials	Shape Factor	Colour	pH	Moisture (max%)	Specific gravity
BLX	60	White	5-7.5	1.5	2.6
BHX	100	White	5-7.5	1.5	2.6

3.1.3: Bentone MA – Hectorite and Na-MMT

Hectorite is a natural high silica clay mineral belonging to the smectite group of minerals. Bentone MA was supplied by Elementis Specialties Inc, UK. Na-MMT (Cloisite®Na+) was supplied by Southern Clay Products, Inc, USA. According to the supplier, the original clay was not chemically modified.

3.1.4: Carbon based fillers

Carbon black (B4040) was purchased from Cobalt Chemicals Company, Belgium. The particle size of CB was about 26nm. Multi-walled carbon nanotubes (MWCNT) were purchased from Chengdu Institute of Organic Chemistry, Chinese Academy of Science. The diameter of the nanotubes was about 8–15 nm. Ultrafine grinding Graphite (UF4) with a particle size of 4-7μm was purchased from Graphite Kropfmühl AG, Germany. All the chemicals used for the production of graphene oxide such as Nitric acid (HNO_3), Sulphuric acid (H_2SO_4), Potassium permanganate ($KMnO_4$), Hydrochloric acid (HCl), Hydrogen peroxide solution (H_2O_2) and Barium chloride ($BaCl_2$) were purchased from Fisher Scientific Company, UK.

3.2: Experimentation

3.2.1: Stability of clay in aqueous media

In order to study the stability of clay (BLX, BHX and Bentone) suspension in aqueous media a sedimentation experiment was carried out. Two basic variables were selected for analysing the stability of clay in aqueous media: Sonication time and pH of the clay in distilled water system.

The concentration for all the clay systems studied was 0.5g clay/100 ml distilled water. The samples were sonicated using an ultrasonic dismembrator (Model 500 Ultrasonic Dismembrator and Disruptor Horn supplied by Fisher Scientific Ltd-fig 3.1). In ultrasonic treatment, the ultrasonic sound produced requires the presence of a liquid to transmit its energy, which is different from the treatment of clay carried out in microwaves or electrochemistry. During ultrasonication the sound waves propagate into the liquid media resulting in alternating high-pressure (compression) and low-pressure (rarefaction) cycles. This applies mechanical stress on the electrostatic forces (van der Waals forces, hydrogen bonding etc) which hold the clay platelets together. One of the phenomenon taking place in ultrasonic treatment is cavitation, in which the small vacuum bubbles created during the low-pressure cycle collapse violently during the high-pressure cycle. Ultrasonic cavitation in liquids causes high speed liquid jets of up to 600mph. Such jets press liquid at high pressure between the particles and separate them from each other [1].

The sonication time was varied from 0 to 40 minutes, while the pH of the systems was maintained above and below pH=7 using acetic acid and sodium hydroxide solutions. The clay was dispersed in water at a concentration of 1mg/ml with a power of 300 W at room temperature. The prepared samples were photographed at regular intervals and then the pictures were compared.

Fig.3.1: Ultrasonic dismembrator with disruptor horn cabinet

3.2.2: Production of graphene oxide

Graphene oxide was produced from UF4 (supplier graphene) according to the procedure mentioned elsewhere [2]. In this method 2.5 g of UF4 was mixed with 57.5 ml of concentrated H_2SO_4 in an ice bath for 30 minutes. In order to keep the temperature of the mixture below 20^oC, $KMnO_4$ was added slowly to the mixture. Using a water bath the mixture was then heated to 35 ± 3^oC with continuous magnetic stirring for 30 min. 115 ml of distilled water was added drop wise into the mixture which increased the temperature of the mixture to 98^oC. The mixture was stirred for 15 minutes at this temperature. Later 350 ml of distilled water and 25 ml of 30% H_2O_2 solution was added to terminate the oxidation reaction. Graphite oxide (GO) was collected by filtering and was successively washed with 5% HCl aqueous solution. HCl washing was repeated three times until there was no sulphate detected by $BaCl_2$ solution. GO collected from the mixture was dried at 50^oC under vacuum

for one week. GO was prepared by carrying out ultrasonication of a 1mg/ml concentrated dispersion of GO in water with a power of 300 W for 1 h at room temperature. The GO-water dispersion was prepared so that it can be incorporated in polymer matrix-water dispersion.

3.2.3: Ball milling of MWCNTs

MWCNT were ground into different sizes by milling them in a ceramic ball mill equipped with stainless steel balls. The samples were milled for 24hrs, 48hrs and 72hrs respectively. Each time the ball mill was loaded with 10 grams of sample and was placed on a motor controlled roller operated at 500 rpm.

3.2.4: Preparation of clay based nanocomposites

In order to ensure better distribution of kaolin clay in the matrix, nanocomposites were prepared in two stages: blending of the two components followed by melt compounding.

Nanofillers (clay and carbon based) with concentrations of 1mg/ml in water were treated by ultrasonication with a power of 300w for 30min at room temperature. The blending of nanofiller dispersion in water with HDPE, LLDPE and Nylon 12 powder was carried out according to patent EB2008/003130.

All the composites were prepared by melt blending inside a lab-scale twin screw extruder (fig 3.2). The samples received from pre-mixing (fig 3.3) were then mixed on a lab scale twin screw extruder operating at 110 rpm. The temperature profile along the length of extruder was maintained at 160, 170, 180, 190, 200^{o}C respectively. The weight fraction of all carbon based fillers (carbon black-HCB, graphene oxide-HG, MWCNT-HM, MWCNT24-HM-24, MWCNT48-HM-48 and MWCNT72-HM-72) was fixed at 1.0 %. For rheological study 0.2, 0.6, 1.0, 2.0, wt. % of BHX/HDPE (HH)

and 1 wt. % of BLX/HDPE (HL), Na-MMT/HDPE (HM), bentone/HDPE (HB), composites were prepared. In case of barrier, thermal and mechanical analysis the weight fraction of all the clay was varied from 0 to 10 wt %. A list of all the specimens prepared along with their abbreviations used throughout the thesis is given in appendix A1.

For mechanical analysis the compounded samples were compression moulded on a hot press at a temperature of 170^{o}C for 10 minutes under a force of 10 tons for LLDPE nanocomposites, at a temperature of 180^{o}C for 10 minutes under a force of 15 tons for HDPE nanocomposites and at a temperature of 200^{o}C for 10 minutes under a force of 20 tons for Nylon 12 nanocomposites. In case of tensile testing dumbbell shaped samples were cut from a sheet using Ray-ran test equipment automatic cutter.

Fig.3.2:Lab scale twin screw extruder for melt blending

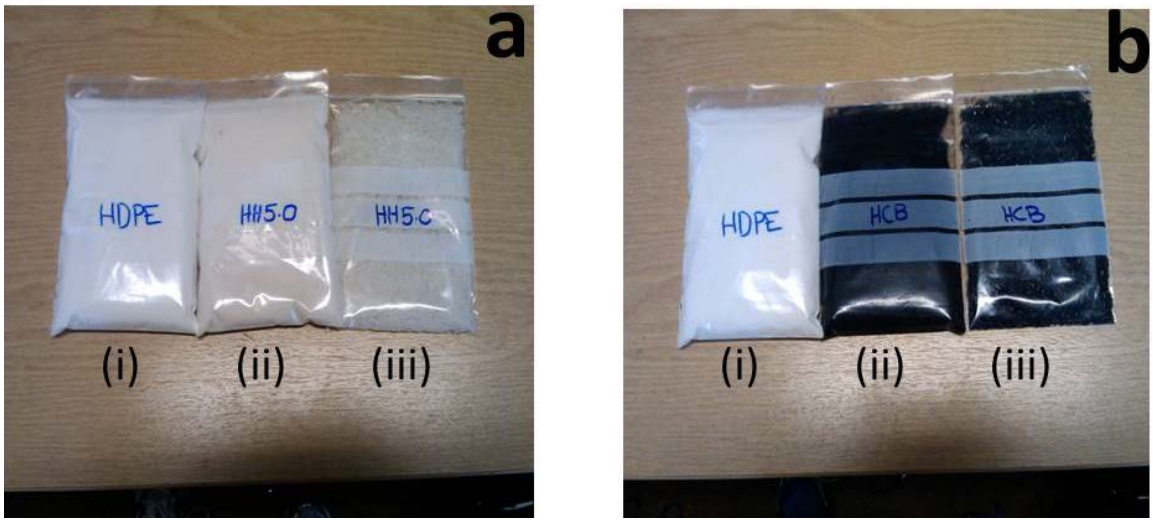

Fig.3.3:Samples prepared by premixing and melt blending: (a) HDPE powder(i), HH5.0 powder from premixing (ii) and HH5.0melt blended granules(iii), (b) HDPE powder(i), HCB powder from premixing (ii) and HCB melt blended granules (iii).

3.2: Wide angle X-ray diffraction (XRD)

A Brüker AXS, D8 Advance X-ray diffractometer at a generator voltage of 40kV and a current of 40mA was used to study the diffraction behavior of the nanocomposites. Nickel-filtered CuKα radiation of wavelength 0.1542 nm was directed at the samples in their through direction. Data was collected over the 2θ range 1°–15° with a step size of 0.02° and a scan speed of 0.02^{o}/s. By applying the Bragg's law, the intensity of the diffracted x-ray is measured as a function of the diffraction angle 2θ and the specimen's orientation. This diffraction pattern is used to identify the specimen's crystalline phases and to measure its structural properties (fig 3.4). Due to its non-destructive test and its less elaborate sample preparations, WAXD is the most widely used technique. [3, 4]

However, WAXD has got its limitations. It cannot provide information about the spatial distribution of the clay layers or structural non-homogeneities in nanocomposites. It is difficult to study a system with broad peaks and weak intensity.

Hence, the data from XRD patterns is not sufficient to reveal the formation mechanism and ultimate structure of nanocomposites [5, 6].

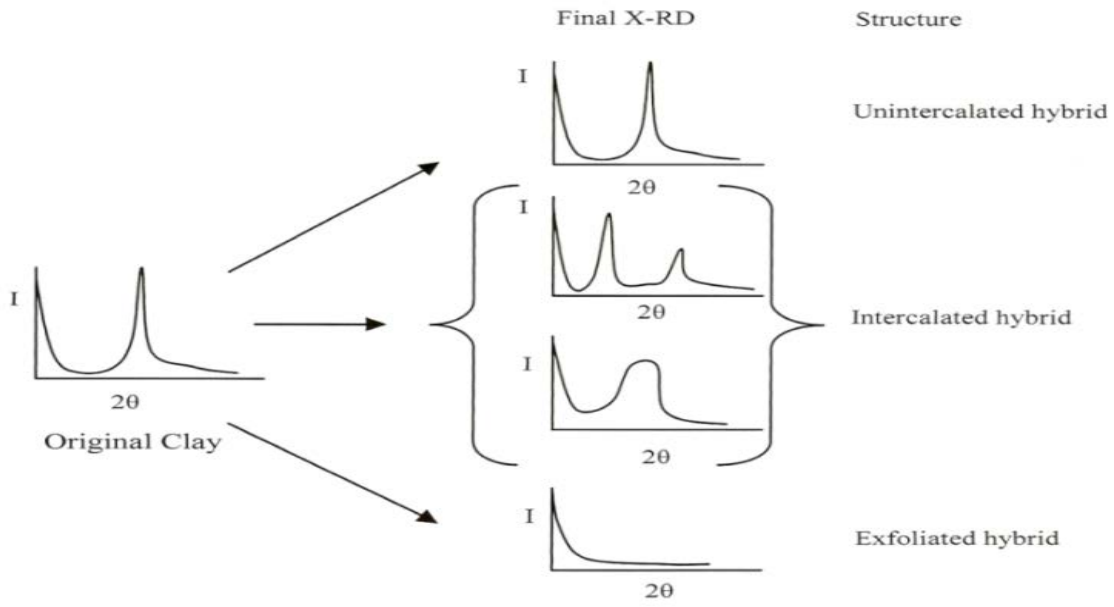

Fig.3.4:The schematic diagram of x-ray diffraction patterns for various types of hybrid structures

3.4: Transmission electron Microscope

The dispersion of clay in the polymer matrix was visualized by using transmission electron microscopy (TEM). The analysis was conducted on JEOL 2100 FX Transmission Electron Microscope (fig 3.5). In order to prepare the samples, the specimens were cut into small isosceles triangle shaped pieces (15 mm in length). These pieces were then mounted in epoxy resin in a plastic container and kept into an oven at 60^{o}C for 24 hours. After the epoxy resin was cured it was taken out of the container and the end of the epoxy resin was cut to expose the specimen embedded in epoxy. Samples were cut into thin sections with an ultra-microtome using a diamond knife at room temperature. Copper grids were used to collect the sections and put them into the equipment for analysis.

Fig.3.5:JEOL 2100 FX Transmission Electron Microscope

3.5: Optical Microscope

Crystalline morphology of nanocomposites and the distribution of clay in polymer matrix were observed using a cross polarized Leica DMRX optical microscope (fig 3.4). Samples were melted and squeezed between a microscope cover glass at 180^{o}C for 10 minutes and then quenched to the room temperature. The thickness of the samples prepared by melt pressing was less than ideal for analysing the clay distribution by optical microscopy. Thin samples (10 µm) were then cut by microtomy (fig 3.6) using liquid carbon dioxide as a freezing agent. The thin samples were placed between two glass surfaces for analysis using Euparal mountant.

Fig.3.6:Leica DMRX microscope and Microtomy setup

3.6: Scanning Electron Microscopy (SEM)

The morphological analyses of nanocomposite samples were also performed by Scanning Electron Microscopy (SEM). The SEM consists of an electron gun producing a source of electrons at an energy range of 1-40keV. The electron lenses then reduce the diameter of electron beam in order to focus a small beam onto the specimen. The electron beam interacts with near-surface region of the specimen to a depth of about 1μm and generates signals used to form an image. The SEM micrographs were taken using a Leica Cambridge Stereoscan S360 instrument. Samples were prepared from the surfaces of the HDPE-nanocomposites that have been cyro-fractured using liquid nitrogen. The surfaces of specimens were sputtered with gold to provide an electrically conductive layer, to suppress surface charge, to minimize radiation damage and to increase electron emission. It is run under a vacuum to minimize beam interaction with gas molecules which would retard resolution.

3.7: Differential Scanning Calorimetry (DSC)

Thermal and crystallization analysis was carried out using a TA Instrument DSC 2920 differential scanning calorimetry (DSC). Typical sample weights were ranged from 10 to 12 mg for the individual sample. Samples were sealed in aluminium pans by pressing. Nitrogen was used as purge gas at the flow rate of 50 ml/min. In non-isothermal experiments heating rate was 10^{o}C/min and each sample was melted at 170^{o}C for 10 minutes and then cooled to room temperature.

3.8: Permeation analysis

3.8.1: Sample preparation and experimentation

The investigation of barrier properties is a key objective of this project since the developed samples are to be used for packaging. For barrier analysis the compounded samples were compression moulded on a hot press at a temperature of 170^{o}C for 10 minutes under a force of 10 tons for LLDPE nanocomposites, at a temperature of 180^{o}C for 10 minutes under a force of 15 tons for HDPE nanocomposites and at a temperature of 200^{o}C for 10 minutes under a force of 20 tons for Nylon 12 nanocomposites.

3.8.2: Water vapour transmission rate (WVTR) analysis

WVTR analysis was performed using a PERMATRAN-W model 398 system (fig. 3.7), in accordance with ASTM F-1249. The compression moulded sheets (0.32+0.02 mm) were cut into the desired shapes using template and knife cutter (fig 3.8). The samples were dried under vacuum at 30^{o}C for 48 hrs before testing to get rid of any existing moisture in them prior to mounting them in the testing chamber. The test temperature was set to ambient temperature (23^{o}C) and a pressure of 760mmHg was used during the testing. Relative humidity of the permeant was set to

be 100% and the testing area of the each sample was 50cm^2. Results are reported in grams/meter^2/day.

Fig.3.7:PERMATRAN-W model 398 system

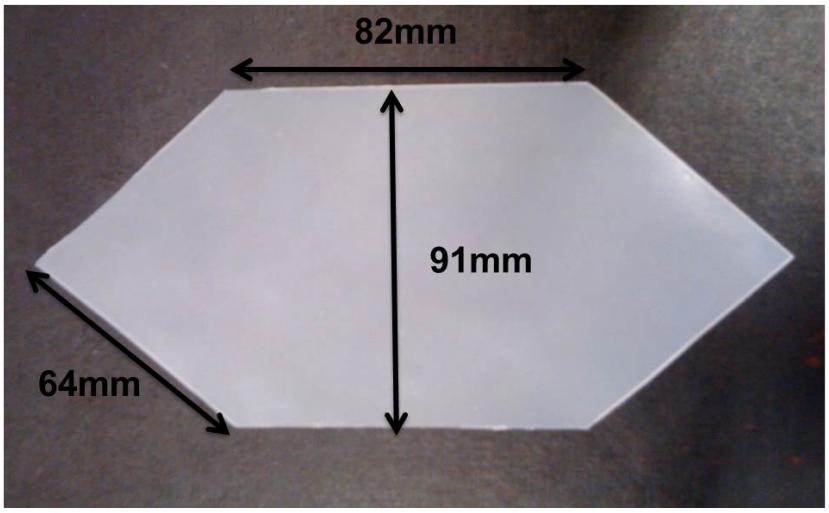

Fig.3.8:Specimen for WVTR analysis

3.9.3: PERMATRAN®-Working principle

The water vapour transmission rate (WVTR) through the polymer films can be measured by using different gravimetric 'cup' analysis or by using the newly developed electronic methods based on ASTM method F 1249 [7]. These electronic methods use an infrared sensor to detect the water vapours permeated through the polymer film samples. The water vapour transmission rate (WVTR) of polymeric films

is commercially measured by different PERMATRAN® models made by Modern Controls Inc., Minneapolis, MN. These machines provide sensitivity to water vapours in the range of parts-per-million (ppm) and can be used at different temperatures and humidity. The polymeric films are tightly sealed just like in OXTRAN® and they divide the measuring cell into the outer and inner chamber (fig. 3.9).

At the start of the experiment, dry N_2 gas is allowed to flow through the inner chamber of the test cell by opening the valves. Before entering the test cell N_2 gas passes through a molecular sieve to ensure that the N_2 gas is completely dry. This process is referred to as the “Purge Cycle”. The valves remain open until the relative humidity (RH) in the chamber drops to the minimum value of the target RH range (75 %). After the minimum value is reached, the valves close and the humidity inside the chamber begins to climb as water vapour permeates through the sample. This process is referred to as the “Test Cycle”.

The water vapour that permeates the specimen are picked up by dry N_2 and then carried through an exit valve to a modulated infrared sensor. The IR sensor generates a voltage which is directly proportional to the amount of water vapour passing through the sensor. The purge cycle and the test cycle repeat until the water vapour transmission rate has come to equilibrium, after which the test is finally completed. The water vapour transmission rate is calculated based on the amount of time it takes the RH to accumulate from the minimum to the maximum values of the test range. The water vapour transmission rate is reported as the amount of water vapour transmitted through an area in a certain time under specified conditions of temperature and humidity [8].

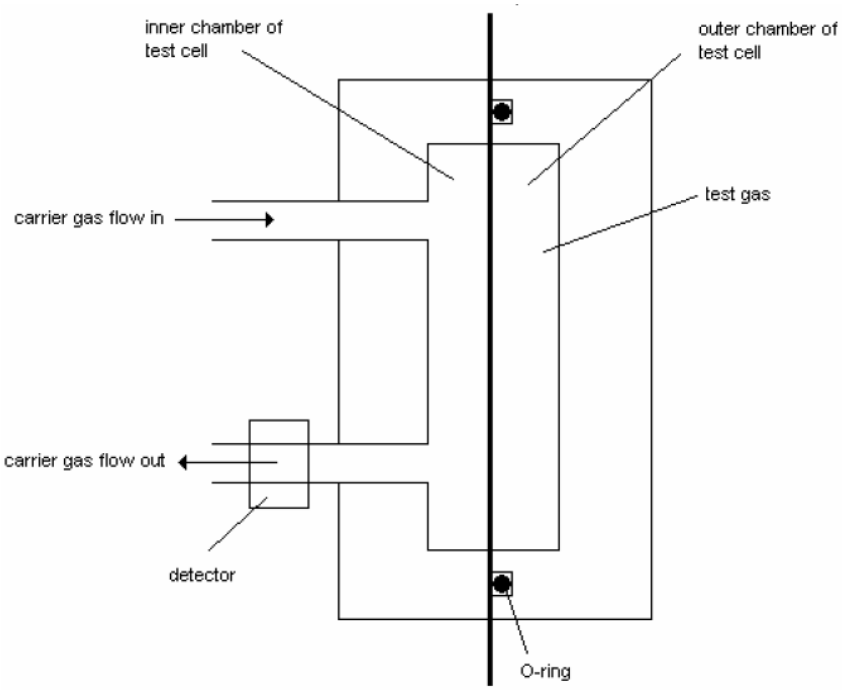

Fig.3.9:Schematic view of the permeation cell in PERMATRAN® machine (40)

3.8.4: Oxygen transmission rate (O2GTR) testing

O2GTR analysis was performed using a MOCON OX-TRAN® model 1/50 system (fig 3.10), in accordance with ASTM D-3985. The compression moulded sheets (0.32+0.02 mm) were cut into the desired shapes using template and knife cutter (fig 3.11). The samples were dried under vacuum at 30^{o}C for 48 hrs before testing. The entire tests were conducted in convergence by cycle's mode at a temperature of 23 °C and 10% relative humidity of oxygen. The entire tests were conducted in mode which is convergence by cycles. In Convergence-by-Cycles mode, the system will compare the latest transmission rate results with those measured at a specified number of exam cycles previously and make the equilibrium determination. The tests were finished when the transmission rate was stable for 20 cycles. Results are reported in cc /m^2/day.

Fig.3.10:MOCON OX-TRAN® model 1/50 system

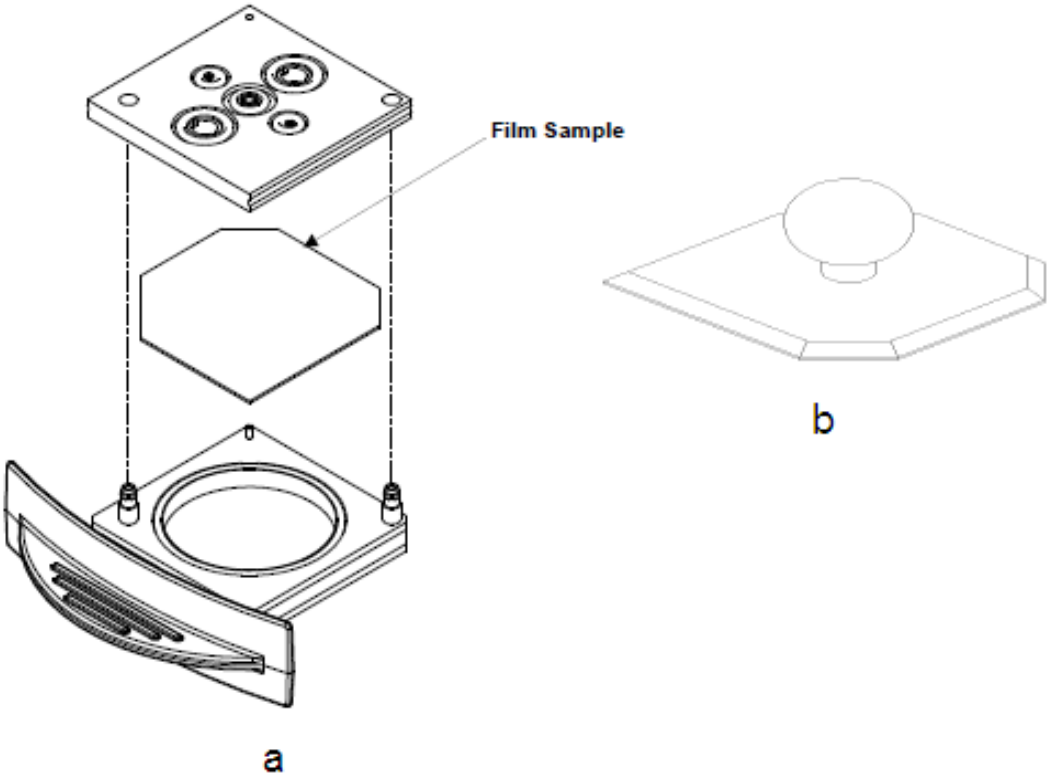

Fig.3.11:Preparation of samples for OX-TRAN, a: mounting the film sample in the holder, b: steel mould for cutting sample

3.8.5: OXTRAN® - Working principle

The permeation of oxygen gas through a polymeric packaging can permanently damage the quality of the packed item. Oxygen can be strongly and irreversibly

absorbed into the food products in a polymer packaging [36].The oxygen transmission rate through polymeric films and membranes is measured commercially by using different OXTRAN® branded machines made by Modern Controls Inc., Minneapolis, MN. In these machines the measurements are made in accordance with ASTM D 3985 [9]. The distinct advantage of all these machines is their ability to measure very small quantities of oxygen (parts-per-billion (ppb) sensitivity to oxygen even in the presence of moisture) at different measuring temperatures and humidity.

All these commercial machines require the sample in the form of a thin film, which is tightly sealed in the test cell to prevent air entering the cell. The placement of packaging film in the test cell divides it into an outer and inner chamber (fig 3.12). During oxygen transmission measurements, the test gas is continuously transferred into the outer chamber, where it contacts the film and exits through an exhaust port. In the inner chamber of the test cell a special mixture of carrier gas (nitrogen and 5% hydrogen) is continuously admitted.

The hydrogen introduced into the carrier gas can react with any oxygen present in the measuring compartment. This step is known as the purge cycle and is usually initiated for 5 minutes. The purge cycle removes any ambient oxygen in the measuring cell. After five minutes, the purge valves are closed and the inside chamber of the cell is directly coupled to the oxygen sensor. The sensor used in these machines is a coulometric fuel cell, which can produce an electrical current when exposed to oxygen. The current generated is directly proportional to the amount of oxygen passing through the sensor. Measurements made by the sensor are given in terms of oxygen transmission rate (OTR). OTR is the quantity of O_2 gas passing through an area in a certain time under specified conditions of temperature, humidity and pressure [10].

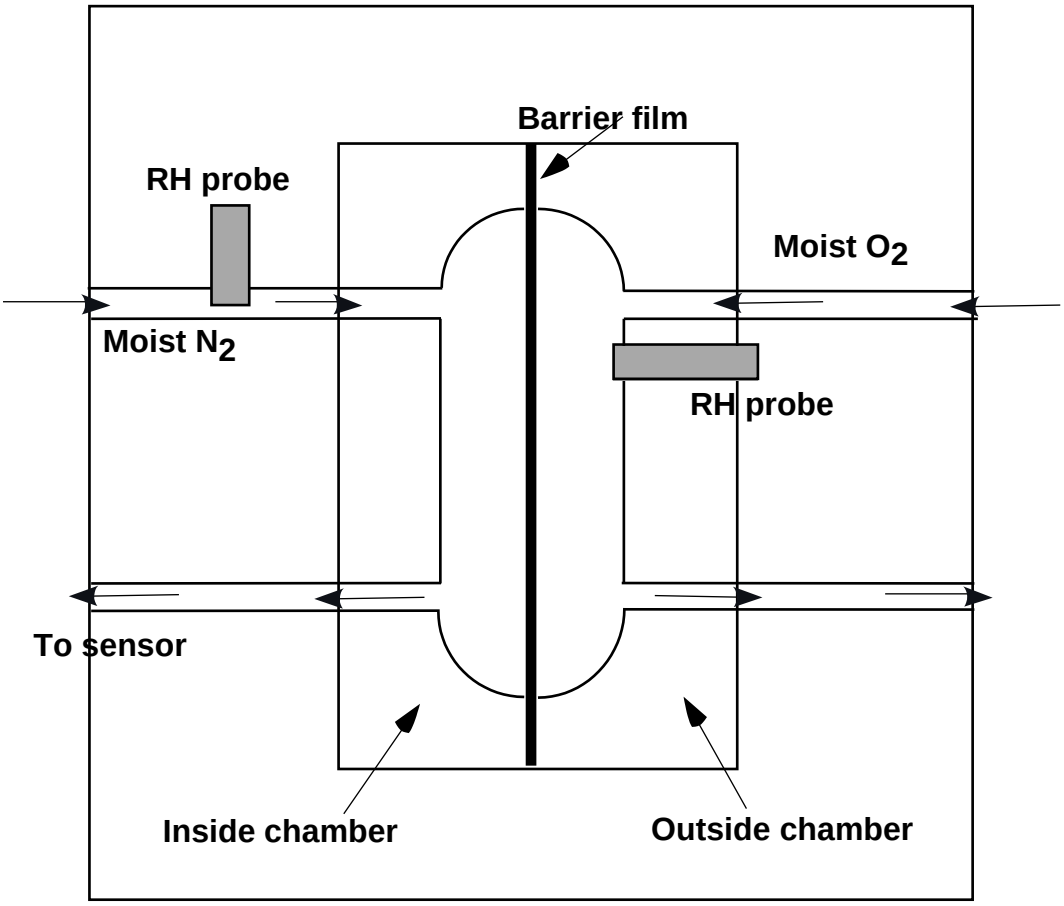

Fig.3.12:Schematic view of the permeation cell in OXTRAN® machine [38]

3.9: Tensile testing and thermal imaging

Tensile tests of polymers are generally carried out to measure the force required to break a specimen and the extent to which the specimen elongates before that breaking point. All tensile tests produce a force displacement diagram, which can be used to produce a stress-strain curve from which various properties such as Youngs modulus, yield strength and ultimate tensile strength can be calculated for design and research. These data points are often used to specify a material, to design parts to withstand specific load and as a quality control check for materials. Tensile testing was performed on a Lloyd Instruments LR50K Plus tensile testing machine at crosshead speed of 50 mm/min. A load cell of 1KN was used for all the specimens

as it covers the required range for HDPE and its nanocomposites. All the tests were carried out at room temperature. The mechanical properties calculated from the force displacement curve were represented as average of 7 values. A thermal camera (FLIR SC3000) was used to measure samples internal thermal change during tensile testing. The temperature range set on camera was from -10 to 150^{o}C and an accuracy of ±1^{o}C was used. The thermal analysis was carried out on 'FLIR Research IR' software. The internal temperature of the samples at the breaking point was recorded for 5 specimens and the results were reported as an average for these 5 readings.

3.10: Instrumented falling weight impact testing (IFWIT).

In IFWIT a known mass is dropped onto a test sample from a pre-selected height. The mass features an impact dart with a hemispherical end of approximately 10mm diameter, and so the test is also known as the instrumented falling dart impact test. A transducer is located just behind the impactor head to measure the force created in response to the impact between the impactor head and the resisting specimen. By assuming that throughout the impact, the velocity of the known mass is constant (due to the vast excess energy), the time domain can be converted to distance. Thus a force-deflection plot can be created for the impact. The duration of the force is in the magnitude of a few milliseconds, so the force data is passed through a charge amplifier and stored with a transient recorder. This data can be analysed by using a computer. For IFWIT a standard dropping mass of 10 Kg, at a speed of 3.12 m/s, was employed on the entire specimens from a drop height of 0.8m. All the reported results were the average of at least five tests.

3.11: Rheological Analysis:

3.11.1: Melt flow index analysis:

Melt flow index (MFI) measurements were carried out on a MP600 Extrusion Plastometer (Tinius Olsen Inc, USA). 5 g of each sample was uniformly compacted into the barrel of plastometer and then preheated for 200 seconds at 190 ºC. The samples were then extruded through the die (2.1 mm × 8 mm) under a constant load of 2.16 kg or 10 kg.

3.11.2: Capillary rheometer analysis:

Rheological analysis of HDPE and its nanocomposites was studied using a twin bore Rosand RH7 capillary rheometer (Rosand Precision Ltd., UK). The rheometer (fig 3.13) barrel is equipped with a pressure transducer situated at the upstream of die and with three thermocouples located at the top, middle and bottom of barrel. The two barrels had identical diameter of 15 mm and length of 210 mm. One of the cylindrical barrel is fitted with a steel capillary die (fig 3.14) with a length to diameter (L/D) ratio of 16/1 (mm/mm) and a flat entrance, while the other cylindrical barrel is fitted with a steel orifice die with a flat entrance and a insignificant L/D-ratio. The orifice die is used for applying Bagley's correction.

For capillary rheometer analysis, the sample was dried in a vacuum oven for 24hrs to remove any moisture in the sample which can generate bubbles or cause discontinuity in the melt. All the parts of the rheometer: twin barrels, dies, pistons and even the die holders were thoroughly cleaned before start up, because the extrusion window according to literature is strongly dependant on the interface between the melt and the die wall and a rough surface can cause the pressure to fluctuate and produce a rough extrudate [11, 12].

After cleaning, the barrels were fitted with the two dies and their outlets were then blocked to maintain the pressure during sample feeding. The barrels were then charged with the sample using a funnel. During charging the sample was compressed thoroughly to avoid any air bubbles build up in the melt. The sample was then heated inside the barrel at 160^{o}C for 10 minutes to relax the chains, remove the grain boundary and produce a uniform melt inside the barrel. The pistons were then fixed to the motor and were programmed to operate at fixed velocity during a single analysis. Because the piston velocity, die and barrel dimensions were fixed, the shear rate remains constant. The melt was then extruded from the capillary rheometer at constant shear rate and a constant cooling rate of 1.5^{o}C/min. The extrudate emerging from the bottom of the rheometer was collected for visual analysis and die swell measurements.

The main data collected from the rheometer was pressure versus temperature and time graphs. Rosand rheometer control software (Flowmaster version 8.3.10) was used for controlling the rheometer and also for analysing the collected data. The die swell of extrudate was measured by an in-situ laser detector situated at 2cm under the capillary die. During the measurement, the extrudates were cut off manually to maintain their length at no more than 15cm so that the sagging effect can be avoided.

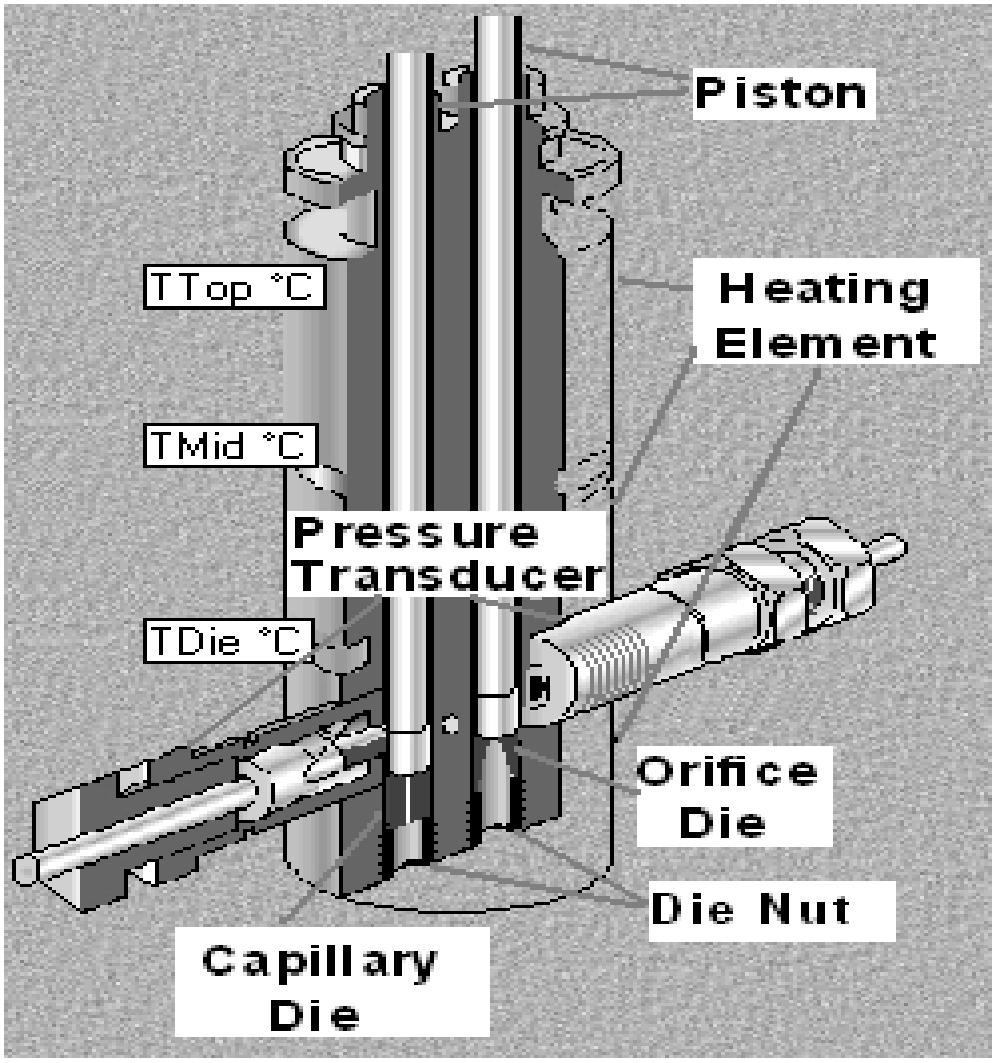

Fig.3.13:Schematic diagram of twin-bore capillary rheometer

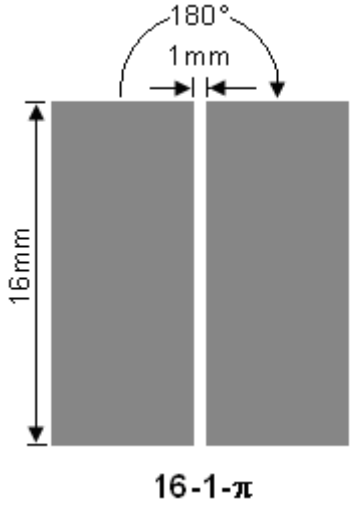

Fig.3.14:Schematic diagram of die used for melt flow singularity study, where 16-1-π indicate the length, diameter and entry angle.

References:

1. http://www.hielscher.com/ultrasonics/disperse.html
2. Rafiq, R.; Cai, D.; Jin, J.; Song, M. Increasing the toughness of nylon 12 by the incorporation of functionalized graphene. Carbon N. Y. 2010, 48, 4309–4314.
3. Thomas, S.; Stephen, R. Rubber nanocomposites: preparation, properties, and applications, chapter 1, page 1, 2010.
4. Mai, Y.W.; Yu, Z.Z.; Polymer nanocomposites. New York, USA, UK: WoodHead publishing; 2006.
5. Mittal, V. Barrier properties of polymer clay nanocomposites; Nova Science Publishers, Inc. New York, 2010.
6. Mittal, V. Mechanical and Gas Permeation Properties of Compatibilized Polypropylene – Layered Silicate Nanocomposites. J. Appl. Polym. Sci. 2007, 107, 1350–1361.
7. ASTM F1249 – 13, Standard Test Method for Water Vapor Transmission Rate through Plastic Film and Sheeting Using a Modulated Infrared Sensor, 2013
8. PERMATRAN-W Model 398, Operator's Manual
9. ASTM D3985- 10, Standard Test Method for Oxygen Gas Transmission Rate through Plastic Film and Sheeting Using a Coulometric Sensor, 2010
10. OX-TRAN Model 1/50, Operator's Manual
11. Xu, H.; Lele, A.; Rastogi, S. The influence of carbon-based nanofillers on the melt flow singularity of linear polyethylene. Polymer. 2011, 52, 3163–3174.

12. Kolnaar, J. W. H.; A. Keller A temperature window of reduced flow resistance in polyethylene with implications for melt flow rheology: 1. The basic effect and principal parameters. Polymer. 1994, 35, 3863–3874.

CHAPTER 4: MORPHOLOGY OF FILLERS, MATRICES AND NANOCOMPOSITES

4.1: Introduction

The methods used for studying the morphology of polymer clay nanocomposites have generally been X-ray diffraction (XRD), transmission electron microscopy (TEM) and scanning electron microscopy (SEM). XRD and TEM are the most commonly employed methods to measure the degree of exfoliation of clay in thermoplastic matrix. However, XRD is a qualitative method whose results can vary depending upon the sample preparation technique, orientation of clay and also by the presence of defects in the crystal structure in the clay [1]. On the other hand TEM only gives the analysis of a very small piece of the whole sample, So these analyses can be misleading and in recent year's characterization technique have been developed which can describe the presence of exfoliation by measuring bulk mechanical and rheological properties [2]. In this chapter a comprehensive analysis of the morphology of the individual fillers along with their nanocomposites is presented to better understand the internal structure and properties of the prepared specimens.

4.2: Morphology of ball-milled MWCNT

In order to determine the change in length of the individual ball milled MWCNT, transmission electron microscopy of the tubes was carried out using acetone as a solvent to disperse the tubes on the copper grids. The micrographs of the MWCNT obtained after 24, 48 and 72 hours of ball milling are shown in fig 4.1. The results indicate a reduction in the overall length of the MWCNT and also indicate that the agglomerate formation of the MWCNT due to their high length is reduced, which is

supposed to help them disperse more efficiently in polymer matrix. The individual length of the MWCNT for all the three samples was measured using ImageJ software. The length of the tubes was reduced from 584 ± 205 nm for the 24hrs ball milling to 417 ± 137 nm for the 48hrs ball milled tubes. In case of 72hrs ball milled tubes the length was reduced to 301 ± 107 nm which represents a 48.5 % reduction in size to the 24hrs ball milled tubes.

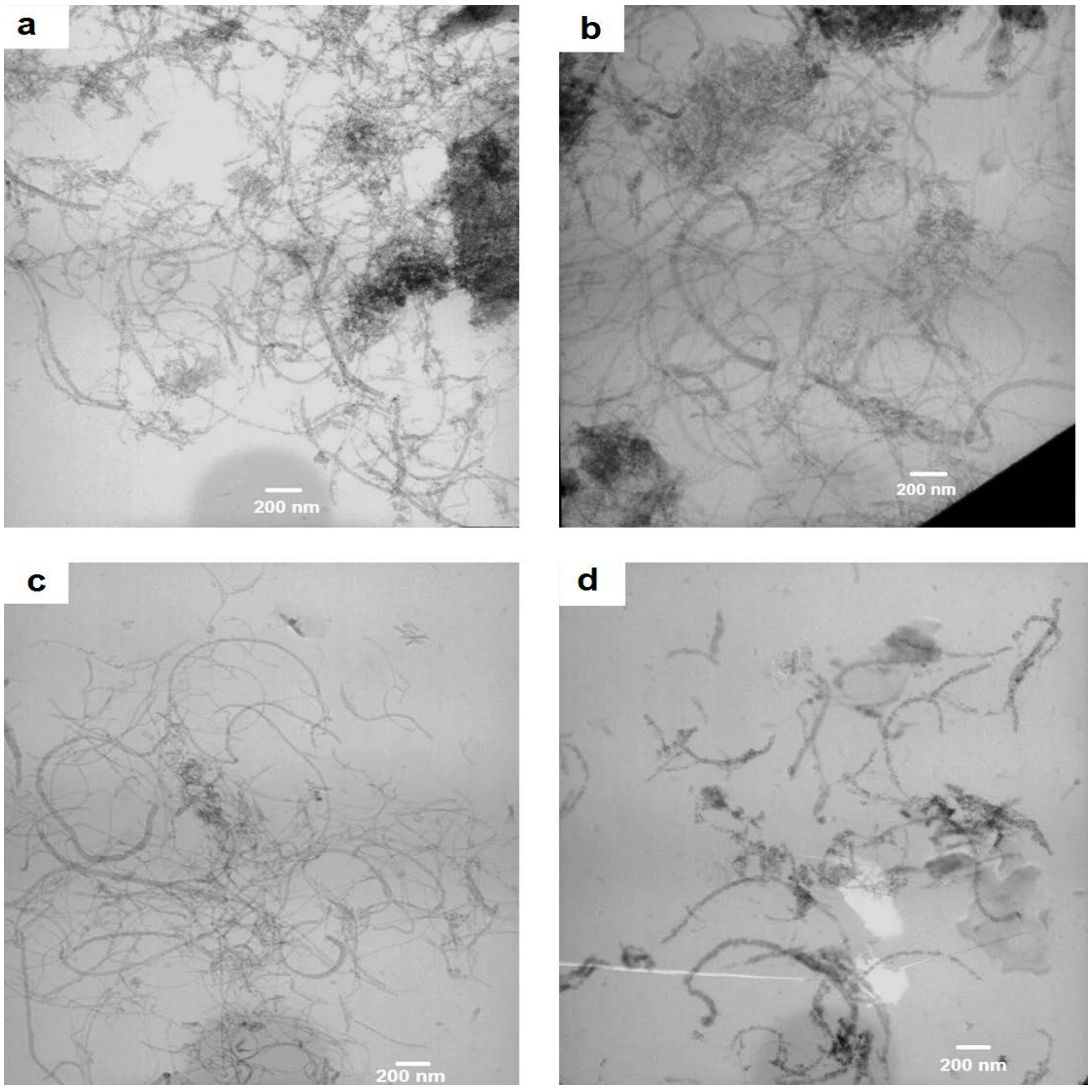

Fig. 4.1: TEM images of ball-milled MWCNT; (a) As received MWCNT, (b) 24hrs ball milled MWCNT, (c) 48hrs ball milled MWCNT and (d) 72hrs ball milled MWCNT

4.3: Morphology of graphene oxide

The morphology of the ultra-sonicated GO sheets dispersed in water was studied using TEM. The micrographs of the GO sheets obtained at two different resolutions are shown in figure 4.2. The results show good dispersion of the individual sheets and indicate some degree of exfoliation.

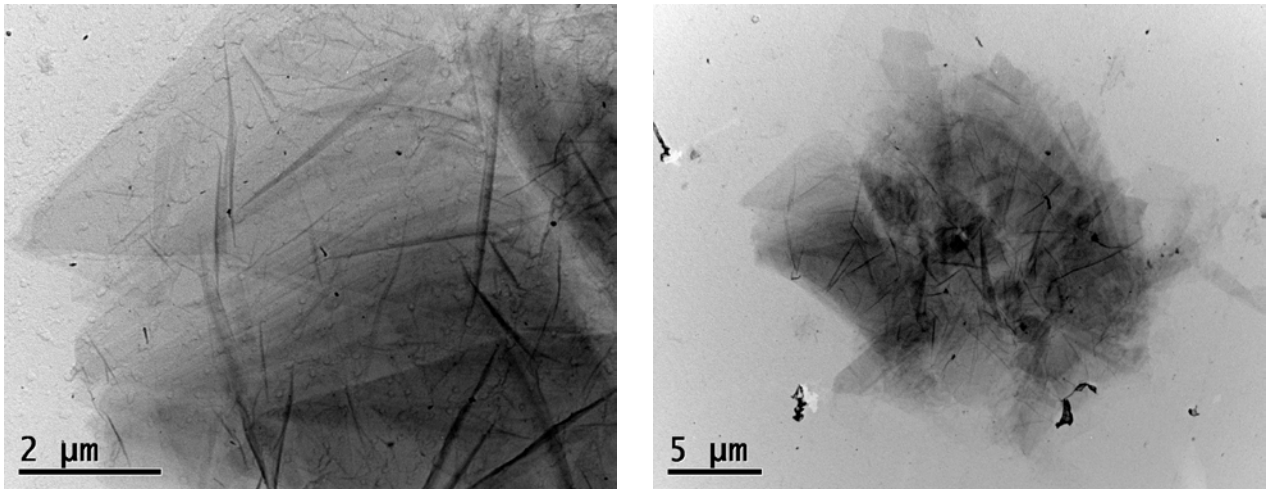

Fig. 4.2: TEM images of GO/water dispersions

4.4: Stability of clay dispersion in aqueous media

Sedimentation characteristics of clay in aqueous media were studied by varying the ultrasonic treatment time and the pH of the dispersion. During the preparation of polymer clay nanocomposites, exfoliation can be promoted by the use of high shear mixing techniques such as high-speed dissolvers, extensive ultrasonic, grinding, or high-pressure mixing. In ultrasonic treatment the separation of clay platelets can be achieved by the shearing action of ultrasonic oscillations, which can result in the nanoscale dispersion of clay in the polymer matrix. Ultrasonication is mainly used in the solution intercalation method for the preparation of polymer clay nanocomposites [3,4]. Exfoliated polystyrene/organoclay [3] and thermoplastic natural rubber/MMT [4]

clay nanocomposites are few of the examples which have been prepared by the ultrasonication assisted solution intercalation method.

The effect of changing the ultrasonication treatment time of BHX, BLX and bentone clay dispersions on their settling (sedimentation) characteristics was observed by taking pictures of the dispersions at regular intervals. The results reported in fig. 4.3 indicate that for both BLX and BHX there is no prominent settling of the clay after 48hrs and all the samples apart from the untreated ones maintained a good level of dispersion with very little settling of clay. However when the samples were analysed after 96hrs there was considerable settling of the clay dispersions and the highest dispersion was observed for 40mins treated samples, although the 30mins treated samples had almost the same dispersion level.

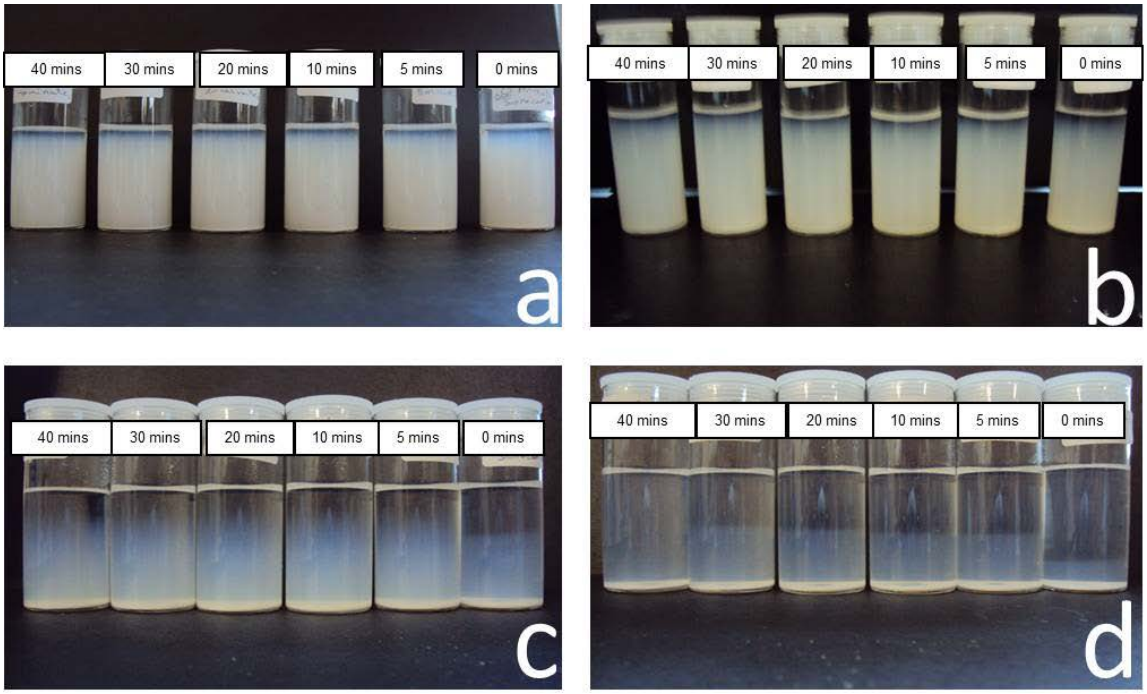

Fig. 4.3: Effect of sonication time (0 to 40 minutes) on sedimentation characteristics of BHX and BLX clay sample, (a) BLX after 48hrs, (b) BLX after 96hrs, (c) BHX after 48hrs and (d) BHX after 96 hrs.

The effects of dispersion media pH on the settling characteristics for both BLX and BHX are reported in fig. 4.4. The two figures show that at pH less than 7 the clay dispersions settle down very quickly, while the excellent dispersion of the clay samples was generally maintained when the pH of the dispersion was greater than 7. The results indicate that higher alkaline pH can be suitable for causing better dispersion of kaolin clay grades in water. However in case of samples with pH less than 7, the drastic effect of all the clay settling down in less than 2 hours is only observed when the pH is less than 4. Although the results show better dispersion for higher alkaline pH, but this requires the addition of chemicals such as sodium hydroxide, sodium carbonate etc. Since in this project the products are mainly developed for food packaging industry, the emphasis is to use no chemical modification and only employ physical modification by machines.

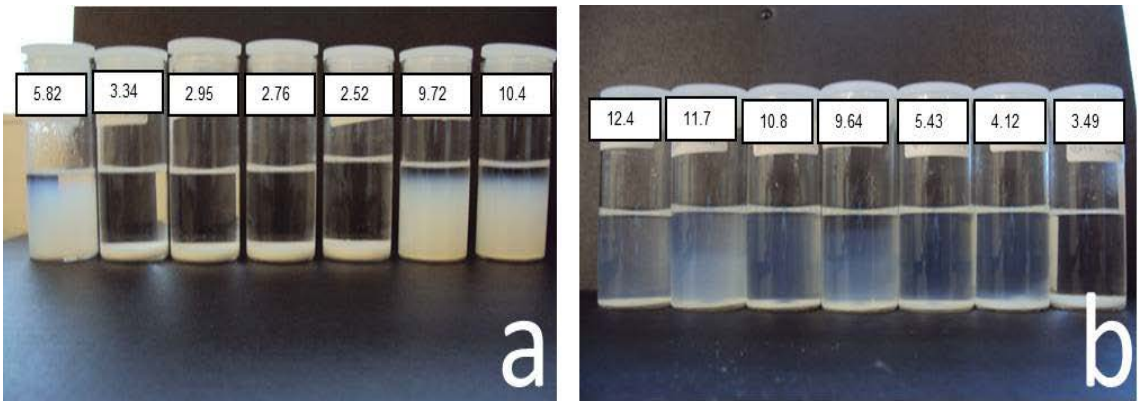

Fig. 4.4: Effect of pH above and below 7 on sedimentation characteristics of BLX clay samples with 30 minutes of sonication time, (a) after 48hrs and (b) after 96hrs.

The comparison of the three clay samples used in this study is shown in fig. 4.5. There are three scenarios analysed in these images: effect of same sonication time; effect of pH<7 and effect of pH>7 on the sedimentation characteristics of BLX, BHX and bentone clay. The images show that bentone and BLX are better dispersed in water than BHX when the sonication time is kept constant at 30 mins. The settling of

BHX clay could be due to its high shape factor which could result in the application of more gravitational forces on the surface area of BHX clay particles. Similar results indicating better dispersion for bentone and BLX were observed when pH of the dispersion was changed.

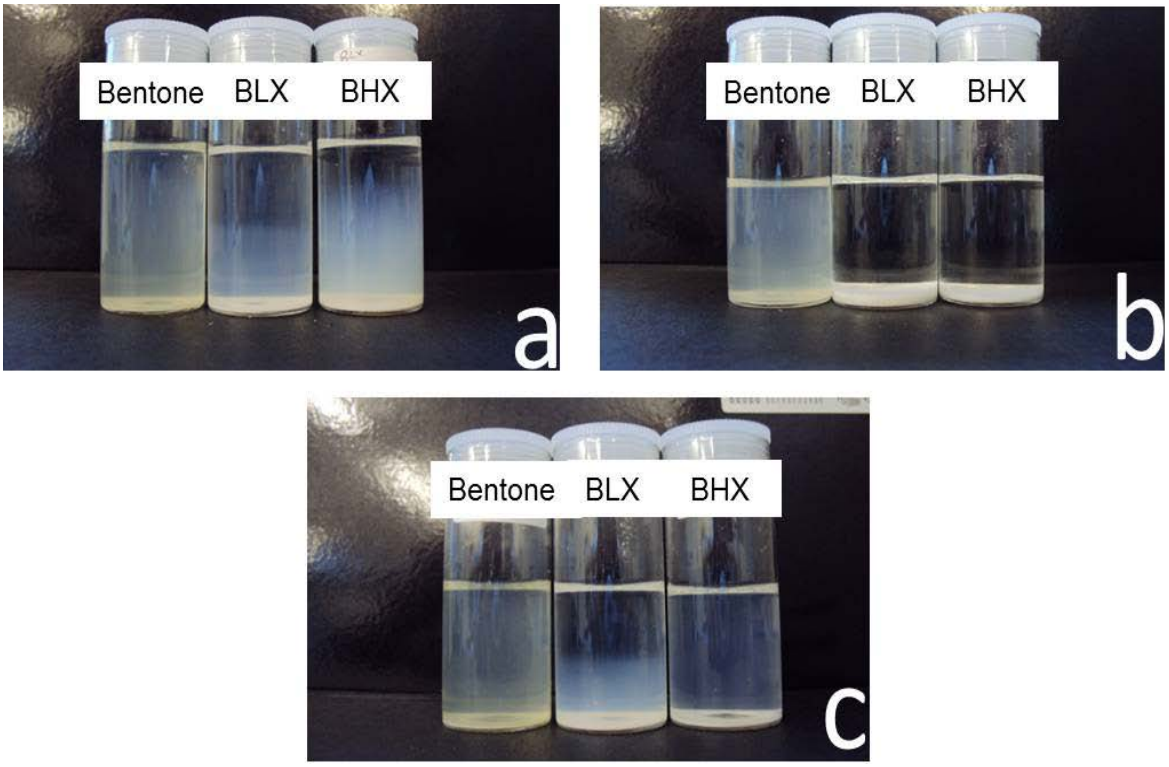

Fig. 4.5:Comparison of the three selected clay, (a) effect of 30 minutes of sonication time on BLX, BHX and Bentone clay (after 96hrs), (b) effect of pH< 7 on BLX, BHX and Bentone clay (after 48hrs) and (c) effect of pH> 7 on BLX, BHX and Bentone clay (after 96h)

4.5: Morphology of nanofiller powder pre-blended with HDPE

The powdered sample produced by the pre-blending procedure was analysed by SEM analysis to visualize the presence and dispersion of the nanoclay on the surface of the powdered matrix sample. Fig 4.6 shows the SEM micrographs of HH1.0 at two different resolutions. The SEM analysis shows that due to the pre blending, clay tactoids are uniformly distributed on the HDPE powdered tactoids surface and the high resolution image (fig 4.16-b) shows that the clay layers are embedded into the

matrix which increases their chances of being distributed uniformly and in some case achieving exfoliation or intercalation.

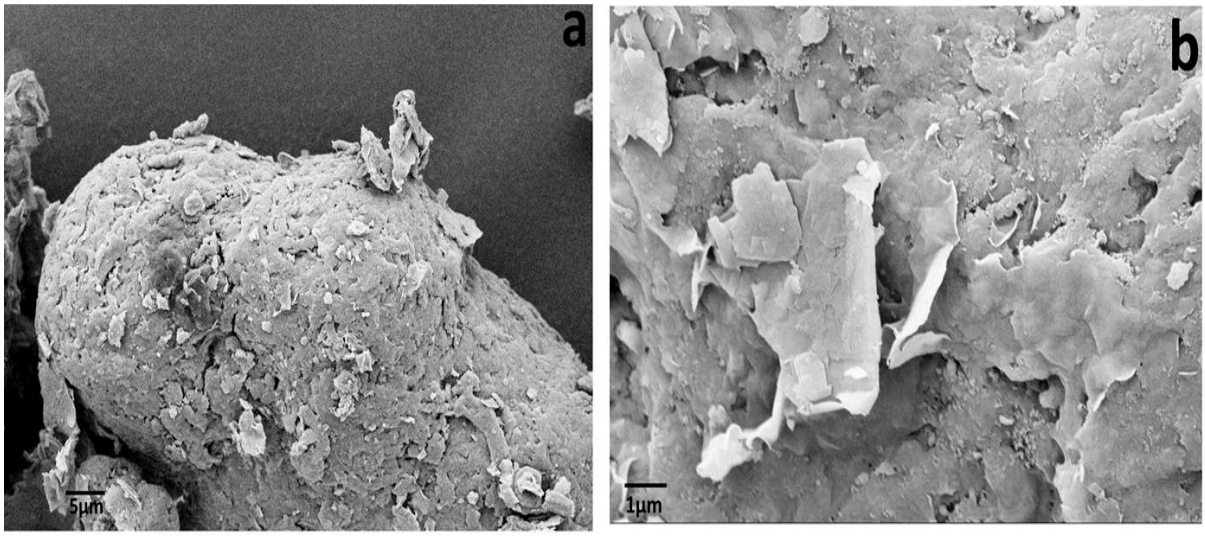

Fig. 4.6: SEM images of HDPE/BHX 1.0 wt % powder nanocomposites at two different resolutions

4.6: Morphology of HDPE/clay nanocomposites

4.6.1: XRD analysis of HDPE/kaolin clay nanocomposites

XRD analysis is widely used to determine the presence or absence of exfoliation, intercalation or microcomposite morphology of the nanocomposite [5]. The XRD data obtained for the different specimens was used for the calculation of the interlayer spacing of the individual clay layers. The calculation of basal plane separation of clay layers can be used to evaluate the interlayer space between clay layers when they are dispersed throughout the polymer matrix. The basal plane separation or d-spacing can be calculated by using Bragg's law [6]. The equation of Bragg's law is

$$d = \frac{n\lambda}{2sin\theta},$$

where n is an integer indication for peak number

λ is the wavelength of the x-ray.

θ is the angle of incidence of the x-ray beam [6].

Fig. 4.7 shows the diffraction patterns of HDPE, BHX clay and their nanocomposites containing different clay concentrations. The XRD analysis of pure HDPE reveals a strong reflection peak at 21.6^{o} and a less intensive peak at 24.1^{o}. The two peaks correspond to the orthorhombic unit cell structure of (110) and (200) reflection planes of pure HDPE [7]. From fig 4.7, it can be seen that BHX has a basal peak (001) at angle 12.4^{o} which is attributed to natural kaolinite clay with a basal spacing of 0.7nm. The same peak is present in all of the nanocomposites, with the sample HH3.0 having the highest intensity. Only in case of HH0.2 and HH0.6 that the intensity of the peak is less than that in BHX clay, which shows that the stack distance is only slightly reduced in these low weight percentage samples whereas in high weight percentage samples the clay remains at its original stack distance.

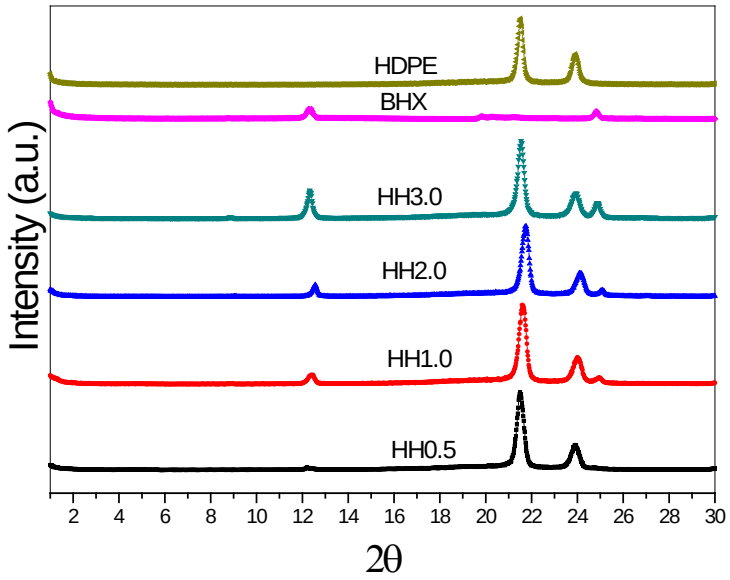

Fig. 4.7: XRD patterns for HDPE, BHX and their 0.5, 1, 2 and 3 wt.% nanocomposites

The basal plane separation calculation results are shown in table 4.1. The d-spacing remains more or less the same in all of specimens and only the intensity of the peak

increases in high weight percentage specimens. There have been a number of reports [8,9,10] where the original basal spacing of an organo-modified kaolin (basal spacing >0.7nm) reappeared in nanocomposites after their manufacturing, which shows that kaolin clay has the tendency to recover its original stack distance if present in large quantities.

Table 4.1: Basal spacing results for BHX and its nanocomposites

Sample	Max peak Intensity	2θ	d (A^o)
BHX	468	12.42	7.17
HH0.5	129	12.20	7.30
HH1.0	437	12.41	7.18
HH2.0	564	12.56	7.09
HH3.0	1260	12.32	7.23

4.6.2: XRD analysis of HDPE/Na-MMT clay nanocomposites

The diffraction intensity profile for HDPE, Na-MMT and their 1 and 3 wt.% nanocomposites are shown in fig 4.8. The basal plane separation for Na-MMT, HM1.0 and HM3.0 calculated from Bragg's law are shown in table 4.2. With respect to Na-MMT clay, no basal spacing was detected for HM1.0 since there was no distinct diffraction intensity peak visible in the range of angle of incidence of x-ray beam used for XRD analysis. In this case the polymer chains are supposed to have entered parallel arranged clay galleries and pushed the clay layers so much far apart that the interlayer clay separation is above the sensitivity of XRD and is hence not detected.

When the clay concentration was increased from 1 to 3.0 wt %, a distinct diffraction peak of intensity 97 (a.u.) is observed at an angle of 6.75 (2θ), which indicates an intercalated clay morphology. In comparison to Na-MMT, the basal spacing for HM3.0 is increased to 13.52A^{o}.

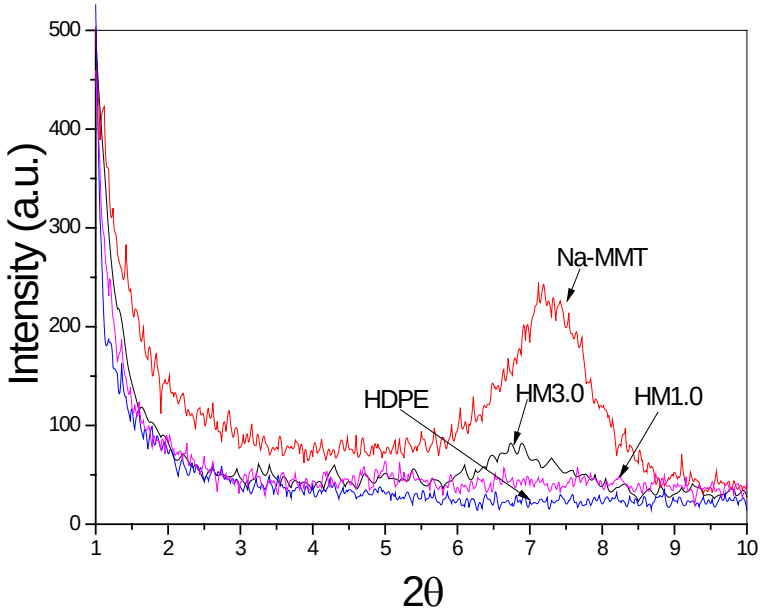

Fig. 4.8: XRD patterns for HDPE, Na-MMT and their 1 and 3 wt.% nanocomposites

Table 4.2: Basal spacing results for Na-MMT and its nanocomposites

Sample	Max peak Intensity	2θ	d (A^{o})
Na-MMT	255	7.2	12.27
HM1.0	-	-	-
HM3.0	97	6.75	13.52

4.6.3: XRD analysis of HDPE/bentone clay nanocomposites

The XRD intensity profiles for HDPE and its nanocomposites with 1 wt. % bentone clay are shown in fig 4.9. The XRD analysis for bentone clay reveals an intercalated morphology for HB1.0, because the distinct diffraction intensity peak still appears in

the diffractograms and shifts from 5.72 (2θ) to an angle of 5.08 (2θ). The d-spacing calculations for bentone and its nanocomposite are shown in table 4.3. The d-spacing of bentone clay in HDPE was increased from 15.45A^{o} to 17.41A^{o}, indicating that the polymer chains had entered the clay galleries and made the platelets lose their crystalline structure and parallel alignment without pushing the platelets much apart. In case of intercalated structure the platelets are no longer parallel but they are only pushed apart and their separation does not exceed the sensitivity of XRD and hence reveals a broadened peak into the base line.

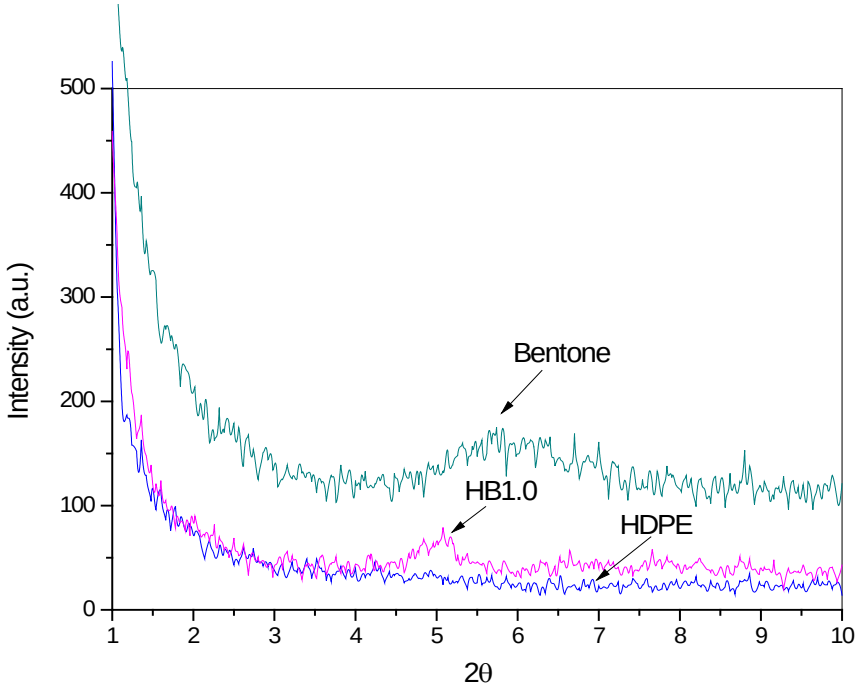

Fig. 4.9: XRD patterns for HDPE, bentone and their nanocomposites

Table 4.3: Basal spacing results for bentone and its nanocomposites

Sample	Max. peak Intensity	2θ	d (A^{o})
Bentone	183	5.72	15.45
HB1.0	79	5.08	17.41

4.6.4: TEM analysis of HDPE/clay nanocomposites

TEM micrographs for HDPE and its nanocomposites with BHX, BLX and Na-MMT clay at a lower and higher scale resolution are shown in fig 4.10. The two resolutions show the dispersion at different scales are selected to qualitatively establish the degree of dispersion of nanoclay within the HDPE matrix and to validate the results of exfoliation obtained from XRD analysis. In these images the dark lines are the cross-section of clay particles or tactoids, while the bright areas indicate the polymer matrix. These images also indicate good adhesion between the clay tactoids and the matrices. The internal structure of these composites mainly consists of tactoids of different sizes that are dispersed throughout the polymer matrix.

The pre-treatment of clay specimens by ultrasonication and the extensive shearing forces applied during the melt blending phase caused most of the clay layers to be separated from their assembly of layered structured aggregates to produce tactoids containing few layers that are uniformly distributed though out the matrix. The disruption of the aggregate is also caused by the polymer melt chains which enter into the inter-aggregate space and hence produce uniformly distributed tactoids.

The TEM micrographs were also used to calculate the length, thickness and aspect ratio of the clay layers or aggregates by using ImageJ-1.47c software. The clay layers or aggregates were identified and traced by ImageJ software and their respective length and thickness were measured. A minimum of 10 clay layers were used for each calculations.

The calculated results for aspect ratio of clay are shown in table 4.4 for BHX, BLX and Na-MMT based HDPE nanocomposites. The aspect ratio calculations show that the type of clay used, morphology of clay has a significant effect on the characteristic dimension of the silicates.

Table 4.4: Aspect ratio calculations for BHX, BLX and Na-MMT based HDPE nanocomposites

Specimen	Mean Length L (nm)	Standard Deviation	Mean Thickness T (nm)	Standard Deviation	Aspect ratio L/T	Standard Deviation
HL1.0	217	53	14	5	15.54	6.1
HL5.0	445	72	18	4	24.75	7.4
HM1.0	318	38	10	2	31.8	5.6
HM3.0	400	54	11	3	36.36	10.2
HH3.0	255	42	12	3	21.25	8.6
HH5.0	473	62	13	4	36.42	10.9

A direct comparison of the low and high weight percentage specimens of BHX, BLX and Na-MMT clay based nanocomposites reveal longer and thicker clay tactoids for high weight percentage specimens because the clay layers get close to each other and form larger tactoids that are still aligned and can form tortuous path for enhanced barrier properties. Similar results were obtained for kaolin based polymer nanocomposites in other studies [11, 12]. The error in the aspect ratio calculations for high weight percentage specimens can be large because at such high concentration the clay layers are difficult to be distinguished and also because of the micrographs focusing error.

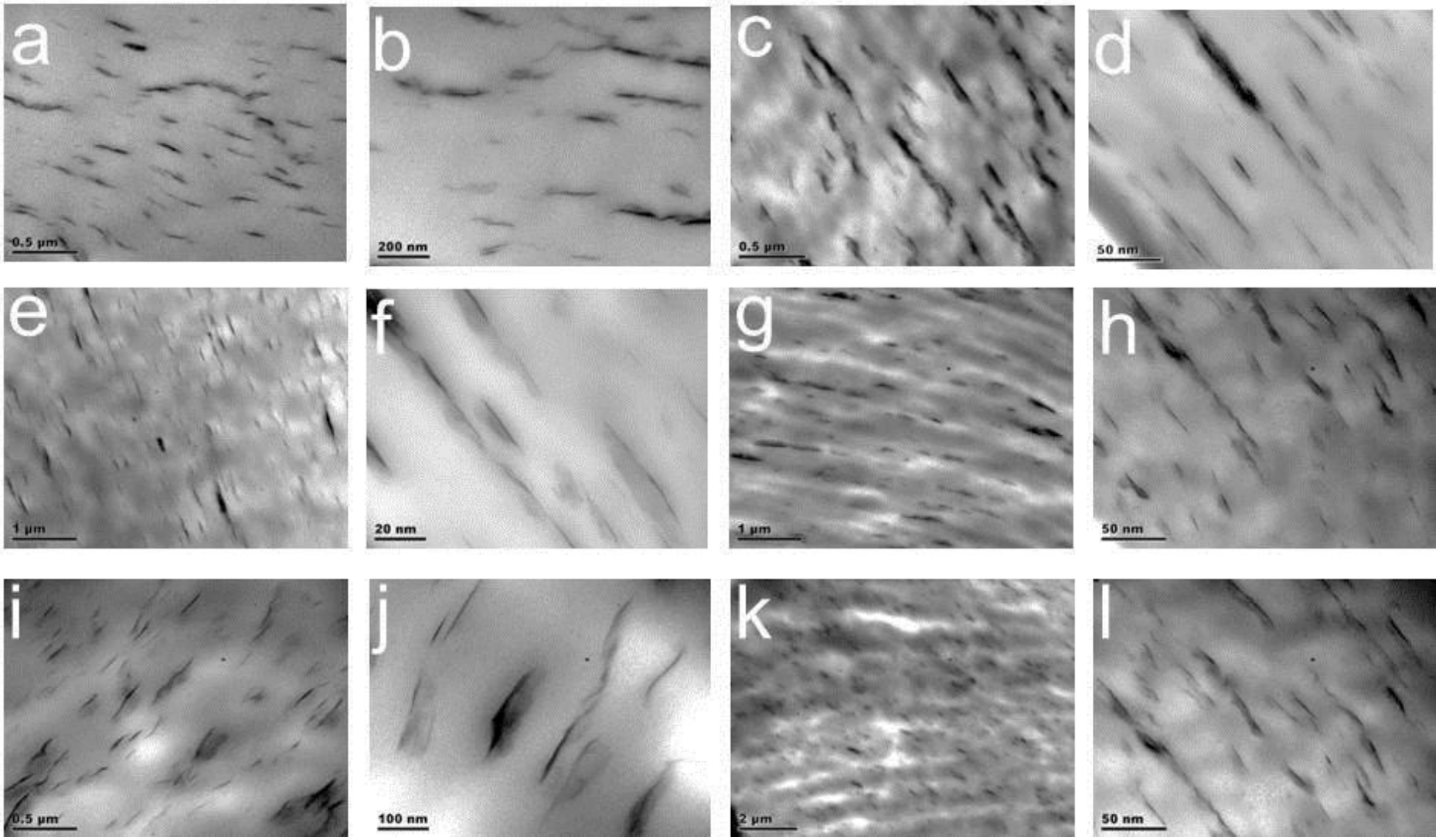

Fig. 4.10: TEM micrographs at two resolutions for HDPE and its nanocomposites with BHX, BLX-kaolin clay and Na-MMT clay. HL1.0 (a, b), HL5.0 (c, d), HM1.0 (e, f), HM3.0 (g, h), HH3.0 (I, j) and HH5.0 (k, l)

The calculated aspect ratio was the highest for Na-MMT in comparison to BHX and BLX clay. The data shown in table 4.4 reveals that the major difference among the three clays selected was due to the thickness of the individual clay layers that were detectable for Na-MMT clay. On the other hand due to their microcomposite morphology, these individual clay layers were not visible for BHX and BLX clays. Among the two kaolin clays, BHX clay had higher aspect ratio than the BLX clay because of lesser agglomerates and a better dispersion throughout HDPE matrix.

Interestingly, it has been observed [1,2] in the past that the smaller clay particles appear to be bended, folded, misaligned or fractured in the matrices, whereas the tactoids observed in our work retain their large length and will be able to better withstand the high shearing forces encountered on the polymer processing machinery.

4.6.5: SEM analysis of HDPE/clay nanocomposites

Fig. 4.11 shows the SEM micrographs of cyrofractured specimens of HDPE and its nanocomposites with BHX-kaolin clay, Na-MMT and BLX-kaolin clay. The SEM observation for pure HDPE (fig 4.11-a) shows that the surface is free from any porous structures and the fractured surface also displays the characteristics of a ductile polymer with small fibrils appearing throughout the specimen. The low weight percentage Na-MMT based nanocomposites (fig 4.11-b,c) showed uniform distribution of clay throughout their fractured surfaces with no appearance of any spherical domains of clay agglomerates. The absence of such domains and a finer microstructure with enhanced clay dispersion indicates strong bonding between the matrix and the filler.

For high weight percentage nanocomposites of Na-MMT (fig 4.11-d) the dispersion was also uniform with few appearance of agglomerates embedded into the matrix. In

case of BHX/HDPE nanocomposites no agglomerate was visible on the fractured surface for 1-5 wt. % specimens (fig 4.11-e-g). Also in case of HH5.0 the appearance of thin white clay aggregates embedded into the matrix with parallel distribution throughout the HDPE matrix indicate that clay distribution can create the necessary tortuosity path for better barrier properties.

In order to visualize the clay distribution throughout the HDPE matrix, the BLX based nanocomposites were analysed by back scattering SEM surface analysis of the compression moulded specimens to see the compositional contrast within the composite. In back scattered SEM analysis backscattered electrons are used to observe the size, dispersion, and orientation of the clay particles. Fig 4.11 (i-k) shows the back scattered SEM images of HL1.0, HL3.0 and HL5.0 respectively. The compositional contrast of clay dispersion within the nanocomposite becomes visible due to the backscattering of the electrons which is dependent upon the atomic number of the specimen being analysed.

Generally clay particles have high atomic number and hence they will appear in the form of particles in the micrographs. The micrographs shown in fig 4.11 (i-k) generally shows uniform distribution of the clay particles throughout the matrix with large agglomerates appearing at higher concentration specimens.

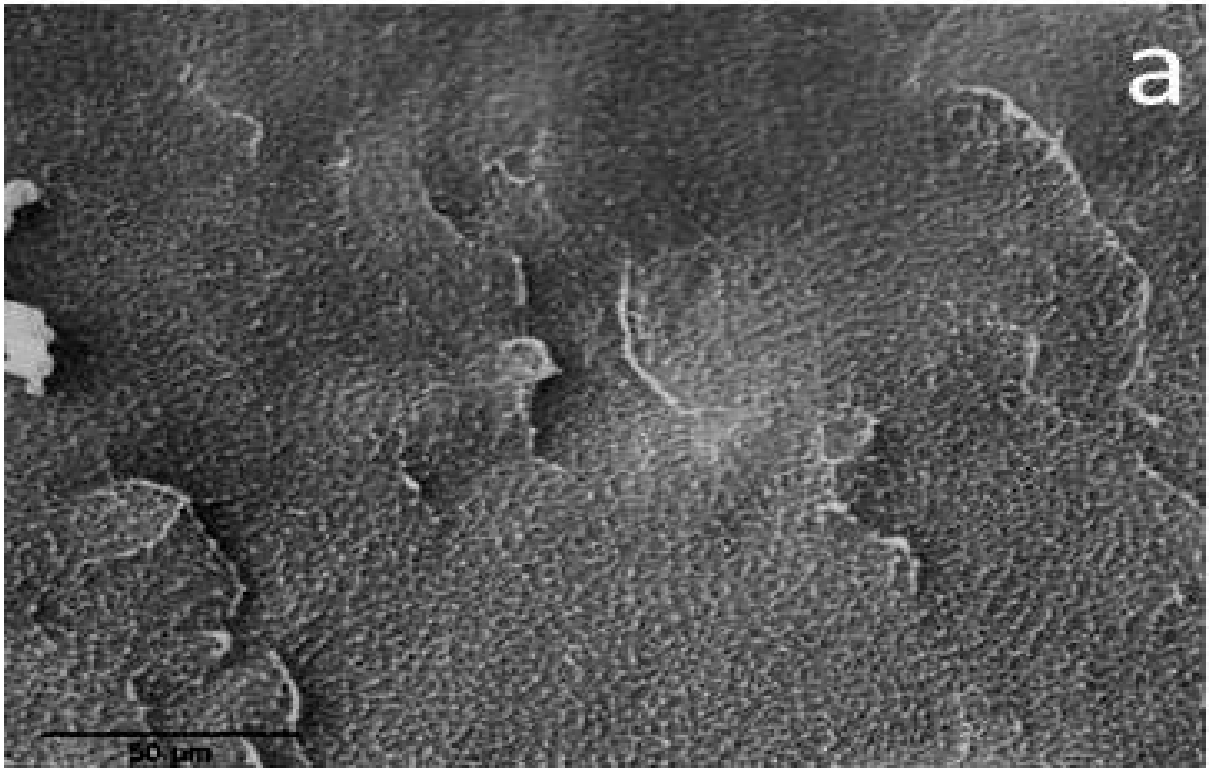
a
50 µm

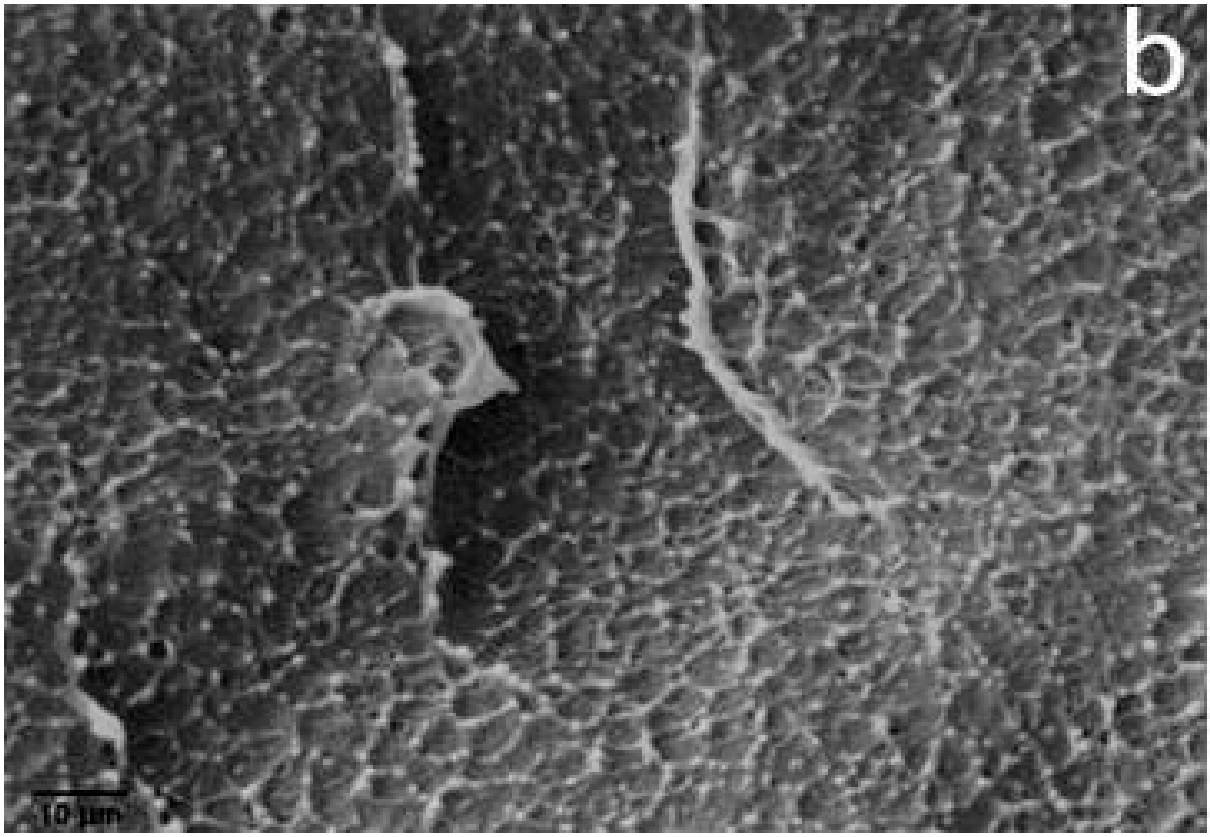
b
10 µm

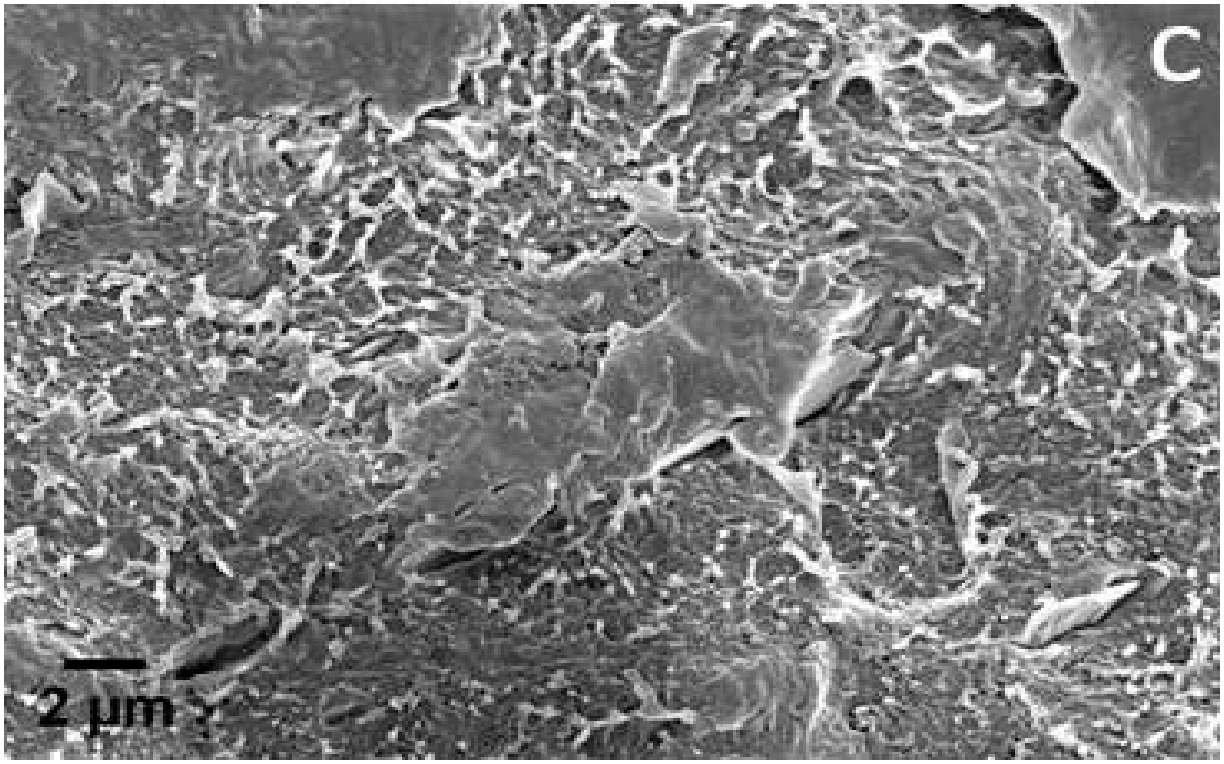
c
2 µm

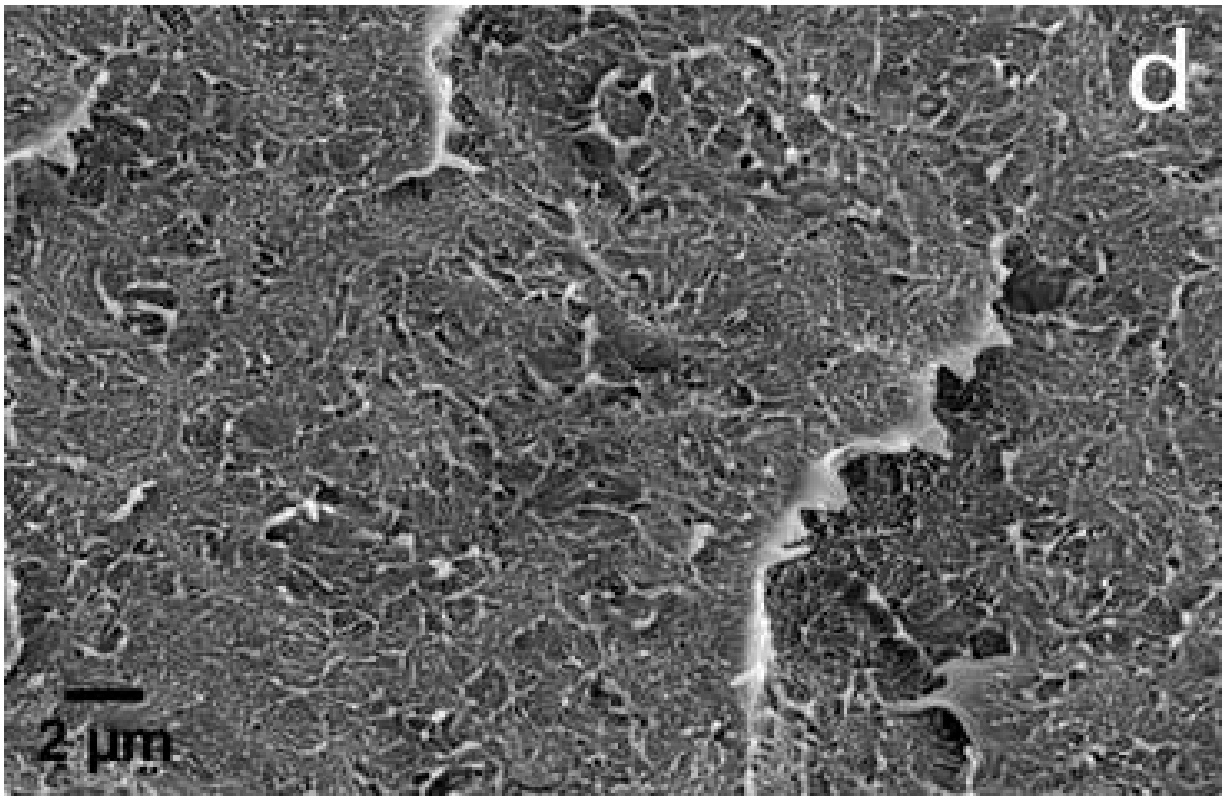
d
2 µm

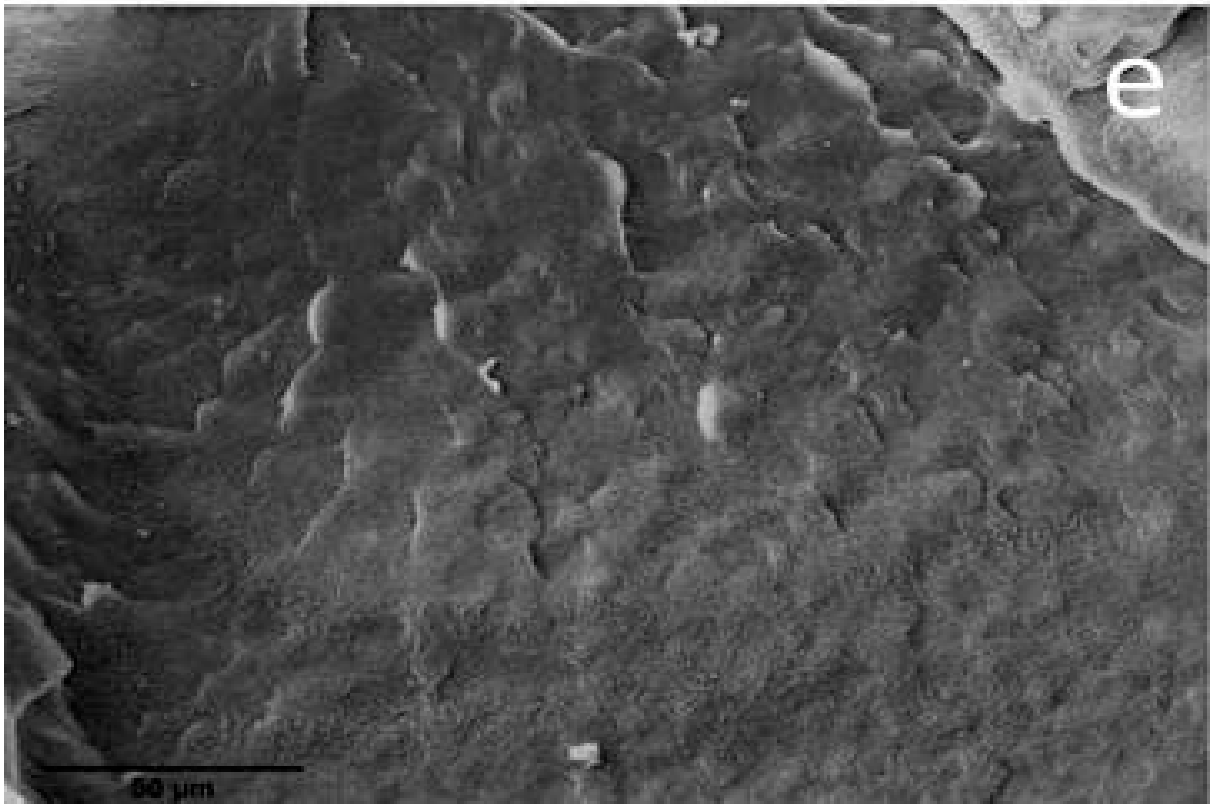
e
50 µm

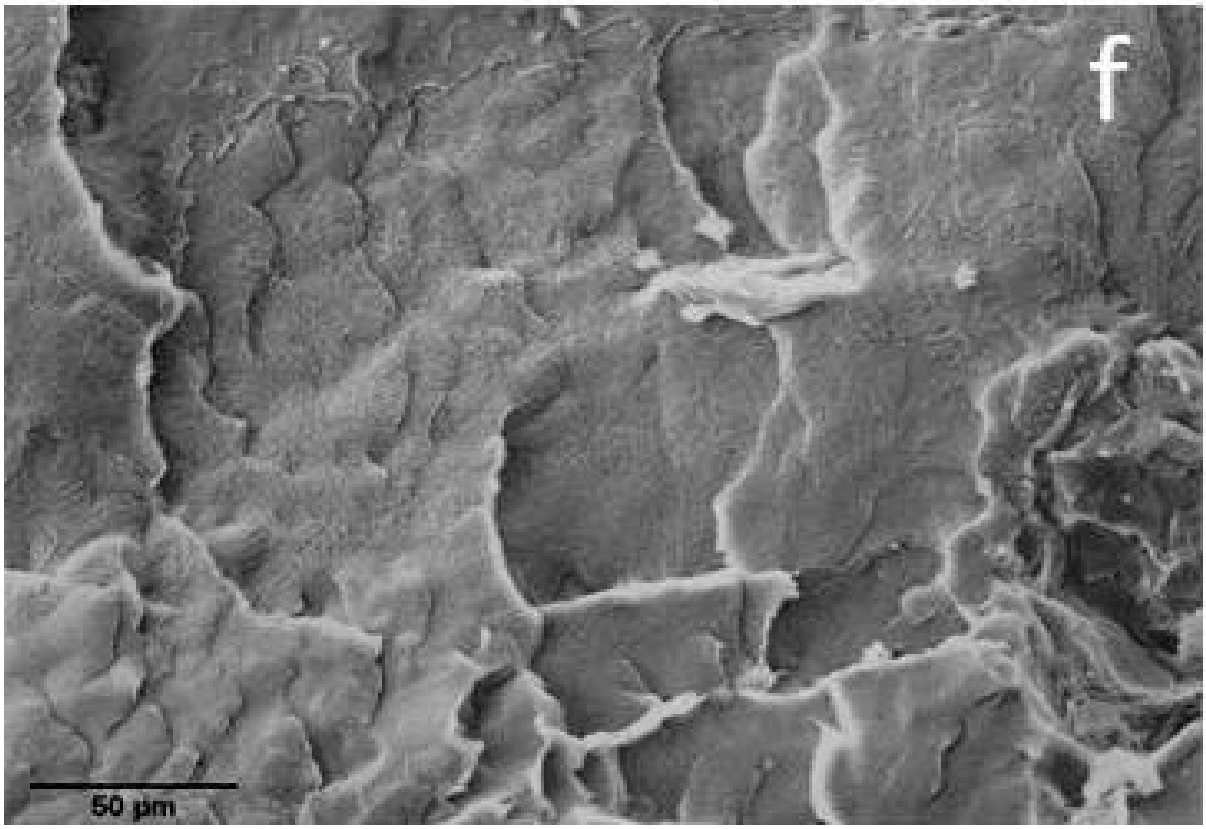
f
50 µm

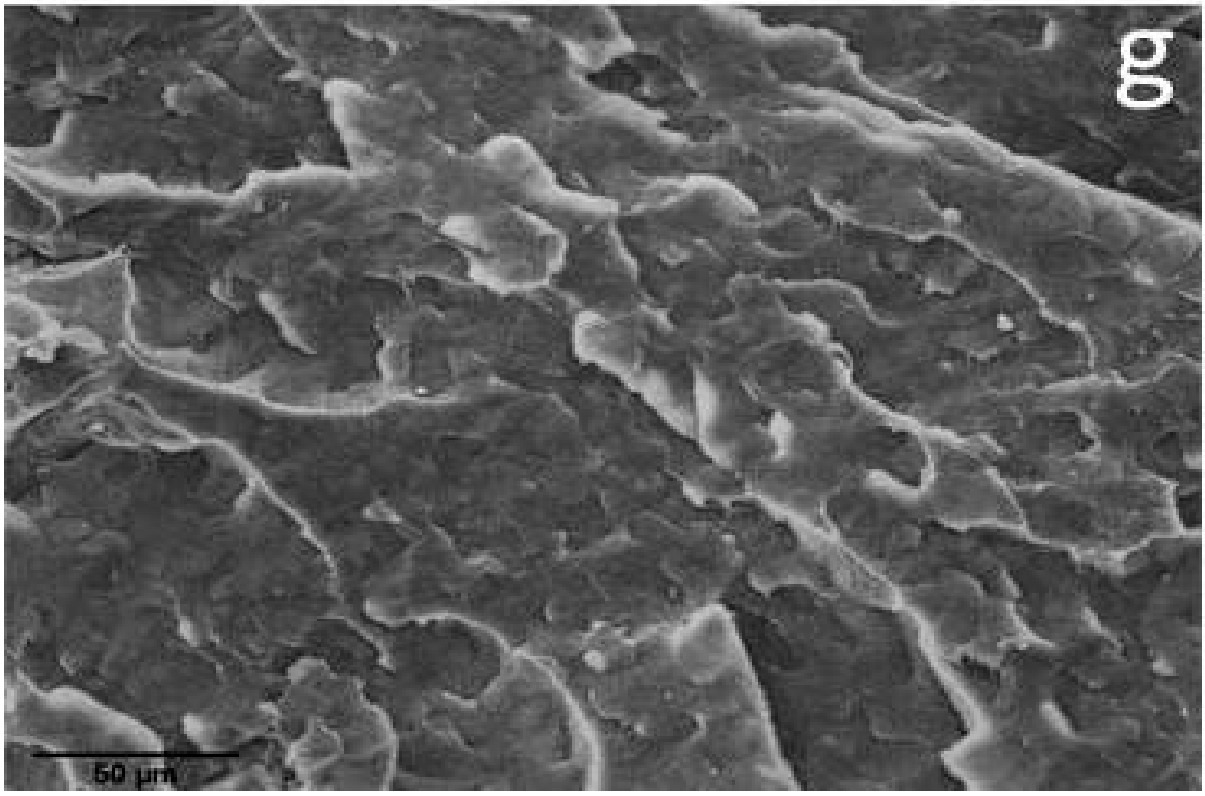
g
50 µm

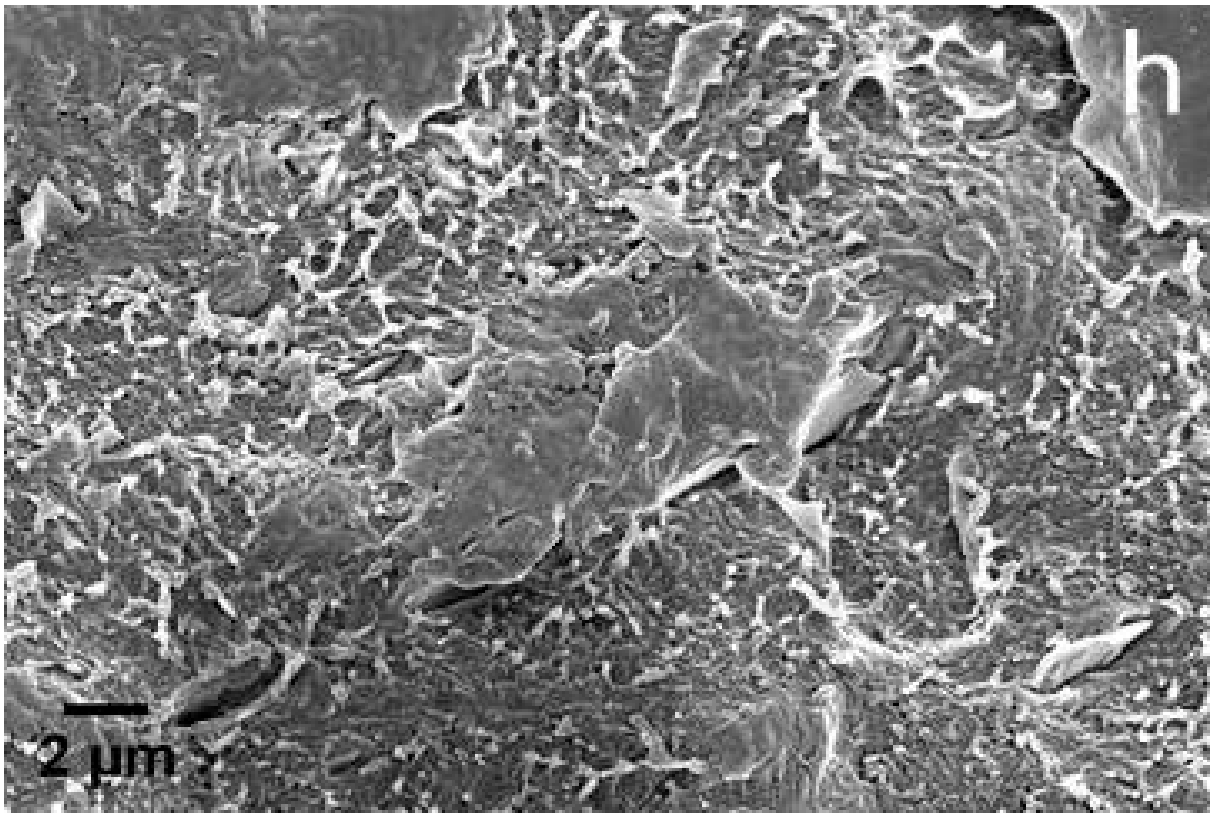
h
2 µm

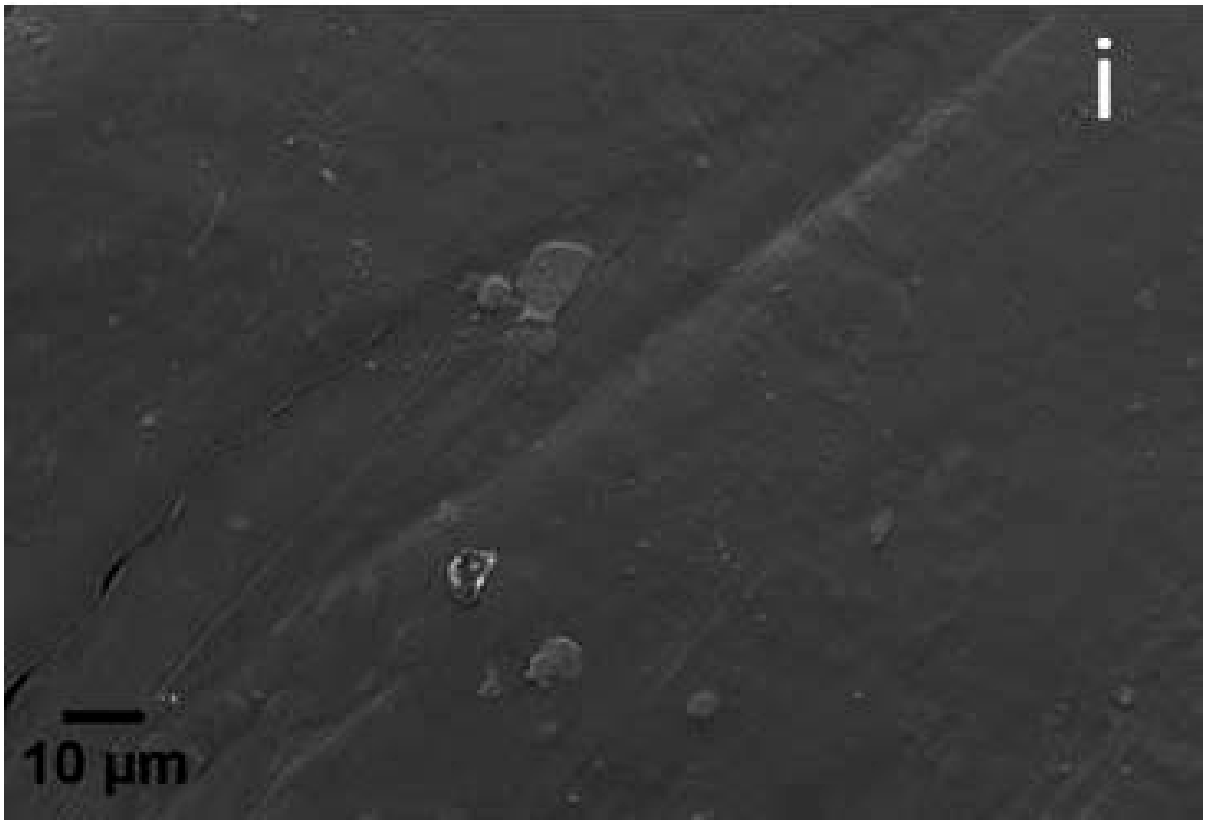
i
10 µm

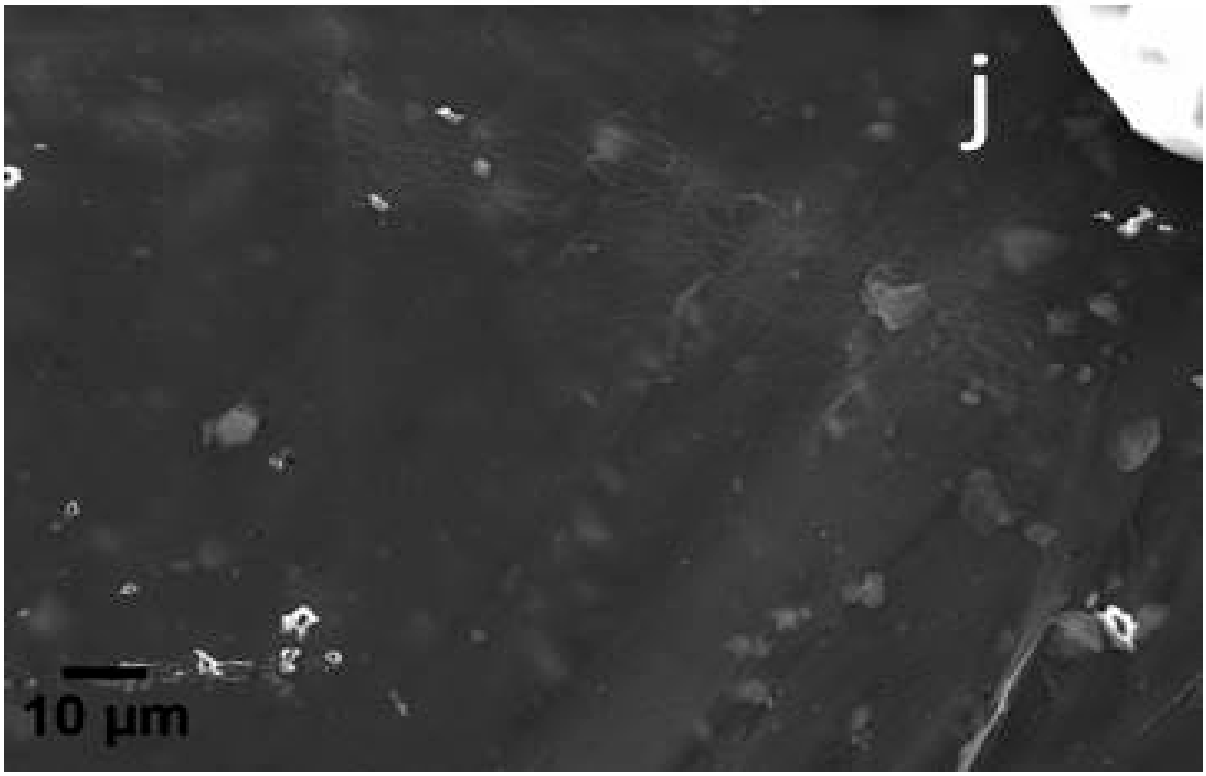
j
10 µm

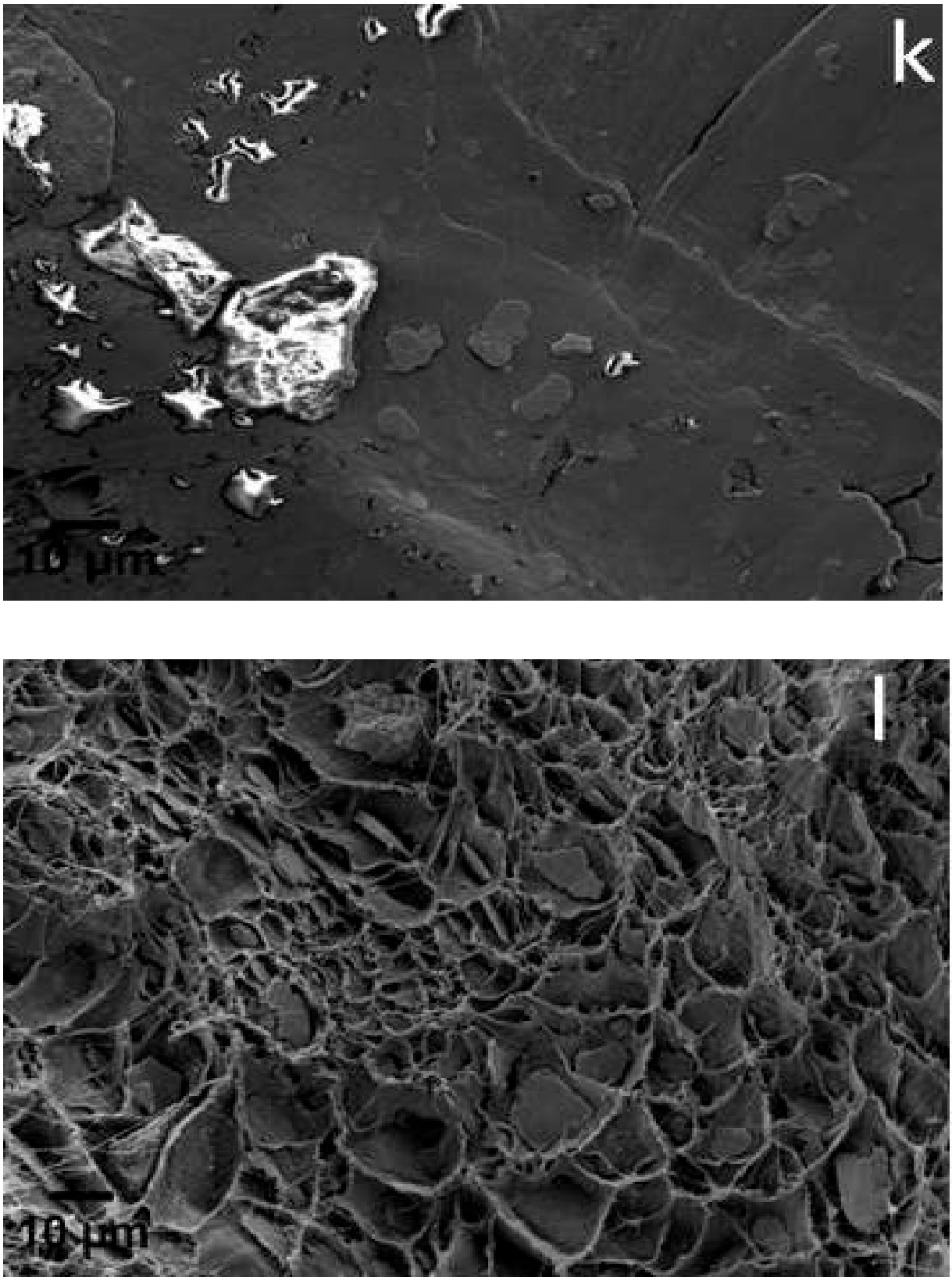

Fig. 4.11: SEM micrographs of HDPE and its nanocomposites with BHX-kaolin clay, Na-MMT and Bentone clay. HDPE (a), HM1.0 (b), HM3.0 (c), HM5.0 (d), HH1.0 (e), HH3.0 (f), HH5.0 (g), HH10.0 (h), HL1.0 (i), HL3.0 (j), HL5.0 (k), HL10.0 (l)

To study the interface morphology of the clay based HDPE nanocomposites, the highest weight percentage specimens for SEM analysis were prepared by a modified cyrofractured technique. In this method the specimens were shredded in a blender after being exposed to liquid nitrogen. By this method the interface between the clay and matrix can be revealed. Fig. 4.11(h, l) shows the cyrofractured micrographs of HH10.0 and HL10.0 respectively. The micrographs reveal uniform distribution of the clay through the nanocomposites but better interfacial adhesion between the clay and polymer was only visible in HH10.0 with only few clay agglomerates visible on the surface. On the other hand the clay agglomerates can be very easily seen on the surface of HL10.0 that is not embedded into the polymer matrix. This agglomerate formation could be attributed to the small aspect ratio of the BLX clay which could enable the clay particles to assemble into large agglomerates.

4.6.6: Optical microscopy analysis of HDPE nanocomposites

In order to study the dispersion of BHX nanoclay tactoids and layers throughout the HDPE matrix at a larger scale that can expose a larger surface area of the nanocomposite, HH5.0 nanocomposite was selected and studied using optical microscopy. The technique used for studying the dispersion was not based on conventional melt pressing method but was rather based on microtomy technique. The samples prepared by melt pressing are quite thicker and this method is not well suited for visualizing the orientation of clay particles in the polymer matrix. In order to produce thinner samples microtomy technique was used to prepare 10μm thick samples. These samples were then analysed by using 100-x lens of the polarized optical microscope. The results for HH5.0 nanocomposite are shown in figure 4.12. The presence of clay particles in a

regular arrangement is clear from these images. This regular arrangement can be considered to create a tortuous path in the nanocomposites which can help increase the barrier properties of the nanocomposites.

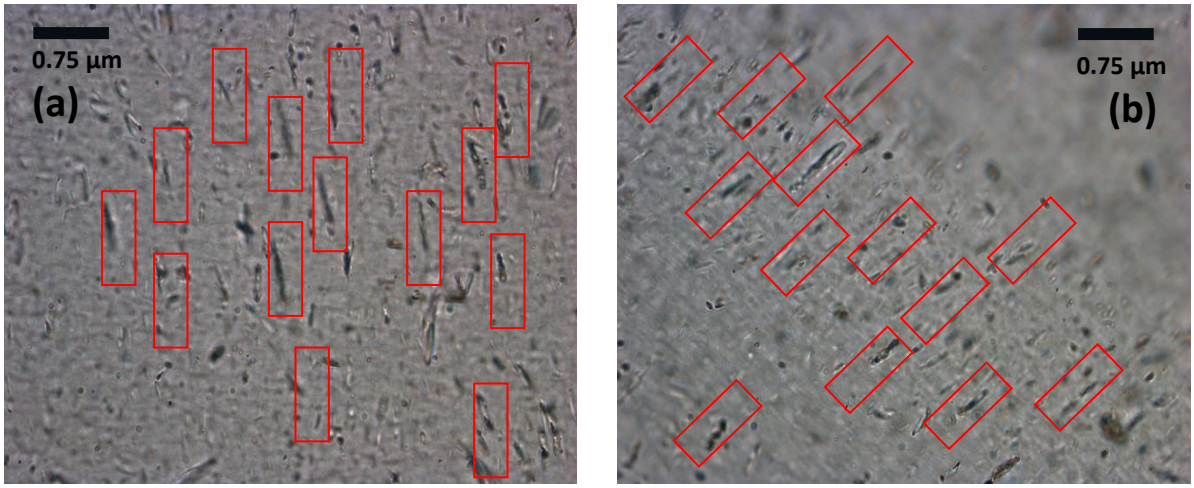

Fig. 4.12:Optical microscopy micrographs of HH5.0

4.7: Morphology of HDPE/carbon filler nanocomposites

In order to understand the morphology of the carbon nanofillers based HDPE nanocomposites a combination of XRD, OM and SEM analysis was carried out to establish the size, distribution and dispersion of the nanofillers inside HDPE matrix after the processing.

4.7.1: XRD of HDPE carbon nanofillers nanocomposites

Fig.4.13 shows the WAXS diffraction patterns of HDPE, GO and their nanocomposite. Also the diffraction pattern of HCB and HM are shown in the figure for comparative analysis. HDPE is a commodity thermoplastic semicrystalline polymer, and therefore the diffraction patterns reveal the presence of two intense maxima at 21.6° and 24° which correspond to the (110) and (200) reflections of the orthorhombic phase of polyethylene. The GO structure consists of several oriented graphene layers and hence the

diffractograms exhibit an intense maxima at 26.2° which corresponds to the (002) reflection from the graphitic layer structure.

The diffraction pattern shows no such maxima at 26.2° for HG, which shows that the ordered structure of graphene layers has been broken down inside HDPE matrix and hence the individual graphene layers are distributed inside HDPE. Also in case of HM and HCB no such peak is observed which shows that these nanofillers are also distributed uniformly inside HDPE matrix. The only two peaks that appear in the diffraction pattern for all the nanocomposites are the two intense maxima at 21.6° and 24° which belong to pure HDPE matrix.

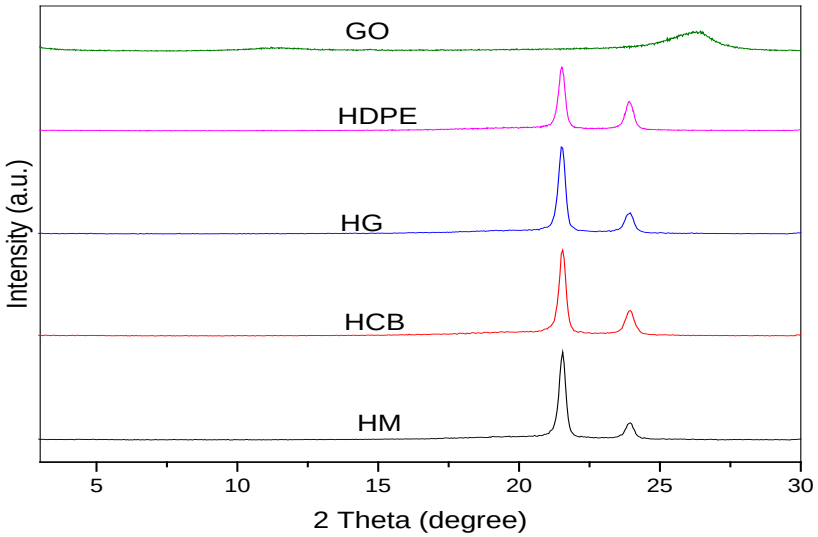

Fig. 4.13: XRD patterns for HDPE, GO, HCB, HG and HM

4.7.2: SEM of HDPE carbon nanofillers nanocomposites

Fig4.14 shows the fractured surface FEGSEM micrographs of the HDPE nanocomposites. In the micrographs for HCB (fig 4.14-a) uniform dispersion of CB particles in HDPE matrix is visible and the distance between CB particles is small. The tendency of the CB particles to form agglomerates is only visible in some areas of the nanocomposite.

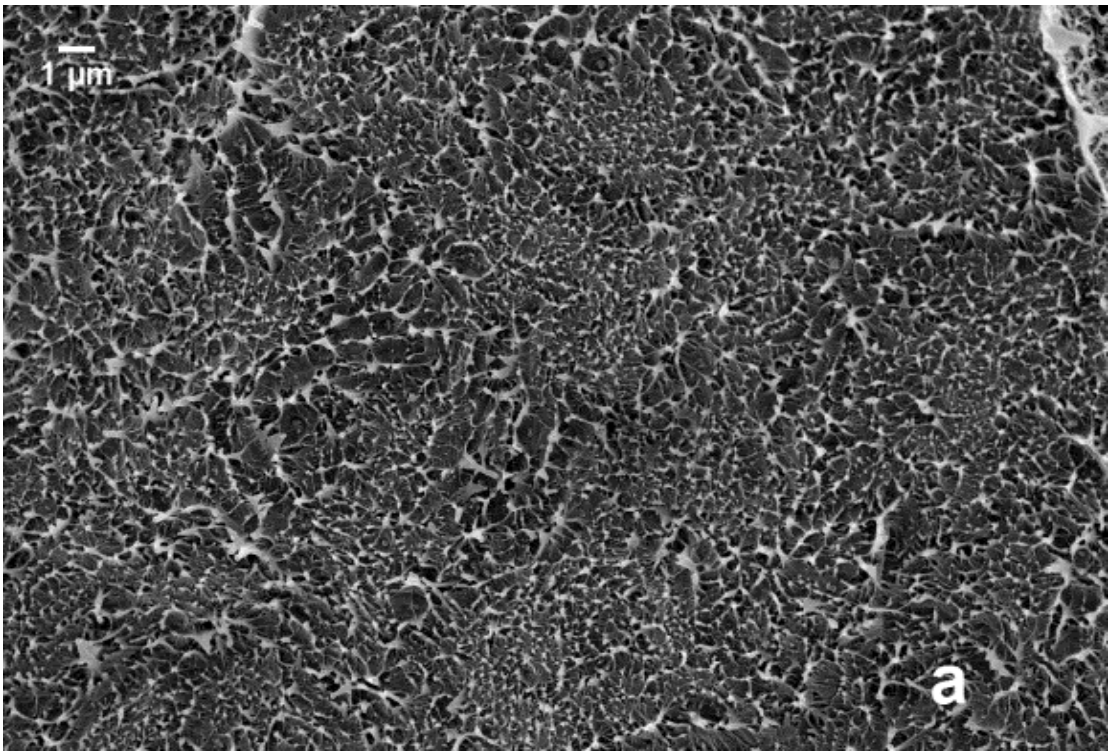
1 µm
a

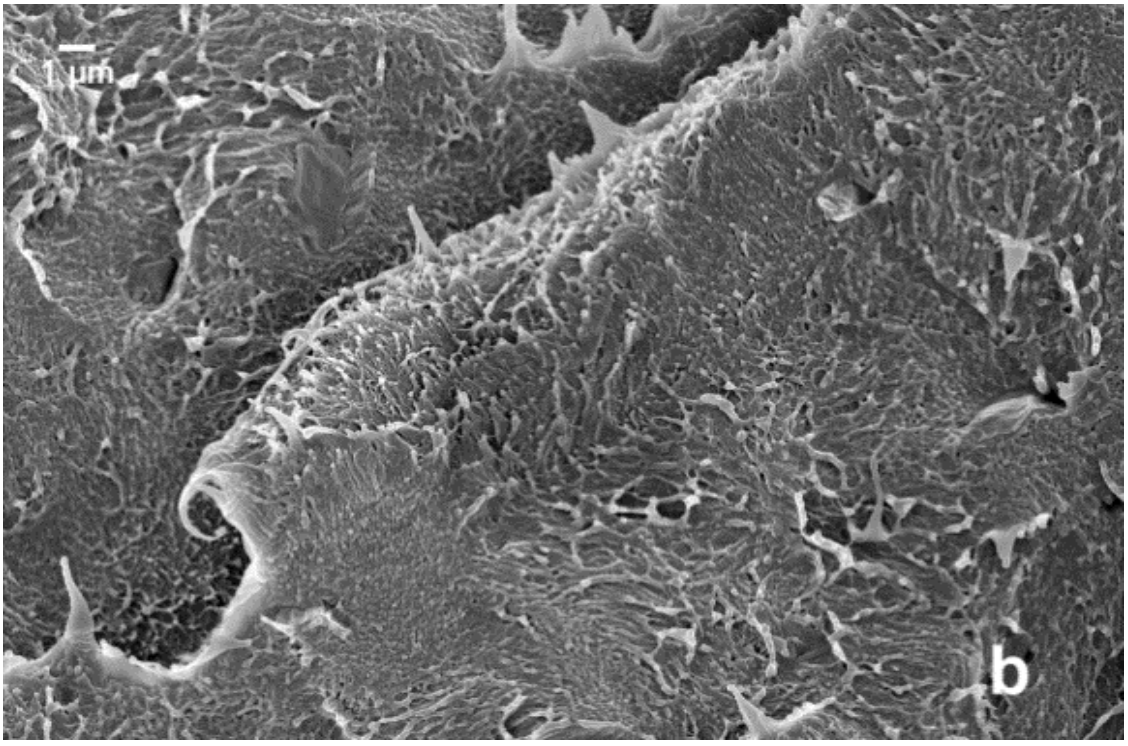
1 µm
b

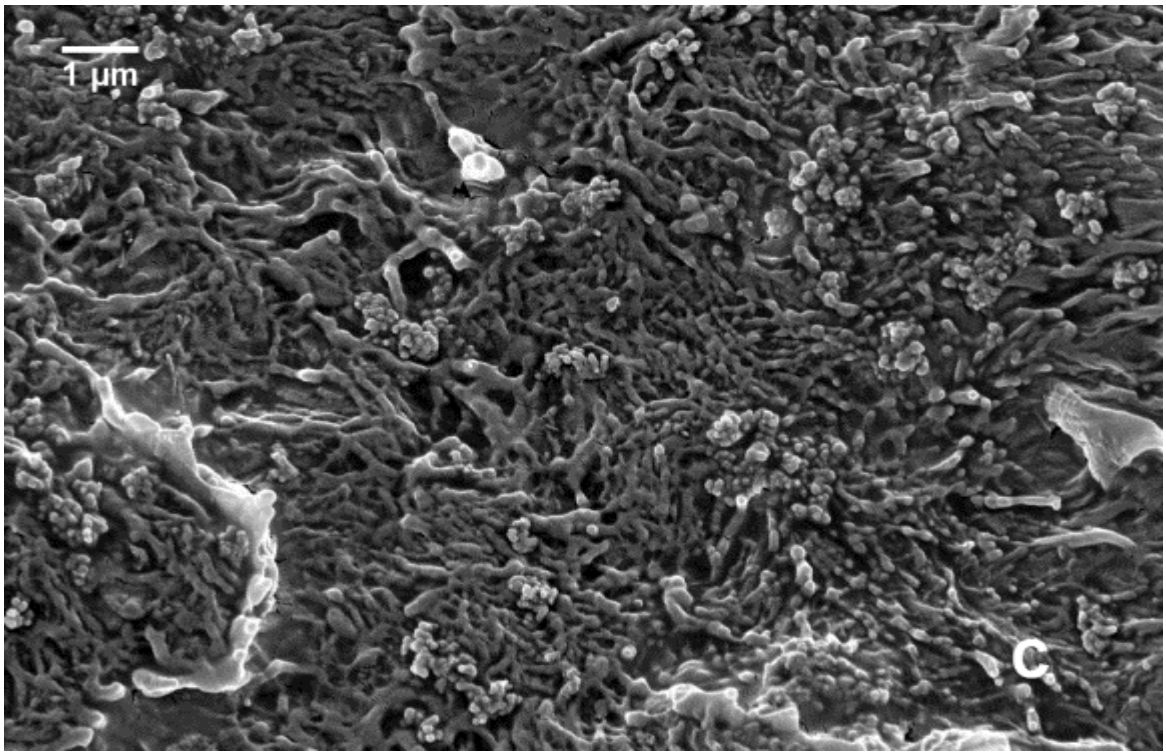
1 µm
c

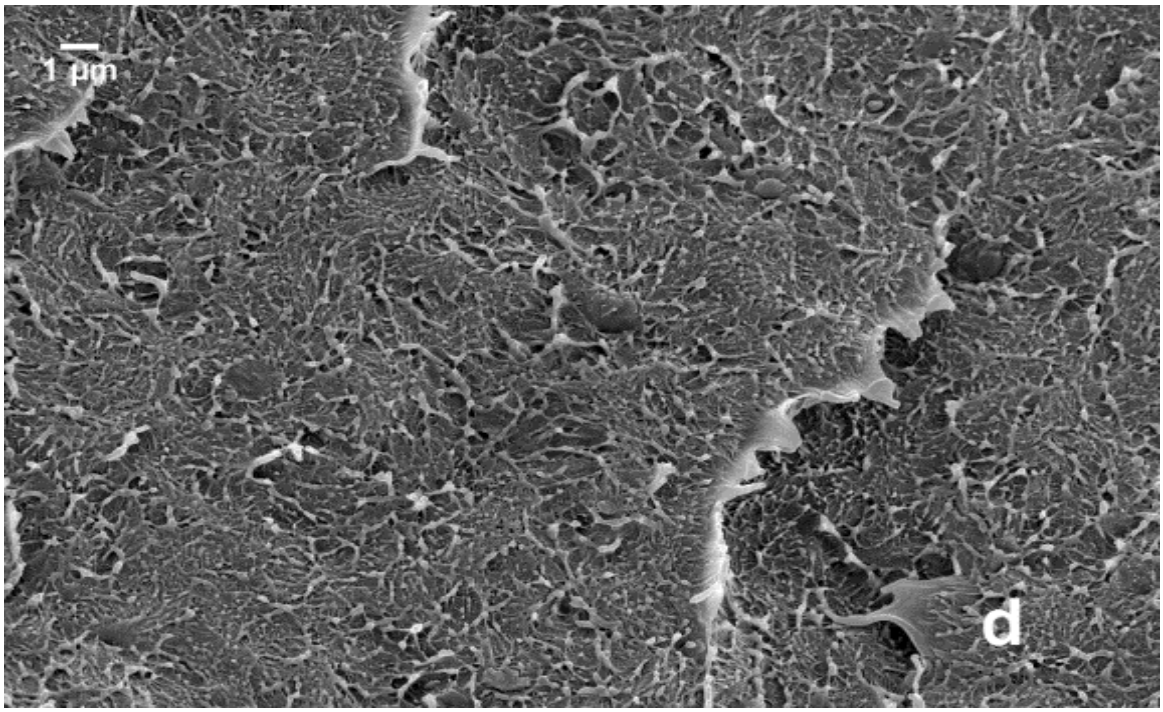
1 µm
d

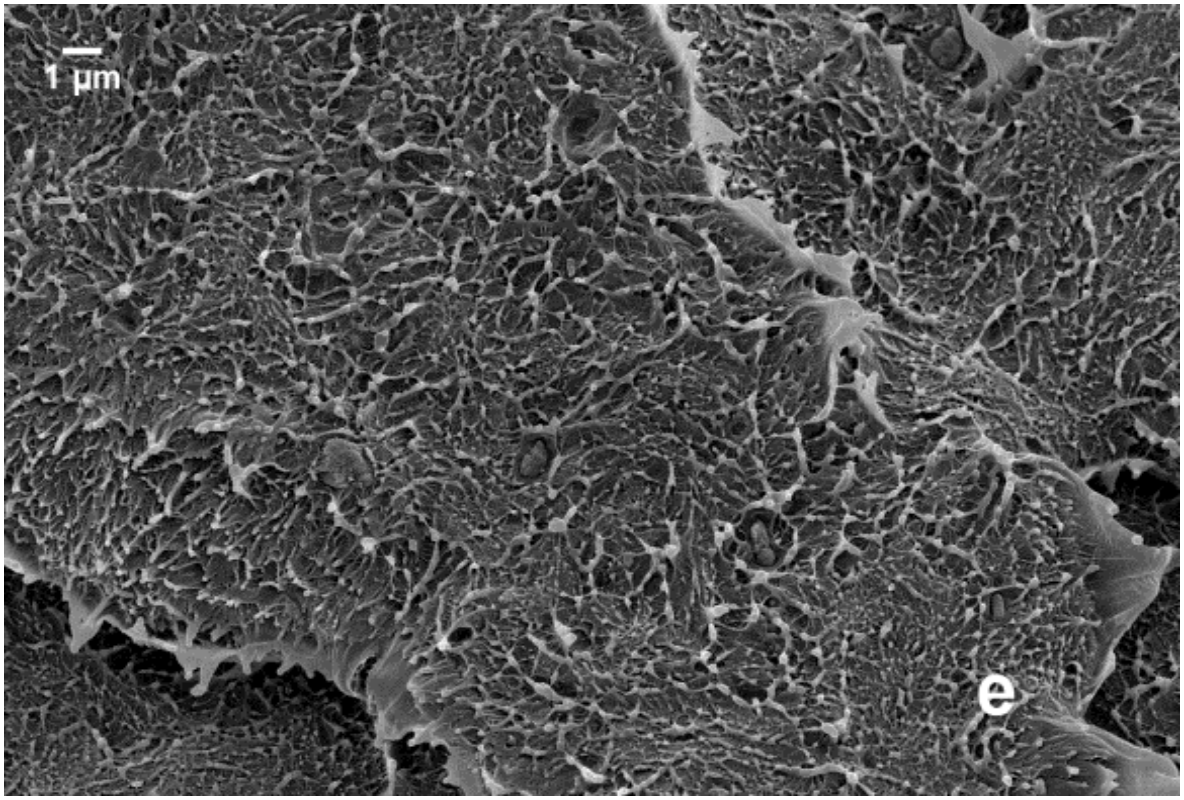

Fig. 4.14: FEGSEM micrographs of cryogenic fractured surface of (a) HCB, (b) HG, (c) HM, (d) HM-24 and (e) HM-72

The average diameter of the CB agglomerate visible is approximately 330nm. The dispersion of GO is also very uniform with only few clusters of GO layers visible in the micrograph (fig 4.14-b). The dispersion of MWCNT in HDPE is not perfect at all (fig4.14-c) and there is a very high concentration of micro-scale MWCNT agglomerates present on the fractured surface. This agglomerate formation could be due to the strong interaction between the MWCNT lengthy tubes.

The picture in fig 4.14-a show more stress concentration points and hence the material should be brittle and the small plastic deformation happens around the CB particles. The dispersion for the short tubes produced by ball milling (fig 4.14-d,e) is much more uniform and there is good interface between the filler and matrix.

4.7.3: OM of HDPE carbon nanofillers nanocomposites

The dispersion of carbon based nanofillers in HDPE was also analysed by optical microscopy. The results revealed the presence of large agglomerates dispersed uniformly throughout the HDPE matrix for both HG (fig 4.15-b) and HM (fig 4.15-d) nanocomposites. The formation of micro-aggregates in these systems reveals poor dispersion and possibly poor interface between the nanofillers and the HDPE matrix. The micrograph for HCB revealed (fig 4.15-c) no such agglomerate and the individual CB particles were not even visible at very high magnification on TEM. A TEM micrograph for HCB 1.0 is also shown in (fig 4.15-f). The micrograph once again shows uniform distribution and no agglomerate formation at the nano-scale.

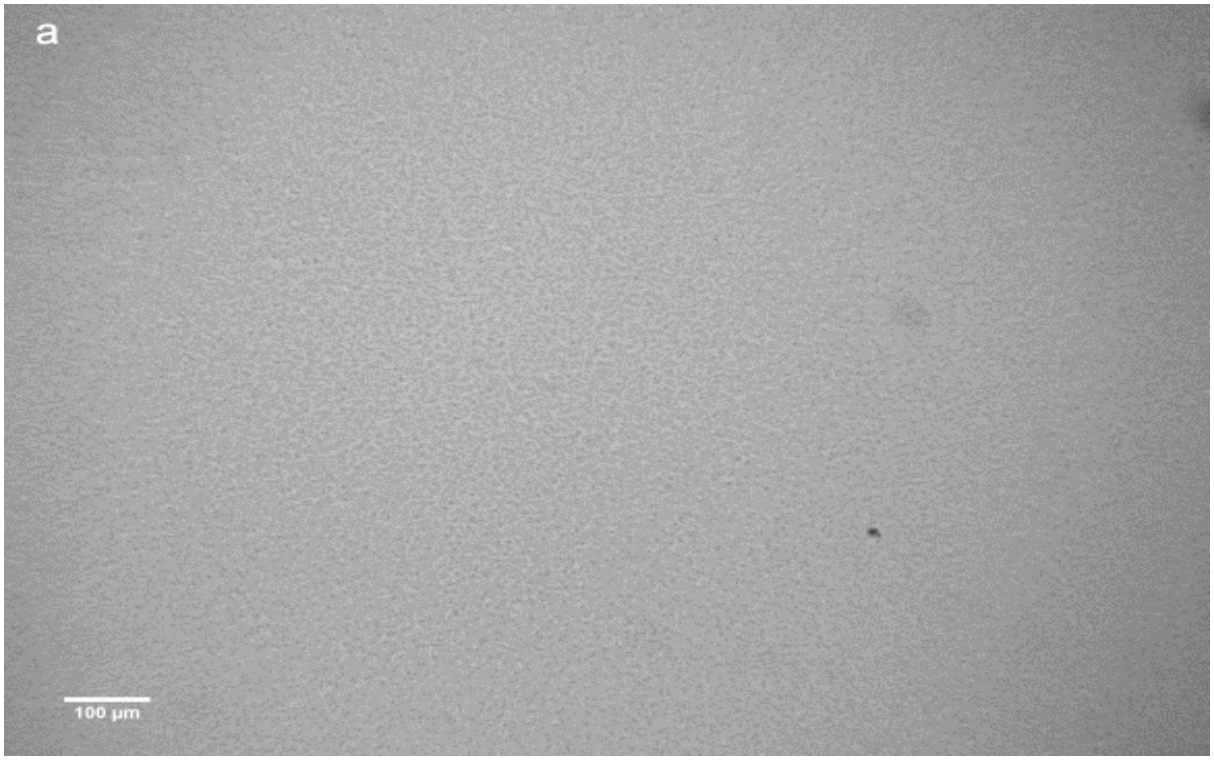
a
100 µm

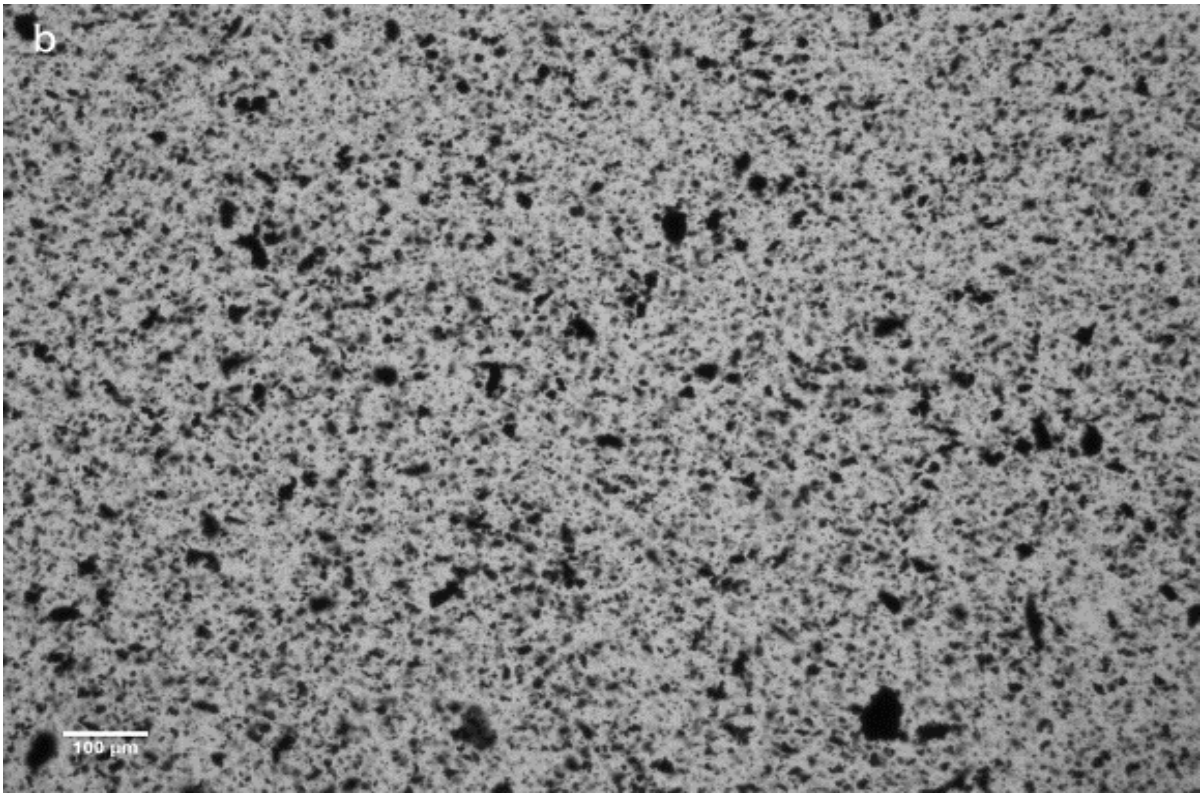
b
100 µm

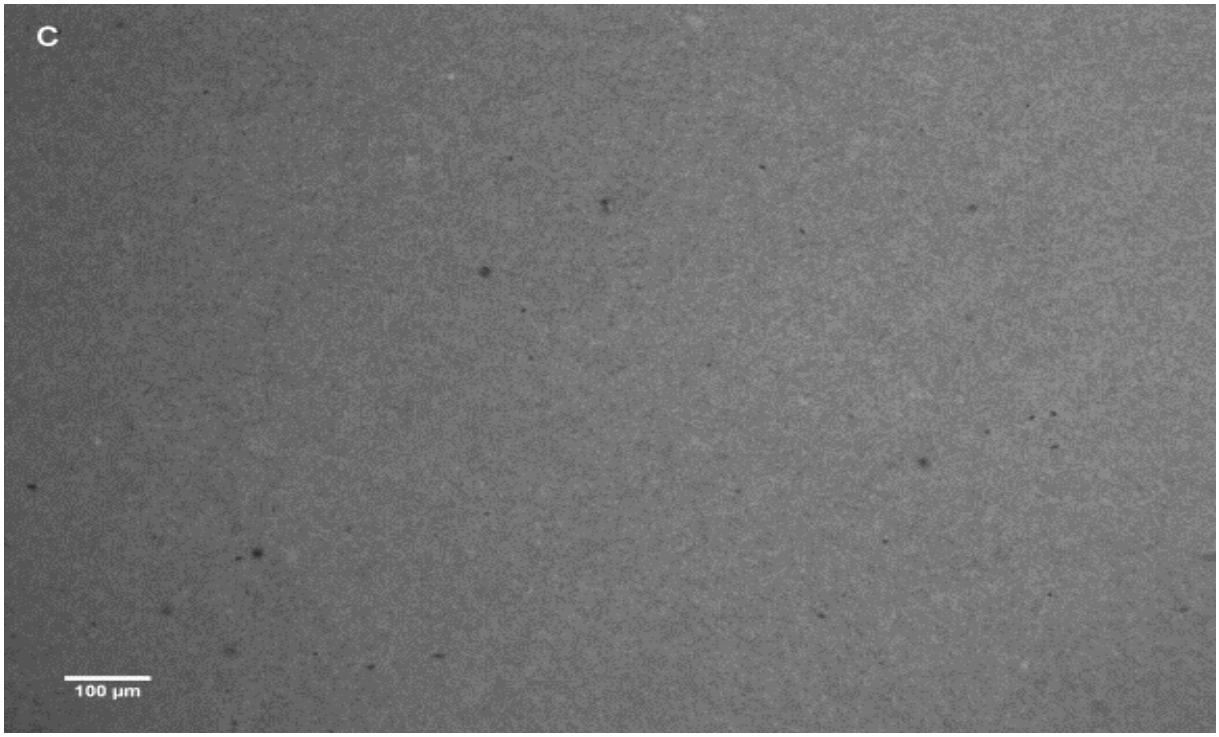
c
100 µm

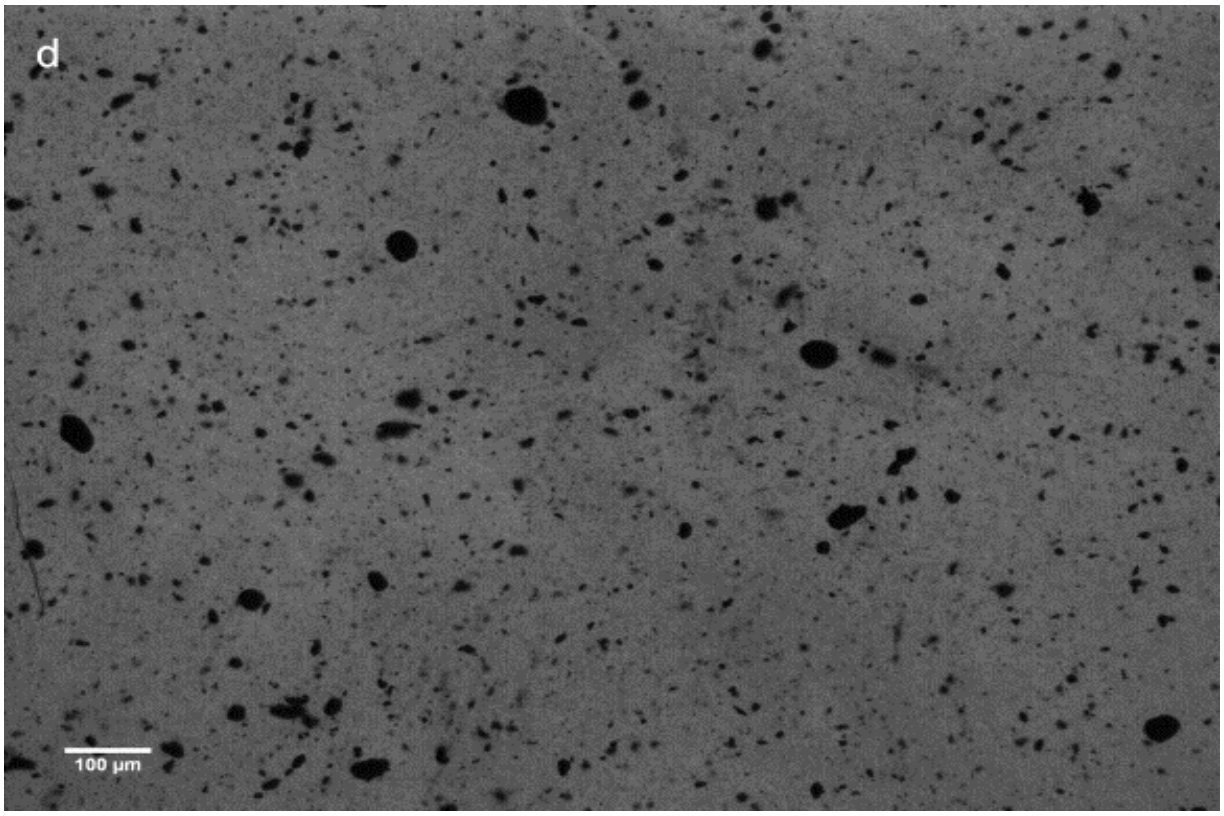
d
100 µm

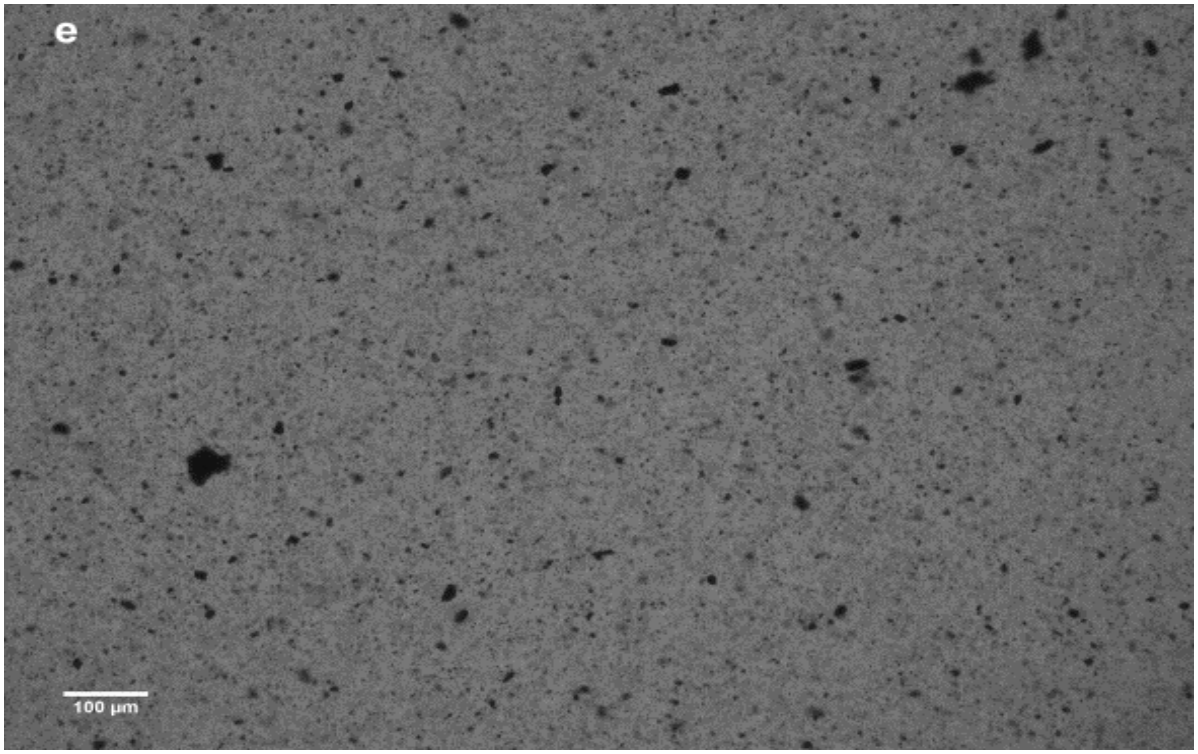
e
100 µm

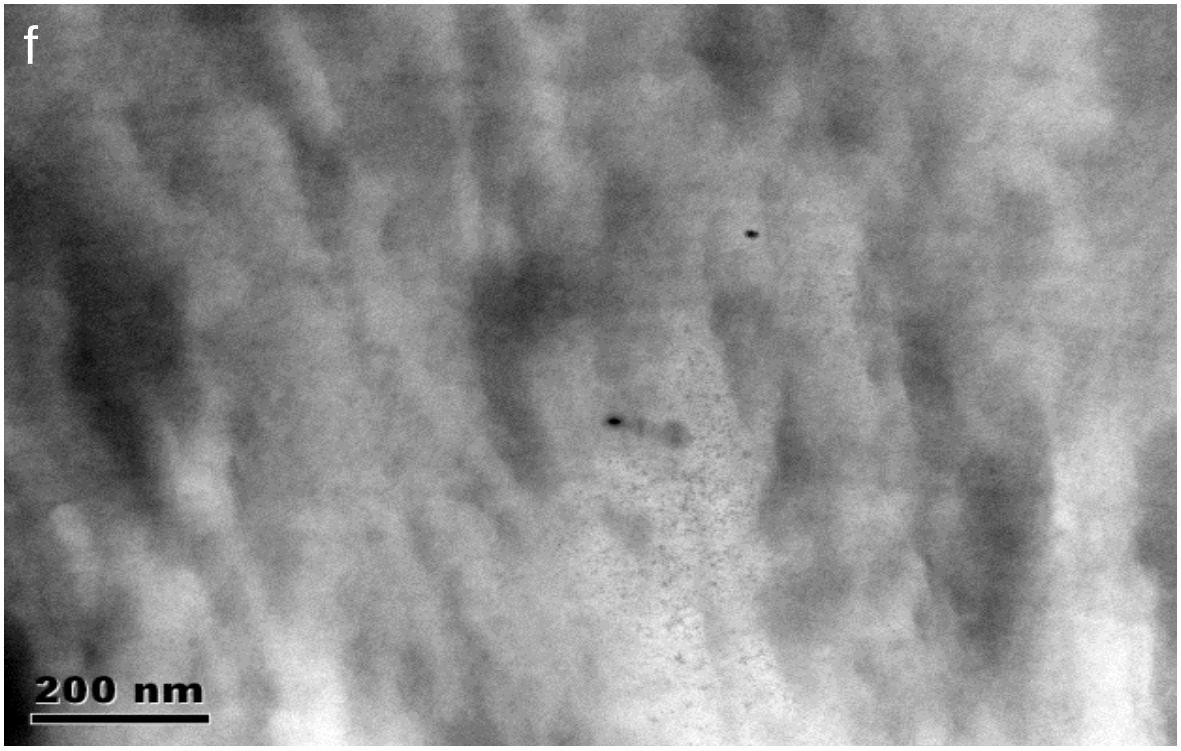
f
200 nm

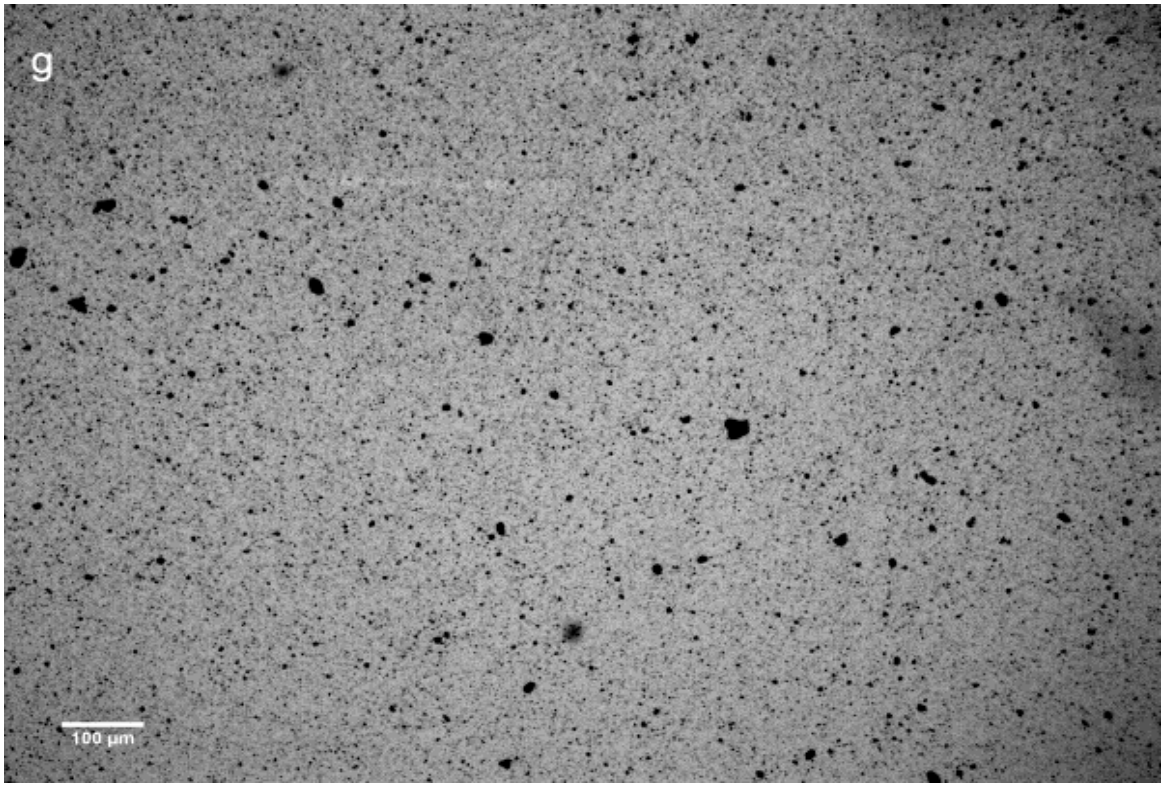

Fig. 4.15: OM micrographs detailing size and dispersion of nanofillers, (a) HDPE, (b) HG, (c) HCB, (d) HM, (e) HM-24, (g) HM-72, (f)HCB-TEM micrograph

These results indicate nano-scale uniform dispersion of CB particles in HDPE matrix which can also lead to better interface and improved mechanical properties for this system due to better load transfer. The ball milled MWCNT nanocomposites micrographs revealed (fig 4.15-e, f) a reduction in the size and density of micro-aggregates in the HDPE matrix. This reduction could be related to the reduction in the length of MWCNT by ball milling which ultimately leads to smaller agglomerates.

4.8: Morphology of Nylon12/clay nanocomposites

The final morphology of Nylon12/clay nanocomposites was characterized by using the combination of XRD, TEM and SEM analysis. The quality of clay dispersion in Nylon12 was evaluated by using both TEM and SEM analysis.

4.8.1: XRD of Nylon12-kaolin clay nanocomposites

Fig 4.16 and 4.17 shows the low 2θ region of the diffraction patterns of nylon 12/BLX and nylon 12/BHX nanocomposites. The diffractograms reveals the same intensity peak at angle 12.4^{o} for both BLX and BHX clay nanocomposites. The basal spacing results for BHX and BLX clay nanocomposites with Nylon12 are shown in table 4.5. The results once again show no significant change in the 2θ at distinct diffraction peak and hence the d-spacing calculated remains almost the same as that of pure BHX and BLX clay.

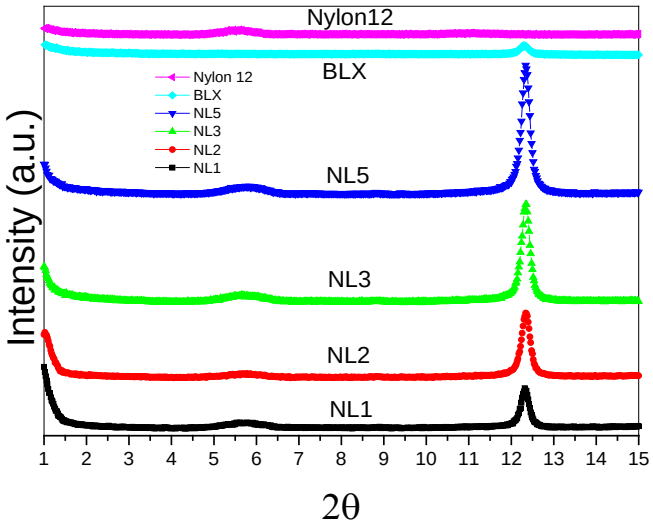

Fig. 4.16: XRD patterns of Nylon12, BLX clay and their nanocomposites

In comparison to polyolefins, nylons have the ability to interact with the clay by hydrogen bonding so it was thought it might be able to increase the basal spacing by either retaining the ordered platelet structure (intercalate) or disrupting them (exfoliate), but no such morphology was observed in nylon nanocomposites.

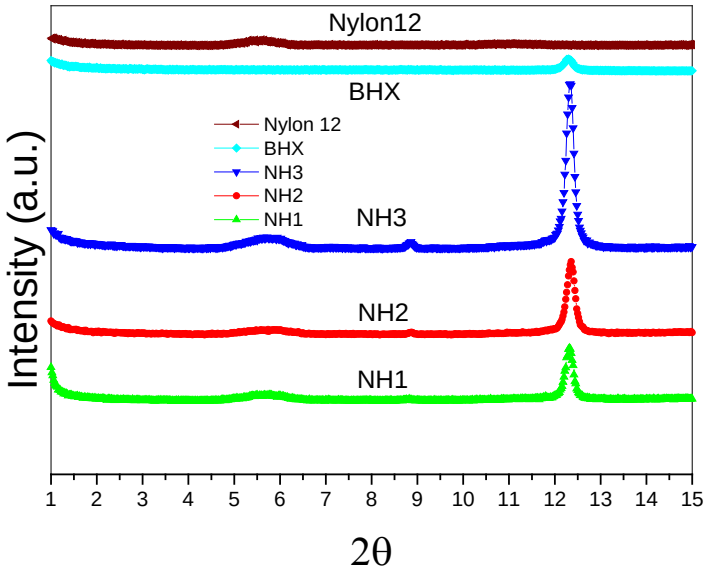

Fig. 4.17: XRD patterns of Nylon12, BHX clay and their nanocomposites

Table 4.5: Basal spacing results for Nylon12 nanocomposites with BHX and BLX clay

Sample	2θ at distinct diffraction peak	d-spacing (d1)/nm
NH1	12.32	1.437
NH2	12.36	1.432
NH3	12.34	1.435
NL1	12.32	1.437
NL2	12.34	1.435
NL3	12.36	1.432
NL5	12.36	1.432

4.8.2: SEM analysis of Nylon12-kaolin clay nanocomposites

The effect of pre-blending and melt compounding on the dispersion of BHX and BLX clay in Nylon12 matrix was examined by SEM analysis. Fig 4.18(a-f) shows the SEM micrographs of cyrofractured specimens of Nylon12/BHX and BLX clay fractured specimens.

The SEM micrographs of all the specimens show no agglomerate formation and generally display nanoclay being distributed uniformly throughout the matrix. The clay tactoids that are still embedded in Nylon12 matrix even after the fracture showing good adhesion and some level of physical interaction between the filler and matrix.

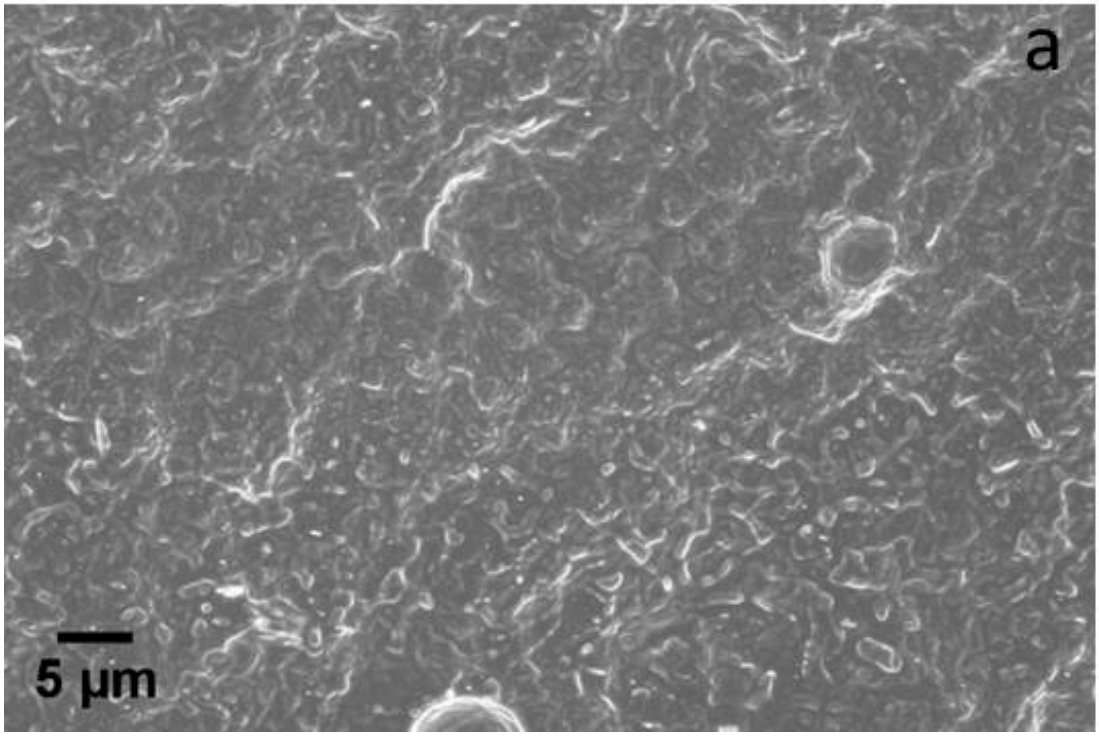

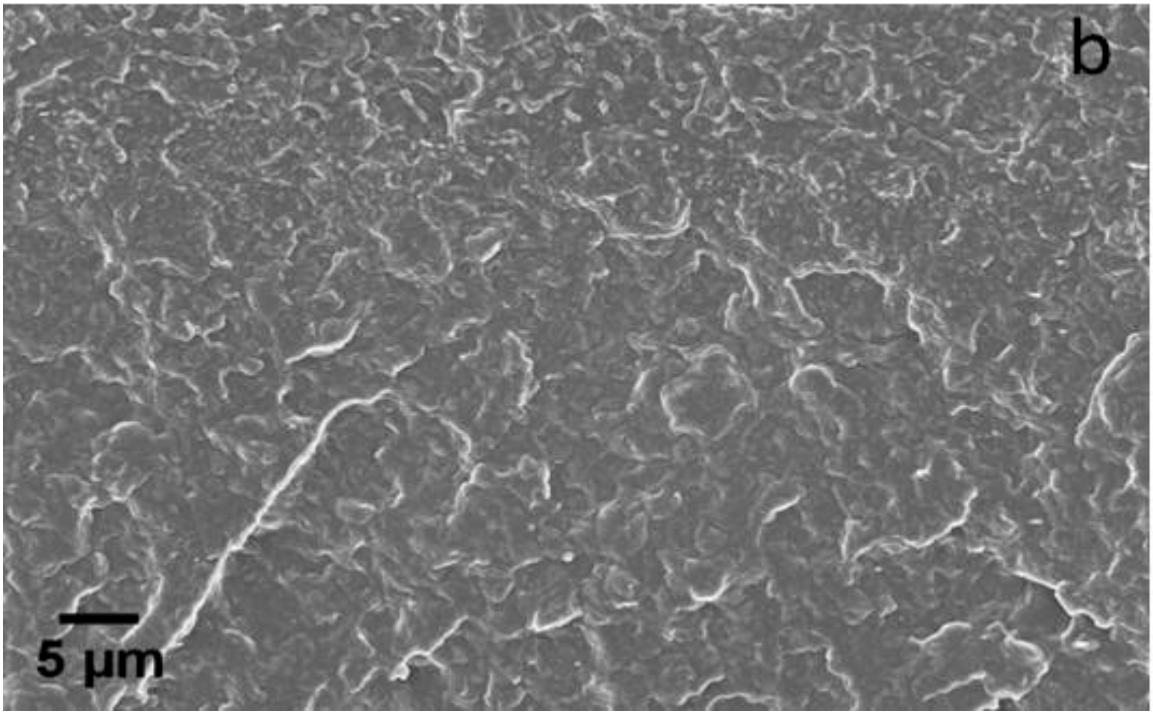
b
5 µm

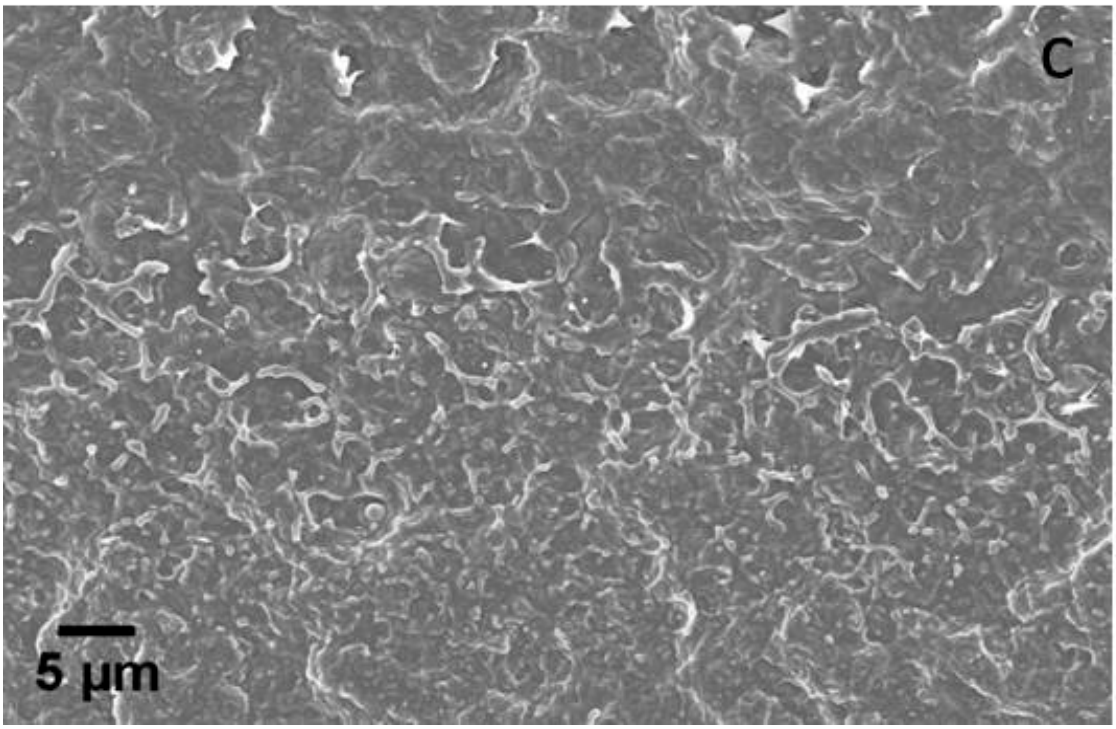
c
5 µm

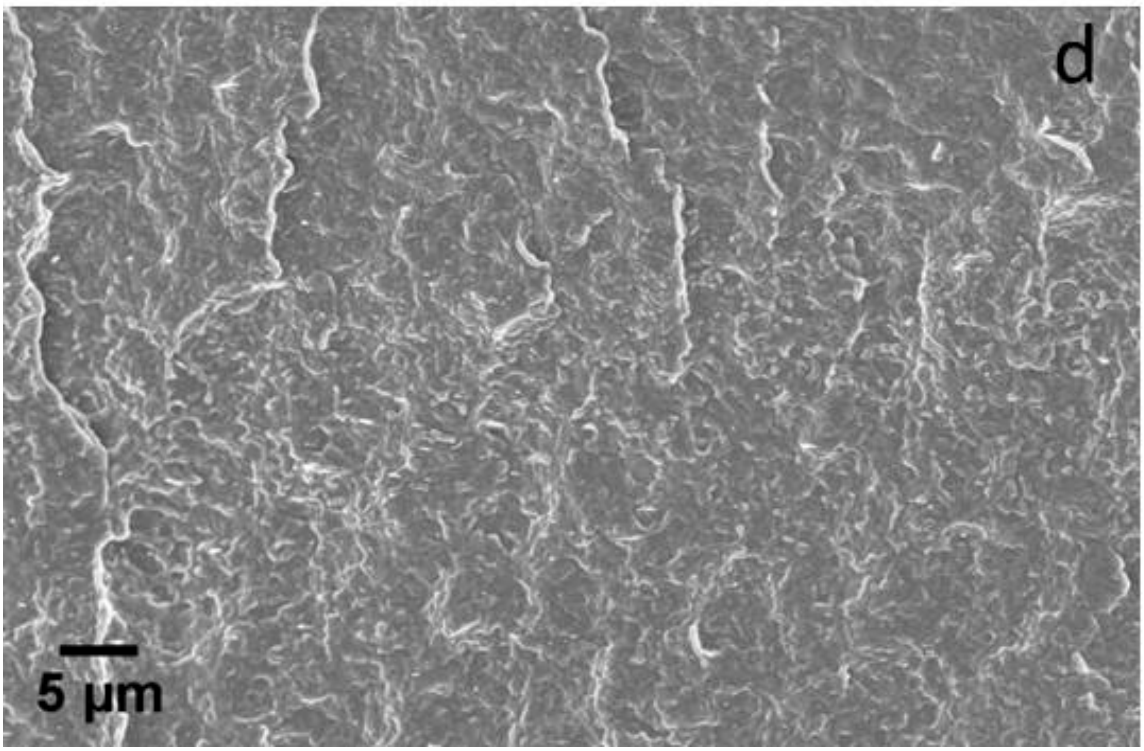
d
5 µm

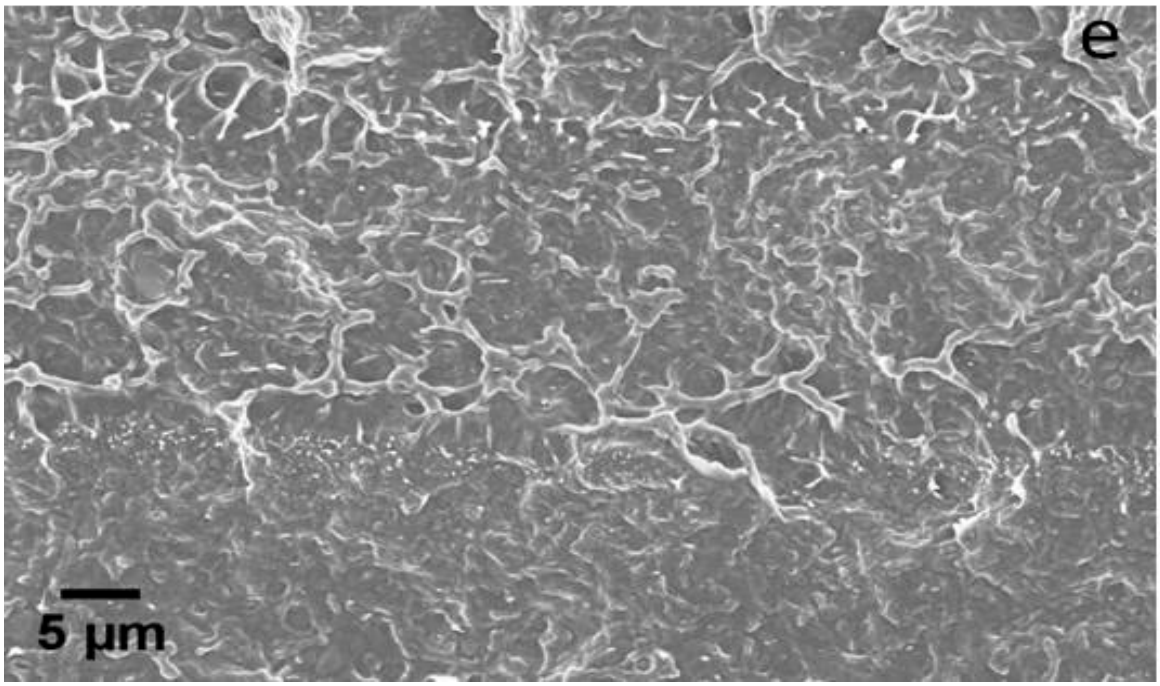
e
5 µm

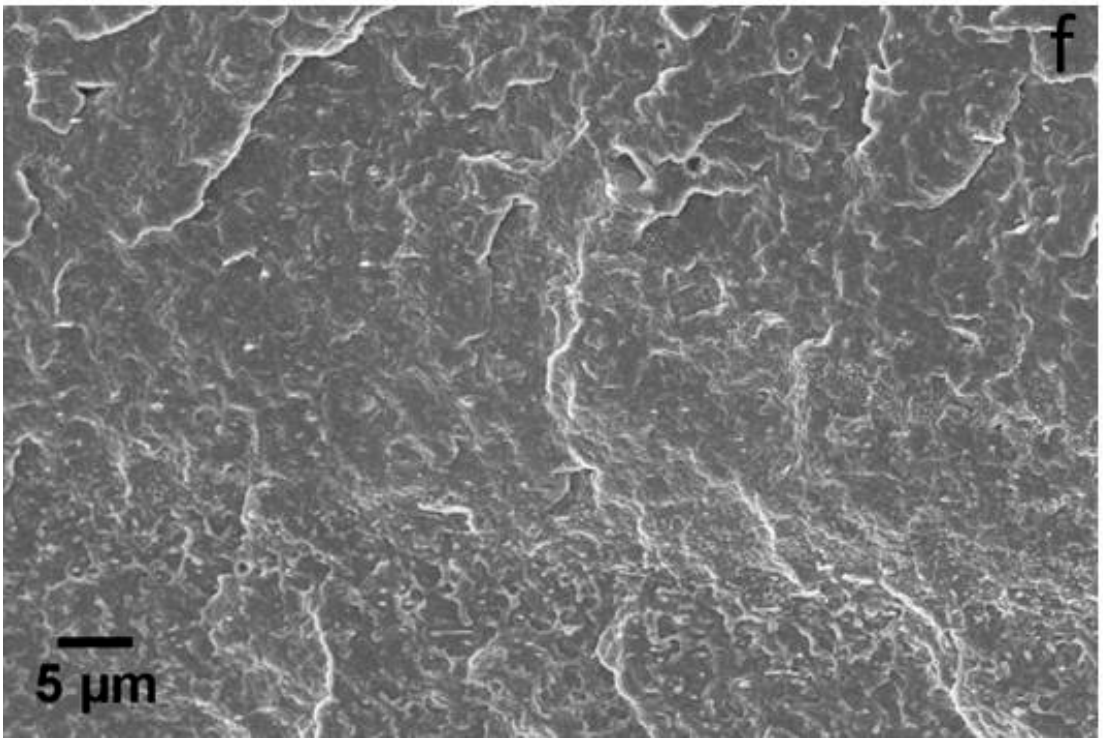

Fig.4.18: SEM micrographs of cyrofractured specimens of Nylon12/BHX and BLX clay nanocomposites. NH1 (a), NL1 (b), NH3 (c), NL3 (d), NH5 (e) and NL5 (f)

Along with clay dispersion, the fractured surface analysis by SEM can also provide information on the failure mechanism which can then be correlated to the actual failure mechanism demonstrated by the material during tensile analysis. Usually the specimens for SEM analysis are dipped in liquid nitrogen for producing a fractured surface but because of its amorphous and glassy nature, the SEM specimens were fractured directly by using a hammer. Hence in this case the nature of fracture will be true representative of the failure mechanism of Nylon12 nanocomposites. The fractured surfaces of Nylon12 and its nanocomposites with both kaolin clay exhibits a brittle mode of fracture due to the absence of any plastic deformation and a flat surface with no fibrils pulled out of the surface.

4.8.3: TEM analysis of Nylon12-kaolin clay nanocomposites

Fig. 4.19 shows the TEM micrographs of Nylon12-BHX and Nylon12-BLX nanocomposites. The TEM micrographs reveal a microcomposite based morphology for all the specimens. THE TEM results for Nylon12 based specimens are in line with the XRD results which also indicated the absence of exfoliation or intercalation.

Although all the specimens indicated tactoids and particle based morphology but in case of NH3.0 as shown in fig 4.19-b some of the individual clay layers were also visible. This indicates a mixed morphology of microcomposites and a low degree of intercalated or exfoliated specimens. The analysis of TEM micrographs by ImageJ software revealed that most of the tactoids have thickness less than 100nm, which qualifies these materials to de donated as nanocomposites.

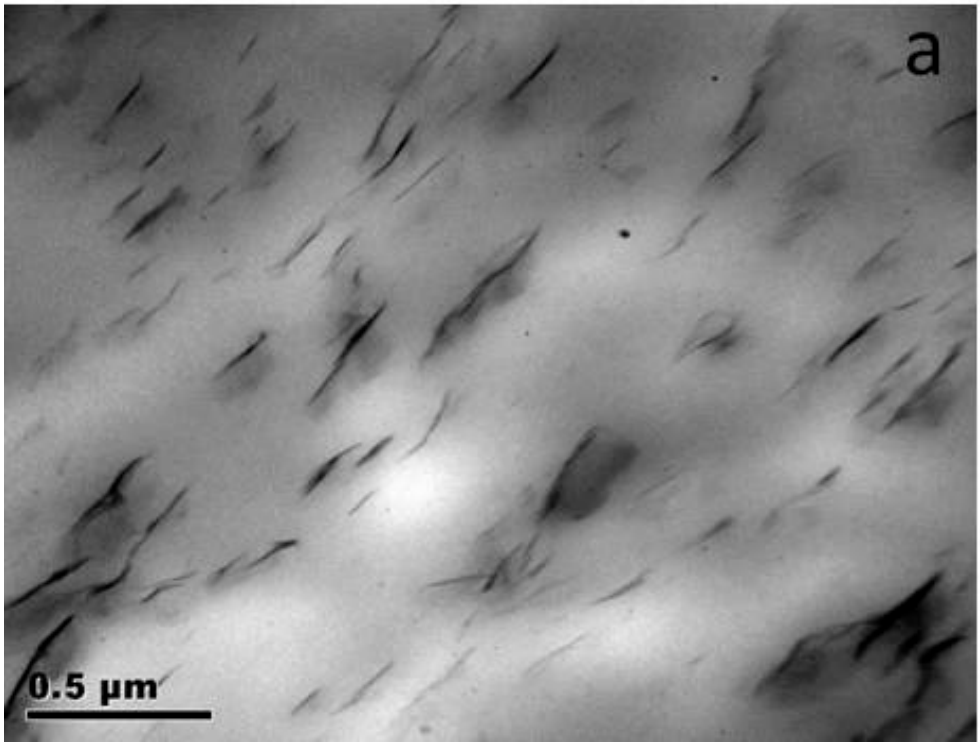
a
0.5 µm

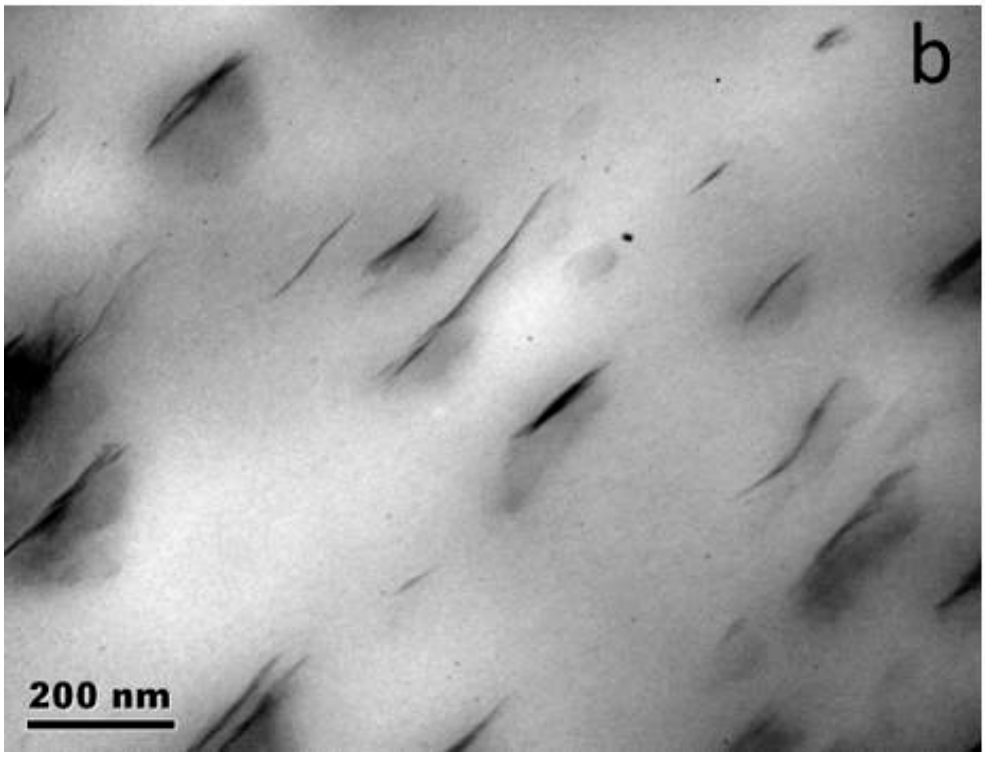
b
200 nm

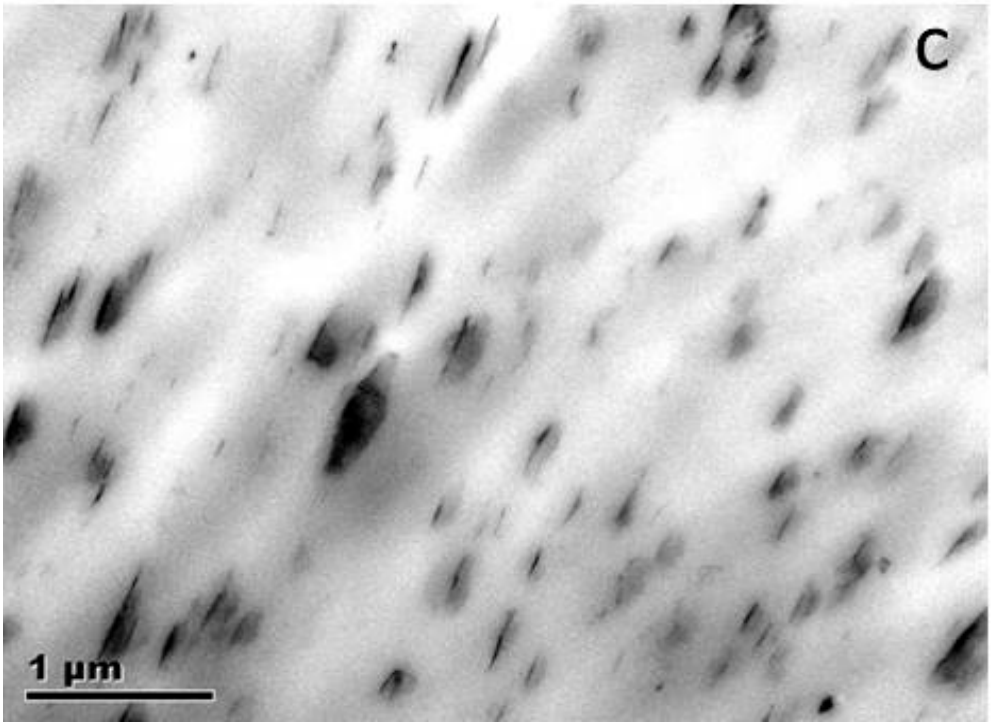
c
1 µm

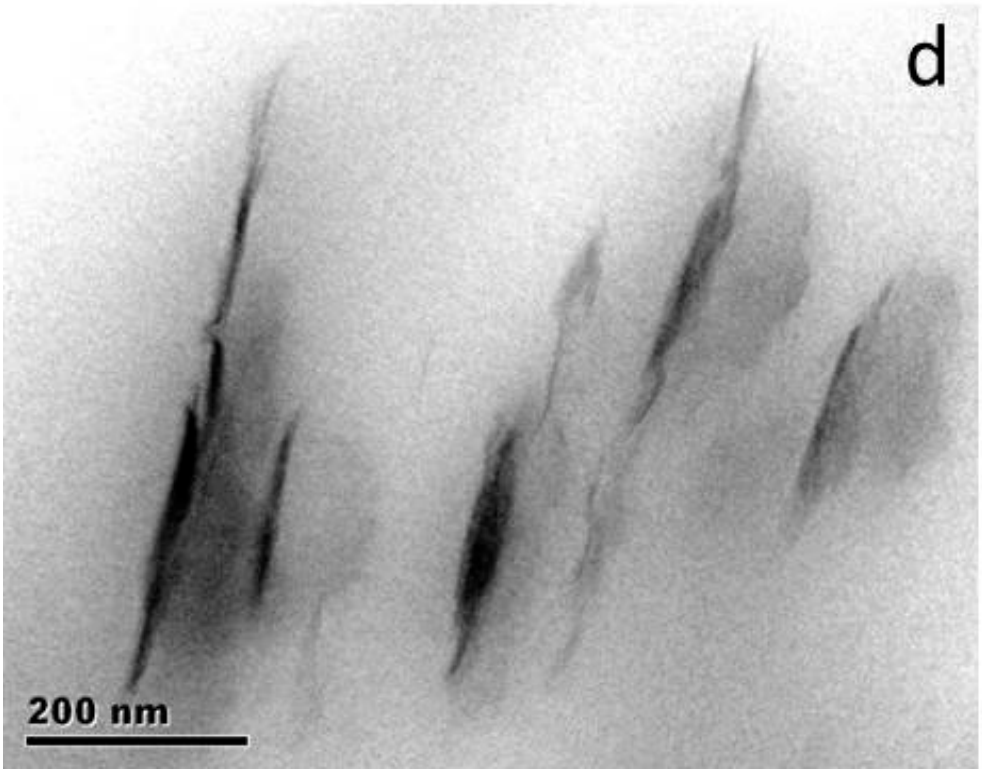
d
200 nm

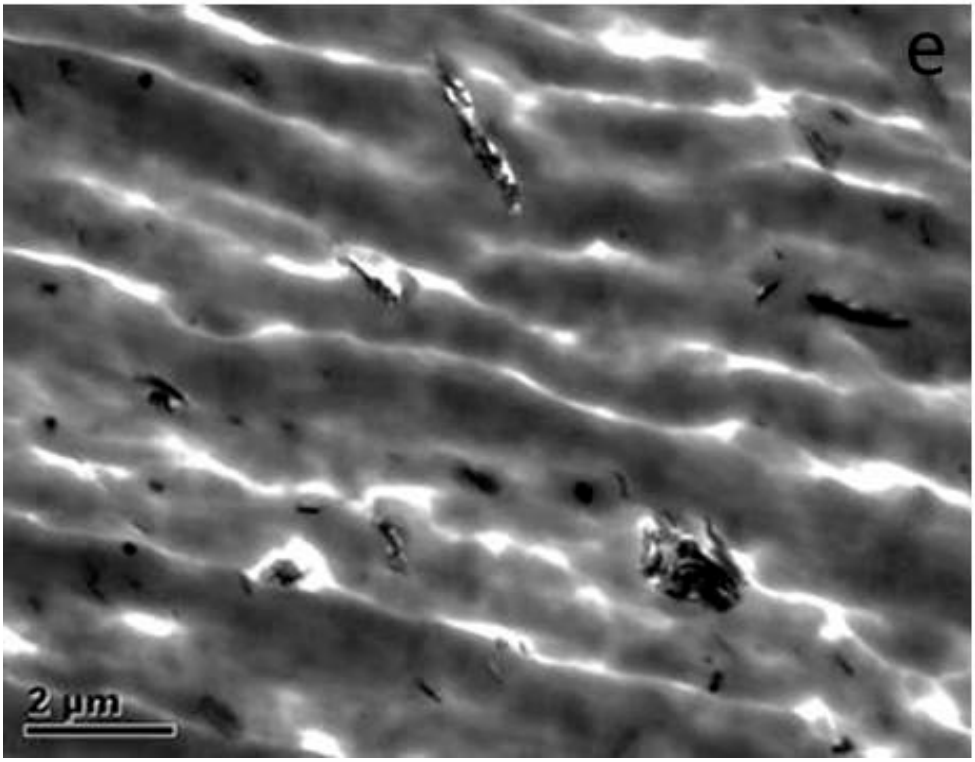
e
2 µm

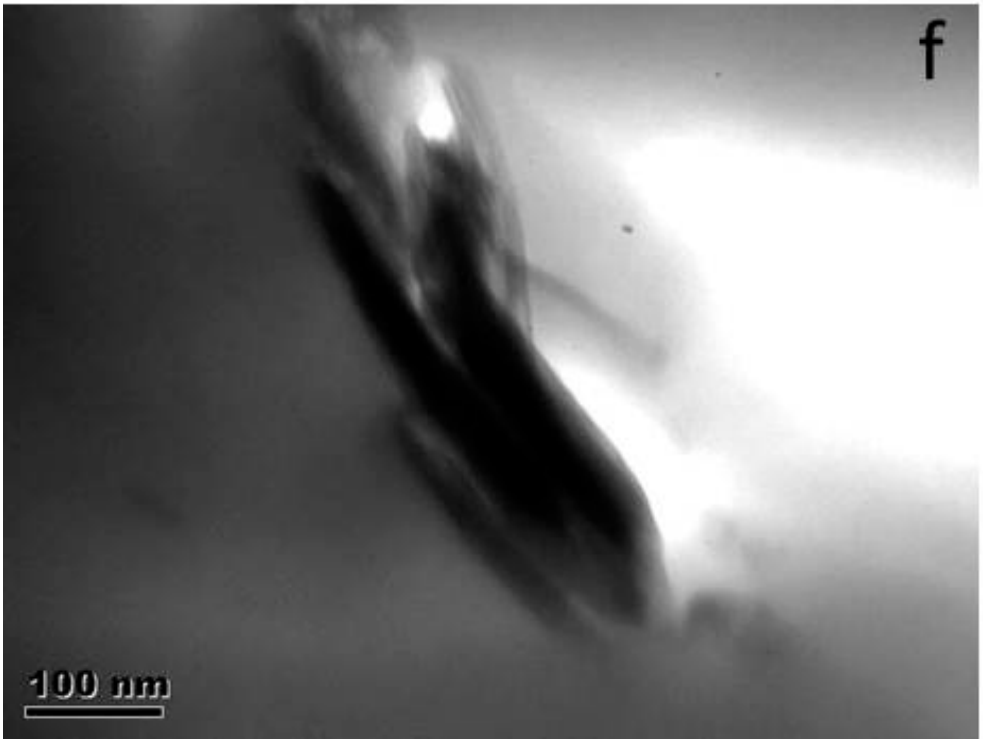
f
100 nm

]

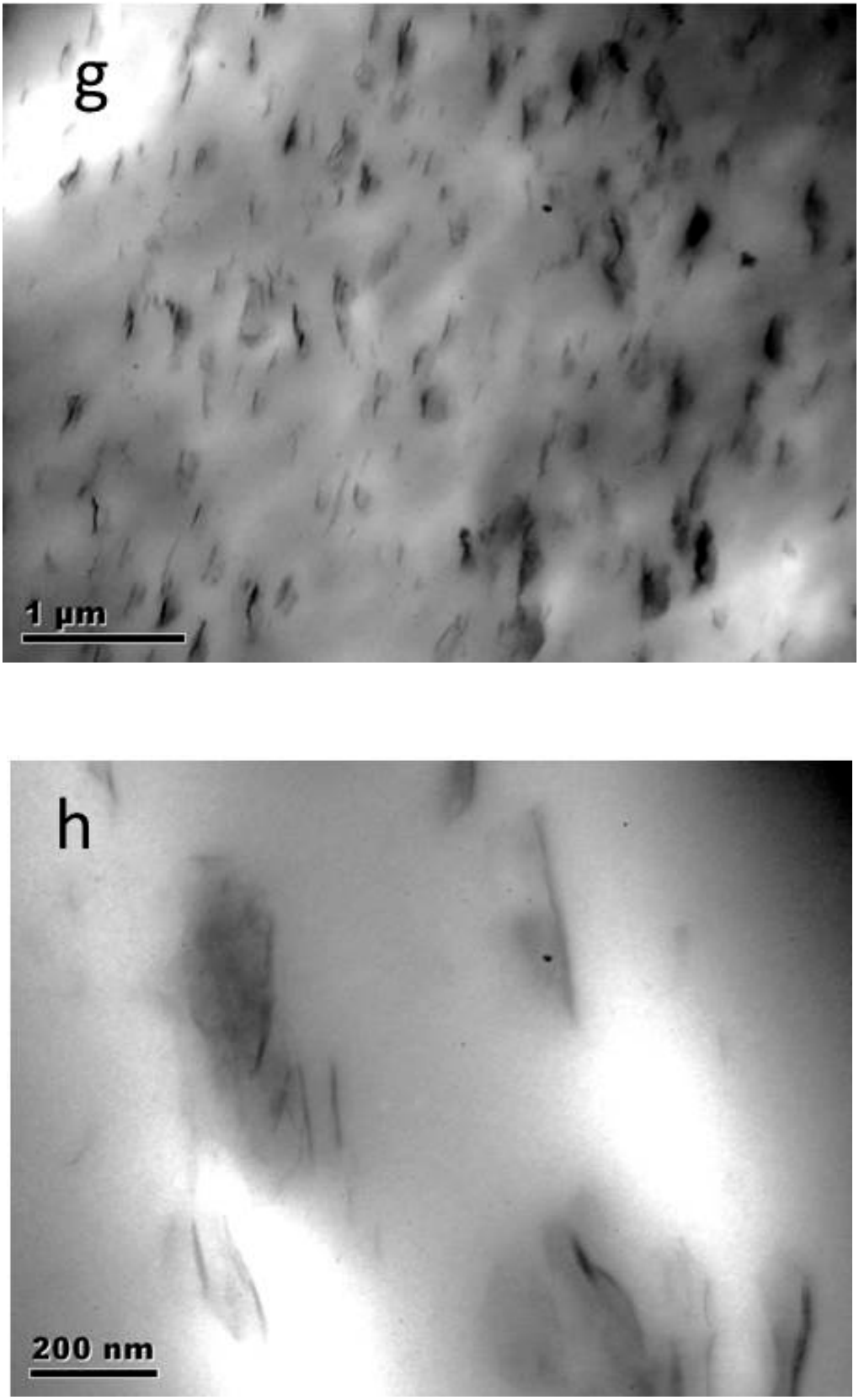

Fig. 4.19: TEM micrographs at two resolutions for Nylon12 and its nanocomposites with BHX, BLX-kaolin clay (a,b) NH3.0, (c,d) NH5.0, (e,f) NL1.0, (g,h) NL3.0

4.9: Morphology of LLDPE/clay nanocomposites

4.9.1: XRD analysis of LLDPE/kaolin clay nanocomposites

The XRD diffractograms for LLDPE, BHX clay and their nanocomposites in the range of 2θ = 1-30^{o} are shown in fig 4.20. The patterns reveal the 110 (21.4^{o}) and 200 (24.2^{o}) diffraction peaks of LLDPE in pure specimen and in all the nanocomposites. The nanocomposites also contain the diffraction peaks for BHX clay which remain at almost the same position as for pure BHX which just like HDPE and Nylon12, suggests no exfoliation or intercalation for LLDPE based nanocomposites.

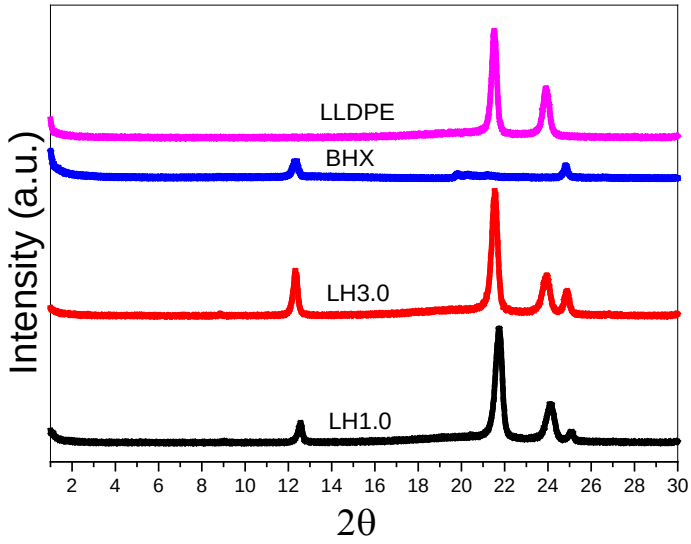

Fig. 4.20: XRD patterns of LLDPE, BHX and their nanocomposites

4.9.2: SEM analysis of LLDPE/kaolin clay nanocomposites

The morphology of fractured surfaces of LLDPE and its nanocomposites with BHX and BLX clay, as revealed by SEM analysis are shown in fig 4.21.

Fig 4.21(a) shows typical fracture morphology of generally low ductile LLDPE matrix fractured at low temperature using liquid nitrogen. The SEM micrographs of cyrofractured surfaces of LL5 and LH5 are shown in fig 4.21(b-c) respectively. The

micrographs for all the nanocomposites do not reveal any distinct clay agglomerate or tactoids even at the high magnifications of SEM analysis.

The SEM micrographs for high weight percentage specimens (LL10.0 and LH10.0) as shown in fig 4.21(d-e) reveal brittle fracture behaviour and as evident in the micrographs that such a behaviour is due to the formation of microvoids distributed throughout the fractured surface. The microstructures are formed in high weight percentage filler base composites and they originate usually during the debonding of the clay tactoids from the matrix. The microvoids are formed around areas of non-homogeneity and they can merge together to produce cracks which can initiate embrittlement at lower levels of applied load. Kin et. al. [25] has reported that these microvoids are also formed due to the deformation of the stacked clay layers when the external load is applied upon them. The deformation of the clay stacks causes splitting or sliding of the clay bundles from the bulk stack which can lead to debonding from matrix and hence result in a brittle fracture.

4.9.3: OM analysis of LLDPE/kaolin clay nanocomposites

Transmission electron microscopy can be used for determining the morphology of the nanocomposites and the distribution of clay in the polymer matrix, but the final micrographs only shows the details in a very small area of the whole sample. In order to visualize the distribution and the orientation of clay in the polymer matrix, polarized optical microscopy is often utilized. The magnification used is at the micrometre scale and the aggregates of clay and their distribution in the nanocomposite can be observed by this technique. The optical microscopy images for LLDPE and its nanocomposites are shown in fig 4.22.

The samples were prepared in the form of thin films by melt pressing the sample between two glass surfaces. The thin films when analysed by polarized optical microscopy indicated good dispersion of both BLX and BHX in LLDPE. The samples analysed by OM revealed uniform dispersion and distribution of both BHX and BLX clay particles throughout the LLDPE matrix. Apparently, there are some small aggregates of clay in the nanocomposites and their density increases with the increase in wt % of clay in LLDPE. These aggregates are also uniformly dispersed in the matrix.

Conclusion:

In this chapter a number of techniques including wide angle X-ray diffraction (XRD), transmission electron microscopy (TEM), scanning electron microscopy (SEM) and optical microscopy (OM), were employed to study microstructure and morphology of these nanocomposites. The TEM analysis of MWCNT and its ball milled samples showed a reduction in the length of MWCNT and also a reduction in their tendency to form agglomerate. The sedimentation analysis of the fillers indicated particle size dependency on the dispersion characteristics of the fillers. Although XRD results showed there was no intercalation or exfoliation in case of both kaolin clay nanocomposites but the combination of OM, SEM and TEM indicated nano-level dispersion (20-80 nm thickness of layers) and parallel orientation of kaolin clay layers in the matrix. On the other hand Na-MMT clay samples showed exfoliation in XRD but microscopy revealed large agglomerate formation for high weight percentage specimens in their nanocomposites with HDPE and LLDPE. Apart from MWCNT, the dispersion of carbon based nanofillers inside HDPE was acceptable and the dispersability of MWCNT was improved by the reducing their lengths by ball milling.

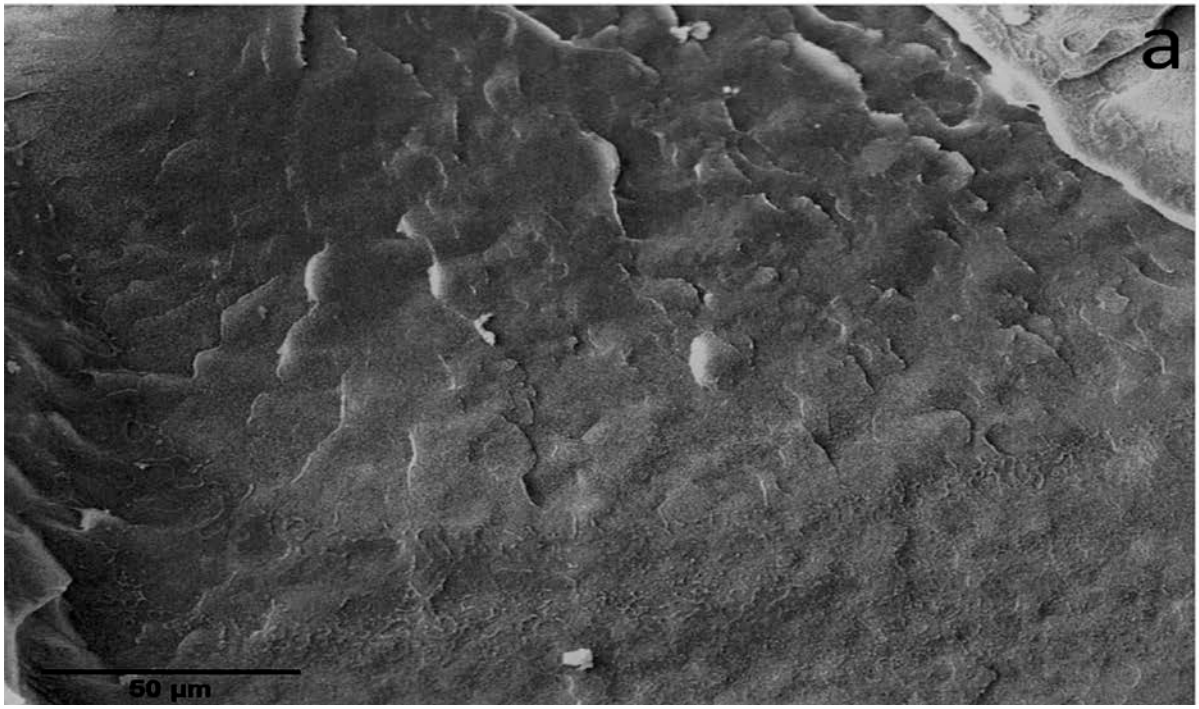
a
50 µm

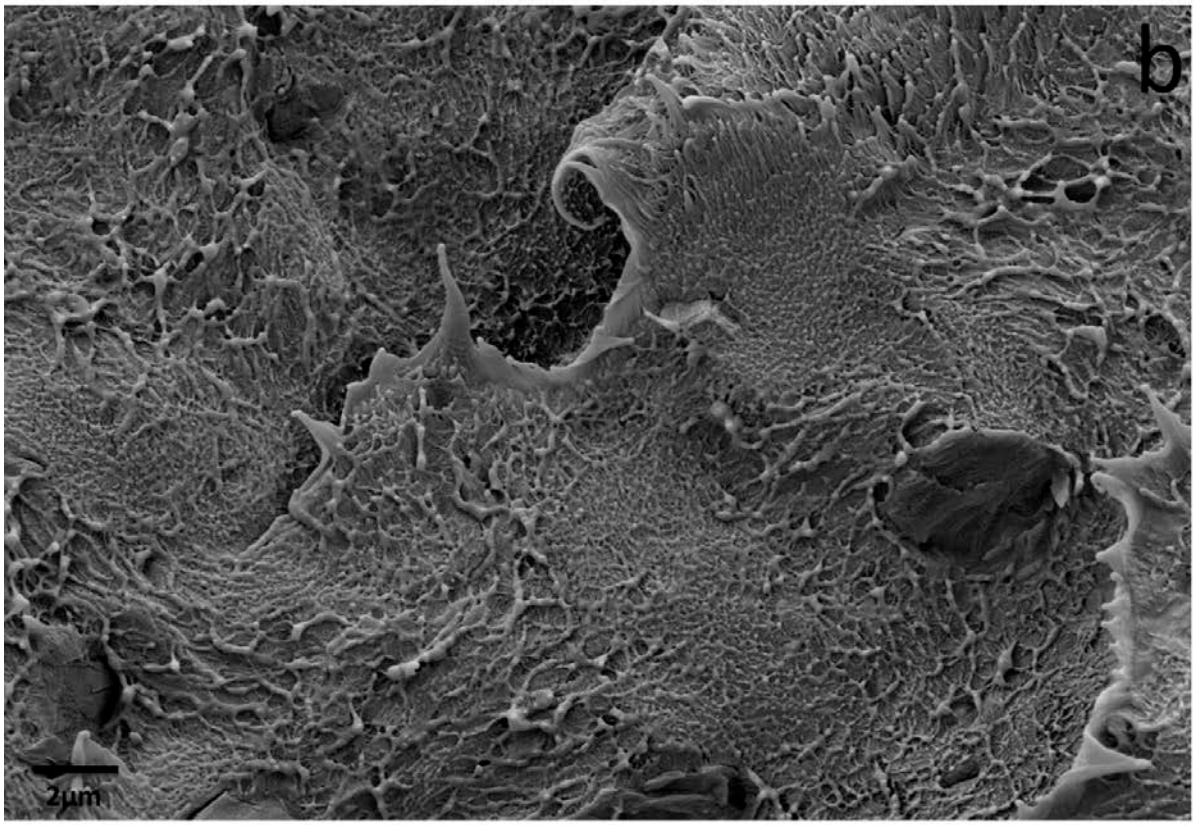
b
2µm

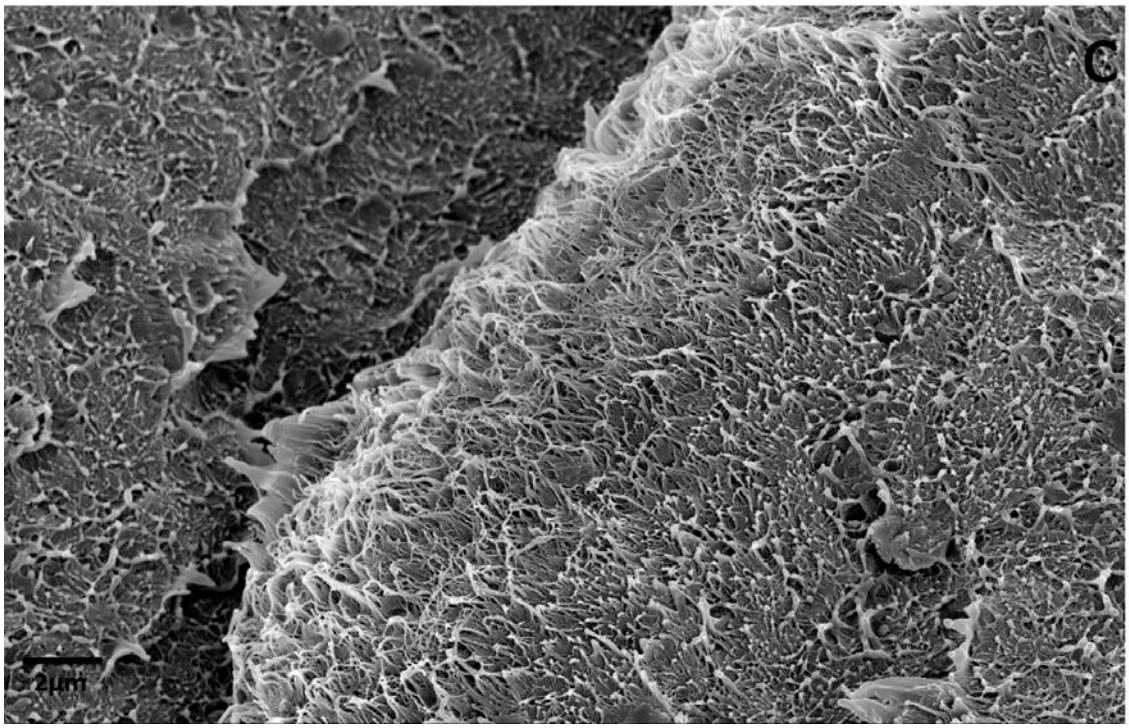
c
2µm

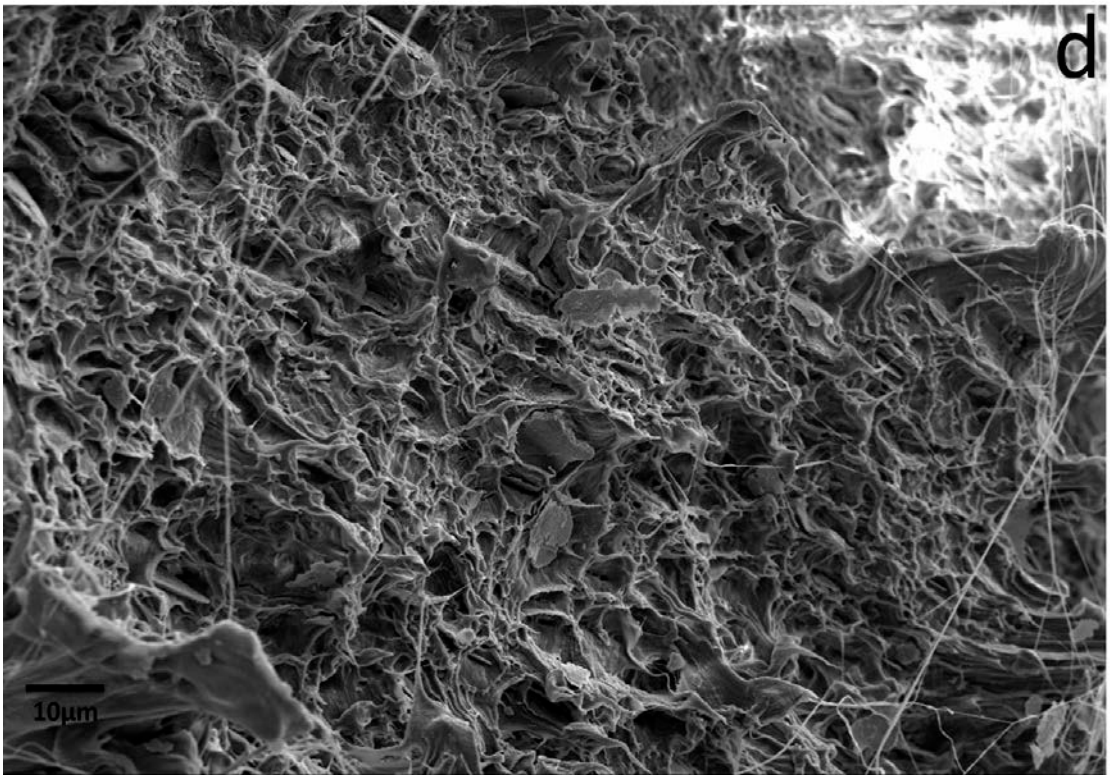
d
10µm

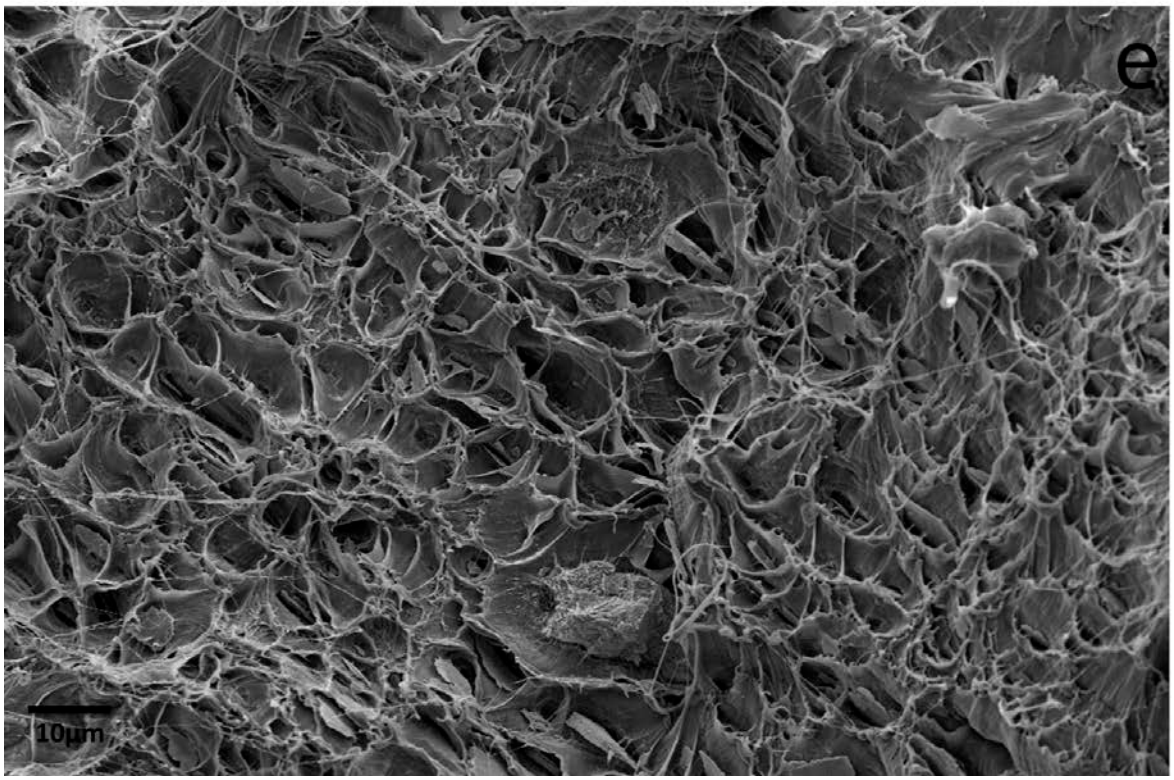

Fig. 4.21: SEM micrographs of LLDPE and its nanocomposites with BHX and BLX clay. (a) LLDPE, (b) LH3.0, (c) LL3.0, (d)LH10.0 and (e) LL10.0

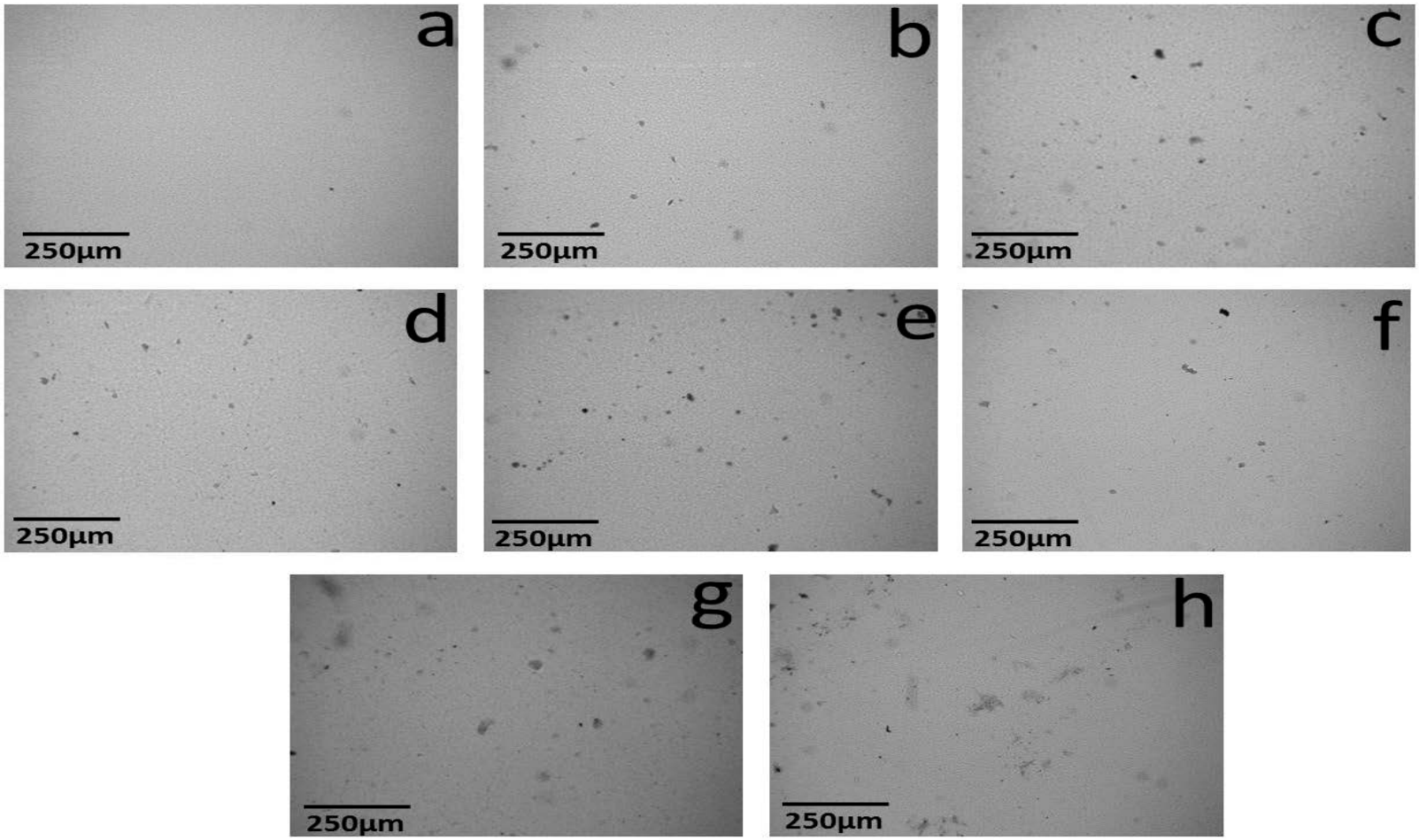

Fig. 4.22: OM micrographs of LLDPE and its nanocomposites with BHX and BLX clay. (a) LLDPE, (b) LH1.0, (c) LH3.0, (d)LH5.0, (e) LH10.0, (f) LL1.0, (g) LL3.0 and (h) LL5

References

1. Mittal, V. Barrier properties of polymer clay nanocomposites; Nova Science Publishers, Inc. New York, 2010.
2. Mittal, V. Mechanical and Gas Permeation Properties of Compatibilized Polypropylene – Layered Silicate Nanocomposites. J. Appl. Polym. Sci. 2007, 107, 1350–1361.
3. Morgan, A. B.; Harris, J. D. Exfoliated polystyrene-clay nanocomposites synthesized by solvent blending with sonication. Polymer . 2004, 45, 8695–8703.
4. Tarawneh, M. A.; Ahmad, S. H. ; Rasid, R. ; Yahya S.Y.;Noum, S.Y.E. The enhancement of properties of TPNR/clay nanocomposites using ultrasonic treatment. Journal of Reinforced Plastics and Composites, 2011, 30, 524-532.
5. Koo, J. Polymer nanocomposites: processing, characterization, and applications, chapter 1, 2006.
6. Dazhu, C.; Haiyang, Y.; Pingsheng, H.; Weian, Z. Rheological and extrusion behaviour of intercalated high-impact polystyrene/organomontmorillonite nanocomposites. Compos. Sci. Technol. 2005, 65, 1593–1600.
7. Reddy, C. S.; Ratna, D.; Das, C. K. Polyethylene nanocomposites by gas-phase polymerization of ethylene in the presence of a nanosilica-supported zirconocene catalyst system. 2008, 291, 282–291.
8. Privalko, V. P.; Calleja, F. J. B. Composition-dependent properties of polyethylene / Kaolin composites Part II Thermoelastic behaviour of blow-moulded samples. 1999, 4, 497–508.

9. Privalko, V. P.; Sukhorukov, D. I.; Privalko, E. G.; Walter, R.; Friedrich, K.; Balta, F. J. Composition-Dependent Properties of Polyethylene / Kaolin Composites . III . Thermoelastic Behavior of Injection-. 1999, 1041–1048.
10. Liu, X. Effects of modified kaolin on the crystallization property of PP/Kaolin nanocomposites. Sci. China Ser. B 2005, 48, 326.
11. Villanueva, M. P.; Cabedo, L.; Giménez, E.; Lagarón, J. M.; Coates, P. D.; Kelly, a. L. Study of the dispersion of nanoclays in a LDPE matrix using microscopy and in-process ultrasonic monitoring. Polym. Test. 2009, 28, 277–287.
12. Villanueva, M. P.; Cabedo, L.; Lagaro´n, J. M.; Gime´nez, E. Comparative Study of Nanocomposites of Polyolefin Compatibilizers Containing Kaolinite and Montmorillonite Organoclays. J. Appl. Polym. Sci. 2010, 115, 1325–1335.

CHAPTER5: RHEOLOGICAL CHARACTERIZATION OF POLYETHYLENE BASED NANOCOMPOSITES

5.1: Introduction

The escalating amounts of energy costs used for producing plastic products throughout the world have resulted in creating serious environmental pollution such as greenhouse emissions. As a result the awareness to re-use or recycle the plastic products had grown. However, these processes have some serious limitations such as the complexity of the waste streams and high costs involved in re-use and recycling. Another route for solving such problems could be to find energy efficient processing routes which can be adopted in developed and developing countries. Based upon their applications, polymers can be classified into commodity thermoplastics, engineering polymers and functional polymers. Different grades of polyethylene (PE) are one of the major commodity thermoplastics used throughout the world because of their low cost, vast availability, easy manufacturing and major advantageous properties like chemical resistance, light weight, reasonable mechanical properties, sub-zero glass transition temperature and recyclability.

There are various grades of polyethylene available in the market such as high density polyethylene (HDPE), low density polyethylene (LDPE), linear low density polyethylene (LLDPE), ultra high molecular weight polyethylene (UHMWPE) etc. These grades have vastly different properties due to their molecular weight and chemical structure and hence they have applications in areas ranging from everyday use commodities like beverage containers to high value engineering products like bulletproof body armours, body implants etc.

In polymer processing industries PE is usually processed at temperatures 160-280^{o}C, these temperatures are much higher than the equilibrium melting point of PE

and are mainly adopted to avoid any interference of melt flow instabilities such as high die swell, shark skin etc. As stated in chapter 2, that one of the routes for solving the problem of processing PE grades at low temperatures without any melt flow instabilities is to employ the melt flow singularity phenomenon. One of the problems with virgin PE is that it can only have a very short window of 2-3^{o}C [1-4], to enhance that window one of the basic routes is to employ nanofillers which have been widely used to modify the rheological [5-7] properties of polymers.

The various types of nanofillers used in this thesis have already been described in detail in chapter 2 and 3. With regards to nanoclay there are various morphologies that these clays can adopt inside the polymer matrix, i.e; intercalation, exfoliation and macro-composite. In order to study the effect of these morphologies on MFS of HDPE, kaolin clay, Na-MMT clay and bentone clay are chosen as the nanofiller because of their abilities to achieve intercalation, exfoliation and macro-composite morphologies in HDPE as stated in detail in chapter 4. Also the effect of clay weight percentage and clay aspect ratio has been studied by using different quantities of BHX clay and then comparing the best result with BLX clay which has a smaller aspect ratio in comparison to BHX clay. Along with clay fillers, the effect of carbon based nanofillers with different shape and dimension on the melt flow singularity of HDPE is also studied.

5.2: Results

5.2.1: MFS of polyethylene and its nanocomposites with clay

Fig 5.1 (a-g) shows the extrusion pressure vs. temperature data recorded under dynamic cooling conditions for HDPE at different shear rates. Fig 5.1 shows that the melt flow singularity does not appear at low shear rates of 200-250s^{-1} and the extrusion pressure at these shear rates remains stable. These rates are too slow for the coil-stretch transformation to set in inside the polymer melt at the die entry region. At 200s^{-1} pressure increases steadily with the decrease in temperature, this increase in pressure is attributed to the increase in polymer melt viscosity with cooling. Similar behaviour was observed at 250s^{-1}. This sort of viscosity behaviour shows a typical Arrhenius type of relationship between viscosity and temperature. For most of the polymers under these cooling conditions the extrusion pressure increases because of the Arrhenius type relationship between extrusion temperature and pressure [1]:

$$\eta = Ae^{E_a/RT} \tag{5.1}$$

where η is the shear viscosity, Ea is the melt/solid state flow activation energy, R is the universal gas constant, A is pre-exponential factor and T is the flow temperature.

Gradual increase in the shear rate revealed the window at a shear rate of 275s^{-1}. At this rate the decrease in pressure during cooling at a temperature of 144.24^{o}C was observed because of the high degree of alignment of polymer melt chains along the flow direction in the rheometer die. This is the critical apparent shear rate $\boldsymbol{\gamma_c^w}$ which corresponds to the onset of extrusion window effect.

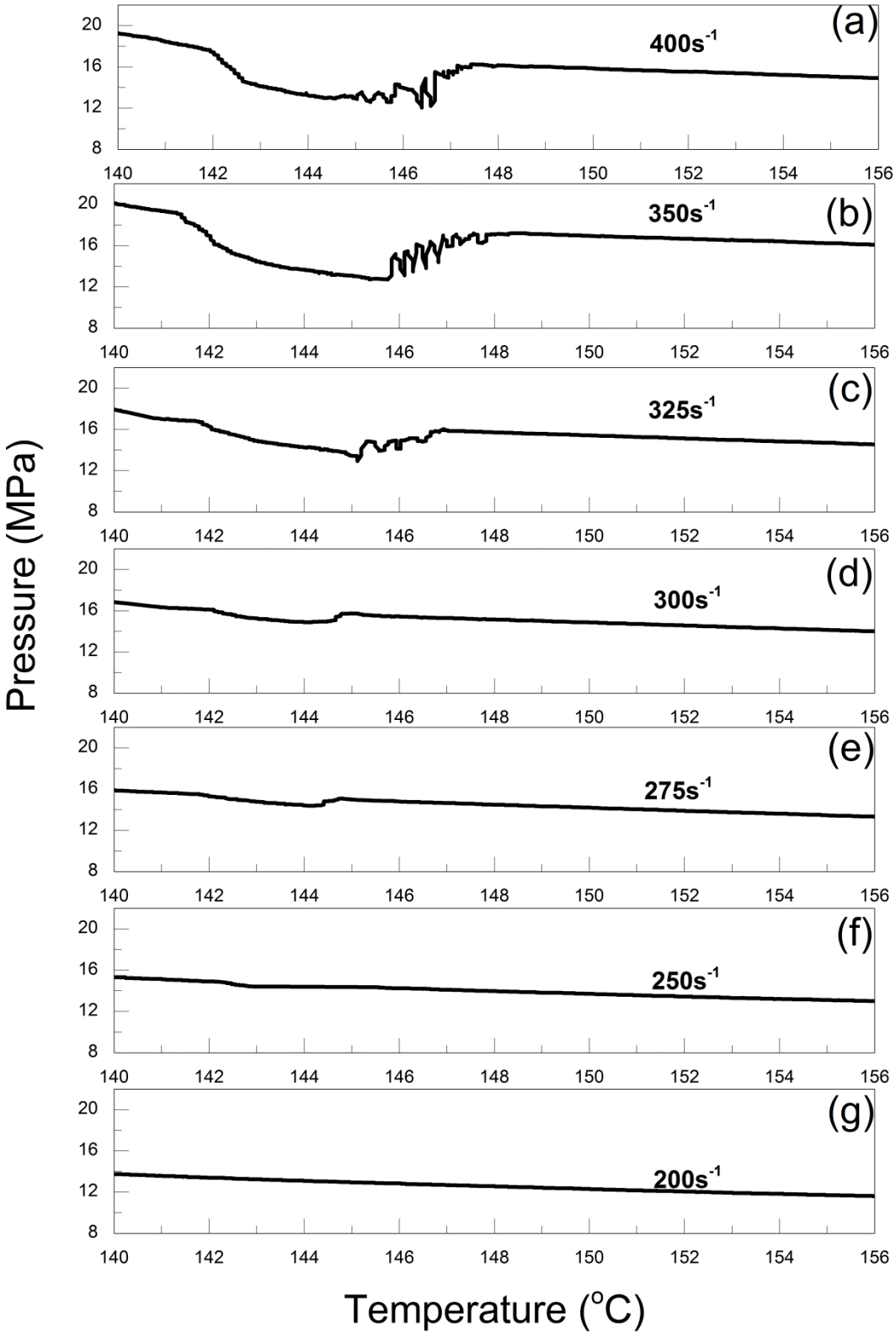

Fig.5.1: Extrusion Pressure vs temperature curves for pure HDPE at different strain rates recorded during the dynamic cooling experiment at a constant cooling rate of 1.5°C/min and using a capillary die with geometry: L-D-A:16-1-π .

At 275s^{-1} and 300s^{-1} the window starts at 144.24 and 144.55^{o}C (T_w^s) and ends at 141.89 and 141.92^{o}C (T_w^e) and the minimum pressure observed during the window (P_{min}) are 14.44 and 14.98 MPa. T_w^e also corresponds to the onset of flow induced solidification region where a sudden increase in the pressure is observed. The window is defined as the difference between T_w^s andT_w^e. With the increase in shear rate to 325s^{-1}, the melt flow singularity phenomenon was also observed in between a stick-slip flow region in which the pressure oscillates with the decrease in temperature and a flow induced solidification region.

At higher shear rates the following distinct changes in the curves are observed:

1: An increase in the T_w^s to higher temperatures and T_w^e to lower temperatures is observed up to 350s^{-1}, this increase is due to the maintenance of stretched chain confirmation.

2: The extrusion window widens up to 350s^{-1} (4.3^{o}C) after which a decrease in the window at 400s^{-1} is observed, because the rate of extrusion is too high to attain the required chain confirmation.

3: The P_{min} observed at 350s^{-1} where the window is largest is even less than the stable pressure observed at strain rate below the $\boldsymbol{\gamma_c^w}$ of 275s^{-1}.

4: The pressure observed during the flow induced solidification region increases with the increase in strain rate.

Fig 5.2 shows the effect of increasing strain rate on the minimum pressure drop recorded during the extrusion window for pure HDPE. The increase in strain rate from 200-400s^{-1} has a significant effect on the pressure drop recoded during the extrusion window. The decrease in pressure drop observed during the dynamic

cooling process is a significant and unconventional phenomenon which goes against all the classical flow and thermodynamic theories of polymer melts where an increase in pressure is observed with decrease in temperature. The minimum pressure drop also suggests lower energy requirement for processing HDPE with no melt flow irregularity.

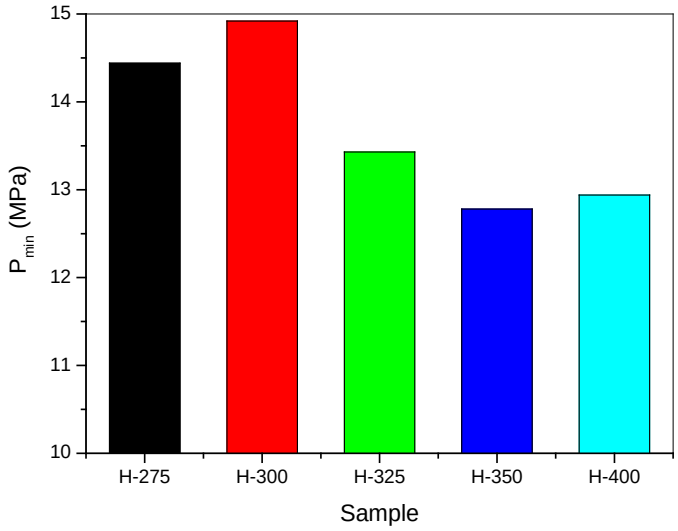

Fig.5 2: Minimum pressure drop (P_{min}) during the extrusion window for pure HDPE at different strain rates (275, 300, 325, 350 and 400 s^{-1}) recorded during the dynamic cooling experiment at a constant cooling rate of 1.5^{o}C/min and using a capillary die with geometry: L-D-A:16-1-π .

Fig 5.3 represents the calculated extrusion window for virgin HDPE at different strain rates. The fig 5.3 indicates that the extrusion window is significantly increased from 2.35^{o}C at 275s^{-1} to 4.33^{o}C at 350s^{-1}. After 350s^{-1}, further increase in strain rate to 400s^{-1} caused a reduction in the extrusion window.

For both figs 5.2 and 5.3, no data for strain rates of 200 and 250 s^{-1} is reported because for both these strain rates a normal pressure vs. temperature flow curve with no pressure reduction with the decrease in temperature is observed. Also from figs 5.2 and 5.3 it is clear that the maximum reduction in pressure drop and the maximum extrusion window is recorded up to 350s^{-1} strain rate after which both

these values don't follow the pattern and a higher pressure drop and smaller window is observed at $400s^{-1}$. So the $350s^{-1}$ strain rate can be described as the threshold strain rate γ_t^w up to which ideal processing conditions can be attained.

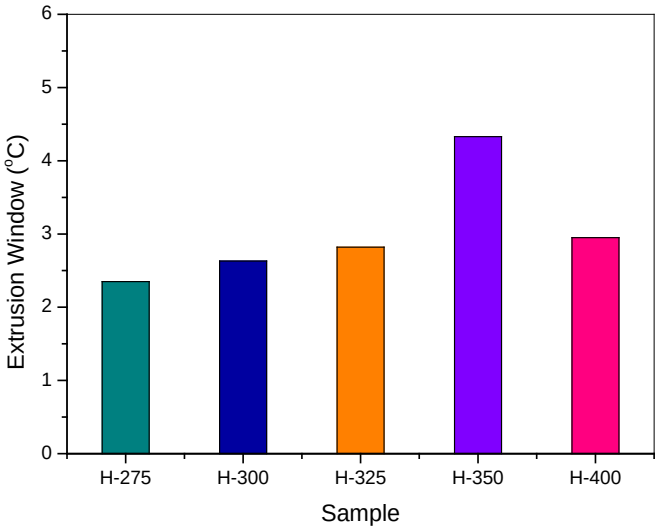

Fig.5.3: Extrusion window for pure HDPE at different strain rates (275, 300, 325, 350 and 400 s^{-1}) recorded during the dynamic cooling experiment at a constant cooling rate of 1.5°C/min and using a capillary die with geometry:L-D-A:16-1-π

5.2.2: Effect of clay weight percentage on MFS of HDPE

The influence of clay wt % on the extrusion window is shown in fig 5.4 (a-e). Fig 5.4 shows the rheological curves for pure HDPE and its composites with different concentrations of BHX at a constant strain rate of $350s^{-1}$ recorded during the dynamic cooling experiment. It is apparent from fig5.4 (a-e) that the addition of BHX clay in HDPE can influence the extrusion window and the enhancement in window is much more apparent than with the increase in strain rate. As shown in fig 5.4, that the addition of BHX clay influenced not only the T_w^s and T_w^e temperatures of extrusion window but also the P_{min} observed during the extrusion window.

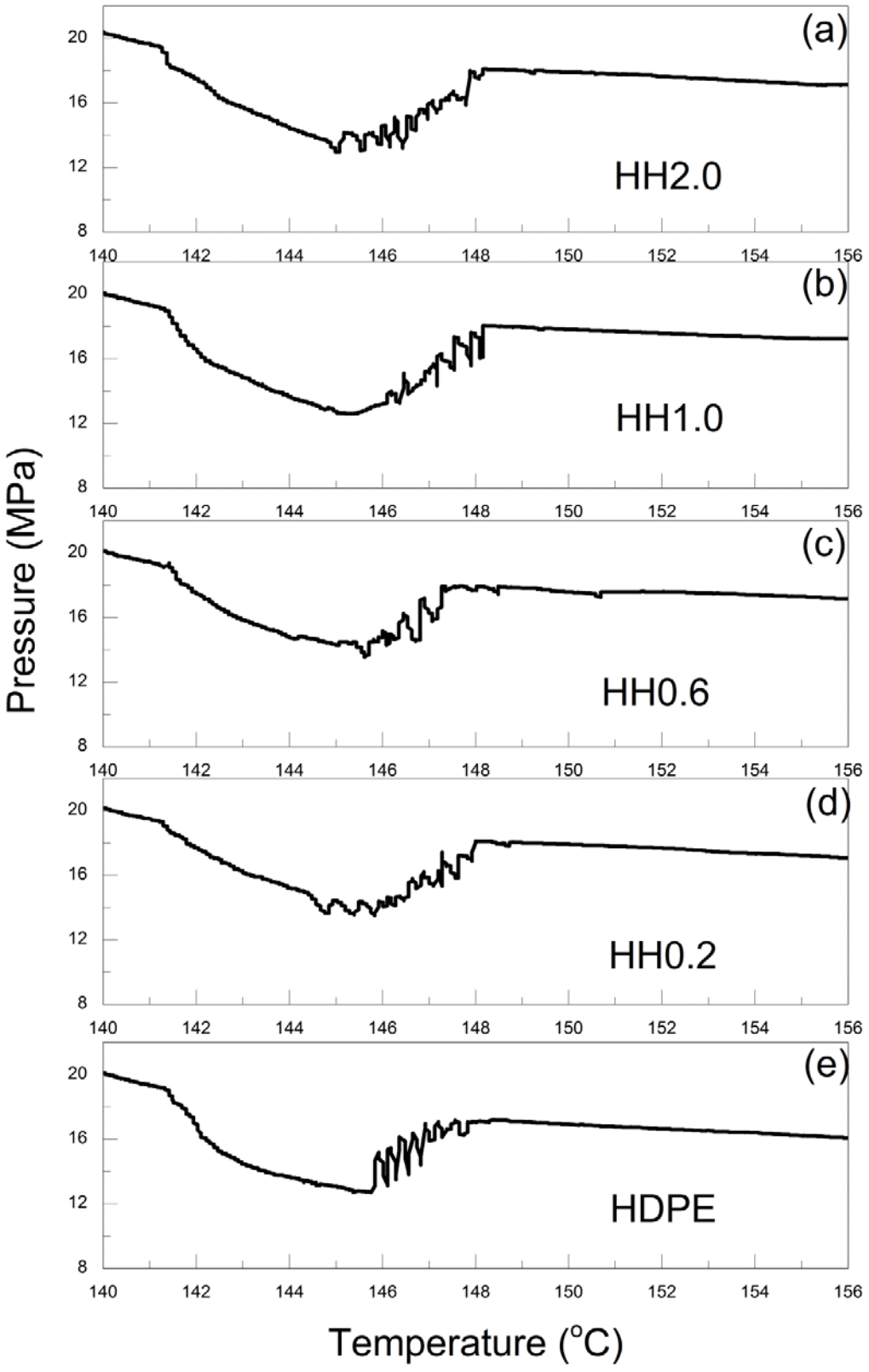

Fig.5.4: Extrusion Pressure vs temperature curves for pure HDPE and its composites with different concentrations of BHX clay at a constant strain rate of 350 s^{-1} recorded during the dynamic cooling experiment at a constant cooling rate of 1.5°C/min and using a capillary die with geometry: L-D-A:16-1-π

With the addition of 0.2 and 0.6 wt % of BHX clay the T_w^s and T_w^e temperatures remains mostly unaffected but an increasing trend in the window over pure HDPE is observed. On the addition of 1 wt% BHX however both the T_w^s and T_w^e temperatures shift to different temperatures and the broadening of window is more pronounced than for 0.2 and 0.6 wt % BHX clay composites. On addition of 2.0 wt % BHX clay in HDPE a reduction in the extrusion window and P_{min} is observed with T_w^s shifting to a lower temperature as compared to other composites, while the T_w^e remains the same as pure HDPE. The addition of high weight percentage of agglomerated kaolin clay particles will offer resistance to flow because of their ability to behave like irregular pentagon structures [5]. Such structures will also assist in the entanglement of the polymer chains and hence reduce the polymer melt flow.

The variation in the minimum pressure drop observed during the extrusion window for HDPE and its nanocomposites with different weight percentage of BHX clay at strain rate of $350s^{-1}$ is shown in fig 5.5. It is clear from the fig 5.5 that the P_{min}values generally decrease as the filler weight percentage increases, with the lowest value observed at 1 wt.% of BHX clay addition in HDPE.

The effect of various loadings of BHX clay on the extrusion window of HDPE at a strain rate of $350s^{-1}$ is shown in fig 5.6. On increasing the weight percentage from 0.2-1.0%, a distinct increase of 4.69^oC in the window of HDPE is observed. Further increase in weight percentage of BHX clay to 2.0 % resulted in slight decrease in window in comparison to HH1.0 which could be attributed to agglomerate formation of clay layers at high weight percentage.

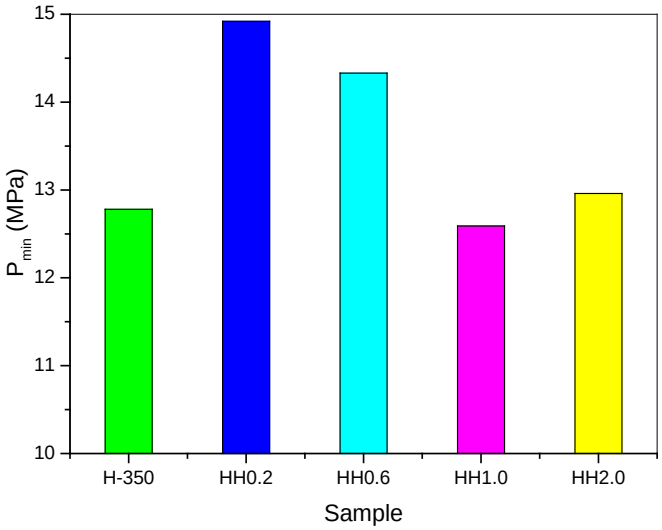

Fig.5.5 Minimum pressure drop (P_{min}) during the extrusion window for pure HDPE (H-350) and its composites with different concentrations of BHX clay at a constant strain rate of 350 s^{-1} recorded during the dynamic cooling experiment at a constant cooling rate of 1.5^{o}C/min and using a capillary die with geometry: L-D-A:16-1-π

.

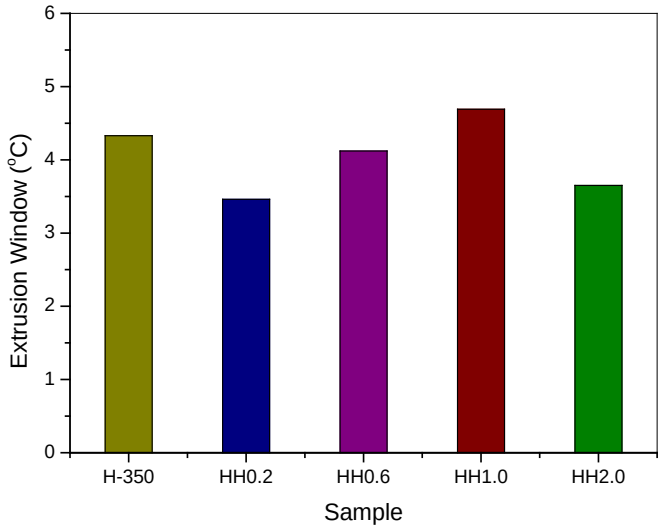

Fig.5.6: Extrusion window for pure HDPE (H-350) and its composites with different concentrations of BHX clay at a constant strain rate of 350 s^{-1} recorded during the dynamic cooling experiment at a constant cooling rate of 1.5^{o}C/min and using a capillary die with geometry: L-D-A:16-1-π

5.2.3: Effect of clay morphology on MFS of HDPE

The effect of clay morphology on the extrusion window is shown in fig 5.7 (a-e). Fig 5.7 shows a comparison of the rheological curves for HDPE (fig 5.7-e) and its composites with Na-MMT (fig 5.7-a), bentone (fig 5.7-b), BLX (fig 5.7-c) and BHX (fig 5.7-d) clay.

All the composites contain 1 wt % of clay and are extruded under the same conditions as all the BHX composites. The addition of all four different types of clays added in HDPE has their own individual effects on the extrusion window interval and the $\mathrm{P_{min}}$ observed during the window. With regards to BLX clay, a reduction in the extrusion window is observed due to the movement of both T_w^s and T_w^e to higher temperatures in comparison to the pure HDPE. Also the P_{min} for HL1.0 is only slightly lesser than that of the pure HDPE.

These results indicate that the BLX clay is not uniformly dispersed and its hexagonal shaped agglomerates actually enhance the interaction between the adhered chains on the die wall and the bulk free polymer melt chains due to their tumbling effect. In comparison to the two kaolin clay composites, the effect of intercalated bentone and exfoliated Na-MMT clay on the melt flow singularity is much more pronounced as depicted in fig 5.7 (a-b). In the presence of bentone and Na-MMT clay T_w^s moves to higher temperatures while T_w^e moves to lower temperatures, which leads to the broadening of the extrusion window. The increase in the extrusion window interval for HM1.0 (6.53^{o}C) is the highest yet reported for a polymer composite.

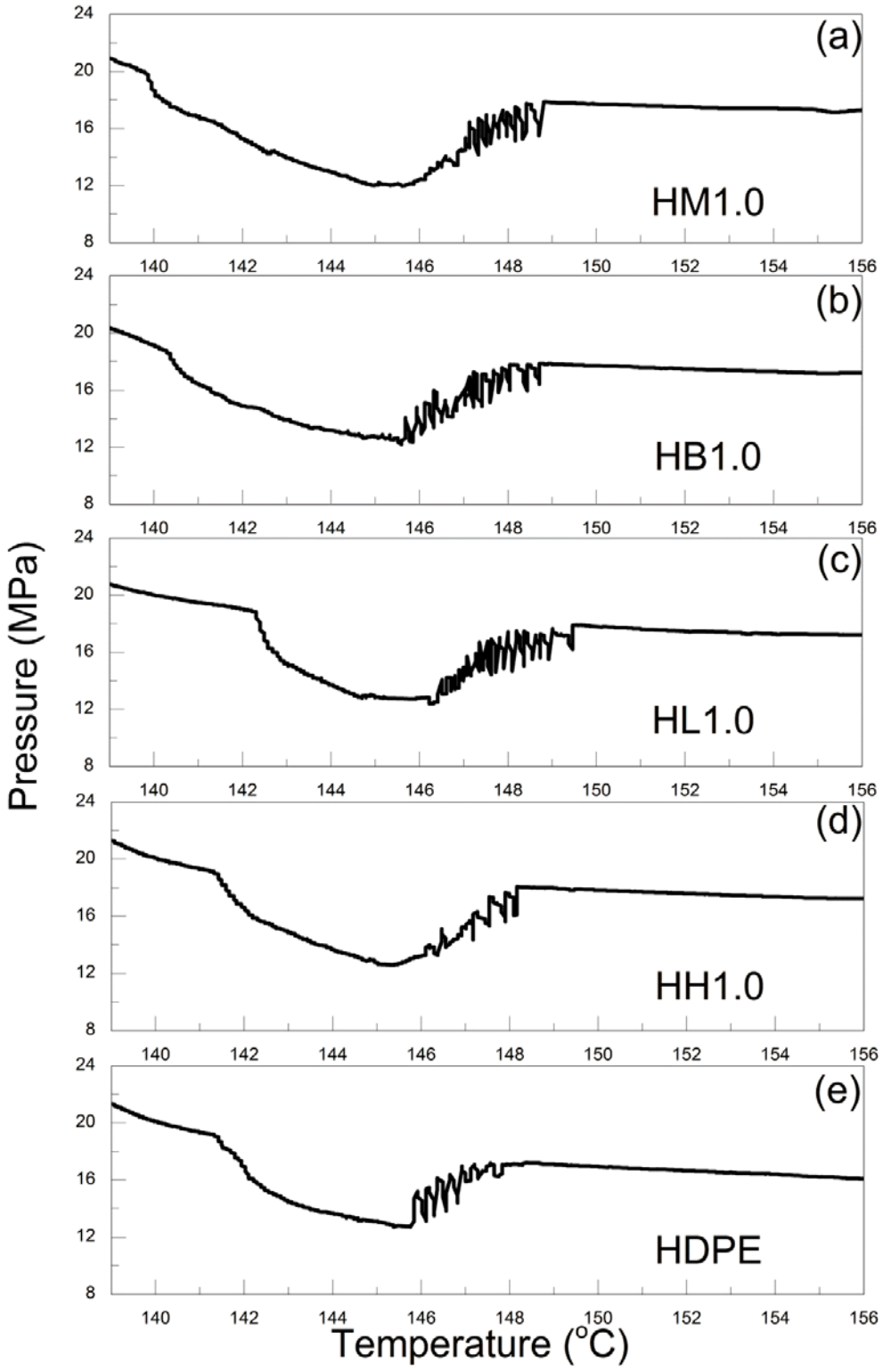

Fig.5.7: Extrusion Pressure vs temperature curves for pure HDPE (e) and its composites with Na-MMT (a), Bentone (b), BLX (c) and BHX (d) at a constant strain rate of 350 s^{-1} recorded during the dynamic cooling experiment at a constant cooling rate of 1.5°C/min and using a capillary die with geometry: L-D-A:16-1-π

The minimum pressure drop during the extrusion window for pure HDPE (H-350) and its composites with Na-MMT, Bentone, BLX and BHX clay at a constant strain rate of 350 s^{-1} are shown in fig 5.8. In case of HM1.0 the P_{min} is 0.81 MPa less than that of pure HDPE at the same strain rate. The observations regarding the P_{min} of HM1.0are that the presence of Na-MMT increases the decrease in pressure during the extrusion window which indicates ease of processing with better product quality. In comparison to Na-MMT, the decrease in P_{min} and the pressure increase in the flow induced solidification region for all other composites are only minor.

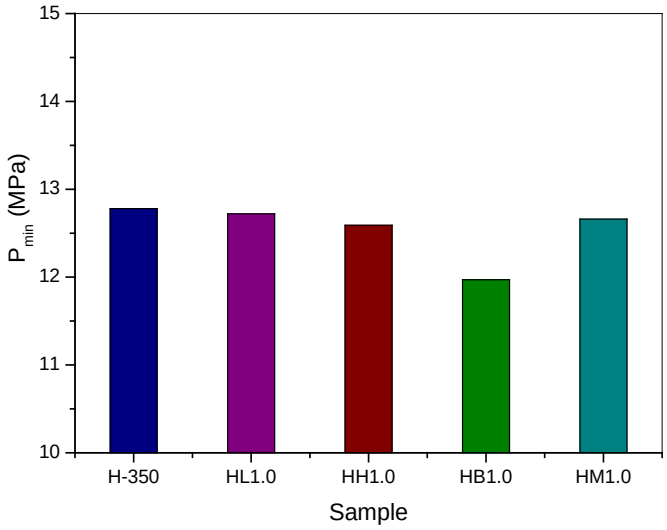

Fig.5.8: Minimum pressure drop (P_{min}) during the extrusion window for pure HDPE (H-350) and its composites with Na-MMT, Bentone, BLX and BHX clay at a constant strain rate of 350s^{-1} recorded during the dynamic cooling experiment at a constant cooling rate of 1.5^{o}C/min and using a capillary die with geometry: L-D-A:16-1-π

The low temperature extrusion window for pure HDPE and its composites with Na-MMT, Bentone, BLX and BHX clay at a constant strain rate of 350s^{-1} recorded during the dynamic cooling experiment is shown in fig 5.9. In comparison to pure HDPE,

HM1.0 shows a 2.2^{o}C rise in the extrusion window and the overall extrusion window of 6.53^{o}C now lies well above the commercial extruder's temperature fluctuations of 5.0^{o}C. The intercalated nanocomposite HB1.0 also shows an increase of window up to 5.21^{o}C. In comparison to the exfoliated and intercalated nanocomposites, the microcomposite HH1.0 shows only a slight improvement in extrusion window to 4.69^{o}C and HL1.0 on the other hand show a reduction of window to 3.89^{o}C.

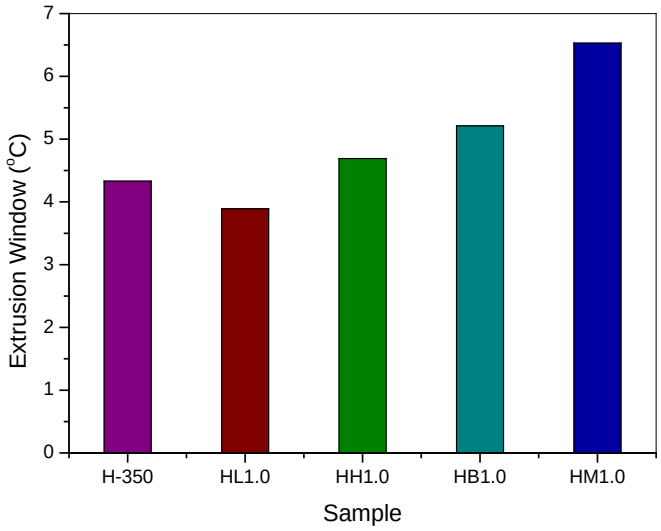

Fig.5.9: Extrusion window for pure HDPE (H-350) and its composites with Na-MMT, Bentone, BLX and BHX clay at a constant strain rate of 350s^{-1} recorded during the dynamic cooling experiment at a constant cooling rate of 1.5^{o}C/min and using a capillary die with geometry: L-D-A:16-1-π

.

5.2.4: Effect of filler shape on MFS of HDPE

In the previous sections, the effect of filler weight percentage, morphology and aspect ratio on the MFS of HDPE was described in detail. Apart from the aforementioned factors, the rheological properties are also dependent upon the shape and size of the fillers. In order to study the effect of filler shape on the melt flow singularity of HDPE, 1D-MWCNT, 2D-graphene oxide and 3D carbon black

based nanocomposites of HDPE are studied. All of these nanocomposites are prepared and extruded through the capillary rheometer under the same conditions as the nanocomposites discussed in the previous sections.

The extrusion temperature-pressure profiles recorded during the MFS phenomenon analysis for HDPE and its nanocomposites with CB, MWCNT and graphene are shown in fig 5.10. The results show the variation in the extrusion pressure recorded during the dynamic cooling process on capillary rheometer at a strain rate of $350s^{-1}$.

In case of HDPE the increase in pressure is observed up to $148^{o}C$, after which the pressure starts to oscillate due to the stick-slip flow observed at lower extrusion temperatures and the extrudate received has a rough surface. After the stick-slip flow phenomenon a region of pressure reduction is observed in which the extrudate leaving the die has a smooth surface with a minimum die swell and the overall process run smoothly. After The extrusion window, the pressure increases rapidly because of the flow induced crystallization which causes rapid solidification of the extrudate and produces a thick extrudate with rough surface. The duration of the extrusion window for pure HDPE is $4.3^{o}C$ and the minimum extrusion pressure recorded during the window is 12.78 MPa. The extrusion window observed for HM and HG (6.2 and $5.7^{o}C$) are broader than HDPE, whereas in case of HCB, a reduction ($3.5^{o}C$) in the extrusion is observed. This reduction explains the effect of particle shape in extending and aligning the polymer melt chains tethered at the die wall which ultimately leads to enhanced slip flow of the disengaged bulk polymer chains on the tethered polymer melt chains.

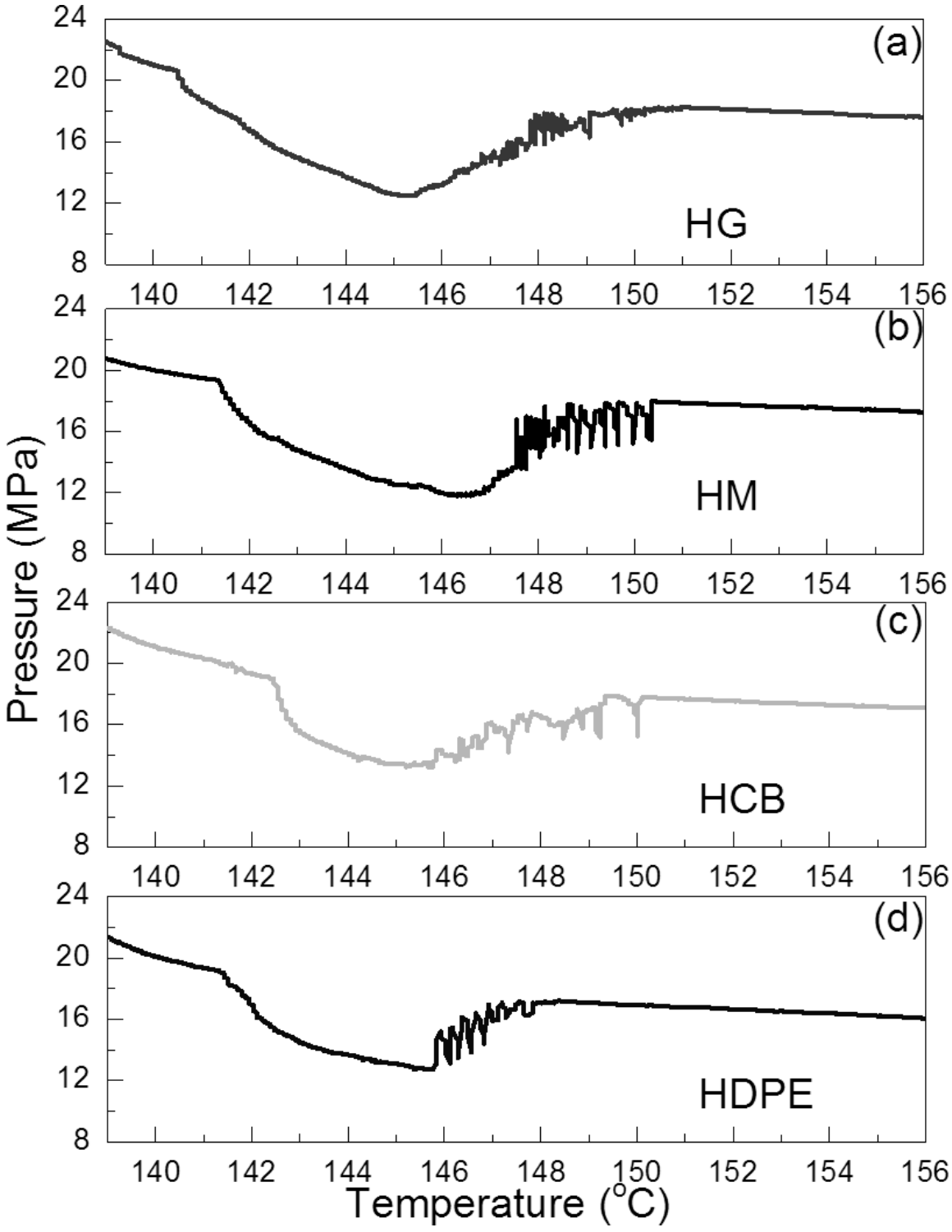

Fig.5.10: Extrusion Pressure vs temperature curves for pure HDPE (d) and its composites with graphene (a), MWCNT (b) and CB (c) at a constant strain rate of $350s^{-1}$ recorded during the dynamic cooling experiment at a constant cooling rate of $1.5^{o}C$/min and using a capillary die with geometry: L-D-A:16-1-π

Due to their circular shape CB enhance the engagement between the tethered and the bulk polymer chains and hence reduce the overall slip flow for the bulk polymer chains. On the other hand the elongated and platy nature of MWCNT and graphene can align the tethered chains and also provide more slippage on surface to the bulk polymer chains. As detailed earlier on, that the spherical CB particles provide more friction to the polymer chains by promoting entanglements and hence the flow of CB composites through the die will be resisted more in comparison to the graphene and carbon nanotubes nanocomposites. Another proof of the resistance offered by the CB particles to appearance of slip flow is the minimum extrusion pressure drop of 13.24 MPa, this value is even higher than that of pure HDPE and is an indication of higher shear stress which is required to transform the stick-slip flow to slip flow of extrusion window. In case of HCB the extrudate diameter observed is slightly larger than pure HDPE.

5.2.5: Effect of filler size on MFS of HDPE

The effect of ball milled CNT on the extrusion window of HDPE is shown in fig 5.11. The effect of shortened MWCNT produced by the ball milling on the extrusion window is much closer to the role played by CB. The shortest CNT produced by 72 hours of ball milling had an effect almost identical to the one which CB addition had on the extrusion window of HDPE.

With the inclusion of different sized MWCNT into HDPE, the MFS characteristics are modified in comparison to virgin HDPE and HM. As shown in fig 5.11-b that the inclusion of MWCNT-24 into HDPE does not modify the rheological characteristics too much in comparison to HM and the T_w^s moves from 147.5 to 146.6^{o}C, while the T_w^e moves from 141.25 to 141.21^{o}C. The changes in the starting and ending

temperatures of extrusion window are negligible with the addition of MWCNT-24 and the overall window remains the same as such.

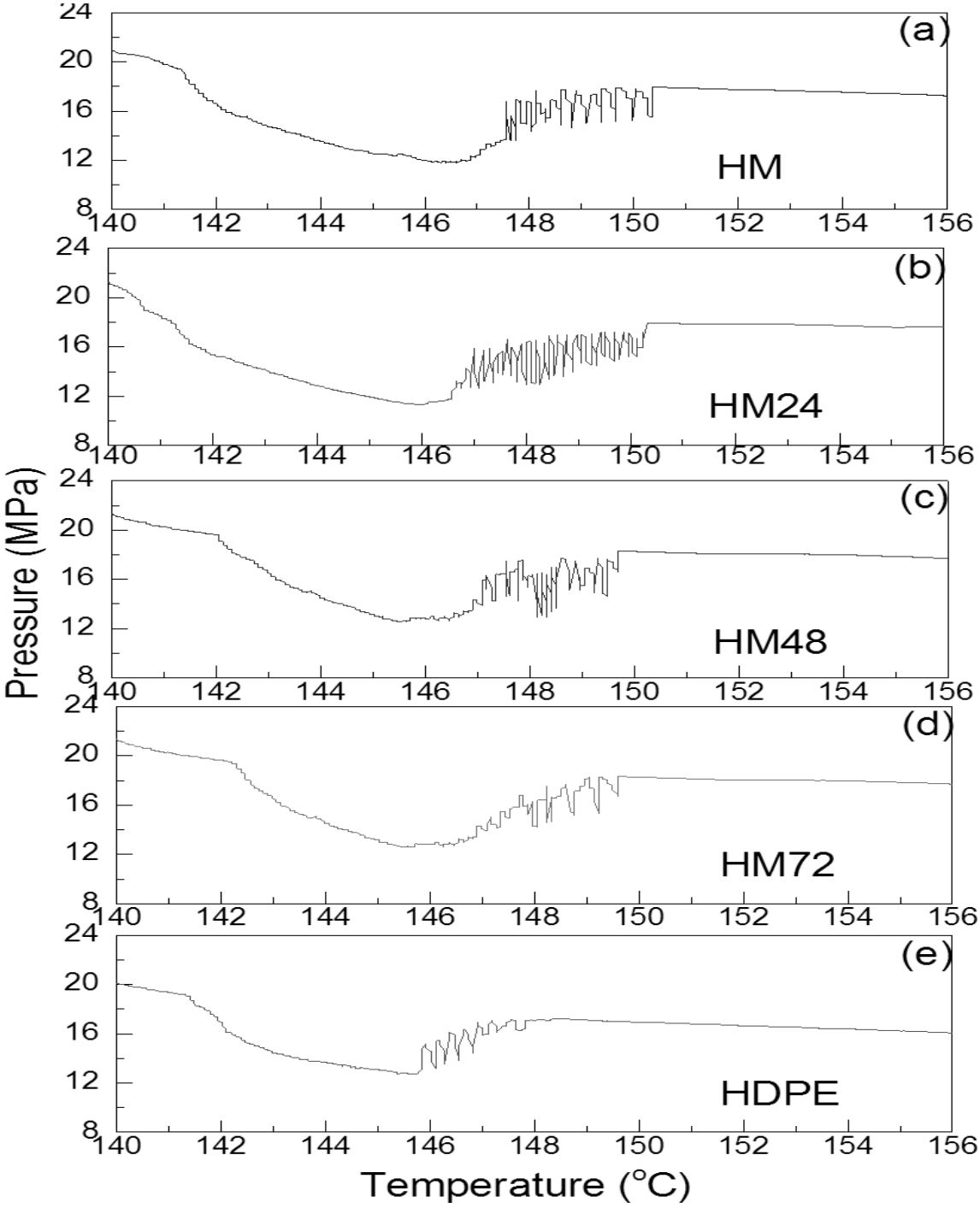

Fig.5.11:Extrusion Pressure vs temperature curves for pure HDPE (e) and its composites with MWCNT (a), MWCNT-24 (b), MWCNT-48 (c), and MWCNT-72 (d), at a constant strain rate of $350s^{-1}$ recorded during the dynamic cooling experiment at a constant cooling rate of $1.5^{o}C$/min and using a capillary die with geometry: L-D-A:16-1-π

In case of HCB the higher value of P_{min} obtained indicates higher wall shear stress for slip flow and is due to the decreasing entanglement distance which will resist in the flow of bulk polymer chains by entangling them with the adsorbed chains on the capillary wall. In case of MWCNT and graphene based nanocomposites the increase in the extrusion window is also attributed to their high aspect ratio and relaxation time, which helps in stretched confirmation and alignment of chains tethered to the metal wall. Also the aligned chains can be easily wrapped up around graphene layers and the MWCNT, making the tethered chains unavailable for entanglements with the bulk of the polymer chains.

Fig 5.11-c reveals that the introduction of 48 and 72 hrs ball milled MWCNT caused a reduction in the extrusion window with both the T_w^s and T_w^e moving to lower and higher temperatures respectively.

As shown in chapter 4, that although the ball milling of MWCNT removed the problem of agglomerate formation and produced HDPE-MWCNT nanocomposites with less agglomerates and a more uniform dispersion of MWCNT, but the inclusion of these does caused a reduction in the overall window because of their shortened dimensions. The characteristics of HM-72 and pure HDPE are very close because of the negligible difference between their measured values of P_{min} and the extrusion window. A summary of all the results obtained from the melt flow singularity testing of HDPE at different strain rates and then for its nanocomposites with different nanofillers is presented in table 5.1. The table 5.1 presents the individual values for window starting temperature (T_w^s), window ending temperature (T_w^e**)** and minimum pressure data (P_{min}) obtained from the pressure versus temperature curves presented in previous sections.

Table 5.1: Rheometer data obtained from the dynamic cooling experiment of HDPE and all its nanocomposites

Sample	Strain rate (1/s)	T_w^s (^oC)	T_w^e (^oC)	Processing Window (^oC)	P_{min} (MPa)
HDPE	200	-	-	-	-
	250	-	-	-	-
	275	144.24	141.89	2.35	14.44
	300	144.55	141.92	2.63	14.92
	325	145.12	141.6	2.82	13.43
	350	145.75	141.42	4.33	12.78
	400	145.02	142.07	2.95	12.94
HH0.2	350	144.75	141.29	3.46	14.92
HH0.6	350	145.54	141.42	4.12	14.33
HH1.0	350	146.01	141.32	4.69	12.59
HH2.0	350	145.01	141.36	3.65	12.96
HL1.0	350	146.2	142.31	3.89	12.72
HM1.0	350	146.4	139.87	6.53	11.97
HB1.0	350	145.5	140.29	5.21	12.66
HG	350	146.72	140.36	6.36	12.48
HCB	350	145.76	142.45	3.31	13.24
HM	350	147.56	141.25	6.31	11.81
HM24	350	146.58	141.21	5.37	11.29
HM48	350	146.64	142.04	4.60	12.59
HM72	350	146.12	142.30	3.82	12.56

5.3: Die Swell

As the temperature is reduced below the processing window temperature interval (<142^{o}C) the extrusion pressure shoots up dramatically and a considerable increase in the die swell of the extrudate is observed. In fig 5.12 the die swell ratio for pure HDPE samples at three different temperatures (140^{o}C, 144^{o}C, 160^{o}C) is plotted against the strain rate (extrusion speed) maintained during the cooling process.

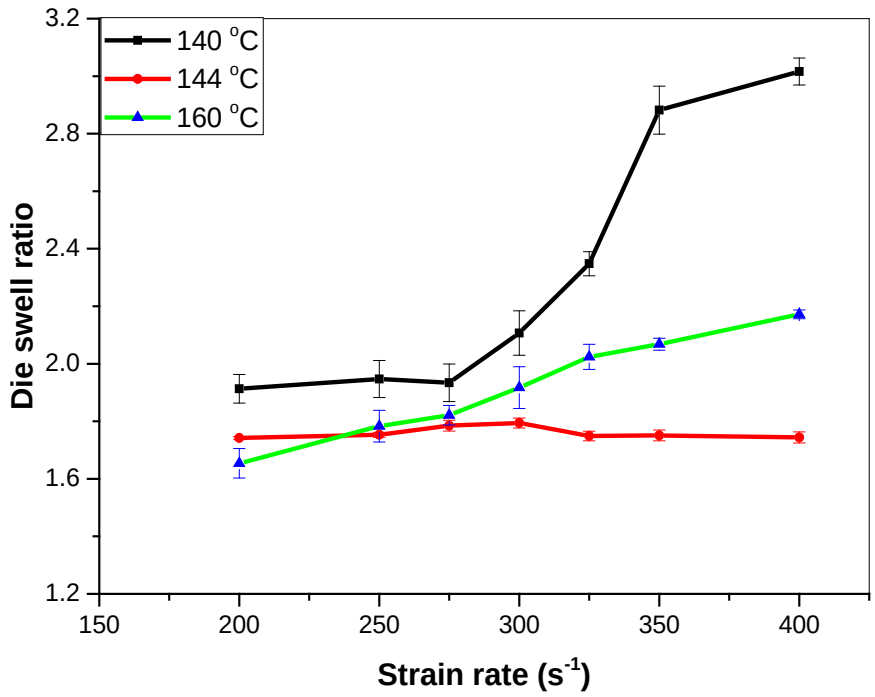

Fig.5.12: Plot of die swell ratio as a function of the strain rate maintained during dynamic cooling experiment for HDPE at three different extrusion temperatures

.

The curve for 160^{o}C represents the normal processing behaviour for HDPE melt in a capillary rheometer where the die swell gradually increases with an increase in shear rate. When the strain rate is increased to 400s^{-1}, the die swell of the extrudate increases rapidly at temperatures 140 and 160^{o}C and the extrudate flow also decreases. In case of die swell measured at 144^{o}C, an increase up to 300s^{-1} is

observed, where the extrusion window effect is minimum and then it decreases at 325 s^{-1} and then remains constant to a low value.

Fig 5.13 shows the die swell of HDPE and its nanocomposites with 1 wt.% of BHX, BLX, Na-MMT and bentone clay at different temperatures that are observed during the dynamic cooling experiment.

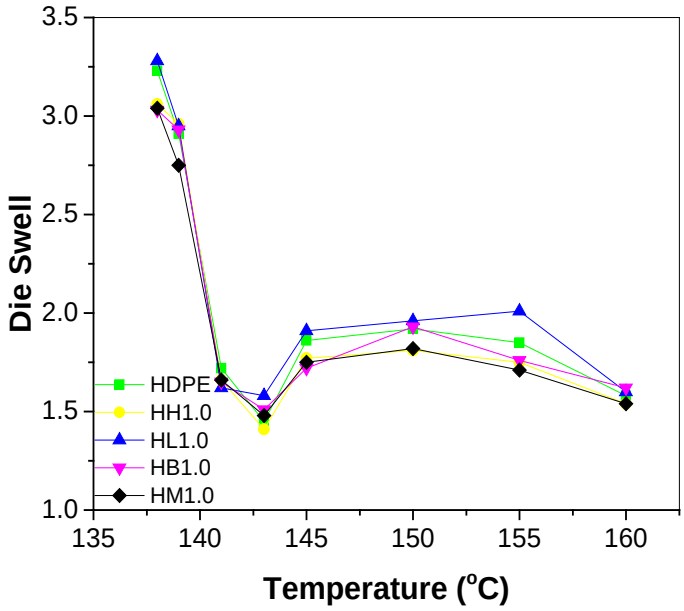

Fig.5.13:Die swell of HDPE and its clay based nanocomposites recorded at different temperatures

.

The variation in the die swell of HDPE and its nanocomposites shown in fig 5.13 indicates a clear dip in the die swell as the temperature is reduced from the flow instability region to the extrusion window zone. As the extrusion window ends at corresponding T_w^e for each specimen, the die swell increases drastically as the temperature reaches to the point where the flow induced solidification of HDPE starts. In comparison to pure HDPE, the die swell observed during the extrusion window for HM1.0, HB1.0 and HH1.0 are slightly lesser, while the die swell of HL1.0 is almost the same as HDPE.

Fig 5.14(a-i) shows the extrudate profile for the pure HDPE, HM1.0 and HH1.0 at 139^{o}C, 143^{o}C and 160^{o}C. The three temperatures selected corresponds to the three distinct flow regimes; flow induced solidification, extrusion window and stable melt flow respectively. As shown in fig 5.14, the die swell is minimum at the extrusion window temperature interval and it increases dramatically during the flow induced solidification. The difference between the die swell at the processing window and the stable melt flow regime indicate that within the processing window the polymer melt extrudes more easily than at high processing temperature and thus validates the applicability of the processing window as an authentic method of processing. The micrographs in fig 5.14 clearly show that the extrudate surface is smooth and free from any melt flow irregularities. One more observation for all the specimens obtained during the extrusion window is that they were much shinier than the specimens obtained during the flow induced solidification and flow instability region. The glow and shine present on the specimen surface is a clear proof that the polymer melt extruding out of the die is actually flowing on a smooth tethered layer of polymer chains on the die.

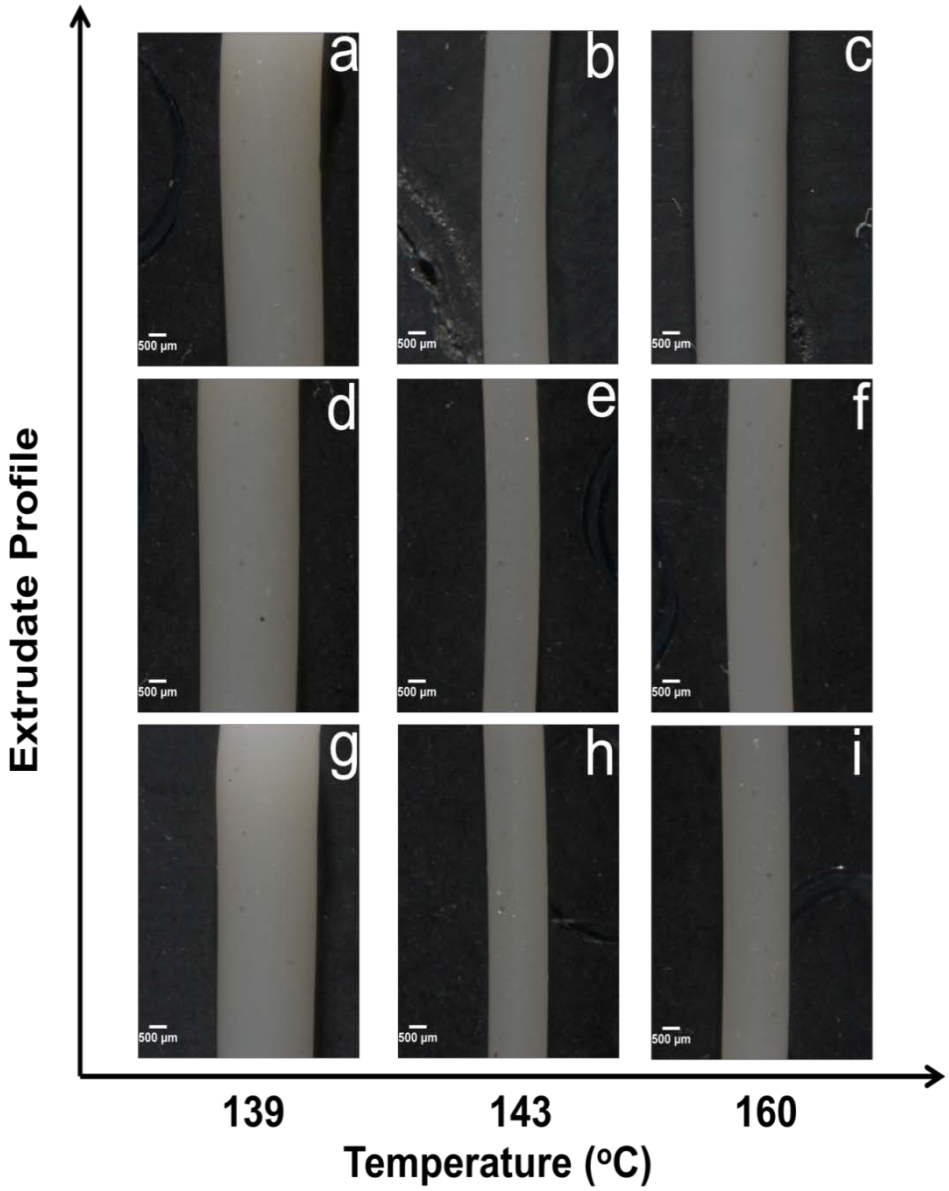

Fig.5.14: Extrudate profiles of pure HDPE (a-c), HM1.0 (d-f) and HH1.0 (g-i) at three different temperatures 139^{o}C, 143^{o}C and 160^{o}C and at 350s^{-1} strain rate, showing the difference between the die swell in the three distinct regions of melt flow singularity phenomenon

The variation in the die swell of the extrudate of HPDE and its nanocomposites with CB, MWCNT and GO obtained at temperatures of 160, 155, 150, 145, 143, 141, 139 and 137^{o}C during the various stages in the melt flow singularity phenomenon is shown in fig 5.15. The temperatures selected correspond to the three distinct flow

regimes; flow induced solidification, extrusion window and stable melt flow respectively.

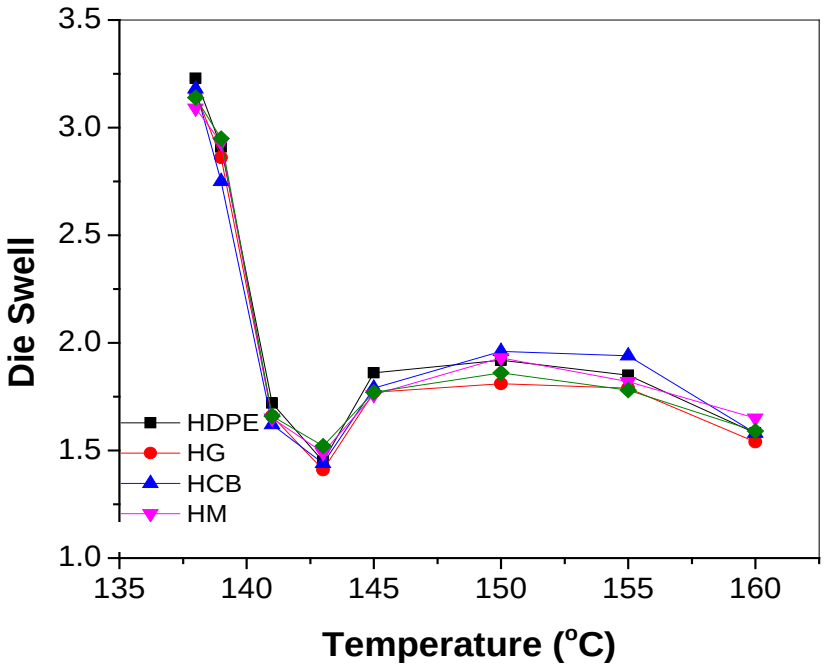

Fig.5.15: Die swell of HDPE and its carbon-based nanocomposites recorded at different temperatures

The extrudate profile for HCB, HG and HM at 3 different temperatures (139,144,160 ^{o}C) and at a strain rate of 350s^{-1} are shown in fig 5.16. The three temperatures correspond to the three zones studied during the melt flow singularity of HDPE. Fig 5.16 shows the difference between the die swell in the three distinct regions of temperature-pressure flow curve. The specimens obtained at 144^{o}C are smooth and free of any abruptions, whereas at 160 and 139^{o}C the surface of extrudate is relatively rough and has a number of indentations. The die swell as shown in fig 5.16 is maximum at 139^{o}C, which is close to 3mm but at 144^{o}C the die swell is reduced to 1.5mm. Once again the extrudate obtained during the extrusion die is remarkably shiny in comparison to the extrudate obtained in the other regions.

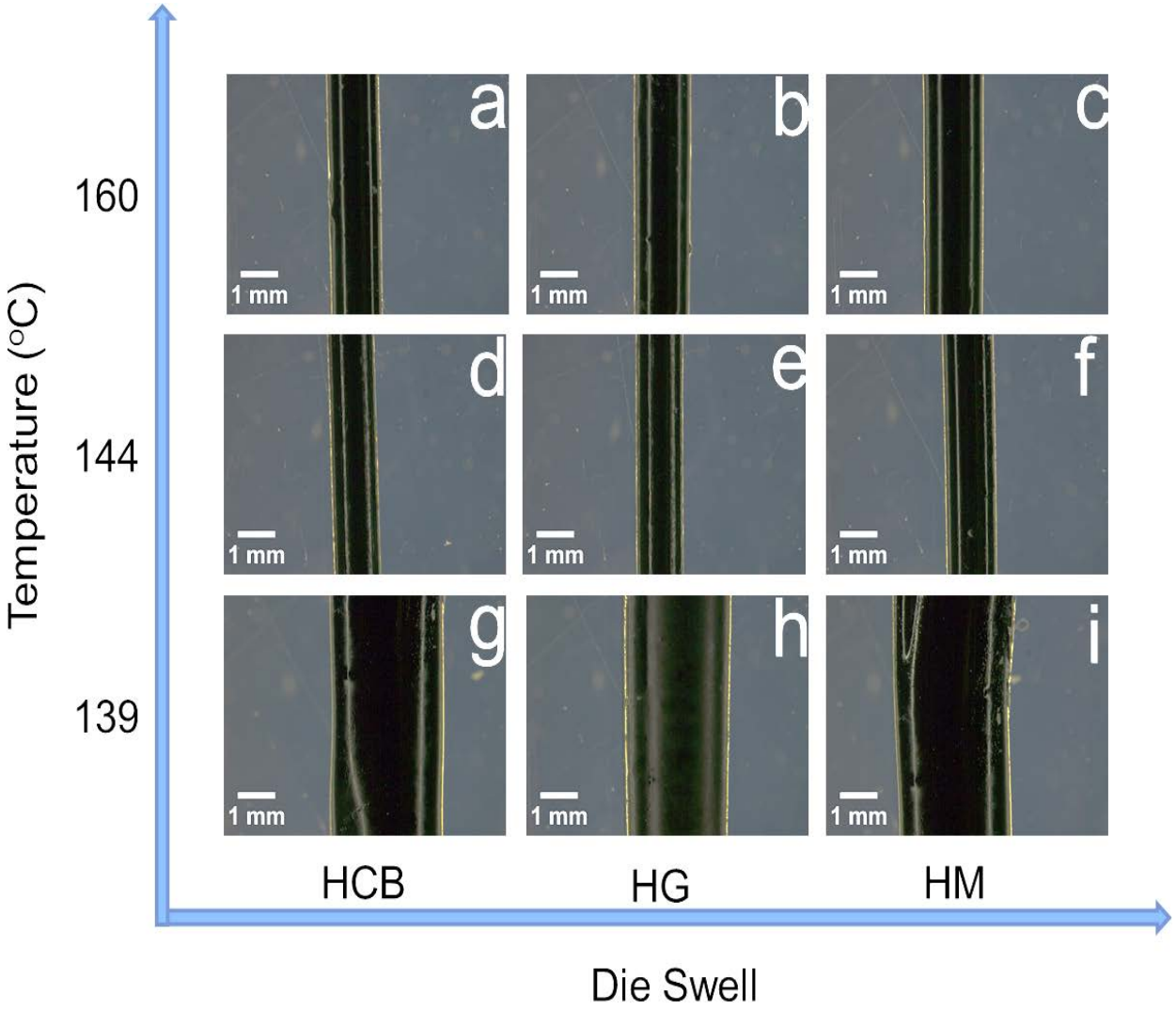

Fig.5.16: Extrudate profiles of pure HCB (a, d, g), HG (b, e, h) and HM (c, f, i) at three different temperatures 139°C, 144°C and 160°C and at 350 s^{-1} strain rate, showing the difference between the die swell in the three distinct regions of temperature- pressure flow curve

5.4: Discussion

The extrusion window is observed in a small region with the transformation of the polymer melt into liquid crystal mesophase. Molecular origin of the singularity is associated with the slip flow phenomenon [2-4] which is influenced by the chain attachment to the die surface and its detachment from the bulk polymer melt. Thus

the singularity is influenced by the interfacial energy between the molecular chains and the wall.

The molecular origin of the extrusion window is described in terms of the appearance of a stretched chain confirmation [1-4]. The stretched chain confirmation of the polymer melt inside the capillary die can be attained and then maintained during slip flow, if the strain rate is greater than the inverse of characteristic relaxation time of polymer chains [8]. The internal relaxation of the absorbed polymer chains, which signifies their coiling back, cannot occur before the free bulk chains are disentangled from the adsorbed chains. One of the main parameter [9] used to define the hydrodynamic boundary conditions (*HBC*) for the transition of coil to stretch conformation of polymer chains is Weissenberg number (W_i):

$$W_i = \frac{\lambda_{rel}}{t} \tag{5.2}$$

where λ_{rel} is the relaxation time of a polymer chain and t is the characteristic time of the fluid deformation rate. In the above equation 1/ t can be replaced by the wall shear rate (γ_w) and the W_i can then be expressed as:

$$W_i = \lambda_{rel}\, \gamma_w \tag{5.3}$$

If $W_i < 1$, then the polymer chains will reach equilibrium to its coil state quickly than the changes arising from the strain applied by the bulk polymer melt. Under these conditions there will be no slip flow. When $W_i = 1$ then there will be coil to stretch transition of polymer melt chains. On the other hand when $W_i > 1$, the *HBC* of a continuous slip flow will take place and the polymer extrudate with no surface distortion will be achieved.

Brochard and de Gennes [10] and Drda and Wang [11] have proposed theories on the possibilities of chain attachment to the wall surface and its disengagement from the polymer melt above a critical shear rate or shear stress. The disengagement process of the chain will be strongly dependent on the topological constraints between the adsorbed chain and the surrounding chains in the bulk, which would be dependent on molecular characteristics and flow conditions. These theories can be used to describe the forces which the bulk of polymer melt applies on the tethered chains. The total friction force (F_v) acting on a single adsorbed chain is given by [12]:

$$F_v = X.a.\eta_p.V \tag{5.4}$$

where X is the number of mobile chains from the melt trapped with the adsorbed chain; a is the molecular size of the monomer with length units; η_p is the viscosity of the melt and V is the velocity of the mobile chains with respect to the adsorbed chains.

When the velocity of the mobile chains increases then the adsorbed chains will be aligned and have the stretched chain confirmation with a mean diameter (D) [12]:

$$D = \frac{k.T}{F_v} \tag{5.5}$$

where k is a constant and T is the absolute temperature. The mean diameter represents the diameter of the stretched chains adsorbed on the capillary wall during flow.

Combining the equations 5.4 and 5.5, the velocity of the mobile chains with respect to the adsorbed chains can be represented by the following equation:

$$V = \frac{k.T}{X.a.\eta_p.D} \tag{5.6}$$

As the velocity of the mobile chains with respect to the adsorbed chains increases then according to above equation the mean diameter of the adsorbed chains will decrease and hence there will come a point where the diameter of the tethered chains will be reduced to such a minimum value that the adsorbed chains can no longer entangle the bulk of the polymer melt and hence slip flow will take place. For normal processing conditions of polymers, a decrease in processing temperature or increase in strain rate will cause stick slip flow due to the entanglement or dis entanglement of the adsorbed chains from the bulk polymers but during MFS stage the adsorbed chains are transformed into a flow induced mesophase which assists their alignment for longer period of time and hence eases the disentanglement. After the extrusion window a rapid increase in pressure is observed due to the formation of solid fibrous crystal which leads to flow induced solidification of the polymer melt and causes the viscosity and extrudate diameter increases rapidly. The solidification takes place because the temperature reaches the static solidification temperature during cooling and orientation induced crystallization causes the viscosity to increase because of fibrous crystal formed inside the melt.

When the polymer chains are aligned the small amount of clay particles added into the composite will act as lubricant surface that can effectively reduce the friction between the polymer chains and hence assist in the flow of polymer melt through the die (fig 5.17-a). The introduction of individual filler particles produced by exfoliation, intercalation or by better dispersion between the polymer chains can effectively decrease the overall friction in the system and hence the polymer chains will flow more easily during the extrusion window. If the polymer chains are entangled (fig 5.17-b) the addition of exfoliated clay particles will produce large internal friction which leads to energy dissipation in composites and can restrict the movement of polymer chains [13]. Also the filler agglomerates act like hexagonal particles (fig 5.17-c) which perturb the orientation of the adsorbed chains and also favour their entanglement with the bulk polymer chains and hence cause a reduction in the extrusion window.

The polymer melt due to their entangled structure have short relaxation time [1,12, 14] which can be altered significantly by the addition of nanofillers. The large platy structure of clay layers, graphene sheets and MWCNT tubes with high aspect ratio and high relaxation time [1,14] can help with alignment of polymer chains during flow and also help maintain the stretched chain confirmation of the adsorbed chains at the die wall. Due to their structure the exfoliated clay layers, graphene sheets and MWCNT tubes could also help in the orientation of the adsorbed chains at the capillary wall because these adsorbed chains can easily wrap themselves around the nanofiller and that would ultimately stop their entanglements with the bulk polymer melt chains, which would lead to better flow and minimum die swell for longer temperature intervals.

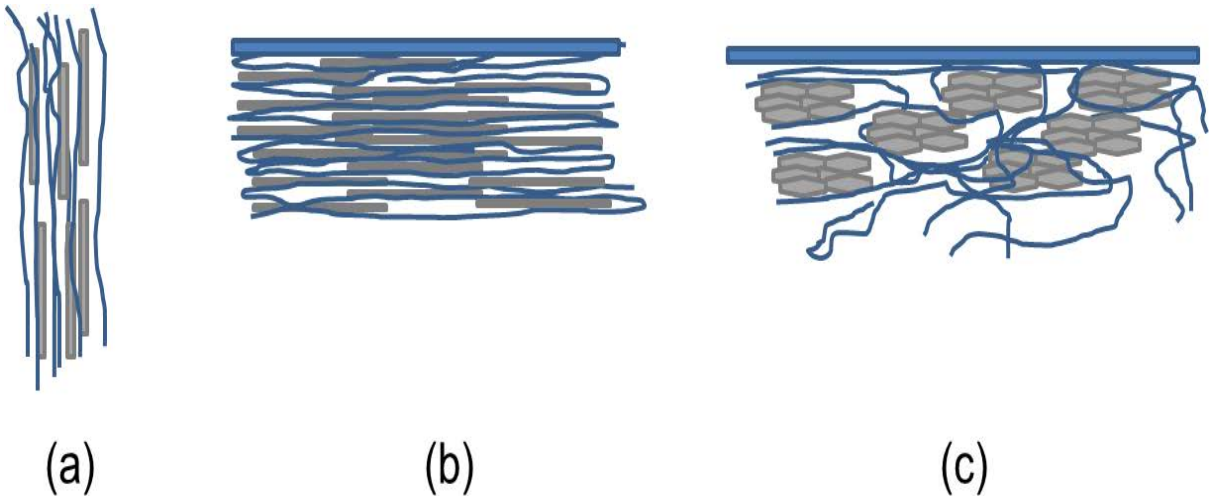

Fig.5.17: Schematic view of the interaction between the (a) exfoliated clay layers and the bulk polymer melt chains, (b) exfoliated clay layers and the adsorbed polymer melt chains on the die surface, (c) hexagonal shaped clay agglomerates and the adsorbed polymer melt chains on the die surface

The critical stress $\sigma_c$for wall slip is presented by the Brochard and de Gennes theory on wall-slip at the metal-solid interface [10], as:

$$\sigma_c = \frac{\upsilon K_B T}{N_e^{\frac{1}{2}} \alpha} \tag{5.7}$$

Where σ_c is the critical shear stress for the stick-slip transition;

ν is the number density of molecular chains adsorbed at the interface;

K_B is constant ;

T is temperature;

$N_e^{\frac{1}{2}}\alpha$ is the entanglement distance;

The % of area covered by the adsorbed chains at the metal wall and melt interface (θ) is obtained using the single layered adsorption model [10]:

$$\theta = \frac{bv_0}{(1 + bv_0)} \tag{5.8}$$

where v_0 is the number density of molecular chains in the bulk polymer melt and b indicates the intensity of adsorption. In case of polymer melt, strong interface adhesion on capillary wall is observed, which shows that bv_0>>1, and hence $\theta = 1$, which basically means saturated adsorption of molecular chains on capillary wall. So for HDPE melt υ (in equation 5.7) would remain same even under the influence of various nanofillers and varying temperature. Also since the amount of clay fillers used is very low so that will also not affect the HDPE melt υ.So in case of HM1.0 the lower value of P_{min} obtained, which indicates lower wall shear stress for slip flow is due to the increasing entanglement distance by the clay incorporation, which will help in the flow of bulk polymer chains by separating them from the adsorbed chains on the capillary wall.

The die swell of the extrudate indicates the dimensional stability of the polymer melt as it exits the die. The main reasons for the appearance of die swell in polymer are the reorientation and recovery of deformed polymer melt chains as the extrudate leaves the die. It is generally accepted in the literature [15,16] that the die swell occurs due to the elastic recovery of the polymer melt after it emerges from the die. The die swell (B) and the temperature of extrusion in a capillary rheometer are correlated by the following linear relationship in the literature [15,16]:

$$B = \alpha_1 - T\beta_1 \tag{5.9}$$

where α_1 and β_1 are coefficients related to material properties. According to equation 5.6, the die swell of the extrudate emerging from the capillary die should decrease with increasing temperature at a particular strain rate and vice versa. Generally, within the literature good linear fit to this equation is reported [15]. A comparison of the curves in fig 5.14 reveal that the dies swell increases with the decrease in temperature and an increase in the strain rate, but such a behaviour is only shown at 160 and 140^{o}C. On the other hand the die swell remains unchanged and almost negligible when determined at 144^{o}C, which lies in the temperature range of extrusion window. Such a small change in extrudate diameter with the increase in strain rate signifies the importance of MFS phenomenon of HDPE in producing a product with limited dimensional variation after it comes out of the extruder.

It is also clear from fig 5.12 that in the flow induced solidification temperature range (140^{o}C) the die swell increases quite steeply with the increase in strain rate, whereas in the extrusion window temperature range (144^{o}C) the die swell remains more or less constant. This result provides another proof for the liquid crystalline nature of the polymeric melt during the processing window because the liquid crystal polymers due to their chain extension characteristics don't show any die swell regardless of the strain rate employed.

The inclusion of nanoclay particles with high surface area and ease of movement in comparison to the entangled polymeric chains can increase the energy dissipation of the composites at a given shear rate [13]. Also during the extrusion window, slip flow of polymeric melt takes place and during the slip flow most of the adsorbed chains remains tethered on the die wall and free chains slip over these tethered chains and are extruded out with minimum die swell.

In case of nanocomposites with carbon based nanofillers, the matrix and the nanofillers will exhibit unequal retractive forces and hence cause changes in the die swell of the polymer nanocomposites. The data in fig 5.13 shows that minimum die swell for pure HDPE is obtained during the extrusion window and then it increases rapidly during the flow induced crystallisation region due to the formation of fibres which ultimately increase the viscosity and hence produce thick extrudate. In comparison to the normal processing temperature of 160^{o}C the die swell experienced during the extrusion is almost non-existence and hence shows the validity of the melt flow singularity phenomenon for practical extrusion of HDPE. The die swell of the nanocomposites is generally closer to that of pure HDPE but the values for HM are slightly lower than that of HG and HCB. Similar nonlinear decrease of die swell has been observed in other studies were also observed in the cases of carbon black-filled polybutadiene [17], TiO_2-filled HDPE composite [18] and glass bead-filled LDPE composite [19]. In all of these studies the incorporation of nanofillers only caused a slight reduction in the die swell. During the flow of the nanocomposites in the die along with the polymeric melt chains the fillers are also oriented under shear and hence the latter will limit the elastic recovery of the confined polymeric chains after they leave the capillary die.

Fig 5.18 shows a schematic view of the difference between the extrudate diameters (D_e) obtained in the stick flow and slip flow inside the capillary die for pure HDPE and its nanocomposites. The black dots represent the end tethered chains on the die wall, while the entangled lines represent the polymer chains.

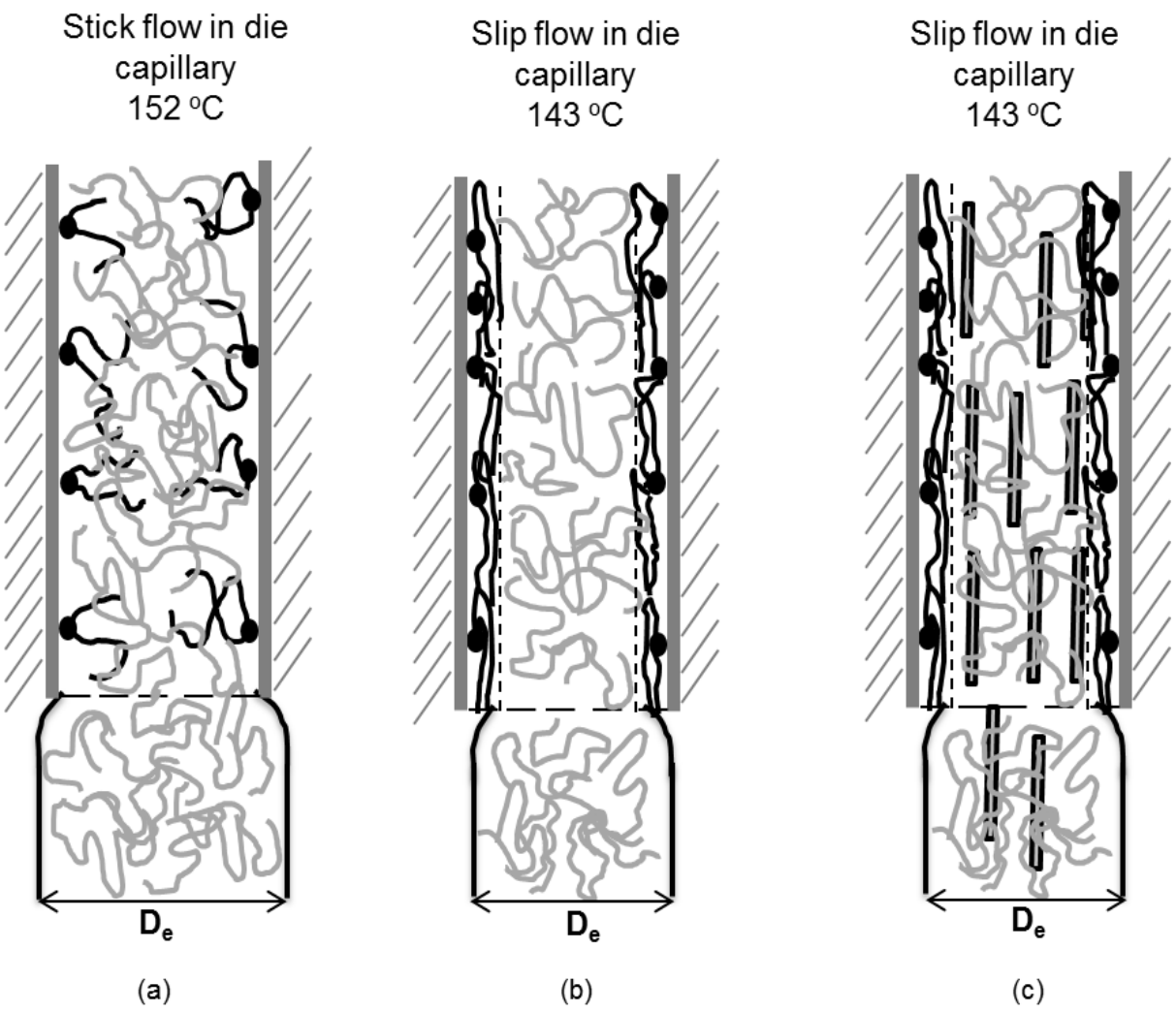

Fig.5.18: Schematic view of the difference between the extrudate diameters (De) obtained in the stick flow at 152°C (a) and slip flow at 143°C (b) inside the capillary die under dynamic cooling conditions and a strain rate of $350s^{-1}$. The black dots represent the end tethered chains on the die wall, while the entangled lines represent the polymer chains. (c) slip flow at 143°C in the presence of clay particles

As the processing temperature of HDPE is decreased, the frequency of adsorption and desorption of the polymer melt chains on the capillary wall will start to increase and the free volume of the polymer melt will also decrease. When the temperature is above the extrusion window (fig 5.18-a) stick flow is likely to occur because the adsorbed chains cannot maintain the stretched chain conformation and they will interact with the bulk polymer chains. In such conditions the die swell of the extrudate will not decrease and the extrudate surface will be rough. When the

temperature is decreased to the extrusion window (fig 5.18-b) the stick flow of the polymer melt will be transformed to slip flow, if the corresponding γ_c^w is applied. Now the die swell of extrudate during this slip flow will depend on the disentanglement degree of the free chains. The slip flow will occur due to the disengagement of the adsorbed chains from the bulk free chains. This disengagement takes place because the stretched chain conformation of the adsorbed chains can be maintained during the temperature scale of the extrusion window. Due to this slip flow the die swell of the extrudate will be reduced as shown in fig 5.18-c.

The platy structure, high aspect ratio and better dispersion of the nanofillers (such as clay, MWCNT and GO) can promote the stretched chain conformation and chain alignment along the flow direction, which ultimately aid in achieving slip flow at higher temperatures and then maintaining it for longer time span than pure HDPE. The addition of oriented high surface area clay layers will limit the elastic recovery of the stretched free polymeric chains and help maintain the disentanglement density achieved in the die capillary, which will ultimately lead to considerably lesser die swell.

5.5: Melt flow Index (MFI)

The melt flow index is one of the simplest tests for measuring the chain mobility of polymers. The MFI values of HDPE and its nanocomposites with Na-MMT, Bentone, BLX and BHX clay were measured at 2.16 and 10.0 kg applied load conditions and then their ratio was calculated to represent the melt flow ratio. The MFI and MFR calculated results are shown in fig 5.19.

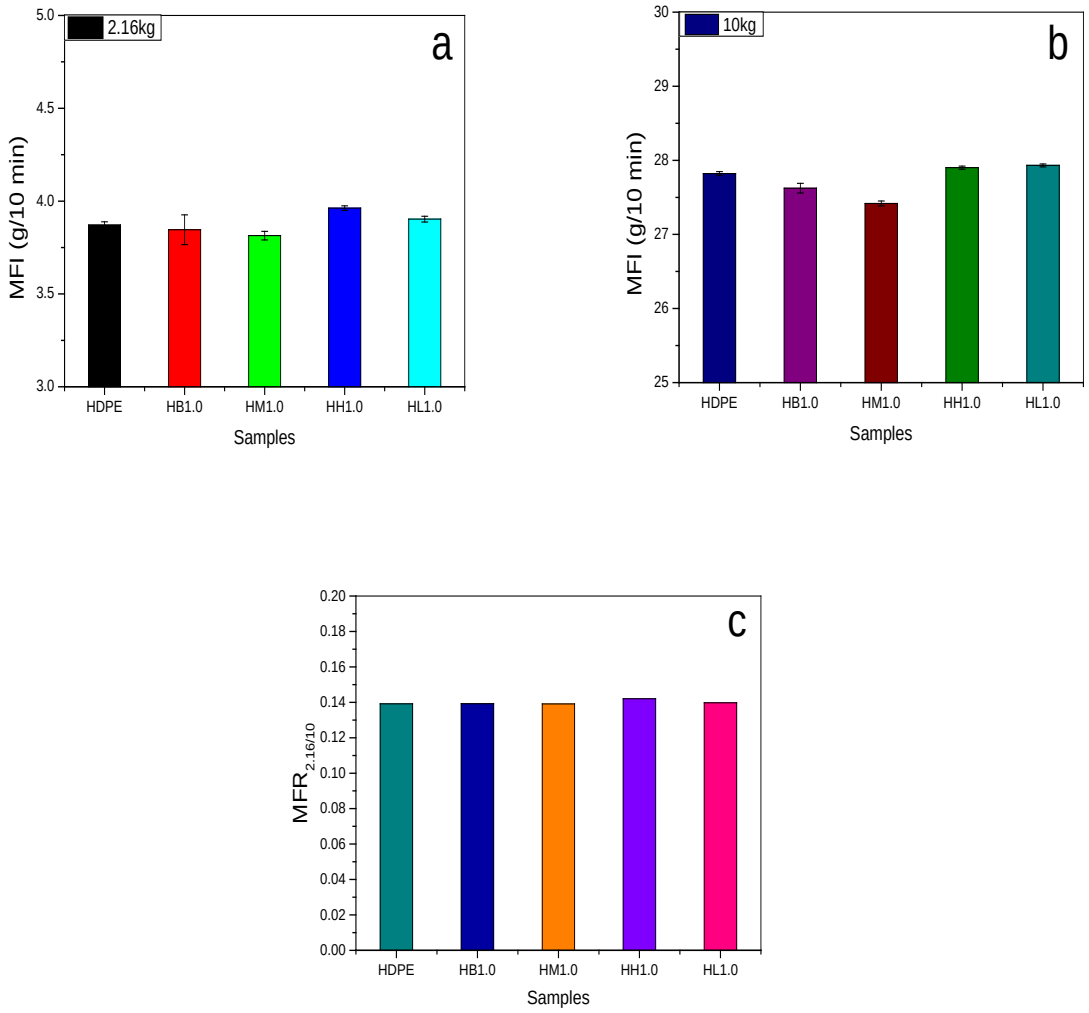

Fig.5.19: MFI results of HDPE and its nanocomposites, (a) MFI values at 2.16 kg load applied, (b) MFI values at 10.0 kg load applied and (c) MFR values which represents the ratio of the MFI at 2.16 kg to the MFI at 10.0 kg

The addition of small quantity of clay that can produce high degree of exfoliation will result in better interaction between the polymer chains and the individual clay platelets and this interaction can reduce chain mobility and hence yield lower values of MFI for nanocomposites (fig 5.19-a). As shown in fig 5.19, the values of MFI for the nanocomposites of HDPE that are exfoliated are slightly lower than pure HDPE and its nanocomposites with two grades of kaolin clay. In case of exfoliated nanocomposites orientation and flow of HDPE chains is restricted because the

HDPE chains are confined in the spacing between clay platelets which causes the MFI of the nanocomposites to decrease. The results are also evident at high strain rate MFI testing (10Kg, fig 5.19-b) although the difference is very minor because at high strain rates nanocomposites tend to show lower pseudoplasticity.

The ratio between the MFI calculated at a lower and higher weight applied is known as MFR (fig 5.19-c) and is often used as a representative of polydispersity index of the polymer. The values of MFR remain almost constant for all the samples and hence indicate that there is very little change in polymer molecular weight as result of all the processing steps. Hence all the samples have degraded to a very small extent during processing.

Conclusion:

In this chapter the melt flow singularity phenomenon of high density polyethylene and its nanocomposites with different clays and carbon based fillers was described in detail. The mechanism of melt flow singularity was analysed by varying the strain rate, filler loading, composite morphology and filler shape along with its dimension, to understand their effect on critical points of the extrusion window recorded during the rheological analysis. The influence of strain rate on the extrusion window indicated an enhancement up to $350s^{-1}$ and after this strain rate the window was reduced due to shorter elastic recovery time. The experimental results also showed that the addition of different clay and carbon based nanofillers resulted in the expansion of extrusion window of HDPE composites and that exfoliated Na-MMT clay/HDPE composites showed the most enhanced window due to the larger interfacial contact area between the polymer chain and the surface of clay layers in the matrix. The HDPE/Na-MMT composites showed the most broadened extrusion window up to $6.5^{o}C$, the best result reported so far. In comparison to the exfoliated clay

composites of HDPE, the intercalated and the micro-composites showed a reduced window with a maximum of 5.2^{o}C window observed for bentone clay composites. In case of extrusion window of nanocomposites based on carbon based nanofiller, 1D carbon nanotubes produced a wide extrusion window of 6.17 ^{o}C, whereas the rest of the fillers apart from CB also contributed in widening the window. The effect of different parameters on the die swell indicated a smooth and shiny extrudate achieved for most of the specimens during the extrusion window interval. In case of extrusion window, 1D carbon nanotubes produced a wide extrusion window of 6.17 ^{o}C, whereas the rest of the fillers apart from CB also contributed in widening the window.

After describing a method of manufacturing HDPE products in this chapter by a low temperature economical technique, in the next chapter a comprehensive review of the effect on barrier and thermal properties of the matrices by different parameters related to the clay fillers are described to help understand the basic mechanism of barrier and thermal resistance offered by polymers nanocomposites. The basic aim of understanding of these mechanisms is to produce cheap polymer products with enhanced barrier and thermal resistance so that the shelf life of polymer packaging products can be improved.

References:

1. Xu, H.; Lele, A.; Rastogi, S. The influence of carbon-based nanofillers on the melt flow singularity of linear polyethylene. Polymer . 2011, 52, 3163–3174.
2. Kolnaar, J. W. H.; A. Keller A temperature window of reduced flow resistance in polyethylene with implications for melt flow rheology: 1. The basic effect and principal parameters. Polymer. 1994, 35, 3863–3874.
3. Kolnaar, J. W. H.; Keller, a. A temperature window of reduced flow resistance in polyethylene with implications for melt flow rheology: 2. Rheological investigations in the extrusion window. Polymer. 1995, 36, 821–836.
4. Kolnaar, J. W. H.; Keller, a. A temperature window of reduced flow resistance in polyethylene with implications for melt flow rheology: 3. Implications for flow instabilities and extrudate distortion. Polymer. 1997, 38, 1817–1833.
5. Wu, Q.; Wang, X.; Gao, W.; Hu, Y.; Qi, Z. Unusual rheological behaviors of linear PE and PE/kaolin composite. J. Appl. Polym. Sci. 2001, 80, 2154–2161.
6. Ariffin, a.; Ariff, Z. M.; Jikan, S. S. Evaluation on extrudate swell and melt fracture of polypropylene/kaolin composites at high shear stress. J. Reinf. Plast. Compos. 2011, 30, 609–619.
7. McNally, T.; Raymond Murphy, W.; Lew, C. Y.; Turner, R. J.; Brennan, G. P. Polyamide-12 layered silicate nanocomposites by melt blending. Polymer. 2003, 44, 2761–2772.
8. Carreau, P.J.; De Kee, D.; Chhabra, R.P. Rheology of Polymeric Systems, Principles and Applications; Hanser, Munich, Vienna, NY, 1997.
9. Bird, R. B.; Armstrong, R. C.; Hassager, O. Dynamics of Polymeric Liquids, Wiley Interscience, NY, 1987.

10. Brochard, F.; De Gennes, P. G. Shear-dependent slippage at a polymer/solid interface. Langmuir 1992, 8, 3033–3037.
11. Wang, S.-Q.; Drda, P. a. Stick-slip transition in capillary flow of linear polyethylene: 3. Surface conditions. Rheol. Acta 1997, 36, 128–134.
12. Brochard-Wyart, F.; Gay, C.; de Gennes, P.-G. Slippage of Polymer Melts on Grafted Surfaces. Macromolecules 1996, 29, 377–382.
13. Jin, J.; Chen, L.; Song, M. A Study of Energy Dissipation in Exfoliated Polyurethane/Organoclay Nanocomposites. J. Nanosci. Nanotechnol. 2009, 9, 6453–6459.
14. Dazhu, C.; Haiyang, Y.; Pingsheng, H.; Weian, Z. Rheological and extrusion behavior of intercalated high-impact polystyrene/organomontmorillonite nanocomposites. Compos. Sci. Technol. 2005, 65, 1593–1600.
15. Muksing, N.; Nithitanakul, M.; Grady, B. P.; Magaraphan, R. Melt rheology and extrudate swell of organobentonite-filled polypropylene nanocomposites. Polym. Test. 2008, 27, 470–479.
16. Liang, J.; Ness, J. The melt die-swell behaviour during capillary extrusion of LDPE/PP blends. Polym. Test. 1998, 17, 179–189.
17. White, J. L.; Crowder, J. W. The Influence of Carbon Black on the Extrusion Characteristics and Rheological Properties of Elastomers : Polybutadiene and Butadiene-Styrene Copolymer. J. Appl. Polym. Sci. 1974, 18, 1013–1038.
18. Minagawa, N.; White, J. L. The influence of titanium dioxide on the rheological and extrusion properties of polymer melts. J. Appl. Polym. Sci. 1976, 20, 501–523.

19. Liang, J.; Li, R. K. Y.; Tang, C. Y.; Cheung, S. W. Die – Swell Behavior of Glass Bead-Filled Low-Density Polyethylene Composite Melts at High Extrusion Rates. J. Appl. Polym. Sci. 1999, 76, 419–424.

CHAPTER 6: BARRIER PROPERTIES OF POLYETHYLENE AND NYLON12 NANOCOMPOSITES

6.1: Introduction

Polymeric materials are now being used throughout the world in packaging industries as alternatives to traditional packaging materials such as glass, metals, paper etc. Polymeric materials are widely used in food, toys, clothes, beverages and in a number of other packaging industries. Although polymeric materials have the distinct advantages of balanced properties such as: light weight, low cost, toughness, flexibility, easy processing, recycling and post-formation printing but they do permeate different gases and vapours to some extent. The use of glass and metal in most of the beverages packaging throughout the world is due to their total barrier to the transfer of different gases and vapours. Barrier polymers being used in the industry have the ability to restrict the passage of gases, aroma, liquids and vapours to some extent but the ideal requirement from the industry is to have a single material which can significantly restrict the flow of different penetrants along with being inexpensive, recyclable and also possess ideal combination of mechanical, optical and thermal characteristics. No such material is available in the polymeric family of materials and therefore the selection of a polymeric material to be used in the packaging industry requires a trade-off between properties and cost.

There are number of approaches adopted in the packaging industry such as multilayer structures, polymer blends, polymer composites etc. that are intended to produce products in an efficient and economical method and with enhanced shelf life. Out of all of these approaches polymeric nanocomposites are a new class of materials where small quantities of high aspect ratio nano platelets can improve the barrier properties of polymers and produce products with significantly reduced

thickness. Since their development in the 1990s polymer clay nanocomposites have been mainly developed and researched for improving mechanical and thermal performance of polymeric products [1, 2, 3]. Apart from these main advantages barrier properties can also be improved by incorporating clay nanoparticles in polymers [4, 5, 6]. Organoclay based nanocomposites of a number of commodity and engineering grade thermoplastic polymers like polypropylene, polyethylene, polyamide, polystyrene, poly(ethylene terephthalate), polyethylene oxide, liquid crystalline polymers, thermoplastic elastomers etc have been studied [7,8].

One of the misconceptions in the early development of nanocomposites was that if mechanical properties improve then the barrier properties of the nanocomposites will improve too, this is not always true because these both properties depend on different microstructural factors [9, 10]. Since the nanofillers are added in very small quantity so they don't affect the optical properties of the polymer matrix because there is very little change in polymer volume and they also help keep the overall packaging light and cheap [11]. The platelet geometry of most of the nanofillers can provide a tortuous path, which hinders the molecular diffusion of penetrant through the polymer and results in decrease in permeability. Permeability of nanocomposite is dependent on different factors such as mass fraction, aspect ratio, dispersion and orientation of nanofiller in polymer matrix [12]. One of the main goals of this research is to develop better polyolefin packaging with enhanced barrier properties. In order to achieve this goal, the effect of clay weight percentage, clay morphology and clay aspect ratio on HDPE and LLDPE barrier and thermal properties are presented in this chapter and then the results are compared to Nylon12 nanocomposites barrier and thermal properties to get a full understanding of the effect of different variables on the final characteristics of the developed nanocomposites.

6.2: Barrier properties of nanocomposites

In this section a detailed analysis of the barrier properties of HDPE, LLDPE and Nylon12 nanocomposites is presented. All of data in the graphs will be presented in terms of the volume fraction of fillers. In order to convert the weight fractions of the fillers inside the nanocomposites to the volume fraction of fillers, the volume and mass fraction have to be defined. The volume fraction of filler (v_f) is defined as the ratio of volume of filler (V_f) and the total volume of composite ($V_f + V_m$):

$$v_f = \frac{V_f}{V_f + V_m} \tag{6.1}$$

In the above equation V_m is the volume of matrix. By using the standard definition of density the volume fraction of filler can be rewritten as:

$$v_f = \frac{\frac{M_f}{\rho_f}}{\frac{M_f}{\rho_f} + \frac{M_m}{\rho_m}} \tag{6.2}$$

In the above equation M_f,ρ_f, M_m, ρ_m represents the mass and density of filler and matrix respectively. The overall mass of the composite (M) is the sum of mass of filler and matrix:

$$M = M_f + M_m \tag{6.3}$$

The mass fraction of filler (m_f) or matrix (m_m) is defined as the ratio of mass of filler (M_f) or mass of matrix (M_m) and the mass of composite ($M_f + M_m$):

$$m_f = \frac{M_f}{M_f + M_m}$$

$$m_f M = M_f$$

$$m_m = \frac{M_m}{M_f + M_m}$$

$$(1 - m_f)M = M_m$$

By placing values of M_f and M_m in equation 2, the volume fraction of filler can be represented as:

$$v_f = \frac{\frac{m_f M}{\rho_f}}{\frac{m_f M}{\rho_f} + \frac{(1 - m_f)M}{\rho_m}}$$

or

$$v_f = \frac{m_f}{m_f + \frac{(1 - m_f)\rho_f}{\rho_m}} \quad (6.4)$$

By using the densities of filler (obtained from the materials supplier's sheet) and densities of matrix, the mass fraction of filler can be converted to the volume fraction of filler.

6.2.1: Water vapour and oxygen permeability of HDPE and its nanocomposites with BHX and BLX clay

The oxygen permeability and water vapour permeability data for HDPE and its nanocomposites with BHX and BLX clay at loadings between 0 and 10 wt % are shown in tables 6.1 and 6.2. The data in both these tables shows that the introduction of inorganic clay material clearly affected the gas and water vapour permeability of HDPE. WVTR for pure HDPE is 9.05 gm-mil/m^2-day, whereas with the addition of 3 wt % of BHX clay the permeability is reduced to 7.11 gm-mil/m^2-day,

which presents a 21.44% decrease of permeability. With the addition of 10 wt % of BHX clay the water vapour permeability decreases to 3.85 gm-mil/m^2-day, which corresponds to 57.46 decreases in permeability. This is not the maximum decrease in permeability recorded for this set of specimens as the % decreases for HH5.0 is 64.20 % and with regards to HH5.0 the permeability slightly increases at HH10.0. The addition of 5 wt % of clay presents a threshold point for the permeability of this system. Also for the whole nanocomposite system the increase in permeability spans across 5 wt % of clay content (fig 6.1) before the permeability gradually levels off.

Table 6.1: Water vapour transmission rate (WVTR) data of HDPE and its nanocomposites with BHX and BLX clay

Specimen	Mass fraction of filler	Volume Fraction of filler	P_C (gm-mil/m^2-day)	P_C/P_P	% decrease
HDPE	0	0	9.05	1.00	0.00
HH1.0	0.01	0.0036	8.74	0.97	3.43
HH2.0	0.02	0.0073	8.01	0.89	11.49
HH3.0	0.03	0.0111	7.11	0.79	21.44
HH5.0	0.05	0.0187	3.24	0.36	64.20
HH10.0	0.1	0.0386	3.85	0.43	57.46
HL1.0	0.01	0.0036	8.87	0.98	1.99
HH2.0	0.02	0.0073	8.12	0.90	10.28
HL3.0	0.03	0.0111	7.85	0.87	13.26
HL5.0	0.05	0.0187	4.22	0.47	53.37
HL10.0	0.1	0.0386	4.86	0.54	46.30

The data in table 6.1 shows that the introduction of BLX clay reduces the water vapour permeability of HDPE, but the relative decrease in the WVTR values for BLX

nanocomposites is less than that of BHX clay. In case of WVTR only a decrease of 13.26 % is observed up to 3 wt % addition of BLX clay whereas for higher wt % nanocomposites HL 5.0 and HL10.0 the WVTR decreases sharply and a percentage decrease of 53.37 % is observed for HL 5.0. The decrease in permeability trend as shown in fig 6.1 once again shows the levelling effect for higher wt % 5 of BLX clay addition and the slight increase in WVTR for HL10.0.

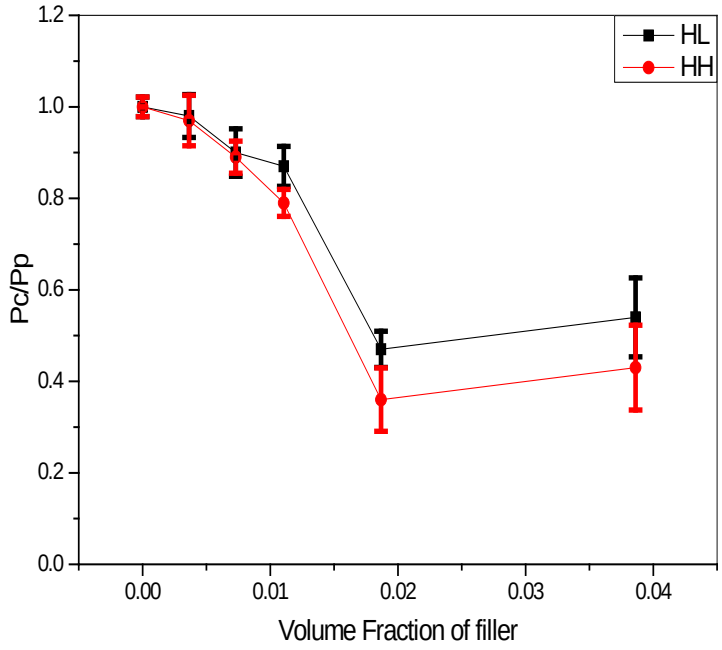

Fig. 6.1: Relative (P_c/P_p) water vapour transmission rate (WVTR) of HDPE and its nanocomposites with BHX and BLX clay

The comparison between the two different grades of kaolin clay clearly shows the dependence of barrier property enhancement on the aspect ratio of the filler. In case of BHX the overall reduction at HH5.0 is almost 12% higher than that of HL5.0. This difference shows the higher that higher diffusion time is required for the water molecules to diffuse through the BHX based nanocomposites in comparison to the

BLX based nanocomposites. The effect of high aspect ratio filler particle on the diffusion path of penetrant thorough a polymer matrix is shown schematically in fig 6.2.

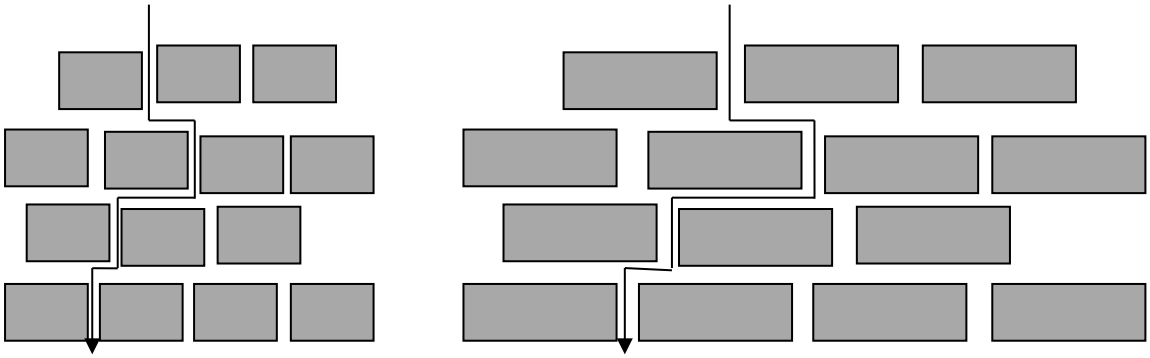

BLX clay dispersed in polymer BHX clay dispersed in polymer

Fig. 6.2: Schematic illustration of effect of clay particles with high aspect ratio on the path of diffusion for penetrants through a polymer

For pure HDPE, the O2TR is 50.42 cc-mm/m^2-days and with the addition of BHX clay the permeability decreases gradually and for HH3.0 the permeability decreases to 35.91 cc-mm/m^2-days. The negative % decrease for HL1.0 could be due to the experimental error introduced during specimen preparation. The % decrease in oxygen permeability up to 3 wt % addition of BHX clay is 28.78%, while the addition of 10 wt % of clay causes a reduction of 41.51%. Just like the WVTR data the threshold point for O2TR is 5 wt % of BHX clay addition, as the decrease in the oxygen permeability is maximum at this point. Also the levelling effect after the addition of 5 wt addition of BHX clay (fig 6.3) is observed for O2TR analysis. The maximum decrease in oxygen permeability is 18.62 % less than that of the decrease in water vapour permeability. In case of BLX clay based nanocomposites, although the permeability decreases with the addition of BLX clay, but for HL1.0 the permeability increases slightly to 53.81 cc-mm/m^2-days. This increase could be due

to any micro-sized air holes present in the specimens which could have caused the permeability to increase. The decreasing trend in the O2TR for BLX based HDPE nanocomposites (fig 6.3) is similar to the BHX based nanocomposites with a maximum decrease of 38.40 % observed for HL5.0 and just like in WVTR the overall reduction is lesser than that of BHX based nanocomposites. The maximum decrease in O2TR for HL5.0 is 7 % less than that of HH5.0.

Table 6.2: Oxygen transmission rate (O2TR) data of HDPE and its nanocomposites with BHX and BLX clay

Specimen	Mass fraction of filler	Volume Fraction of filler	P_C (cc-mm/m^2-day)	P_C/P_P	% decrease
HDPE	0	0	50.42	1.00	0.00
HH1.0	0.01	0.0036	43.93	0.87	12.87
HH2.0	0.02	0.0073	42.46	0.84	15.79
HH3.0	0.03	0.0111	35.91	0.71	28.78
HH5.0	0.05	0.0187	27.44	0.54	45.58
HH10.0	0.1	0.0386	29.49	0.58	41.51
HL1.0	0.01	0.0036	53.81	1.07	-6.72
HL2.0	0.02	0.0073	46.65	0.93	7.48
HL3.0	0.03	0.0111	42.56	0.84	15.59
HL5.0	0.05	0.0187	31.06	0.62	38.40
HL10.0	0.1	0.0386	33.42	0.66	33.72

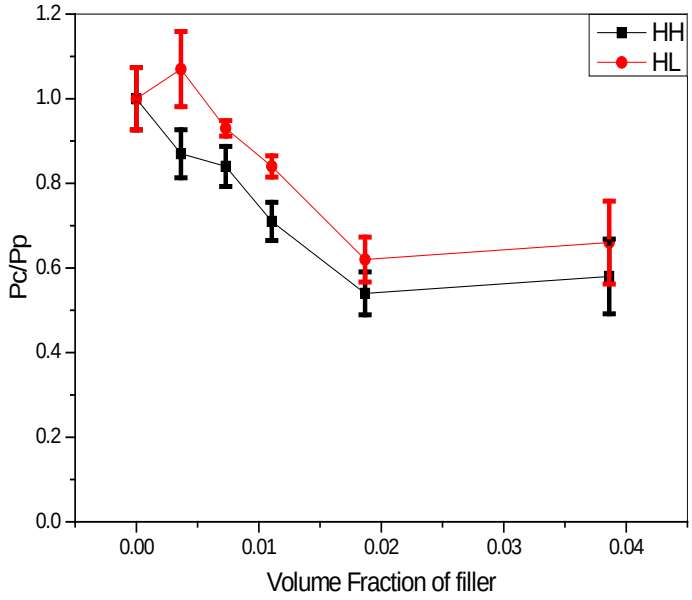

Fig. 6.3: Relative (P_c/P_p) Oxygen transmission rate (O2TR) of HDPE and its nanocomposites with BHX and BLX clay

The van der Waals volumes of oxygen and water molecules are similar but the transport mechanisms of these penetrants in a flexible polymer are different and are dependent on the repeating unit of the polymer [13, 14]. If a polymer is nonpolar, then the transfer of water vapours through it will be difficult and these nonpolar polymers such as different polyolefins will have very small WVTR, however the transfer of polar water molecule through polar polymers such as different polyamides and polyesters will be high because of the ability of the water molecules to form water clusters inside polymer matrix and defuse more easily through polar polymers. Also the water molecules have the ability to plasticize the polar polymer and hence reduce its glass transition temperature and the overall crystallinity, which would ultimately cause a reduction in WVTR.

.On the other hand the transfer of non-polar oxygen is very high through non-polar polymer due to the formation of oxygen clusters in non-polar polymers and the change in polarity caused by the addition of different clay layers [15]. The clusters formation can increase the void volume in polymer matrix and this leads to enhanced permeation. Also for low weight percentage of clay addition the solubility of penetrant in polymer matrix is not changed much and the permeability is governed by the diffusivity of the penetrant through the polymer matrix, but for high weight percentage of clay addition the solubility of penetrant in the polymer will be increased and that can increase the enthalpy of solution and this increase will ultimately increase the permeability of penetrant. This increase in permeability of penetrant is evident because of the dependence of permeability on the phenomenon of penetrant solubility through the matrix.

Although in case of all HDPE kaolin clay nanocomposites, no exfoliation of the individual clay layers was observed but through uniform dispersion and distribution of clay stacks achieved by the patented pre-mixing method along with the melt compounding, a labyrinth or a stair case structure of clay stacks was attained that can create a more tortuous path for the permeant molecule to diffuse through the HDPE matrix. Also the clay stacks will maintain their original layer length and not break down or bend during processing because they are able to withstand the harsh stress condition the nanocomposites have to experience while flowing through the extruders and the post extrusion steps. This high resistance of the clay stacks along with enhanced barrier properties give them an added advantage over exfoliated individual clay layers which can be damaged during processing.

6.2.2: Water vapour and oxygen permeability of LLDPE and its nanocomposites with BHX and BLX clay

LLDPE is the second polymer matrix utilized for studying the effect of BHX and BLX on its barrier properties. In comparison to HDPE, density and percentage crystallinity of LLDPE are slightly lower but the basic chain structure of LLDPE is also different from HDPE because of the short chains attached to its basic backbone chain which can create more free volume. The short chain branching distribution (SCBD) of LLDPE is not uniform across all polymer chains and hence their heterogeneous SCBD leads to non-uniform distribution of thicker crystallites and lower optical clarity [16]. LLDPE is mainly used as a sealant in layered barrier packaging and improvement in its barrier properties are required because of the harsh conditions of relative humidity and temperature variations that the outer layer of packaging product come across during their whole product life. THE O2TR and WVTR data for LLDPE and its nanocomposites with 1 to 10 wt % of BHX and BLX clay are shown in table 6.3 and 6.4.

The WVTR for pure LLDPE is 9.57 gm-mil/m^2-day and this value is very close to the WVTR for HDPE. With the addition of 1 wt % of BHX clay the WVTR of LLDPE was reduced by only 7.31 % and this reduction in the WVTR continued up to LH5.0 where the water vapour permeability was reduced to 6.17 gm-mil/m^2-day which corresponds to a % decrease of almost 36 %. The negative % decrease for LL1.0 could be due to the experimental error introduced during specimen preparation. In comparison to BHX the addition of BLX in HDPE caused only a 29 % maximum reduction in the WVTR. In case of BLX based nanocomposites the reduction in WVTR is almost 7 % less than that of BHX based nanocomposites of HDPE. Also the maximum reduction in WVTR of LLDPE (LH5.0=36%) based clay

nanocomposites is 28 % lesser than that of the HDPE (HH5.0=64%) based clay nanocomposites. This difference clearly indicates that the distribution and alignment of clay inside HDPE is much more uniform with very small clay agglomerate formation as revealed by the OM, TEM and SEM analysis.

Table 6.3: Water vapour transmission rate (WVTR) data of LLDPE and its nanocomposites with BHX and BLX clay

Specimen	Mass fraction of filler	Volume Fraction of filler	P_C (gm-mil/m^2-day)	P_C/P_P	% decrease
LLDPE	0	0	9.57	1.00	0.00
LH1.0	0.01	0.0036	8.87	0.93	7.31
LH2.0	0.02	0.0072	7.89	0.82	17.55
LH3.0	0.03	0.0108	7.36	0.77	23.09
LH5.0	0.05	0.0182	6.17	0.64	35.53
LH10.0	0.1	0.0377	6.84	0.71	28.53
LL1.0	0.01	0.0036	10.65	1.11	-11.29
LL2.0	0.02	0.0072	9.07	0.95	5.22
LL3.0	0.03	0.0108	8.25	0.86	13.79
LL5.0	0.05	0.0182	6.81	0.71	28.84
LL10.0	0.1	0.0377	8.21	0.86	14.21

The trend in the WVTR decrease for BHX and BLX based LLDPE nanocomposites is different from their HDPE nanocomposites as shown in fig 6.4. Instead of observing a sharp decline at 5 wt % the permeability decreases gradually up to LH5.0 and LL5.0 and then for LH10.0 and LL10.0 the water vapour permeability rises steeply. This increase in permeation rate could be due to the creation of free space at the interface of clay agglomerate and the polymer matrix. The formation of agglomerates

at higher weight fractions also limits the uniform distribution of the clay inside the LLDPE matrix.

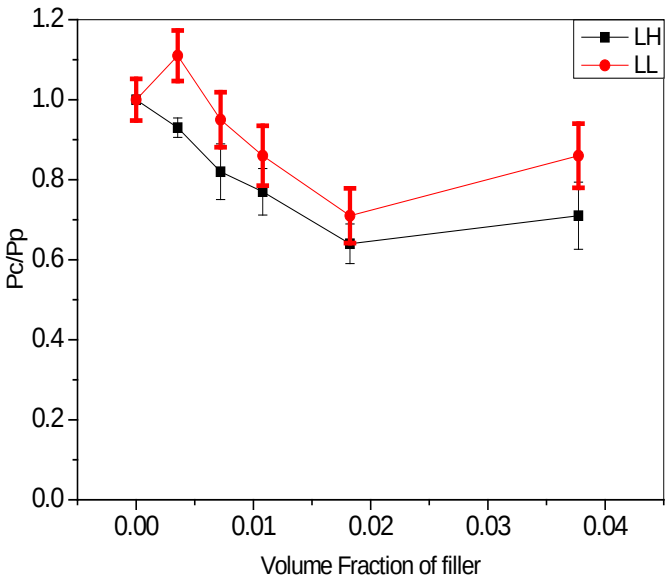

Fig. 6.4: Relative (P_c/P_p) water vapour transmission rate (WVTR) of LLDPE and its nanocomposites with BHX and BLX clay

The O2TR for pure LLDPE is 78.95 cc-mm/m^2-days and with the inclusion of 2 wt % of BHX clay the permeability decreases to 74.28 cc-mm/m^2-days which represent a decrease of only 5.92 %. With further addition of BHX clay up to 5 wt % a sharp decline of 28.04% is observed. For the highest wt % BHX clay specimens of 10 wt % the permeability once again slightly increases with respect to the decrease observed at LH5.0. In comparsion to BHX clay the addition of BLX clay caused a steady decrease of permeability up to 5 wt% after which the decrease was levelled off. The maximum decrease in permeability of 26% was observed for LL5.0 which is 2% less than in comparison to LH5.0.

Table 6.4: Oxygen transmission rate (O2TR) data of LLDPE and its nanocomposites with BHX and BLX clay

Specimen	Mass fraction of filler	Volume Fraction of filler	P_C cc/m^2-day	P_C/P_P	% decrease
LLDPE	0	0	78.95	1.00	0.00
LH1.0	0.01	0.0036	76.82	0.97	2.70
LH2.0	0.02	0.0072	74.28	0.94	5.92
LH3.0	0.03	0.0108	64.59	0.82	18.19
LH5.0	0.05	0.0182	56.81	0.72	28.04
LH10.0	0.1	0.0377	57.94	0.73	26.61
LL1.0	0.01	0.0036	77.83	0.99	1.42
LL2.0	0.02	0.0072	74.31	0.94	5.88
LL3.0	0.03	0.0108	67.54	0.86	14.45
LL5.0	0.05	0.0182	58.46	0.74	25.95
LL10.0	0.1	0.0377	60.21	0.76	23.74

In case of LLDPE/BHX and LLDPE/BLX nanocomposites the oxygen barrier properties follow the same trend (fig. 6.5) as the HDPE nanocomposites but the relative decrease in the maximum permeability is considerably lower, e.g. in case of HH5.0 the maximum decrease of 46 % was observed which is 18 % more than that of LH5.0 and for LL5.0 the difference between the permeability with HL5.0 is 12 %.These differences clearly shows the effect of clay aspect ratio on the oxygen barrier properties of LLDPE and how even better dispersion requires larger clay layer to reduce the barrier properties.

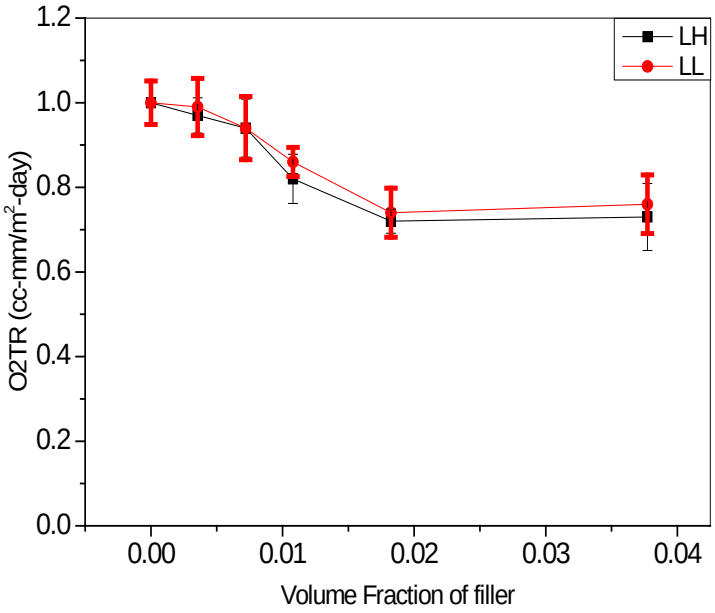

Fig. 6.5: Relative (P_c/P_p) oxygen transmission rate (O2TR) of LLDPE and its nanocomposites with BHX and BLX clay

6.2.3: Water vapour and oxygen permeability of Nylon12 and its nanocomposites with BHX and BLX clay

The oxygen permeability and water vapour permeability data for Nylon12 and its nanocomposites with BHX clay at loading between 0 and 5 wt % and with BLX clay at loading between 0 and 5 wt % are shown in tables 6.5 and 6.6. The data in both these tables shows that the dispersion and distribution of BHX and BLX clay in Nylon12 clearly affected the oxygen and water vapour permeability of Nylon12 and the reduction in permeability is once again affected by the clay aspect ratio, degree of dispersion, distribution and clay quantity.

Table 6.5: Water vapour transmission rate (WVTR) data of Nylon12 and its nanocomposites with BHX and BLX clay

Specimen	Mass fraction of filler	Volume Fraction of filler	P_C (gm-mil/m^2-day)	P_C/P_P	% decrease
Nylon12	0	0	26.40	1.00	0.00
NH1.0	0.01	0.0040	25.80	0.98	2.27
NH2.0	0.02	0.0080	23.56	0.89	10.76
NH3.0	0.03	0.0121	21.37	0.81	19.05
NH5.0	0.05	0.0204	19.50	0.74	26.14
NL1.0	0.01	0.0040	24.63	0.93	6.70
NL2.0	0.02	0.0080	23.91	0.91	9.43
NL3.0	0.03	0.0121	22.05	0.84	16.48
NL5.0	0.05	0.0204	21.08	0.79	22.39

The WVTR for pure Nylon12 is 26.40 gm-mil/m^2-day and with addition of 1 wt % of BHX and BLX clay the permeability is only reduced by 2.27 and 6.7 %. Although the water vapour permeability is only slightly decreased by the addition of 1 wt % of both kaolin clays but at higher concentrations the barrier properties are significantly reduced. In case of NH5.0 the WVTR is reduced to 19.50 gm-mil/m^2-day which represents a % decrease of 26.14 in comparison to pure Nylon12. On the other hand the WVTR for NL3.0 is 22.05 gm-mil/m^2-days, which is slightly lesser than in comparison to NH3.0. Once again the maximum decrease in the WVTR is observed for the BHX clay which has higher aspect ratio in comparison to the BLX clay and thus represents a higher diffusion time for the water vapours to penetrate through the Nylon12 matrix. The threshold point for WVTR in Nylon12 is observed at 5.0 wt % of

clay addition. The decrease in WVTR for both the BHX and BLX based nanocomposites of Nylon12 is shown in fig. 6.6.

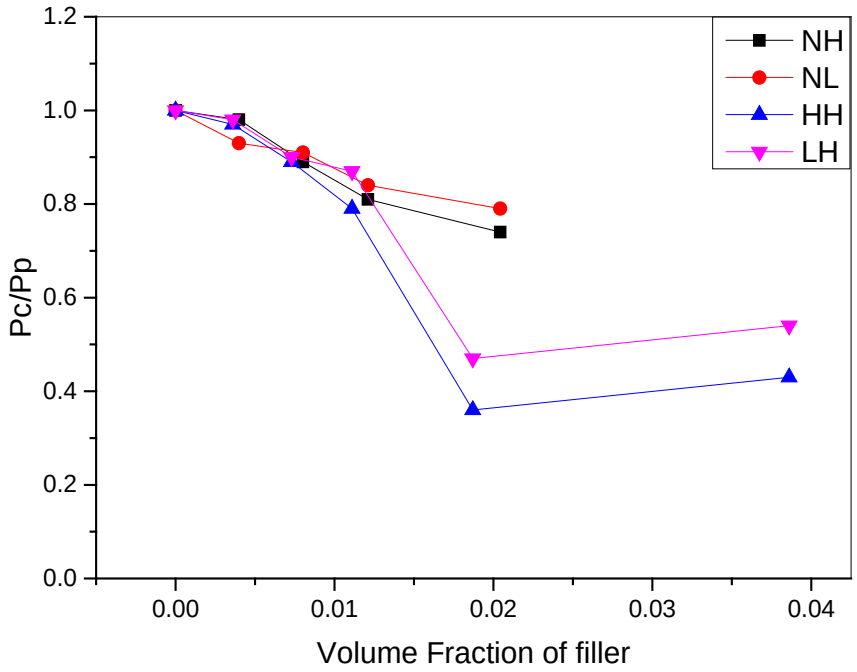

Fig. 6.6: Relative (P_c/P_p) water vapour transmission rate (WVTR) of Nylon12, HDPE, LLDPE and their nanocomposites with BHX clay

Although the decreasing trend for Nylon12 nanocomposites is similar to the one observed in case of HDPE nanocomposites and LLDPE nanocomposites but the % decrease in WVTR for Nylon 12 nanocomposites is much less in comparison to the HDPE and even LLDPE nanocomposites. Both HDPE and LLDPE are non-polar polymers and therefore they offer very high resistance to the penetration of water molecules through their structure. Also both HDPE and LLDPE have a higher degree of crystallinity present in them in comparison to Nylon12 and therefore the free volume and the amorphous region in these polymers is much lesser as compared to Nylon12. Also the enhanced crystalline regions for the polyolefins would create an

increased tortuosity path for the permeant molecules. All these factors lead to a decrease in the solubility and diffusion of the permeant gas molecule.

Table 6.6: Oxygen transmission rate (O2TR) data of Nylon12 and its nanocomposites with BHX clay

Specimen	Mass fraction of filler	Volume Fraction of filler	P_C (cc-mm/m^2-day)	P_C/P_P	% decrease
Nylon12	0	0	15.56	1.00	0.00
NH1.0	0.01	0.0040	9.75	0.61	39.36
NH2.0	0.02	0.0080	8.10	0.50	49.62
NH3.0	0.03	0.0121	6.88	0.43	57.21
NH5.0	0.05	0.0204	6.09	0.38	62.14
NL1.0	0.01	0.0040	11.05	0.71	28.95
NL2.0	0.02	0.0080	8.71	0.56	44.03
NL3.0	0.03	0.0121	7.93	0.51	49.03
NL5.0	0.05	0.0204	7.04	0.45	54.76

The O2TR for pure Nylon12 is 15.56 cc-mm/m^2-day. The O2TR for Nylon12 is less than the polyolefin studied in this report because of the polar nature of amide groups present in its chain. The decrease in oxygen permeability of Nylon12 with the addition of even small amounts of clay addition showed a remarkable decrease in the permeability. In case of BHX based nanocomposites the permeability decreased by 50% with the addition of only 2 wt% of clay and for NH5.0 the permeability was decreased to 6.09 cc-mm/m^2-day, which represents a 62 % decrease in permeability.

On the other hand the permeability of the BLX based nanocomposites of Nylon12 also showed a decreasing trend but the decrease in permeability was relatively lower

in comparison to BHX nanocomposites. For NL1.0 the O2TR was reduced to 11.05 cc-mm/m^2-day and with the further addition of 3 wt % BLX clay an almost 50 % decrease in permeability was observed. This remarkable reduction in the oxygen permeability could be due to the well dispersed clay layers in Nylon12 and also because of the internal hydrophilic structure of Nylon12. The decrease in O2TR for both the BHX and BLX based nanocomposites of Nylon12 is shown in fig 6.7.

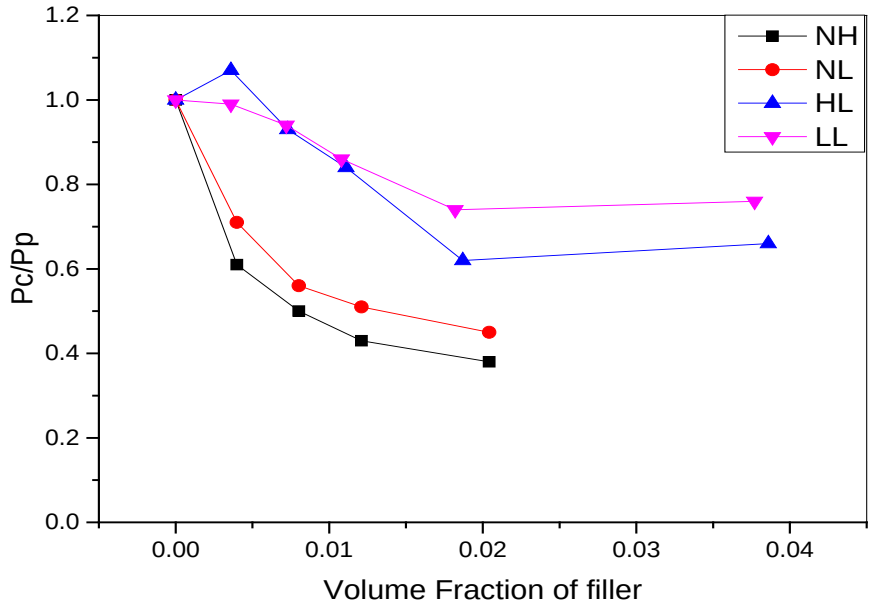

Fig. 6.7: Relative (P_c/P_p) oxygen transmission rate (O2TR) of Nylon12, HDPE, LLDPE and their nanocomposites with BLX clay

The decrease in nylon nanocomposites WVTR is less dramatic as compared to their O2TR values because of the polar and highly hydrophobic nature of nylon12. The solubility of small amount of water in a hydrophilic polymer can disrupt its intermolecular bonds because of the plasticizing nature of water molecules. Such structural changes lead to enhanced chain mobility and a decrease in glass transition temperature that would ultimately effect the density of the nanocomposite and hence its permeability. Since the water molecules plasticizes nylon12 and

causes high mobility of its chains, the tortuous path created by the inclusion of platy clay particles may vary and affect the barrier properties of nylon12 nanocomposites.

6.2.4: Water vapour and oxygen permeability of HDPE, LLDPE and their nanocomposites with Na-MMT clay

The Na-MMT clay based nanocomposites for both HDPE and LLDPE matrices showed either exfoliation or varying degree of intercalation as presented by the XRD analysis and based on the microscopic analysis these morphologies were also confirmed. In case of high weight percentage specimens of Na-MMT clay the specimens produced by the pre-blending technique showed larger agglomerates of clay and polymer particles, hence they were further grinded by using a mortar and pestle to produce a fine powder of polymer coated with clay particles. These specimens were initially extruded and compression moulded but the specimens showed large clay agglomerates dispersed throughout the specimens but after the mortar and pestle treatment almost all of these micron sized agglomerates were not visible.

The WVTR and O2TR data for HDPE, LLDPE and their nanocomposites with Na-MMT clay are shown in table 6.7 and 6.8. The decrease in the water vapour permeability of Na-MMT based HDPE and LLDPE nanocomposites showed a gradual decreasing trend with the addition of 5 wt % of Na-MMT clay after which the permeability levelled off (Fig 6.8, 6.9).

For the low weight percentage specimens of HDPE and LLDPE filled with Na-MMT, a maximum decrease of 29.25 % and 25.65 % in water vapour permeability was observed for HM2.5 and LM2.5, which in comparison to HH3.0, LH3.0, HL3.0 and LL3.0 is significantly higher as HH3.0, LH3.0, HL3.0 and LL3.0 showed relatively

lower water vapour permeability. These results indicate the effectiveness of clay exfoliation or partial intercalation on the barrier properties of HDPE and LLDPE matrices. At low wt % of clay addition the results for WVTR show that an exfoliated or intercalated specimen will show better barrier properties in comparison to non-exfoliated or non-intercalated composites based on kaolin clay, whereas for specimens containing high weight percentage of Na-MMT the morphology as revealed by XRD and TEM analysis is that of a macro-composite.

Table 6.7: Water vapour transmission rate (WVTR) data of HDPE, LLDPE and their nanocomposites with Na-MMT clay

Specimen	Mass fraction of filler	Volume Fraction of filler	P_C (gm-mil/m^2-day)	P_C/P_P	% decrease
HDPE	0	0	9.05	1.00	0.00
HM0.5	0.005	0.0018	9.12	1.01	-0.77
HM1.0	0.01	0.0054	7.35	0.81	18.76
HM2.5	0.025	0.0090	6.40	0.71	29.25
HM5.0	0.05	0.0183	5.10	0.56	43.62
HM10.0	0.1	0.0379	5.22	0.58	42.32
LLDPE	0	0	9.57	1.00	0.00
LM0.5	0.005	0.0019	8.66	0.91	9.46
LM1.0	0.015	0.0059	7.99	0.83	16.52
LM2.5	0.025	0.0099	7.11	0.74	25.65
LM5.0	0.05	0.0179	6.74	0.70	29.57
LM10.0	0.1	0.0370	6.83	0.71	28.63

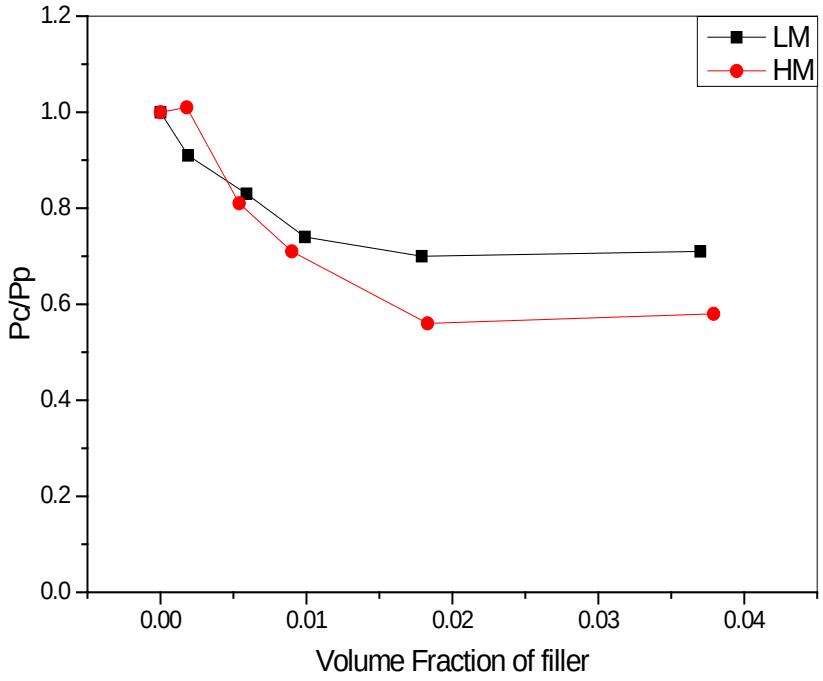

Fig. 6.8: Relative (P_c/P_p) water vapour transmission rate (WVTR) of HDPE, LLDPE and their nanocomposites with Na-MMT clay

In case of HM5.0 and LM5.0, the water vapour permeability was reduced to 5.10 gm-mil/m^2-day and this represented a maximum decrease of 43.62% while for HM10.0 the permeability was reduced by 42.32%. A maximum of 39.61 % decrease in water vapour permeability for LLDPE filled with Na-MMT clay was also observed. The WVTR for LM5.0 was 6.74 gm-mil/m^2-day, while the permeability for LM10.0 was 6.83 gm-mil/m^2-day. Both these nanocomposites showed a 29% reduction in the overall permeability of LLDPE matrix with Na-MMT clay addition. In comparison to their high wt% kaolin clay based specimens the relative decrease in the permeability for Na-MMT based HDPE and LLDPE nanocomposites were relatively lower.

The decrease in O2TR for both HDPE and LLDPE nanocomposites with Na-MMT is shown in fig 6.9. In case of low weight percentage specimens of HDPE and LLDPE filled with Na-MMT, the O2TR decreases up to 15 and 20 % for HM2.5 and LM2.5

respectively. With the increase in filler quantity up to 5 wt%, the O2TR decreases up to 40.45cc-mm/m^2-day and 61.94cc-mm/m^2-day for HM5.0 and LM5.0 respectively, these values indicate that the decreasing trend in the O2TR is less steep just like the WVTR data and the oxygen permeability remains almost the same when the weight percentage is further increased. In comparison to both the kaolin filled HDPE and LLDPE nanocomposites, their Na-MMT specimens showed much less decrease in permeability which could be attributed to the agglomerate formation tendency of Na-MMT clay at high weight percentage.

Table 6.8: Oxygen transmission rate (O2TR) data of HDPE, LLDPE and their nanocomposites with Na-MMT clay

Specimen	Mass fraction of filler	Volume Fraction of filler	P_C cc-mm/m^2-day	P_C/P_P	% decrease
HDPE	0	0	50.42	1.00	0.00
HM0.5	0.005	0.0018	48.75	0.97	3.31
HM1.0	0.01	0.0054	43.49	0.86	13.74
HM2.5	0.025	0.0090	42.57	0.84	15.57
HM5.0	0.05	0.0183	40.45	0.80	19.77
HM10.0	0.1	0.0379	40.03	0.79	20.61
LLDPE	0	0	78.95	1.00	0.00
LM0.5	0.005	0.0019	74.37	0.94	5.80
LM1.0	0.015	0.0059	66.76	0.85	15.44
LM2.5	0.025	0.0099	62.63	0.79	20.67
LM5.0	0.05	0.0179	61.94	0.78	21.55
LM10.0	0.1	0.0370	62.32	0.79	21.06

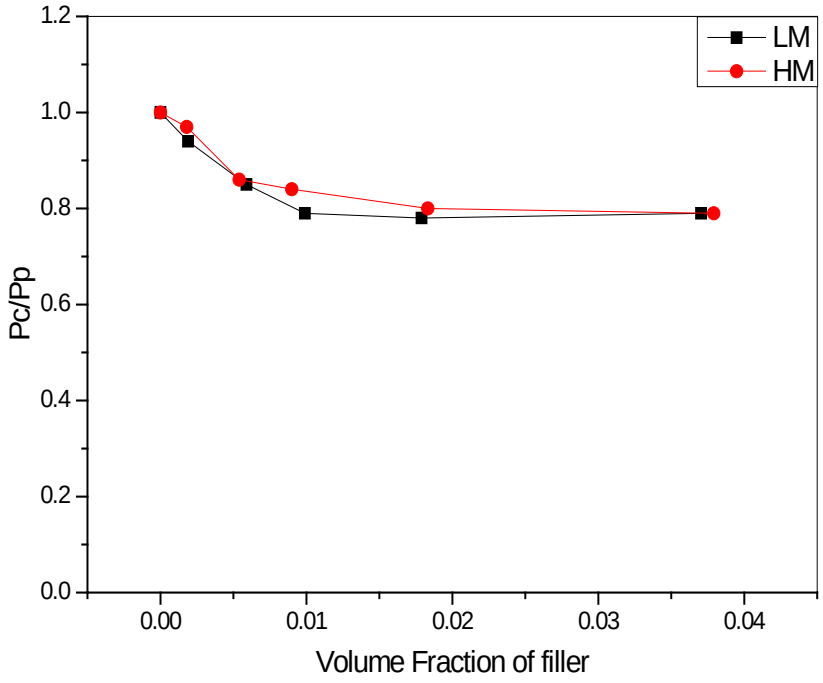

Fig. 6.9: Relative (P_c/P_p) oxygen transmission rate (O2TR) of HDPE, LLDPE and their nanocomposites with Na-MMT clay

6.3: Theoretical modelling for prediction of barrier properties

In the past few decades, a number of models have been used to describe the permeation behaviour of polymer nanocomposites. Most of these models are based upon the tortuous path theory, which was based upon three assumptions: (1) The nanofillers added to polymer matrix are totally impermeable to gas and liquid permeant, (2) The interface between the nanofiller and the matrix is perfect and is totally impermeable to gas and liquid permeant, (3) The barrier properties of the matrix are not altered by the addition of nanofiller. All of the models thus assume that the addition of fillers will create a tortuous path which will force the permeant to wiggle around the filler particles in a random fashion and hence increase the permeation path of permeant which will lead to effective decrease in permeability. In

this section, different models developed for permeant transport though a media (Nielsen, and Cussler) are applied to the permeability data described in the previous sections to explain the disparity between the experimental and theoretical data of clay based nanocomposites.

6.3.1: Nielsen Model

Nielsen model [17] is one of the most popular models used for predicting and modelling the gas barrier properties of polymer nanocomposites. The Nielsen model describes the tortuosity effect of plate-like fillers on the gas barrier properties of polymer composites structures. The Nielsen model was proposed as the first tortuous path model to explain the permeability of filled composites in 1967. The basic assumptions adopted in developing this model are that the particles added to the polymer matrix are uniform platelets that are impermeable to the diffusing gas or liquid molecules and the particles are homogeneously dispersed and oriented perpendicular to the diffusion direction.

$$\frac{P_c}{P_o} = \frac{\left(1 - \phi_f\right)}{1 + \alpha\phi_f} \tag{6.5}$$

In the above equation 6.1, $\frac{P_c}{P_o}$ represents the relative permeability of the polymer with P_c representing the permeability of composites and P_o representing the permeability of pure polymer. Also ϕ_f and α represents the volume fraction and aspect ratio of filler. The relative permeability coefficient of the Nielsen model for various volume fractions of filler is plotted in fig 6.10. Each curve shown in fig 6.10 is plotted for a specific aspect ratio of filler. The aspect ratio of the filler is varied from 10-500 in fig

6.10. The curves represent the ideal plots for a filler quantity and aspect ratio effect on the permeability of a polymer matrix according to Nielsen model.

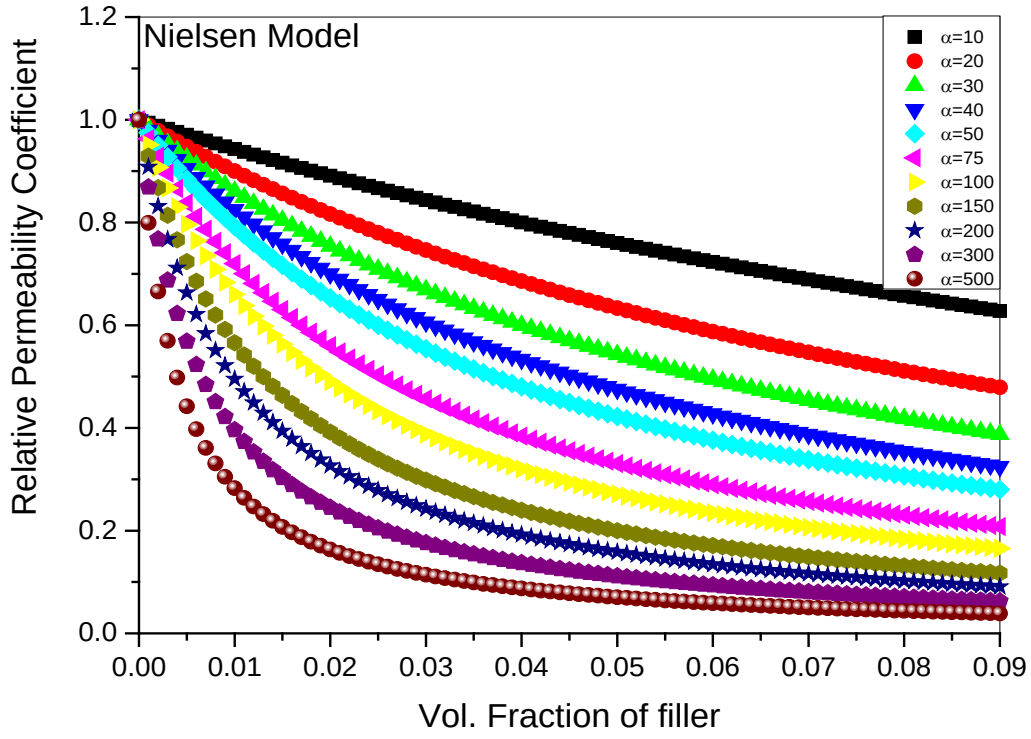

Fig. 6.100: Relative permeability coefficient vs. volume fraction plot of Nielsen model for different aspect ratio of filler

Fig 6.11 represents the water vapour permeability data for HH, HL, LH, LL, NH, NL, HM and LM nanocomposites plotted on the Nielsen model curves for different clay aspect ratios. The experimental data for nanocomposites fits the Nielsen model for aspect ratio between 10 and 200 and the maximum aspect ratio is observed for HH nanocomposites. In order to represent a singular value for the aspect ratio of clay in a particular matrix, α_{avg} (average aspect ratio) was calculated using the values presents the curve closet to each relative permeability point. Standard deviation for the data of each nanocomposite was also calculated to represent the variation

between the individual values. Since no chemical modification of the fillers was carried during sample preparation, so it can be assumed that this aspect ratio represents the size dimension of the clay agglomerate instead of individual clay layers.

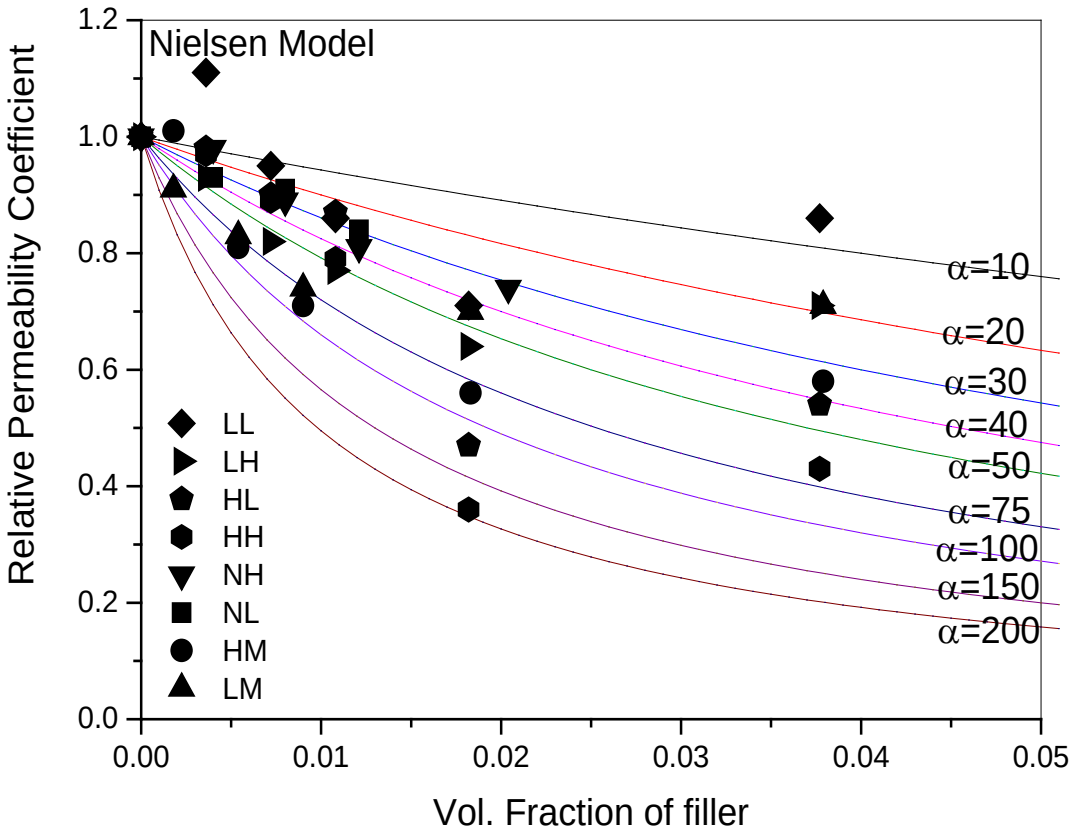

Fig. 6.11: Relative water vapour permeability coefficient of the nanocomposites (HH, HL, LH, LL, NH, NL, HM and LM) as a function of their filler content, plotted along with the solid lines which represents the Nielsen model curves for different aspect ratio (10-200) of the filler

As shown in fig 6.11, the Nielsen model was better fitted for the Nylon12 based system instead of the two polyolefin based nanocomposites. In case of both HDPE and LLDPE matrices, a critical percolation threshold is observed at 5 wt% of kaolin clay addition and hence these nanocomposites show large variation from the ideal

Nielsen model. In case of Nylon12 based systems, no such critical percolation threshold was observed and hence the Nylon12 nanocomposites permeability data is better fitted by Nielsen model. The maximum aspect ratio (α_{max}) observed for a particular nanocomposite permeability data is shown in table 6.9. The table also shows the α_{avg} values and their corresponding standard deviation values. The variation in the values of α_{max} and α_{avg} shown in table 6.9 for the same clay are there because they represent the values for clay agglomerate and not their individual layers.

The α_{max} values reported in table 6.9 show that the highest value of 200 is observed for HH nanocomposites and the minimum values of 40 is observed for both Nylon12 nanocomposites. The α_{max} values show that HH and HM nanocomposites produced maximum reduction in permeability as compared to LLDPE and Nylon12 nanocomposites. The α_{avg} values calculated from the relative permeability indicate the highest aspect ratio of 71 for BHX clay and a minimum of 12 for BLX clay. The α_{avg} values indicate that the BHX clay has much more surface area in comparison to BLX clay and the values of Na-MMT clay are also closer to BHX clay for both HDPE and LLDPE. The higher standard deviation values for HH(67.05), HL(31.62), HM(36.82) and LM(28.39) are because of the drastic reduction in permeability as the weight percentage is increased from 3 to 5 wt%. The standard deviation values of LL, LH, NH and NL nanocomposites are much lower in comparison to other nanocomposites and hence indicate a better fit of Nielsen model for these systems.

The relative oxygen permeability data for HH, HL, LH, LL, NH, NL, HM and LM nanocomposites plotted on the Nielsen model curves for different clay aspect ratios is shown in fig. 6.12.

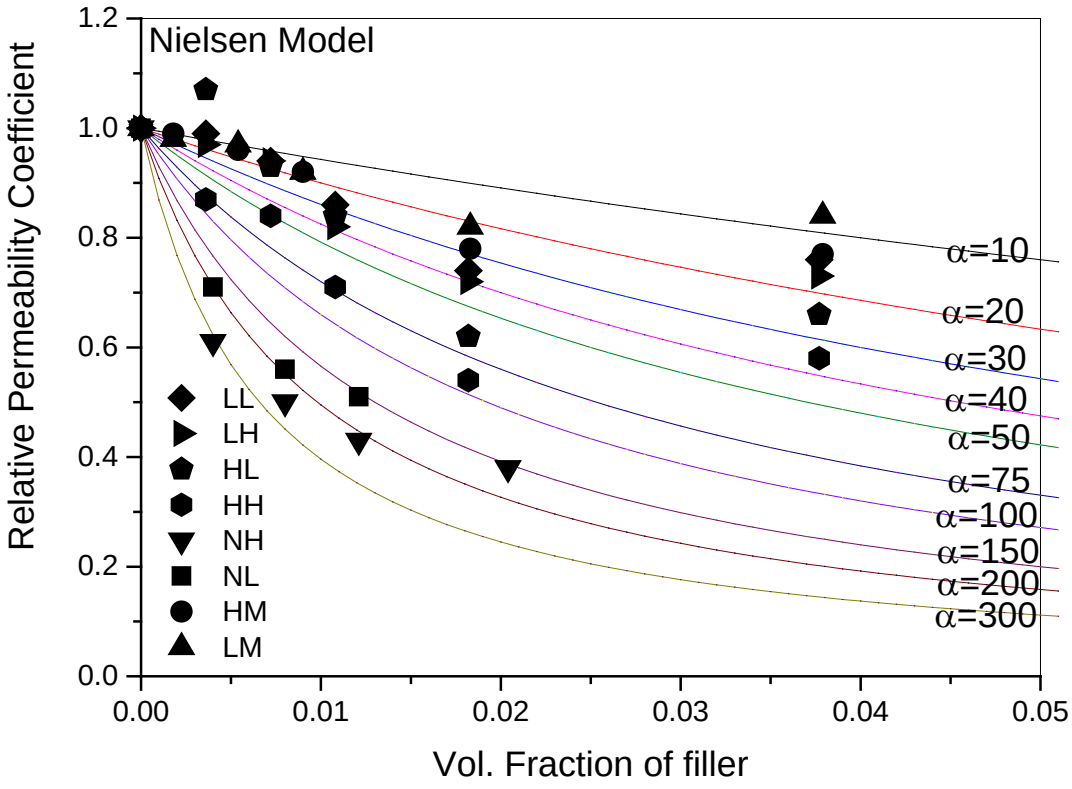

Fig. 6.12: Relative oxygen permeability coefficient of the nanocomposites (HH, HL, LH, LL, NH, NL, HM and LM) as a function of their filler content, plotted along with the solid lines which represents the Nielsen model curves for different aspect ratio (10-300) of the filler

The experimental data for nanocomposites is fitted on the Nielsen model for aspect ratios between 10 and 300. The Nielsen model calculated maximum aspect ratio (α_{max}), average aspect ratio (α_{avg}) and related standard deviation values of nanocomposites (HH, HL, LH, LL, NH, NL, HM and LM) for WVTR and O2TR analysis are shown in table 6.9. In case of oxygen permeability data, the highest α_{max} (200) and α_{avg} (188, 183) is observed for NH and NL specimens respectively. Although the rest of the specimens show lower values of both α_{max} and α_{avg}, but their values are much closer to the microscopic aspect ratio values calculated from the TEM analysis in chapter 4.

Table 6.9: Nielsen model calculated maximum aspect ratio (αmax), average aspect ratio (αavg) and related standard deviation values of nanocomposites (HH, HL, LH, LL, NH, NL, HM and LM) for WVTR and O2TR analysis

Specimen	WVTR			O2TR		
	α_{max}	α_{avg}	Standard deviation	α_{max}	α_{avg}	Standard deviation
HH	200	71	67.05	100	53	24.82
HL	100	38	31.62	75	27	22.89
LH	75	48	21.12	40	24	9.8
LL	50	12	16	40	20	11.66
NH	40	27.5	10.89	200	188	21.65
NL	40	30	8.16	200	183	23.57
HM	100	62	36.82	30	18	7.48
LM	100	63	28.39	30	18	7.48

6.3.2: Cussler Model

The Cussler model [18] was developed for the diffusion of small gas molecules through a matrix filled with impermeable particles. Based on systematic studies, Cussler and his co-workers brought additional factors (shape, dimensional polydispersity and array of the dispersed nano-platelets) to consider during modelling than Nielsen model. Just like the Nielsen model, the particles are assumed to be oriented perpendicular to the direction of permeant diffusion and the filler particles have high aspect ratio which makes the diffusion two dimensional. The diffusion is mainly related to three factors: the tortuous wiggles to get around the

flakes, the tight slits between the flakes and the resistance of going from the wiggle to the slit.

The relative permeability coefficient of the Cussler model for various volume fractions of filler is plotted in fig 6.13. Each curve shown in fig 6.13 is plotted for a specific aspect ratio of filler. The aspect ratio of the filler is varied from 10-500 in fig 6.13. The curves represent the ideal plots which indicate the effect of filler quantity and aspect ratio on the permeability of a polymer matrix according to Cussler model.

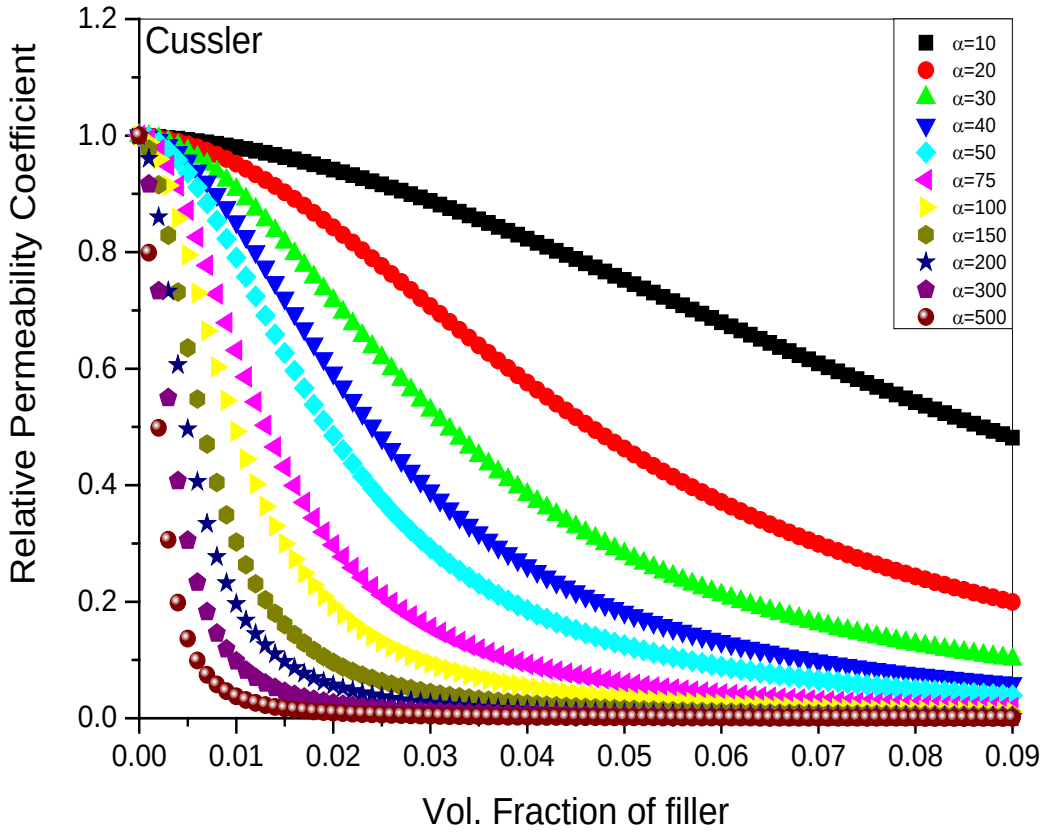

Fig. 6.13: Relative permeability coefficient vs. volume fraction plot of Cussler model for different aspect ratio of filler

The basic correlations for the Cussler model are given below:

$$\frac{D_c}{D_o} = \frac{1-\phi_f}{\left(1-\phi_f\right)+(\tau-1)^2} = \left(1+\frac{\alpha^2\phi_f^2}{1-\phi_f}\right)^{-1} \quad (6.6)$$

$$\frac{P_c}{P_o} = \frac{\left(1-\phi_f\right)^2}{\left(1-\phi_f\right)+\alpha^2\phi_f^2} \quad (6.7)$$

In the above equation 6.1, $\frac{\mathrm{D}_c}{\mathrm{D}_o}$ represents the relative diffusivity of the polymer with D_c representing the diffusivity of composites and D_o representing the diffusivity of pure polymer. Also ϕ_f and α represents the volume fraction and aspect ratio of filler. Fig 6.14 and 6.15 represents the water vapour and oxygen permeability data for HH, HL, LH, LL, NH, NL, HM and LM nanocomposites plotted on the Cussler model curves for different clay aspect ratios.

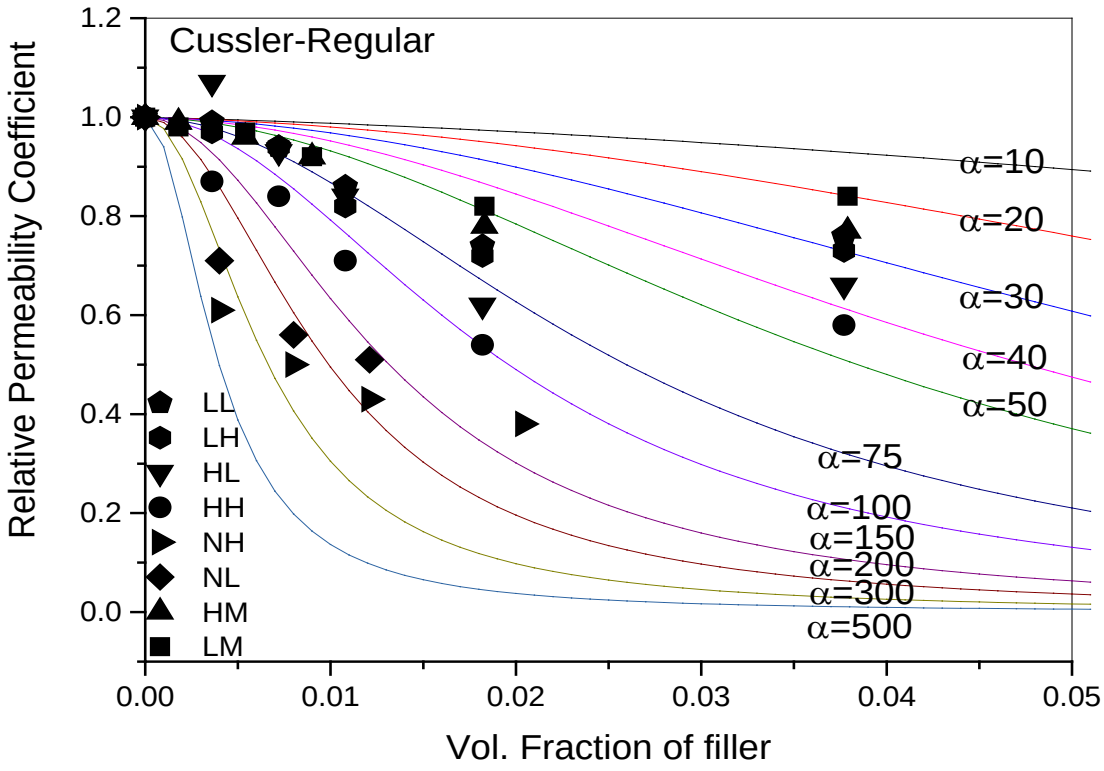

Fig. 6.14: Relative water vapour permeability coefficient of the nanocomposites (HH, HL, LH, LL, NH, NL, HM and LM) as a function of their filler content, plotted along with the solid lines which represents the Cussler model curves for different aspect ratio (10-500) of the filler

The Cussler model calculated maximum aspect ratio (α_{max}), average aspect ratio (α_{avg}) and related standard deviation values of nanocomposites (HH, HL, LH, LL, NH, NL, HM and LM) for WVTR and O2TR analysis are shown in table 6.10.

In case of Cussler model, the highest α_{max} (300) is achieved for O2TR of NH and NL specimens, these values are even higher than the values predicted by the Nielsen model for NH and NL specimens. Also in comparison to Nielsen model the values of α_{max} for the rest of specimens are higher for the Na-MMT specimens (HM=200, LM=150) and lower for the kaolin based nanocomposites with the exception of LH (150) where an increase is observed. The standard deviation values are once again

higher for the larger values and lower for the specimens which showed lower average aspect ratio. The difference between the values predicted by these models is once again vey higher in comparison to the aspect ratio values obtained from the TEM analysis presented in chapter 4.

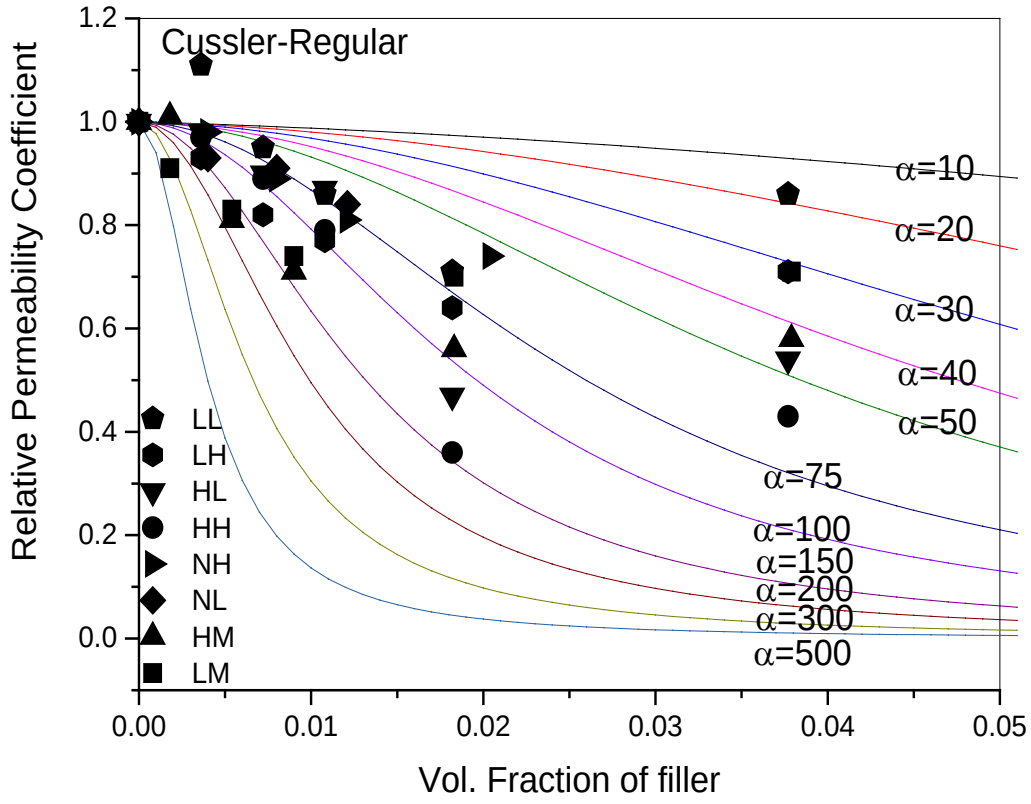

Fig. 6.15: Relative oxygen permeability coefficient of the nanocomposites (HH, HL, LH, LL, NH, NL, HM and LM) as a function of their filler content, plotted along with the solid lines which represents the Cussler model curves for different aspect ratio (10-500) of the filler

Table 6.10: Cussler model calculated maximum aspect ratio (αmax), average aspect ratio (αavg) and related standard deviation values of nanocomposites (HH, HL, LH, LL, NH, NL, HM and LM) for WVTR and O2TR analysis

Specimen	WVTR			O2TR		
	α_{max}	α_{avg}	Standard deviation	α_{max}	α_{avg}	Standard deviation
HH	150	100	31.62	200	108	51.54
HL	150	90	33.91	75	55	26.27
LH	150	101	45.87	100	71	22.67
LL	75	46	27.09	75	54	18.28
NH	75	69	10.83	300	188	73.95
NL	120	90	21.21	300	217	62.36
HM	200	100	69.57	75	56	17.15
LM	150	111	49.84	75	49	17.44

6.4: Thermal analysis of nanocomposites

DSC is a fundamental thermal analysis technique that is widely utilized in polymer science to measure a range of thermal polymer transitions. In DSC analysis, a sample of known mass is heated or cooled, under a controlled time-temperature program, and changes in the heat capacity of the sample are determined through changes in heat flow that occur to or from the sample, against a reference.

Differential scanning calorimetry (DSC) was utilized to measure the melting temperatures (T_m), crystallization temperatures (T_c), and fusion enthalpy (ΔH_m) of the polymer matrixes and their nanocomposites.

The degree of crystallinity of pure matrix and the nanocomposites was calculated as expressed by the following equation:

$$Crstallinity(\%) = \left[\frac{\Delta H_m}{(1-\theta)\,\Delta H^0{}_m}\right] * 100$$

Where ΔH_m is the apparent melting enthalpy, θ is the mass fraction of added filler and $\Delta H^0{}_m$ is the enthalpy corresponding to the melting of 100 % crystalline HDPE () [19], LLDPE and nylon 12 (209.2 J/g) [20].

6.4.1: Thermal analysis of HDPE and its nanocomposites

The DSC analysis of HDPE and its nanocomposites with BHX and BLX clays was carried out under non-isothermal conditions to analyse the effect of kaolin clay addition on the thermal characteristics of HDPE. The melting and cooling curves observed during the DSC analysis for HDPE and its nanocomposites with BHX and BLX clays are shown in fig 6.16. The curves shown in fig 6.16 are plotted using the "Stacked lines by Y offsets" functions of Origin9.1® software. The DSC data (melting and crystallization temperatures, percentage crystallinity and the relative crystallinity of HDPE) is shown in table 6.11. The variation in the thermal transition temperature of HDPE nanocomposites with the increase in filler weight percentage is shown in fig 6.17. The data in table 6.11 and fig. 6.17 shows that with the addition of 3 wt.% of BHX and BLX kaolin clays, both the T_c and T_m remains unchanged and the thermal characteristics of these HDPE nanocomposites are comparable to those of pure HDPE matrix. On the other hand when the filler quantity is increased to 5 weight

percentage, both the thermal transition temperature increases and with the further increase in filler quantity the increasing trend is less steep as shown in fig 6.17.

Xin Wang et al [21] observed the increase in melting temperature for ultra-high molecular weight polyethylene (UHMWPE)/Kaolin composites prepared by a polymerization-filling process. The increase in melting temperature was observed for 5wt. % composites and for higher wt. % specimens the increase gradually levelled off. The increase in melting temperature was attributed to good interaction between polyethylene chains and kaolin particles.

C.S. Reddy et al [22] also observed an increase in the melting temperature for kaolin filled polyethylene nanocomposites. They also compared the kaolin based specimens with Cloisite-20A and nanosilica filled nanocomposites and detected that only kaolin filler caused an increase in melting temperature of polyethylene. The difference in melting temperature of the nanocomposites was attributed to the nucleating capability of nanofiller in the respective nanocomposites.

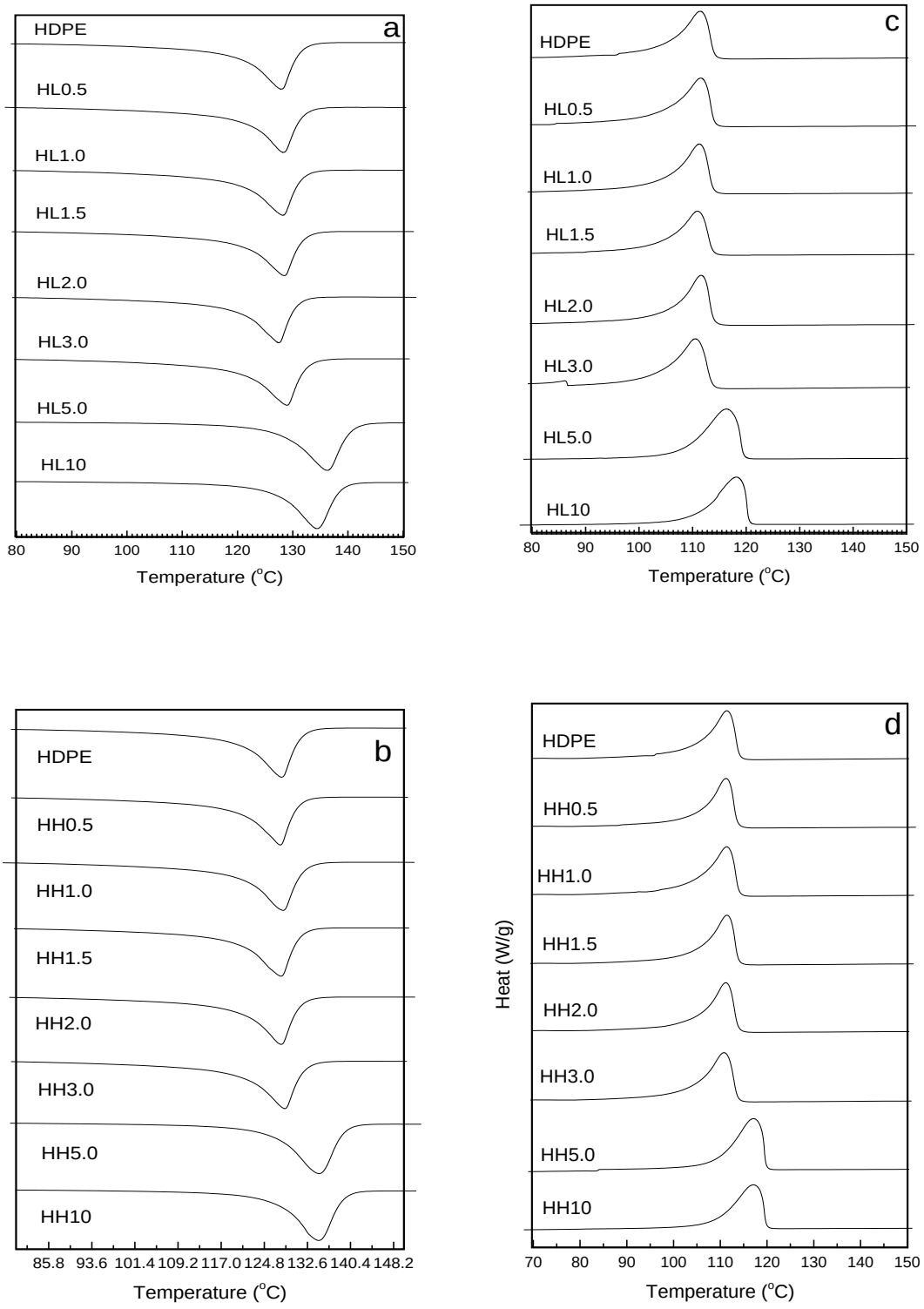

Fig. 6.16: Melting (a, b) and cooling (c, d) curves for HDPE and its nanocomposites with BLX and BHX kaolin clays

Table 6.11: DSC data for HDPE and its nanocomposites with BHX and BLX clay

Samples	T_c (^oC)	T_m (^oC)	$X_{c\ (total)}$ (%)	$(X_c)_c/(X_c)_p$
HDPE	111.40	127.93	53.41	1.00
HL0.5	111.51	128.31	47.74	0.74
HL1	111.25	128.22	46.16	0.80
HL1.5	110.92	128.46	48.08	0.78
HL2	111.58	127.48	49.73	0.86
HL3	110.51	128.95	48.81	0.67
HL5	113.80	139.09	62.15	1.16
HL10	118.70	134.40	63.87	1.19
HH0.5	111.22	129.64	54.44	0.94
HH1	111.38	128.21	51.85	0.90
HH1.5	111.44	127.84	51.28	0.89
HH2	110.80	127.86	49.00	0.85
HH3	111.59	128.52	47.50	0.82
HH5	115.77	136.96	61.29	1.17
HH10	118.17	134.63	64.26	1.18

The data in table 6.11 also clearly shows that the Xc slightly changes with the addition up to 3wt.% of both kaolin clays. The percentage crystallinity of the nanocomposites decreases with the addition of both kaolin clays up to 3 wt.% and after that when the clay quantity is increased up to 5 wt.% the percentage crystallinity increases up to 62 and 61 % for BLX and BHX based nanocomposites respectively. The increasing trend of percentage crystallinity continues up to 10 wt.%

of both BHX and BLX clay addition. Overall the variation in percentage crystallinity of the developed nanocomposites still remains close to 10% which is close to the limits of experimental error involved during the DSC analysis. In order to observe that whether with the increment of clay addition from 3 to 5 wt.% the overall crystallinity of HDPE increases, polarized optical microscopy of the nanocomposites was carried out.

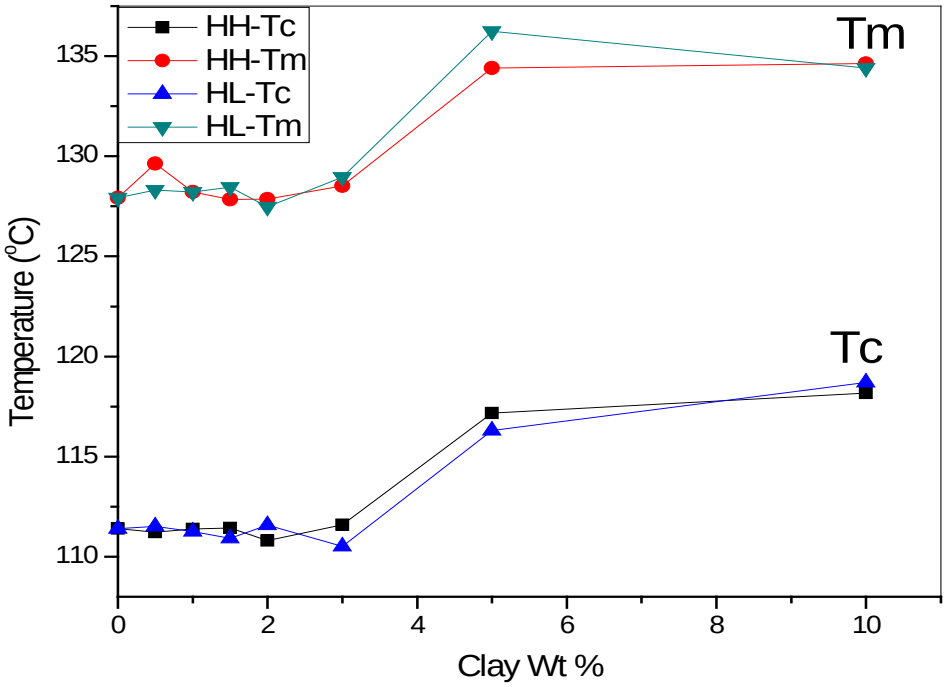

Fig. 6.17: Thermal transition temperatures (Tm and Tc) of nanocomposites (HH and HL) as a function of the clay weight percentage

Fig 6.18 shows the polarized optical micrographs of HDPE and its nanocomposites with BHX and BLX clay. The figures reveal the usual maltese cross patterns which indicate the spherulite structure for HDPE and its nanocomposites.

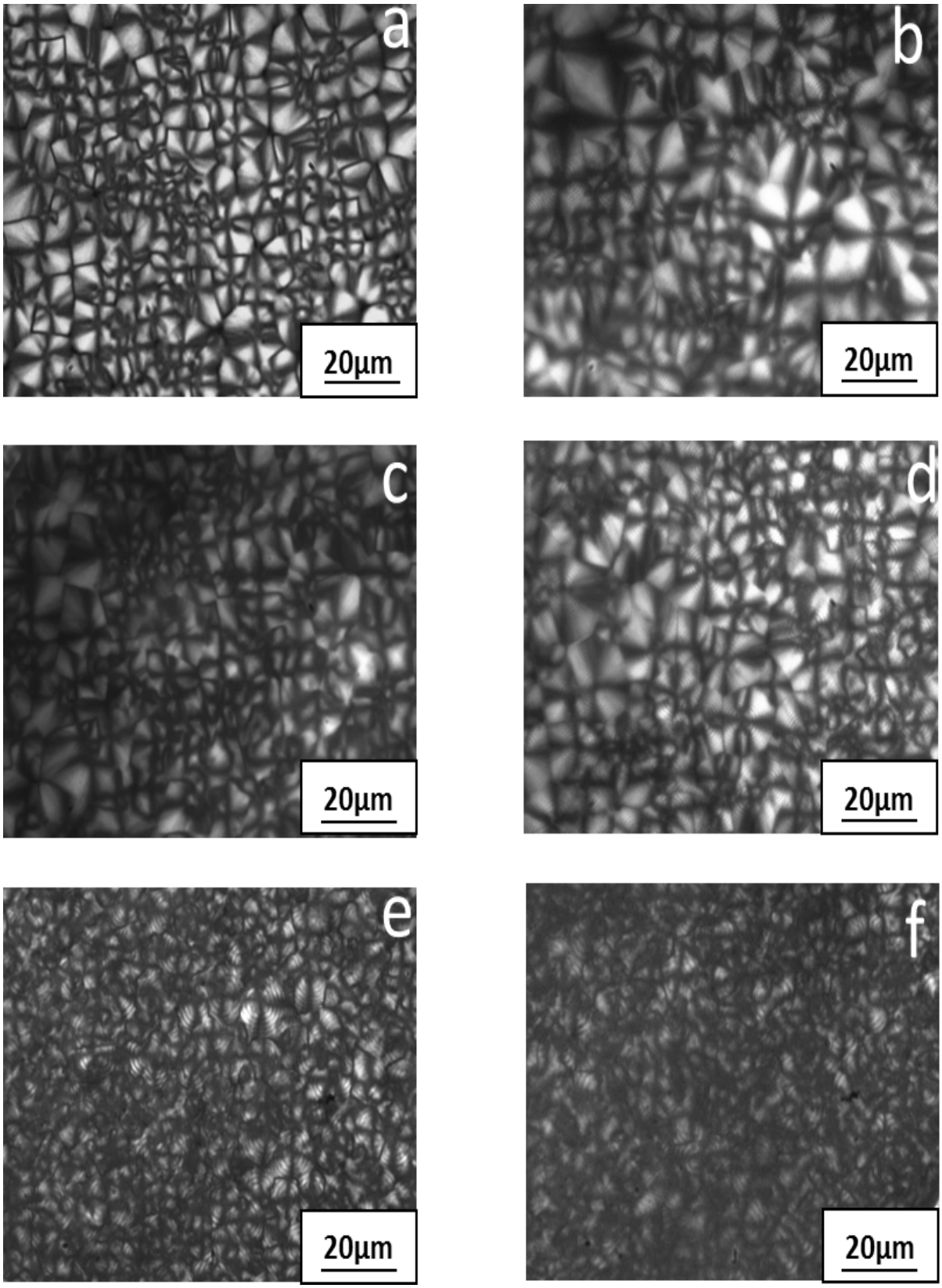

Fig. 6.18: Polarized optical micrographs revealing the spherulite structural morphologies of (a) pure HDPE, (b) HH1.0, (c) HH3.0, (d) HL3.0, (e) HL5.0 and (f) HH5.0

The average diameter of the spherulites for pure HDPE is 5.2µm. With the introduction of the BHX and BLX clay the size of spherulite starts to decrease but in case of HH1.0, HL3.0 and HH3.0 the right angled intersection between the spherulites remain clearly evident. A sharp decrease in the spherulite size and the disappearance of the intersection between the spherulites is observed when the clay content is increased to 5 wt.% for both BHX and BLX clay nanocomposites.

The addition of both the kaolin clay did not lead to a marked change in the crystallinity of HDPE, but the crystalline morphology of HDPE is altered due to the increase in the number of small size spherulites per volume. The reduction in the size of spherulites is because of the colliding and impacting of the uniformly distributed clay layers with the growing spherulites. This phenomenon reduces the chances of forming perfect circular crystalline spherulite structures. The increase in the number of spherulites in confined space is attributed to the increase in nucleation rate of the nanocomposites, which implies that the added clay particles act as nucleating agents for the polymer matrix and hence lead to enhanced heterogeneous nucleation. The large number of nuclei centres created by the addition of clay layers will lead to crystalline defects as shown in fig 6.18 (e and f).

6.4.2: DSC analysis of LLDPE and its nanocomposites

The crystallisation data which consists of melting and crystallization temperatures, percentage crystallinity and the relative crystallinity of LLDPE and its nanocomposites with BHX and BLX clay are summarized in table 6.12.

In contrast to HDPE where the thermal characteristics were changed by the addition of 5 wt. % of both kaolin clays, the thermal characteristics of LLDPE remain mostly unchanged. The addition of BLX clay in LLDPE caused a 6% reduction in the overall percentage crystallinity, but this value is still quite lower than the experimental error of 10 % involved in the calculation of percentage crystallinity from DSC analysis. The addition of higher aspect ratio BHX clay caused a 6% maximum reduction in the percentage crystallinity of LLDPE but this was also with in the experimental error range.

Table 6.12: DSC data for LLDPE and its nanocomposites with BHX and BLX clay

Samples	T_c (^oC)	T_m (^oC)	$X_{c\ (total)}$ (%)	$(X_c)_c/(X_c)_p$
LLDPE	110.92	127.73	52.15	1.00
LL0.5	111.59	127.70	51.67	0.99
LL1	111.44	127.72	48.50	0.93
LL1.5	111.04	127.77	50.31	0.96
LL2	110.53	128.35	47.46	0.87
LL3	110.84	128.55	46.72	0.84
LL5	112.55	127.00	46.28	0.89
LL10	112.56	127.43	47.51	0.91
LH0.5	111.11	127.31	51.60	0.99
LH1	111.18	130.96	47.60	0.87
LH1.5	111.79	128.16	51.64	0.99
LH2	112.15	127.62	50.96	0.98
LH3	112.41	128.14	50.07	0.96
LH5	111.86	127.90	46.79	0.90
LH10	112.49	127.46	46.21	0.89

The effect of clay addition on the melting and crystallization temperatures of LLDPE is shown in fig. 6.19. Both the thermal points remain unaffected with the addition of even higher percentage of both kaolin clays. These results indicate that the branched structure is not favourably compatible with the kaolin and as such tends to promote the agglomerate formation which would prevent nucleation effect of the clay particles and as a result the thermal characteristics remain unchanged.

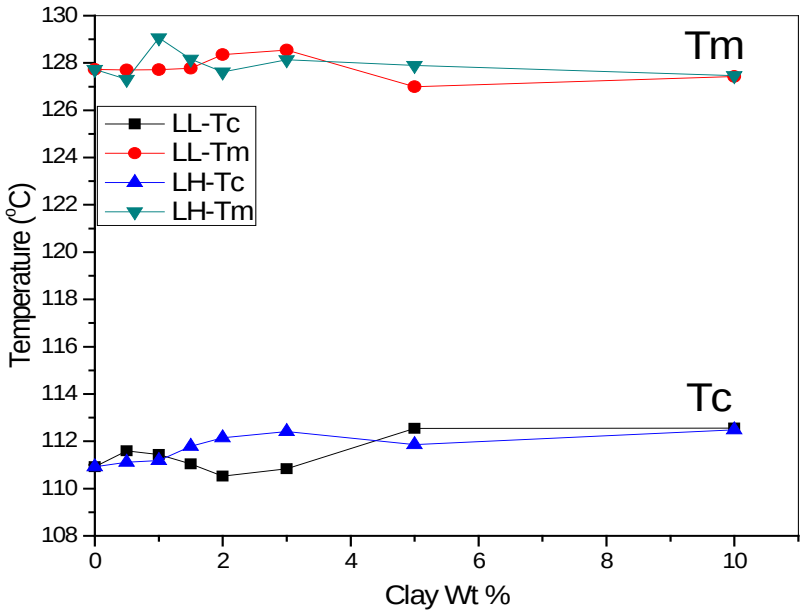

Fig. 6.19: Thermal transition temperatures (Tm and Tc) of nanocomposites (LH and LL) as a function of the clay weight percentage

6.4.3: Thermal analysis of Nylon12 and its nanocomposites

The thermal behaviour of Nylon12 and its nanocomposites with BHX and BLX clay was also analysed by using differential scanning calorimeter. For the DSC analysis the sample size of almost 12mg was used for all the specimens. The relative crystalline content in the composites was calculated by assuming the ΔHm for a theoretically 100% crystalline Nylon12 to be 209.2 J/g .The data extracted from the

DSC thermograms for pure Nylon12 and its nanocomposites with BHX and BLX clay is shown in table 6.13. The increase in crystallinity of any polymer can alter their final characteristics and hence change their real life application portfolio. From the data shown in table 6.13, it can be observed that the percentage crystallinity remains more or less unchanged with the addition of both BHX and BLX clays. The overall 5% improvement can be included in the experimental error of estimating the percentage crystallinity from DSC analysis.

Table 6.13: DSC data for Nylon12 and its nanocomposites with BHX and BLX clay

Samples	**T_c (^oC)**	**T_m (^oC)**	**$X_{c\ (total)}$ (%)**	**$(Xc)_c/(Xc)_p$**
Nylon12	155.17	178.93	15.23	1.00
NL1	154.92	181.21	17.08	1.12
NL2	154.67	180.42	19.51	1.28
NL3	157.54	183.24	16.28	1.07
NL5	157.21	182.71	19.27	1.26
NH1	155.85	181.38	20.22	1.33
NH2	156.37	181.29	17.99	1.18
NH3	156.8	182.76	16.87	1.11
NH5	158.56	181.51	20.42	1.34

As shown in figure 6.20, thermal transition temperatures also only slightly increase with the addition of both clays in Nylon12. In comparison to HDPE and LLDPE, the thermal characteristics of Nylon12 nanocomposites remains unaltered when the

weight percentage is increased from 3 to 5 weight percentage of BHX and BLX kaolin clays. This behaviour could be because of the formation of clay network structures at higher loadings. These clay network structures can hinder their mobility and diffusion of Nylon12 chain segments to form crystalline fronts. Two possibilities are generally observed with the addition of clay or any nanofiller in a polymer matrix, the growing crystallites during thermal altercations could either cover the nanofillers or the nanofillers could be expelled into the amorphous phase. The chances of nanofillers being expelled into the amorphous increases as the clay weight percentage are increased and as a result the thermal characteristics remain unaltered. The migration of the additional nanofiller into the amorphous phase would cause the barrier properties to be enhanced but the overall effect on the thermal characteristics would be negligible.

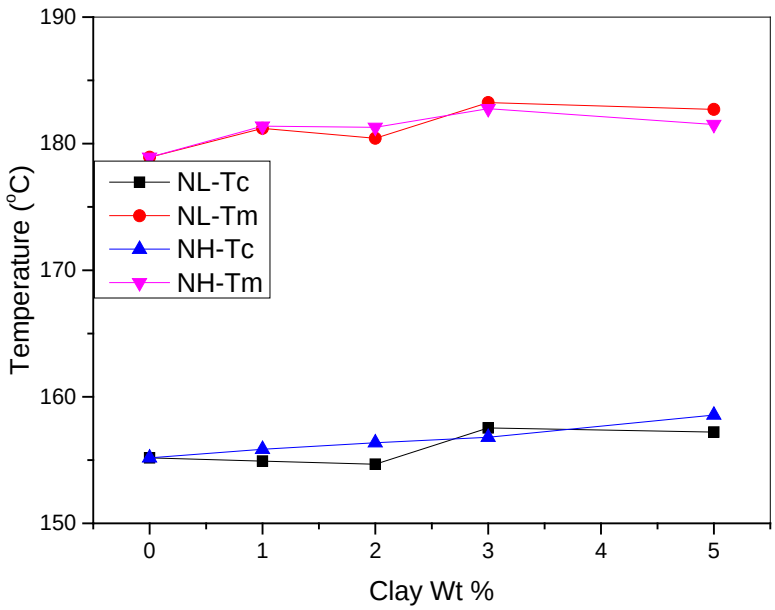

Fig. 6.20: Thermal transition temperatures (Tm and Tc) of nanocomposites (NH and NL) as a function of the clay weight percentage

Conclusion:

This chapter focussed on the barrier properties of a series of linear low density polyethylene (LLDPE), high density polyethylene (HDPE) and Nylon 12 nanocomposites based on Na-MMT clay and two different aspect ratio grades of kaolinite clay. Apart from oxygen and water barrier properties, thermal characteristics of the nanocomposites were also investigated. The kaolin clay with the higher aspect ratio showed the maximum improvement in barrier and thermal properties among the three matrices used, which could be due to the high platy structure, parallel orientation and nano-level fine dispersion of the kaolin clay layers. Maximum enhancement in barrier properties was achieved for HDPE kaolin clay nanocomposites with water barrier properties showing a reduction of more than 60 % in comparison to pure HDPE. The Nylon12 nanocomposites showed much better enhancement in oxygen barrier properties than their water barrier properties, whereas both the polyolefins nanocomposites exhibited better enhancement in their water barrier properties than their oxygen barrier characteristics.

References:

1. Kojima, Y.; Usuki, Ar.; Kawasumi, M.; Okada, A.; Kurauchi, T.; Kamlgalto, Osam. Synthesis of Nylon 6-Clay Hybrid by Montmorillonite Intercalated with e-caprolactam. J. Polym. Sci. Part A Polym. Chem. 1993, 31, 983–986.
2. Vaia, R. A.; Ishii, H.; Giannelis, E. P. Synthesis and Properties of Two-Dimensional Nanostructures by Direct Intercalation of Polymer Melts in Layered Silicates. Chem. Mater. 1993, 249, 1694–1696.

3. Kiliaris, P.; Papaspyrides, C. D. Polymer/layered silicate (clay) nanocomposites: An overview of flame retardancy. Prog. Polym. Sci. 2010, 35, 902–958.
4. Zhong, Y.; Janes, D.; Zheng, Y.; Hetzer, M.; Kee, D. De Mechanical and Oxygen Barrier Properties of Organoclay-Polyethylene Nanocomposite Films. 2007.
5. Feijoo, L.; Villanueva, P.; Gime, E. Optimization of Biodegradable Nanocomposites Based on aPLA / PCL Blends for Food Packaging Applications. Macromol. Symp. 2006, 233, 191–197.
6. Villanueva, M. P.; Cabedo, L.; Lagaro´n, J. M.; Gime´nez, E. Comparative Study of Nanocomposites of Polyolefin Compatibilizers Containing Kaolinite and Montmorillonite Organoclays. J. Appl. Polym. Sci. 2010, 115, 1325–1335.
7. Arora, A.; Padua, G. W. Review: nanocomposites in food packaging. J. Food Sci. 2010, 75, R43–9.
8. Sinha Ray, S.; Okamoto, M. Polymer/layered silicate nanocomposites: a review from preparation to processing. Prog. Polym. Sci. 2003, 28, 1539–1641.
9. Lei, Y.; Wu, Q.; Clemons, C. M. Preparation and Properties of Recycled HDPE / Clay Hybrids. J. Appl. Polym. Sci. 2006, 103, 3056–3063.
10. Wu, Q.; Wang, X.; Gao, W.; Hu, Y.; Qi, Z. Unusual rheological behaviors of linear PE and PE/kaolin composite. J. Appl. Polym. Sci. 2001, 80, 2154–2161.
11. Moggridge, G. D.; Lape, N. K.; Yang, C.; Cussler, E. L. Barrier films using flakes and reactive additives. Prog. Org. Coatings 2003, 46, 231–240.

12. Xu, B.; Zheng, Q.; Song, Y.; Shangguan, Y. Calculating barrier properties of polymer/clay nanocomposites: Effects of clay layers. Polymer. 2006, 47, 2904–2910.
13. Lotti, C.; Isaac, C. S.; Branciforti, M. C.; Alves, R. M. V.; Liberman, S.; Bretas, R. E. S. Rheological, mechanical and transport properties of blown films of high density polyethylene nanocomposites. Eur. Polym. J. 2008, 44, 1346–1357.
14. Koros, W.J.; Hellums, M.W. Transport properties, Encyclopedia of polymer science and engineering, supplement volume. John Wiley and Sons; 1989.
15. Marini, J.; Branciforti, C.; Maria, R.; Alves, V.; Marini, J. Effect of EVA as compatiblizer on the Mechanical Properties , Permeability Characteristics , Lamellae Orientation , and Long Period of Blown Films of. J. of Applied Polymer Sci. 2010, 118, 3340–3350.
16. Yam, K. L. The Wiley Encyclopedia of Packaging Technology; Third Edit.; John Wiley & Sons, Inc., Publication, 2009.
17. Bhattacharya, M.; Biswas, S.; Bhowmick, A. K. Permeation characteristics and modeling of barrier properties of multifunctional rubber nanocomposites. Polymer. 2011, 52, 1562–1576.A
18. Alexandre, B.; Colasse, L.; Langevin, D.; Médéric, P.; Aubry, T.; Chappey, C.; Marais, S. Transport mechanisms of small molecules through polyamide 12/montmorillonite nanocomposites. J. Phys. Chem. B 2010, 114, 8827–37.
19. Lei, Y.; Wu, Q.; Clemons, C. M. Preparation and Properties of Recycled HDPE / Clay Hybrids. J. Appl. Polym. Sci. 2006, 103, 3056–3063.
20. Alexandre, B.; Langevin, D.; Médéric, P.; Aubry, T.; Couderc, H.; Nguyen, Q. T.; Saiter, a.; Marais, S. Water barrier properties of polyamide

12/montmorillonite nanocomposite membranes: Structure and volume fraction effects. J. Memb. Sci. 2009, 328, 186–204.

21. Wang, X.; Wu, Q.; Qi, Z. Unusual rheology behaviour of ultra-high molecular weight polyethylene/kaolin composites preparedvia polymerization-filling. Polym. Int. 2003, 52, 1078–1082.
22. Reddy, C. S.; Ratna, D.; Das, C. K. Polyethylene nanocomposites by gas-phase polymerization of ethylene in the presence of a nanosilica-supported zirconocene catalyst system. Polym. Inter 2008, 291, 282–291.

CHAPTER 7: COMPARATIVE STUDY OF 1D-2D-3D CARBON BASED NANOFILLERS ADDITION FOR IMPROVING THE PROPERTIES OF HDPE

7.1: Introduction

In this chapter the role of carbon based nanofiller in improving the toughness, thermal and barrier properties of HDPE is studied and the change in properties are also linked to the morphology of the nanocomposites. When incorporated into polymer the carbon based nanofiller such as MWCNT generally form micro-size agglomerates, which eventually cause the ductile polymers such as HDPE to become brittle and hence make them loose one of their biggest advantages of being elastic and flexible. In order to solve this problem MWCNT samples were ball milled to produce short tubes (as detailed in chapter 4) that can stop the agglomerate formation and hence produce a better interface between the polymer and the nanofiller. In this work, HDPE and its nanocomposites with CB, MWCNT, different ball milled grades of MWCNT and GO have been prepared by melt blending. Along with mechanical testing, a detailed analysis of the thermal and barrier properties of the nanocomposites and the thermal imaging camera analysis for the temperature build up inside the nanocomposites during tensile analysis are also presented.

7.2: Mechanical Properties of HDPE/carbon nanofillers

7.2.1: Tensile properties

Fig 7.1(a) shows the representative stress strain curves for HDPE and its nanocomposites. As shown in the figure the mechanical behaviour of pure HDPE is like that of a ductile polymer with enlarged necking and cold drawing regions. The effect of each filler addition on the percentage strain at break of HDPE is shown in fig

7.1(b). The data in fig. 7.1 clearly indicates that the presence of MWCNT caused a reduction in the ductility of HDPE and its nanocomposite samples behaved like a brittle material in tensile testing with only a small amount of necking following the yielding point. The effect of CB on the other hand on the mechanical properties of HDPE is totally different and their inclusion had produced a high degree of toughness in HDPE matrix. The enlargement in the necking and cold drawing region is observed for HCB which would indicate internal toughening of HDPE by CB particles. The addition of GO also caused some embrittlement effect on HDPE by reducing mainly the cold drawing region but the mechanical properties are more or less close to HDPE matrix. In comparison to CB, GO and ball milled samples of MWCNT, the embrittlement effect caused by the presence of MWCNT is most severe.

The results indicate that MWCNT is dispersed inside HDPE in the form of large agglomerate which can cause premature flaws and that can result in raising localized stress before failure. This assumption is justified by the SEM and OM results of MWCNT based HDPE nanocomposites, as shown in chapter 4.

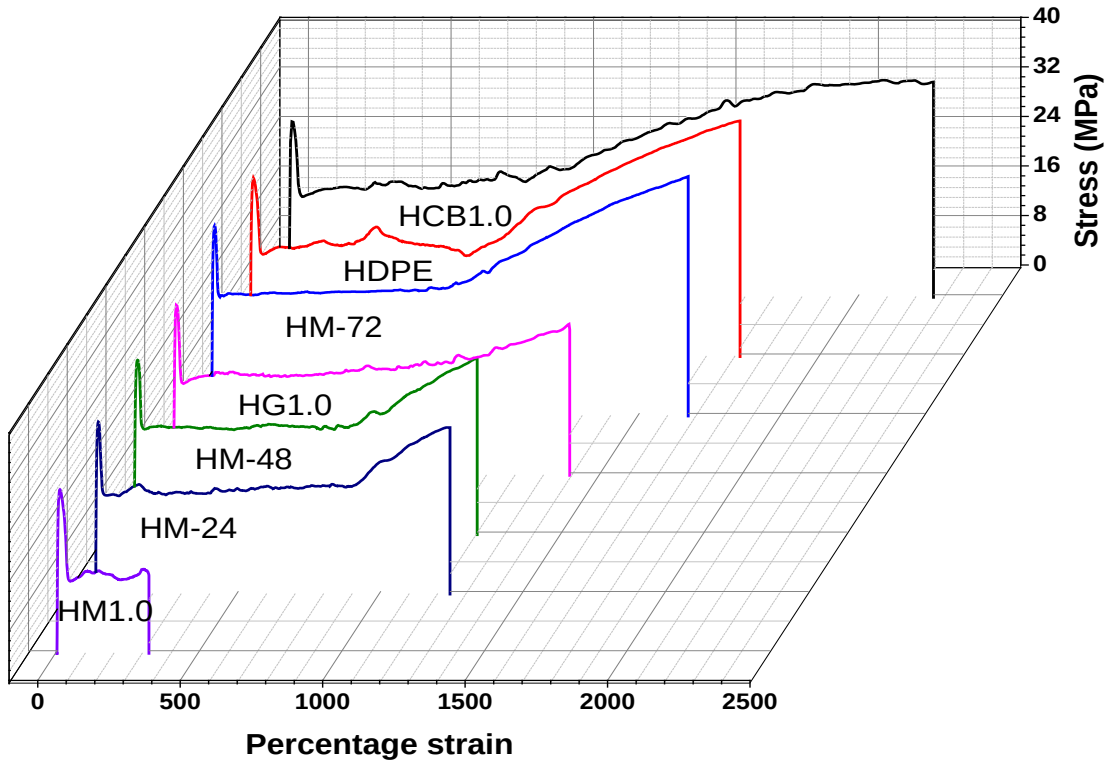

(a)

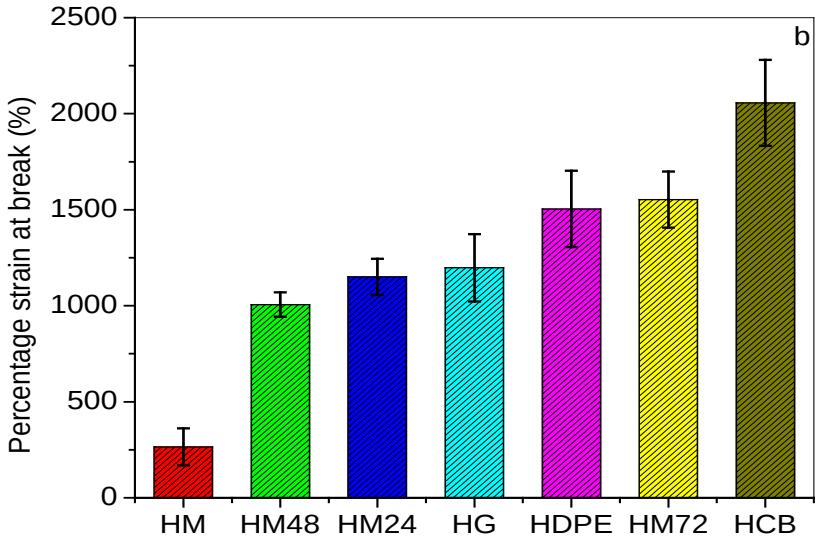

FIg.7.1: Tensile properties: (a) Representative stress strain curves of HDPE and its nanocomposites, (b) percentage strain at break of the individual samples

The embrittlement effect of MWCNT was somehow solved by the ball milling, which caused shortening of the tubes length and as a result less agglomerates were produced in HDPE matrix. The ball milling of MWCNT might have reduced the internal defect but still the toughness of HM24 and HM48 is less than HDPE (fig 7.2) with only slight improvement in HM-72. In case of GO the mechanical properties were reduced because of agglomerate formation which caused poor load transfer and poor interfacial adhesion between GO and HDPE. The enhancement in toughness was most evident in HCB where the extension in the cold drawn region is a lot more in comparison to other samples. The improvement could be attributed to uniform dispersion which leads to better mechanical properties.

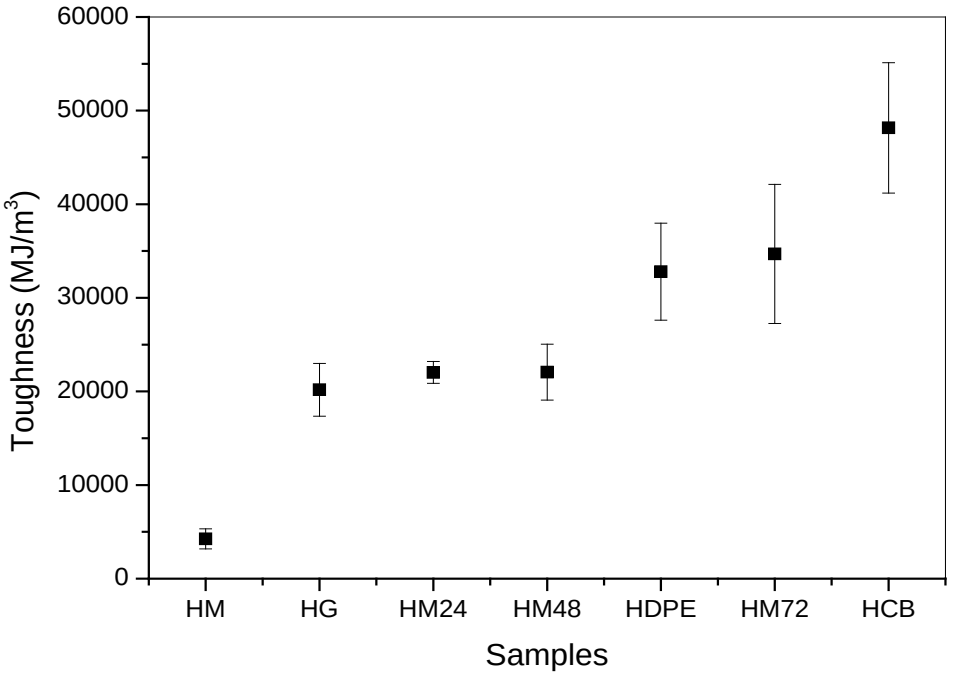

FIg.7.2: Toughness of neat HDPE and its nanocomposites; evaluated by calculating area under the stress strain curves

7.2.2: Impact properties

IFWIT was also applied to investigate the impact performance of HDPE and its nanocomposites. The representative force-distance curves obtained from IFWIT of HDPE and its nanocomposites are shown in fig 7.3. As shown in fig 7.3(a), impact properties were also improved for HCB and HM-72 whereas the rest of nanofillers failed to impart any strength to HDPE. The energy at failure for all the samples shown in fig. 7.3(b) is calculated on the basis of the impact area volume. Also in this case the results are similar to the one shown during tensile testing. In impact testing of nanocomposites if the nano fillers are dispersed uniformly throughout the matrix then these fillers can absorb part of the impact energy and contribute to improving the toughness of the samples.

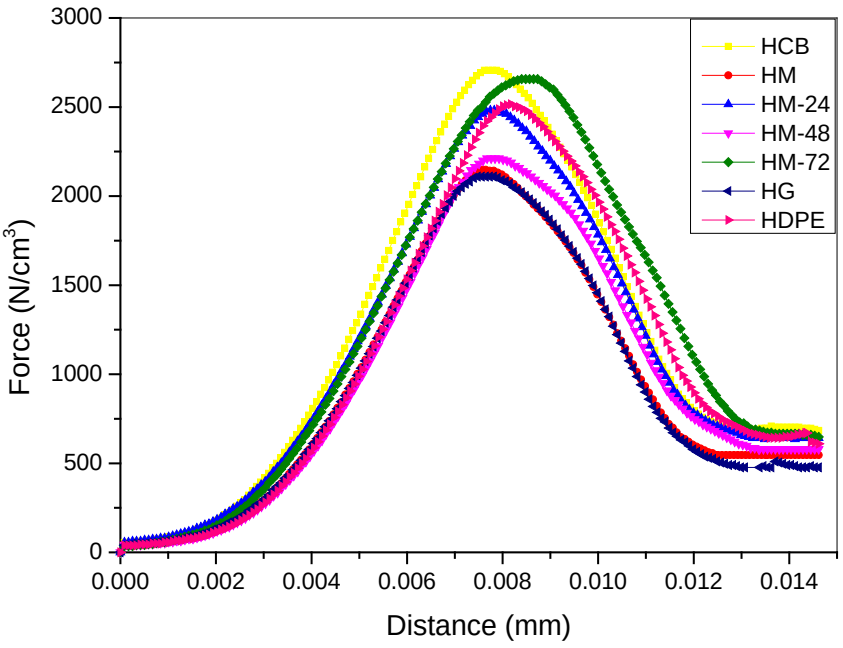

(a)

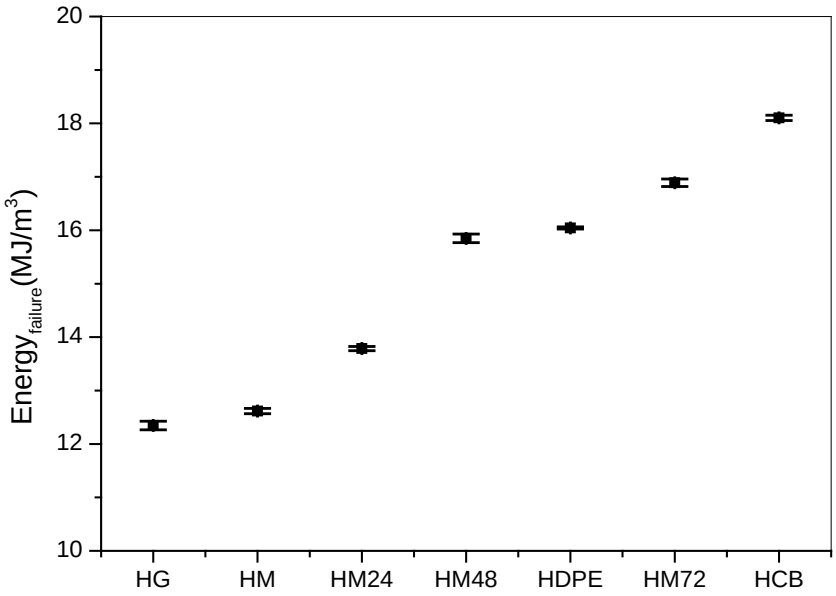

(b)

FIg.7.3: Impact properties: (a) Force distance curves for HDPE and its nanocomposites, (b) Energy at failure for all the samples

7.2.3: Sample investigation during and after tensile testing

The improved toughness of HDPE can be related to the appearance of crazing and stress whitening on the surface of the nanocomposites during the tensile testing. The incorporation of CB (fig 7.4(a)) and MWCNT-72 (fig 7.4(b)) resulted in the production of large number of crazes on the testing samples, which increases the plastic work of fracture, produces high energy absorption and extensive stress whitening, while HM samples (fig 7.4(c))showed no stress whitening or crazing on the surface. The crazes are formed at right angles to the applied stress and consist of microscopic voids with strands of polymer. The crazes are mainly developed during tensile deformation of polymers and they act as the cracks precursor which ultimately leads to the macroscopic fracture. The crazing that occurred on the surface of specimen was of the order of 1 to 3 μm.

In comparison to true cracks, craze fibrils are generally load-bearing elements because they are aligned in parallel to the loading direction and their appearance can also delay the production of crack. During tensile deformation the growth of stable crazes can help dissipate energy and hence contribute to the increase in the fracture toughness. The crazes break when their fibrils reach a critical length and hence transform the crazes into true cracks. In comparison to MWCNT, the CB particles are dispersed more uniformly which provides a number of sites where the crazes can be formed due to stress concentration and hence prevent the localization of deformation. In case of HCB, the production of shorter (fig 7.4 (d,e)), stronger and stable crazes on the surface without any cracks appearing along with them showed their load bearing characteristics and hence their contribution towards the enhancement in toughness.

The cloudy appearance due to the stress whitening of the composites during the tensile testing is due to the formation of micro voids whose dimension is equal to or greater than the wavelength of light. The deformation mechanism of thermoplastic crystalline polymers during tensile testing consists of stretching of amorphous chains which is followed by the shear yielding of crystallites. If a thermoplastic polymer shows enhanced necking region then the void formation in the polymer will be high and this will lead to more stress whitening and recrystallization with high degree of orientation.

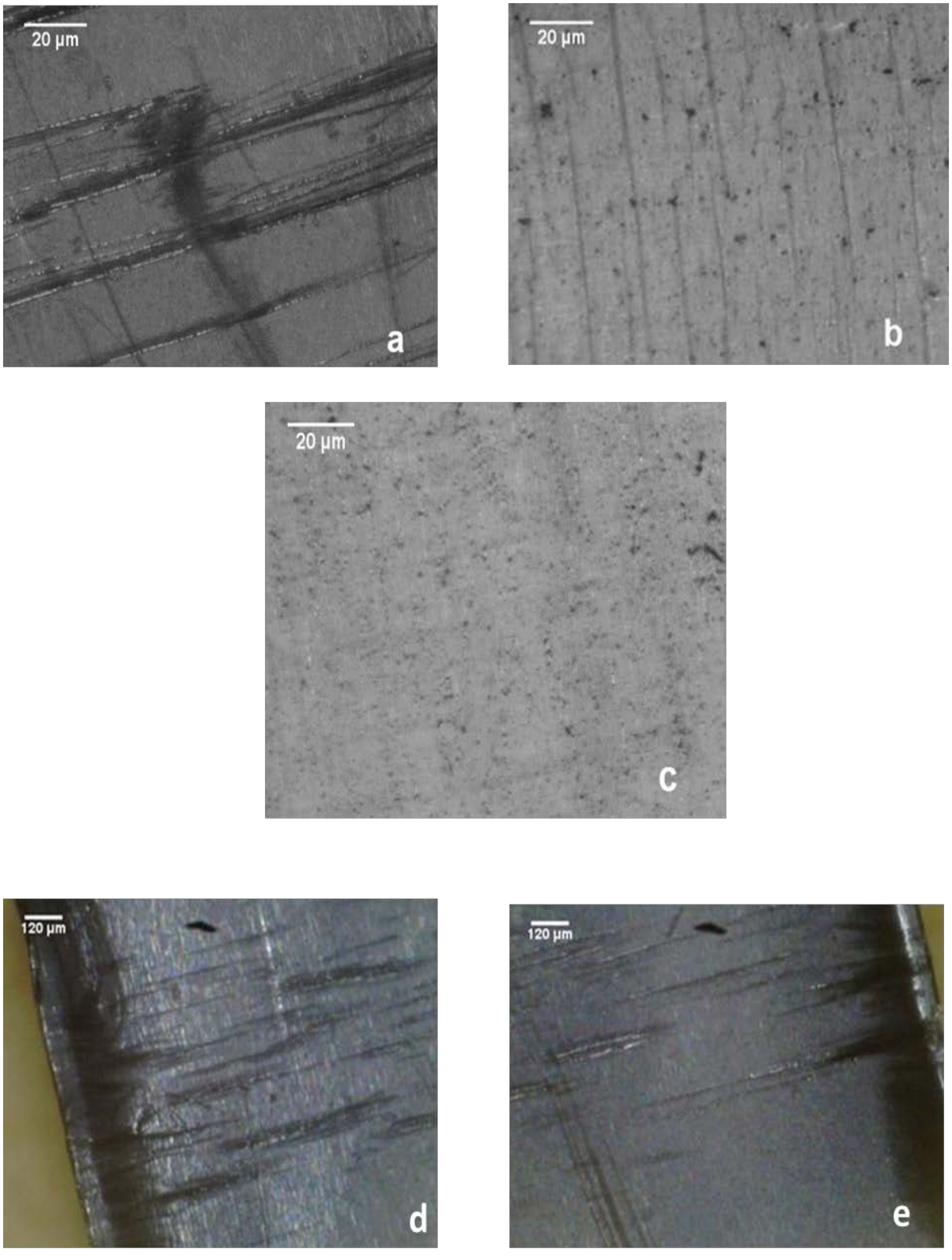

FIg.7.4: Crazing produced during tensile testing on the surface of (a,d,e) HCB, (b) HM-72 and (c) HM

Another reason for the enhancement of toughness could be related to the temperature build up inside the nanocomposites due to the nanoscale distribution of the fillers. The heat generated inside nanocomposites could be due to the friction produced by sliding movement of polymer chains during tensile testing and the amount of friction would rise due to the presence of uniformly dispersed nanofillers. Also the nanofillers added have very high thermal conductivity and they can dissipate the heat to the polymer more effectively and result in thermal softening. If the filler is not dispersed uniformly then it can produce a number of flaws inside the nanocomposite which can lead to premature cracks and from these cracks the heat generated can be dissipated to the surroundings instead of being transferred to the polymer matrix.

Fig 7.5 shows the internal temperature of the specimen at the breaking point of tensile testing. The results indicate that the temperature generated inside the nanocomposites is strongly dependent on the agglomerate size of the nanofiller present inside the HDPE matrix. The maximum temperature change was observed for HCB (90.8 ^{o}C), while for HDPE (45.2^{o}C), HG (68.3^{o}C) and HM-72(64.9^{o}C) there was not much temperature rise. In tensile testing the temperature rise normally occurs in the neck region of the polymer during cold drawing. This temperature build up could cause the nanocomposite to become softer and hence produce a quasi-rubber like behaviour in the nanocomposite after necking.

The gradual increase in the temperature of dog bone shaped specimen of HCB recorded during the tensile testing by a thermal imaging camera is shown in 7.6. The maximum rise in temperature to 90.8 ^{o}C recorded during the testing was observed just before the breaking point of the specimen. As shown in fig 7.1(a), for HCB the behaviour after necking is considerably different from the other samples and instead

of having a typical cold-drawing phenomenon, the sharp increase in stress is less evident with the increase in strain. Such a quasi-rubber like behaviour occurs in brittle polymers at high temperature.

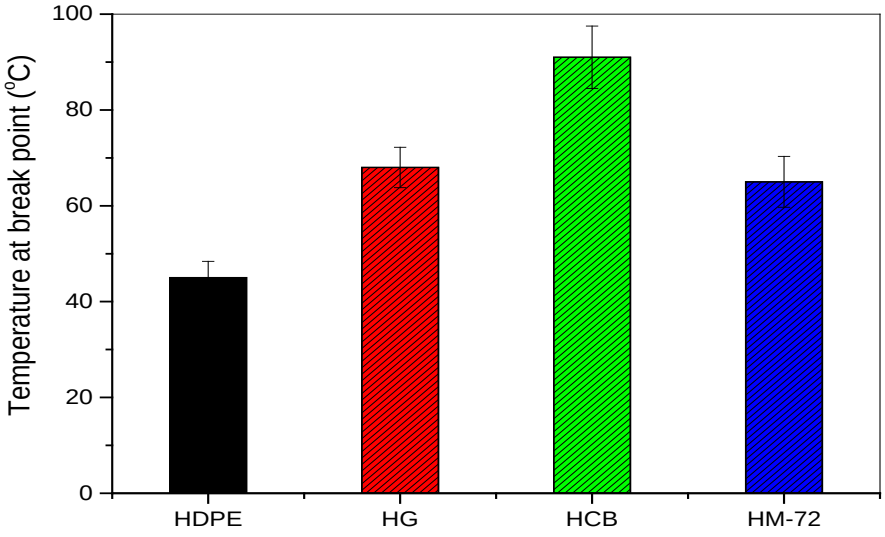

FIg.7.5: Temperature at break point for HDPE and its nanocomposites

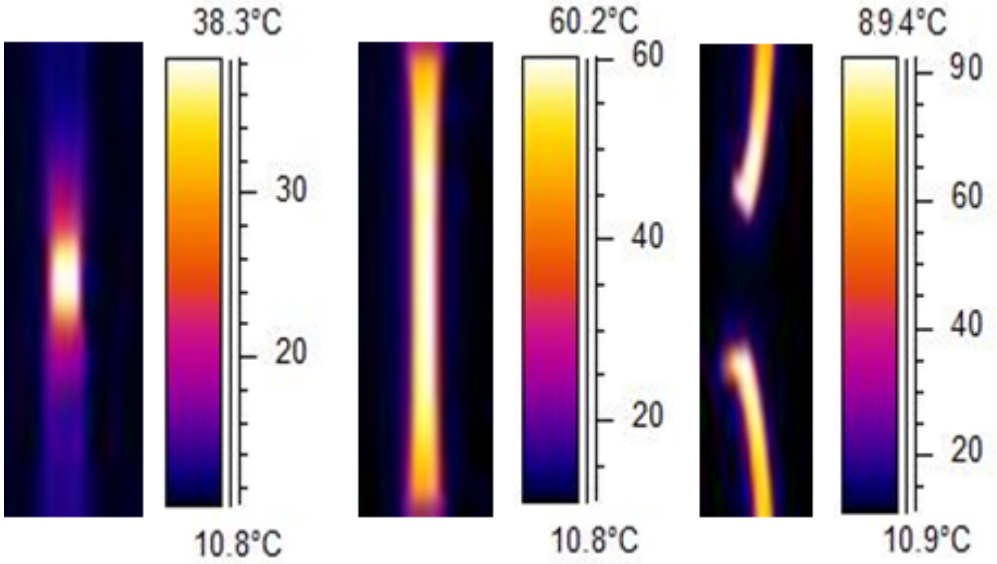

FIg.7.6: Increase in temperature of HCB specimen recorded during the tensile testing by thermal imaging camera

7.3: Thermal Properties

DSC results for HDPE and its nanocomposites are shown in table 7.1. It is found that melting temperature (T_m) does not vary significantly with the addition of nanofillers. A slight increase in the crystallization temperature (T_c) is observed for all the nanocomposites, which indicates that crystallization started earlier in the nanocomposites than in pure HDPE. The crystallization temperature was raised by 3.8^oC for the HM nanocomposites

Table 7.1: Non-isothermal DSC analysis data for HDPE and its nanocomposites

Samples	T_c (^oC)	T_m (^oC)	ΔH_m (J/g)	X_c (%)	$(Xc)_c/(Xc)_p$
HDPE	114.93	138.50	207.10	70.68	1.00
HM	118.72	135.30	219.10	75.53	1.07
HM24	118.58	134.75	218.80	75.43	1.07
HM48	117.06	135.04	220.10	75.88	1.07
HM72	118.41	134.91	226.30	78.02	1.10
HCB	118.09	135.05	217.20	74.88	1.06
HG	116.98	135.57	228.40	78.74	1.11

As shown in fig 7.7, X_c increased for all the samples. Increase in X_c was more evident in case of 1D and 2D nanofillers samples than in 3D nanofiller composites.

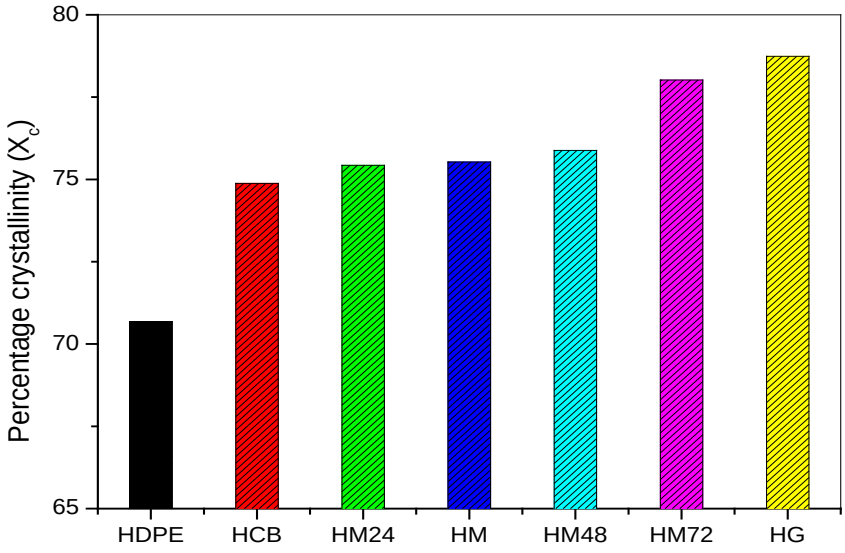

FIg.7.7: Percentage crystallinity for HDPE and its nanocomposites

EGO and MWCNT possess a platy structure and very high aspect ratio, which can lead to more nucleating sites and better crystal growth in HDPE matrix. Although the microscopic results indicated the presence of agglomerate formation in these samples due to the presence of strong intermolecular van der Waal's interactions between EGO sheets and MWCNT individual tubes, but a major portion is still distributed in the form of individual sheets and tubes, on which crystal growth has taken place. In comparison to EGO and MWCNT, CB has a low aspect ratio and although HCB had uniform nanoscale distribution of CB particles inside HDPE with very little agglomeration, but any appreciable increase in X_c was not observed because the low amount of CB particles cannot form enough nucleation centres inside HDPE matrix. The effect of ball milling on the agglomerate formation of

MWCNT inside HDPE matrix was also evident from DSC results. The maximum increase in X_c for HM-72 indicates that the agglomerate formation is considerably reduced inside HM-72 and the individual tubes still have a high aspect ratio which can aid in crystal growth.

7.4; Barrier Properties

One of the misconceptions in the early development of nanocomposites was that if mechanical properties improve then the barrier properties of the nanocomposites will improve too, this is not always true because these properties depend on different microstructural factors such as mass fraction, aspect ratio, dispersion and orientation of nanofiller in polymer matrix [1, 2]. The platelet geometry and high aspect ratio of most of the nanofillers can provide a tortuous path, which hinders the molecular diffusion of penetrant through the polymer and results in decrease in permeability. The WVTR and O2TR for HDPE and the decrease in the permeability of its nanocomposites are shown in table 7.2. WVTR for pure HDPE is 9.05 gm-mil/m^2-day, whereas with the addition of 1 wt % of CB the permeability is reduced to 7.44 gm-mil/m^2-day, which presents a 17.8 % decrease of permeability. On the other hand a much higher decrease of 32.6 and 24.9 % in permeability is observed for HG and HM. For pure HDPE the O2TR is 50.42 cc-mm/m^2-days and with the addition of nanofillers maximum oxygen permeability decrease of 28.3 % and a minimum decrease of 11.2 % was observed for HG and HCB, respectively.

Table 7.2: WVTR and O2TR for HDPE and its nanocomposites

Sample	WVTR (gm-mil/m^2-day)	% reduction	O2TR (cc-mm/m^2-days)	% reduction
HDPE	9.05	0	50.42	0
HM	6.80	24.87	40.25	20.17
HG	6.10	32.62	36.13	28.34
HCB	7.44	17.79	44.77	11.2
HM-24	6.91	23.63	41.08	18.52
HM-48	7.10	21.52	42.55	15.61
HM-72	7.25	19.91	43.10	14.52

In comparison to other nanofillers, a much higher decrease in permeability of graphene based nanocomposites indicates the reliance of penetrant permeation through a nanocomposite on filler dimensionality and its structure. Also the decrease in water permeability of HDPE and its nanocomposites is higher than their oxygen permeability (fig 7.8). The van der Waals volumes of oxygen and water molecules are almost similar but the transport mechanisms of these penetrants in a flexible polymer are different and are dependent on the repeating unit of the polymer. If a polymer is nonpolar, then the transfer of water vapours through it will be difficult and these nonpolar polymers such as different polyolefins will have very small WVTR, however the transfer of polar water molecule through polar polymers such as different polyamides and polyesters will be high because of the ability of the water molecules to form water clusters inside polymer matrix and defuse more easily

through polar polymers [3, 4, 5]. Also the water molecules have the ability to plasticize the polymer and hence reduce its glass transition temperature and the overall crystallinity, which would ultimately cause a reduction in WVTR. On the other hand the transfer of non-polar oxygen is very high through non-polar polymers due to the formation of oxygen clusters in non-polar polymers and the change in polarity caused by the addition of different nanofillers. For low weight percentage nanofiller addition in polymer matrix, the solubility of penetrant in polymer matrix is only slightly altered and the permeability is governed by the diffusivity of the penetrant through the polymer matrix, but for high weight percentage of nanofiller addition, the solubility of penetrant in the polymer will be increased due to the increase in the heat of sorption and this increase will ultimately increase the permeability of penetrant [6].

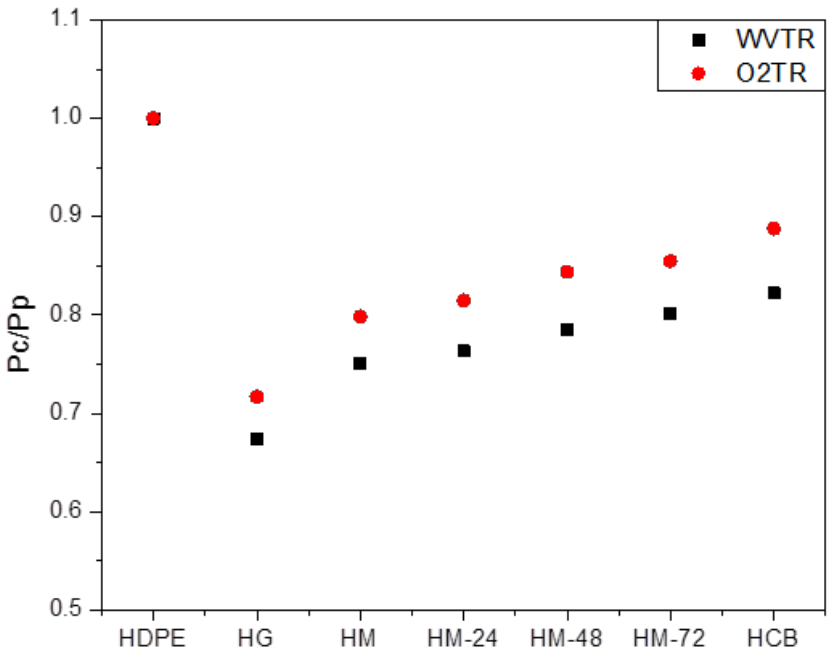

FIg.7.8: Relative permeability (Pc/Pp) of HDPE and its nanocomposites

In order to understand the property enhancement of HDPE nanocomposites, TEM analysis of MWCNT (fig 7.9(a)), CB (fig 7.9(c)) and graphene (fig 7.9 (b, d)) nanocomposites was carried out to study the nanoscale morphology of nanofillers inside HDPE.

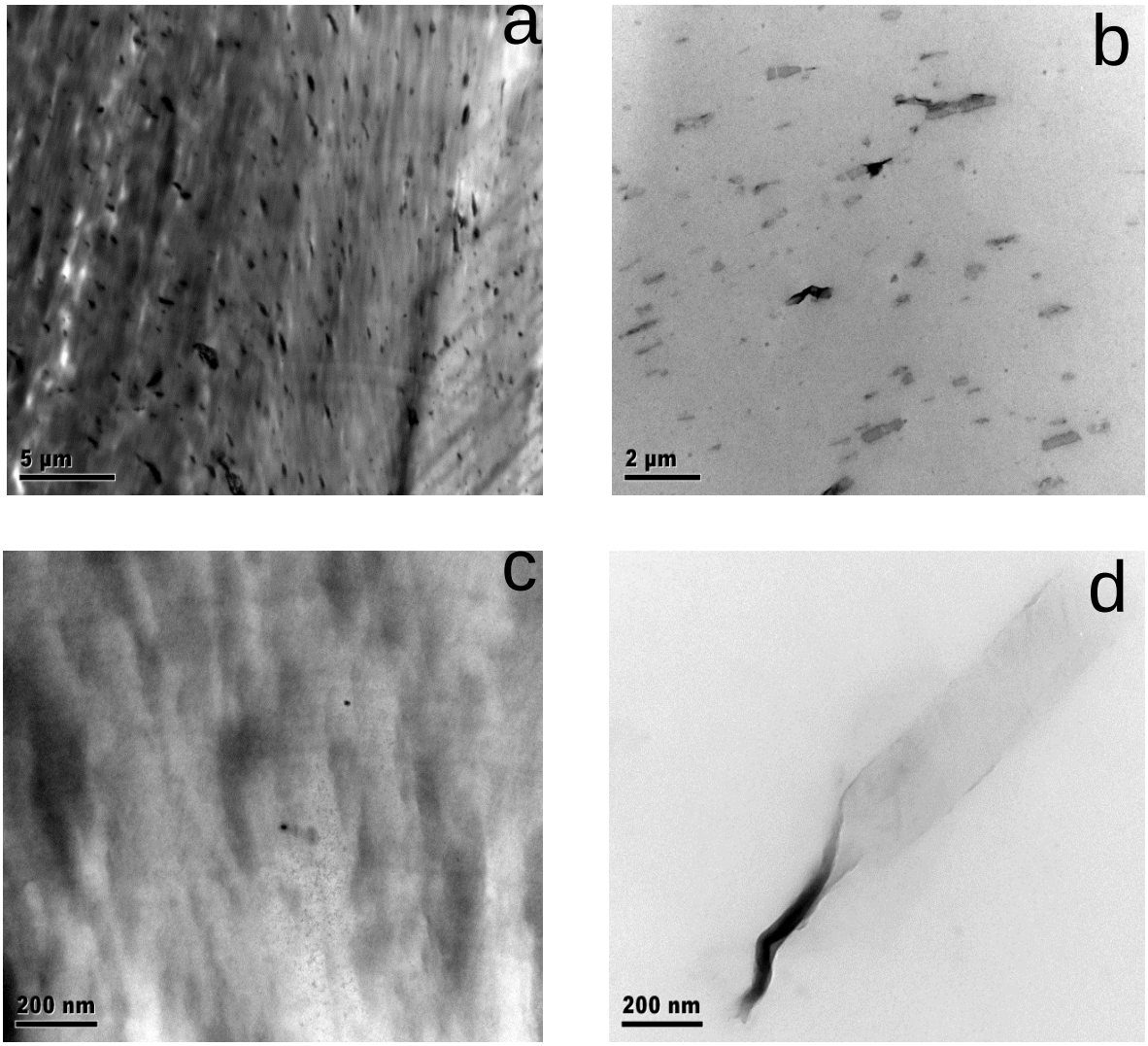

FIg.7.9: TEM micrographs of HM (a), HG (b,d) and HCB (c)

The micrographs indicate agglomeration for HM but also show the uniform distribution of MWCNT throughout the matrix which could have led to better barrier properties and enhanced extrusion window of HM. The distribution of CB inside

HDPE was not even visible at higher magnification which shows the nanoscale distribution of spherical CB particles inside HDPE. The distribution of graphene (fig 7.12(b, d)) shows the unique characteristics of graphene sheets which can only be visualized if the 2D sheets are individually separated from each other. Graphene sheets are known to be flexible, transparent and very soft. Due to its soft nature the graphene can be folded over by the shearing action of extruder to produce a spool of graphene which is clearly shown in (fig 10 (d)). This folding could cause a reduction in the aspect ratio of graphene sheets and hence result in diminishing their reinforcing capability. But such spools of graphene have minor visibility throughout the HDPE matrix which shows that at the nanoscale most of the graphene sheets had retained their platy structure and hence contributed to the barrier and rheological properties.

Conclusion

The addition of CB in HDPE significantly increased its toughness, but the improvement in impact, barrier and thermal properties with the addition of CB was not that drastic. The improvement was attributed to the surface and thermal softening of the material during testing. Also the improvement of mechanical and thermal properties was linked to particle shape and its distribution. The increase in thermal and barrier properties was more significant for 1D and 2D particles nanocomposites while the 3D nanofillers had not much of an effect. The increase in thermal and barrier properties was linked to the platy structure of 1D and 2D nanofillers. The mechanical properties on the other hand were improved only by the 3D CB nanofillers and the 1D and 2D nanofillers due to their agglomeration and relatively poor dispersion caused serious reduction in the mechanical properties.

References

1. Mittal, V.; Barrier properties of polymer clay nanocomposites. Nova Science Publishers, Inc. New York. 2010.
2. Thomas, S.; Stephen, R. Rubber nanocomposites. Preparation, properties and applications. John Wiley & Sons (Asia) Pte Ltd. 2010.
3. Nguyen, Q. T.; Favre, E.; Ping, Z. H.; Neel, J. Clustering of solvents in membranes and its influence on membrane transport properties. J. Memb. Sci. 1996, 113, 137–150.
4. Strathmann, H.; Michaels, A. S. Polymer-water interaction and its relation to reverse osmosis desalination efficiency. Desalination 1977, 21, 195–202.
5. Koros, W. J.; Hellums, M. W. In Encyclopedia of polymer science and engineering; Kroschwitz, J. I., Ed.; Wiley: New York, 1990.
6. Villaluenga, J. P. G.; Khayet, M.; López-Manchado, M. a.; Valentin, J. L.; Seoane, B.; Mengual, J. I. Gas transport properties of polypropylene/clay composite membranes. Eur. Polym. J. 2007, 43, 1132–1143.

CHAPTER 8: CONCLUSIONS AND FUTURE RECOMMENDATIONS

The objective of this research was to investigate if nanofillers can be incorporated in HDPE to produce HDPE nanocomposites for food packaging that can have better barrier properties and can be processed at low cost. HDPE was the main polymer of research while LLDPE and Nylon12 were selected thermoplastics for comparative analysis. The main nanofillers utilized for developing food packaging nanocomposites were kaolin clay with two different aspect ratios and Na-MMT clay. Apart from the different clay nanofillers, carbon nanofillers were also deployed to study the effect of filler shape, size and dimension on the final characteristics of HDPE. The novelty of this work is in deploying a premixing technique for producing nanocomposites with better properties and also developing HDPE nanocomposites with enhanced low temperature processing window.

8.1: Conclusions

The detailed literature review of chapter 2 indicated that there is a shortage of research data related to the enhancements of low temperature processing and barrier properties of HDPE and in order to fulfil this research gap a series of samples were prepared and then analysed by a combination of morphological, rheological, mechanical, barrier and thermal characterization techniques. From the morphological analysis reported on all the nanocomposites in chapter 4, the following conclusions can be drawn. Using the combination of XRD, TEM, SEM and OM analysis on HDPE nanocomposites with different type of clays and carbon based nanofillers, the results obtained conclusively demonstrated exfoliated nanocomposites only for low weight percentage HDPE/Na-MMT specimens and in all other cases an intercalated or macrocomposites morphology was observed, but the size of most of the dispersed

clay was lower than 100 nm which satisfies one of the basic condition of producing nanocomposites. All of the HDPE nanocomposites showed better dispersion and distribution of nanofiller tactoids throughout the matrix with only slight formation of agglomerate in high weight percentage clay specimens and MWCNT based nanocomposites. The morphology of Nylon12 and LLDPE nanocomposites morphology but the dimension of most of the tactoids was once again less than 100 nm and the distinct clay agglomerate were only scarcely visible in high weight percentage specimens.

In order to produce the nanocomposites using energy efficient processing techniques the melt flow singularity of high density polyethylene (HDPE) and its composites with different clays and carbon based nanofillers was studied. The mechanism of melt flow singularity was analysed with respect to the strain rate and filler loading dependence of the critical points of the extrusion window recorded in the experiment. The effect of strain rate on the extrusion window indicated an enhancement up to $350s^{-1}$ and after this strain rate the window was reduced due to shorter elastic recovery time. The experimental results also showed that the addition of different clay resulted in the expansion of extrusion window of HDPE composites and that exfoliated Na-MMT clay/HDPE composites showed the most enhanced window due to the larger interfacial contact area between the polymer chain and the surface of clay layers in the matrix. The HDPE/Na-MMT composites showed the most broadened extrusion window up to $6.5^{o}C$, the best result reported so far. In comparison to the exfoliated clay composites of HDPE, the intercalated and the micro-composites showed a reduced window with a maximum of $5.2^{o}C$ window observed for bentone clay composites. In case of extrusion window of HDPE composites with carbon based nanofillers, 1D carbon nanotubes produced a wide

extrusion window of 6.17 ^{o}C, whereas the rest of the fillers apart from CB also contributed in widening the window. The effect of different parameters on the die swell indicated a smooth and shiny extrudate achieved for most of the specimens during the extrusion window interval.

Apart from oxygen and water barrier properties, thermal characteristics of the nanocomposites were also investigated. The kaolin clay with the higher aspect ratio showed the maximum improvement in barrier and thermal properties among the three matrices used, which could be due to the high platy structure, parallel orientation and nano-level fine dispersion of the kaolin clay layers. Maximum enhancement in barrier properties was achieved for HDPE kaolin clay nanocomposites with water barrier properties showing a reduction of more than 60 % in comparison to pure HDPE.

The effect of filler characteristics (shape and dimensions) on the final properties of HDPE was also studied by preparing HDPE/carbon filler composites with 1D-multiwalled carbon nanotubes (MWCNT), 2D- graphene oxide (GO) and 3D-carbon black (CB) on a twin screw extruder. In comparison to 1D and 2D nanofillers, the 3D-CB filler showed remarkable contribution to toughness but caused a reduction in extrusion window and barrier properties of HDPE, the increase in toughness was attributed to uniform dispersion of the filler, enhanced mechanical interlocking between filler and polymer, appearance of high degree of crazing on tested samples and increase in nanocomposite internal temperature during tensile testing. The increase in thermal properties was more significant for 1D and 2D particles nanocomposites while the 3D nanofillers had not much of an effect. The increase in thermal properties was linked to the platy structure of 1D and 2D nanofillers.

8.2: Recommendations for the future work

In this work nanocomposites of HDPE, LLDPE and Nylon12 with enhanced barrier, mechanical and thermal were developed using different nanofillers. Although the results indicate that the products have improved characteristics but for these products to be utilized inside the polymer processing industries the following aspects of further development could be included:

- The extrusion window data generated for HDPE nanocomposites showed that the processing window is greater than $6^{o}C$ and is the above the normal temperature fluctuations of 3-$5^{o}C$ for the polymer processing machinery. In this study nanocomposites developed with such high processing window can be studied further by processing them on industrial scale extruder or internal batch mixers such as the Haake mixer.
- The premixing method can be modified to apply it to polyolefins containing high percentage of filler. During the premixing stage the fillers tend to agglomerate after drying and they separate themselves from the polymer surface when the percentage of filler is above 5.0 wt. % and this causes degradation in optical appearance and general properties of the nanocomposites. Few of the suggestions for the modification of the premixing method are given below:

  1: Drying the specimens using the rapid cyro-evaporator operation.

  2: Drying the specimens using the spray drying Operation.

- The kaolin clay based nanocomposites are developed for food packaging and these can be tested further for their food and hygienic compatibility so that these products can be used by the vendors.

- The mechanical characteristics and the distribution of filler inside the polymer can be further studied by using nanoindentation analysis.
- The melt flow singularity phenomenon can be further studied by blending HDPE with different polymers to study the effect of blending on the extrusion window of HDPE
- The developed nanocomposites are intended for food packaging applications and are hence produced utilizing no chemical modification of the filler or the polymer matrix, but if these are to be utilized in other packaging areas then the chemical modifications can be used to study the effect of compatibility on the final properties of the nanocomposites.
- The premixing technique can be used for producing commodity thermoplastic-biopolymer blends. Most of the biopolymers can be dissolved in water and can hence be distributed more uniformly throughout the polymer matrix using the premixing technique.

Appendix A1: Lists of all the specimens prepared along with their abbreviations used throughout the thesis are given below.

1: HDPE clay nanocomposites

Sample		Mass fraction of filler	Mass fraction of matrix
HDPE/1.0 BLX	HL1	0.01	0.99
HDPE/2.0 BLX	HL2	0.02	0.98
HDPE/3.0 BLX	HL3	0.03	0.97
HDPE/5.0 BLX	HL5	0.05	0.95
HDPE/10.0 BLX	HL10	0.1	0.9
HDPE/1.0 BHX	HH1	0.01	0.99
HDPE/2.0 BHX	HH2	0.02	0.98
HDPE/3.0 BHX	HH3	0.03	0.97
HDPE/5.0 BHX	HH5	0.05	0.95
HDPE/10.0 BHX	HH10	0.10	0.90
HDPE/0.5 Na-MMT	HM0.5	0.005	0.995
HDPE/1.0 Na-MMT	HM1.0	0.01	0.99
HDPE/2.5 Na-MMT	HM2.5	0.025	0.975
HDPE/5.0 Na-MMT	HM5.0	0.05	0.95
HDPE/10.0 Na-MMT	HM10.0	0.10	0.90
HDPE	HDPE	0	1

2: HDPE carbon filler nanocomposites

Sample		Mass fraction of filler	Mass fraction of matrix
HDPE/1.0 MWCNT	HM	0.01	0.99
HDPE/1.0 GO	HG	0.01	0.99
HDPE/3.0 CB	HCB	0.01	0.99
HDPE/5.0 MWCNT24	HM-24	0.01	0.99
HDPE/10.0 MWCNT48	HM-48	0.01	0.99
HDPE/1.0 MWCNT72	HM-72	0.01	0.99
HDPE	HDPE	0	1

3: LLDPE clay nanocomposites

Sample		Mass fraction of filler	Mass fraction of matrix
LLDPE/1.0 BLX	LL1	0.01	0.99
LLDPE /2.0 BLX	LL2	0.02	0.98
LLDPE /3.0 BLX	LL3	0.03	0.97
LLDPE /5.0 BLX	LL5	0.05	0.95
LLDPE /10.0 BLX	LL10	0.1	0.9
LLDPE /1.0 BHX	LH1	0.01	0.99
LLDPE /2.0 BHX	LH2	0.02	0.98
LLDPE /3.0 BHX	LH3	0.03	0.97
LLDPE /5.0 BHX	LH5	0.05	0.95
LLDPE /10.0 BHX	LH10	0.10	0.90
LLDPE /0.5 Na-MMT	LM0.5	0.005	0.995
LLDPE /1.0 Na-MMT	LM1.0	0.01	0.99
LLDPE /2.5 Na-MMT	LM2.5	0.025	0.975
LLDPE /5.0 Na-MMT	LM5.0	0.05	0.95
LLDPE /10.0 Na-MMT	LM10.0	0.10	0.90
LLDPE	LLDPE	0	1

4: Nylon12 clay nanocomposites

Sample		Mass fraction of filler	Mass fraction of matrix
Nylon12/1.0 BLX	NL1	0.01	0.99
Nylon12/2.0 BLX	NL2	0.02	0.98
Nylon12/3.0 BLX	NL3	0.03	0.97
Nylon12 /5.0 BLX	NL5	0.05	0.95
Nylon12 /10.0 BLX	NL10	0.1	0.9
Nylon12 /1.0 BHX	NH1	0.01	0.99
Nylon12 /2.0 BHX	NH2	0.02	0.98
Nylon12 /3.0 BHX	NH3	0.03	0.97
Nylon12/5.0 BHX	NH5	0.05	0.95
Nylon12/10.0 BHX	NH10	0.10	0.90
Nylon12	Nylon12	0	1

Appendix A2: Aspect ratio calculations by ImageJ®

The aspect ratio of the fillers inside the nanocomposites was analysed by using the ImageJ® software on TEM micrographs. ImageJ® is an image processing tool which is used for editing, analysing and modifying images. In the field of polymer microscopy, morphology based images obtained from TEM or SEM micrographs are analyzed by ImageJ® software. ImageJ® is able to calculate angles and distances and creates density histograms and line profile plots by using tools such as contrast manipulation, sharpening, smoothing, edge detection and median filtering.

The steps involved during the calculations of aspect ratio of the fillers inside the nanocomposites by ImageJ® software are given below:

1. Open ImageJ® software and select the “file > open”
2. Set measurement scale by using “scale bar” from the image directly.
3. Crop the image by selecting the “rectangular tool” button on the menu bar.
4. Adjust the “image brightness” from the menu bar “Image >Adjust>Brightness”
5. Threshold the particles to remove the unwanted background information “Image>Adjust> Threshold”
6. Measure the Particle dimension lengthwise using the “measure” button from the menu bar and add it to ROM manager list
7. Repeat the step 6 to measure as many as possible particles dimensions to get the average value at the end.
8. Repeat the whole process for measuring the thickness of the particles.

9. At the end the average value of length and thickness of the particles is calculated to determine the aspect ratio of the particle.